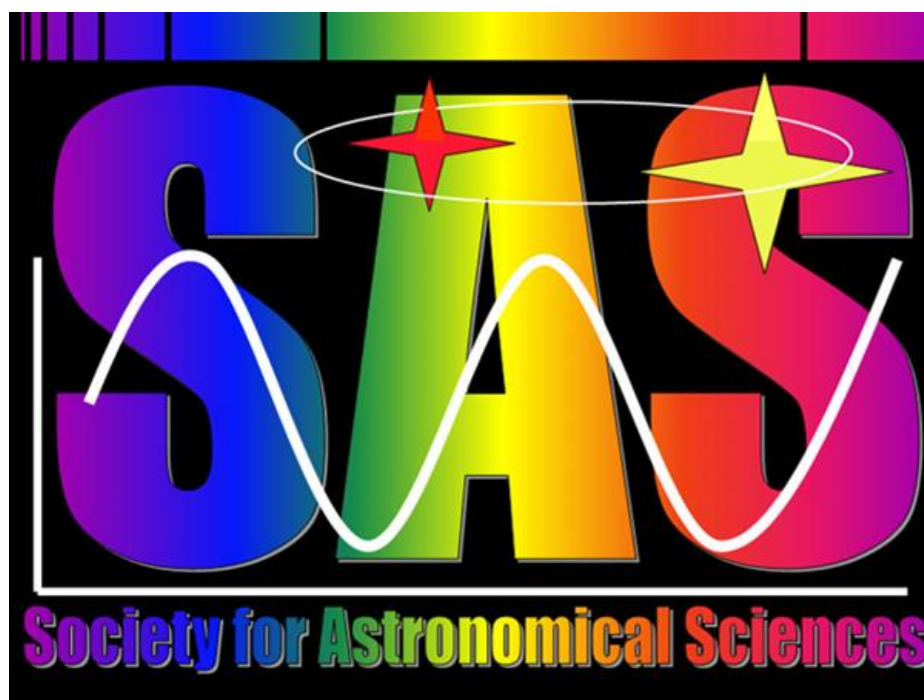


Proceedings for the 43<sup>rd</sup> Annual Conference of the  
Society for Astronomical Sciences

**SAS-2024**

**The Symposium on Telescope  
Science**



Editors:  
John C. Martin  
Robert K. Buchheim  
Robert M. Gill  
Wayne Green  
John Menke

June, 2024  
Ontario, CA

## **Disclaimer**

The acceptance of a paper for the SAS Proceedings does not imply nor should it be inferred as an endorsement by the Society for Astronomical Sciences of any product, service, method, or results mentioned in the paper. The opinions expressed are those of the authors and may not reflect those of the Society for Astronomical Sciences, its members, or symposium Sponsors

Published by the Society for Astronomical Sciences, Inc.  
Rancho Cucamonga, CA

First printing: June 2024

## **Photo Credits:**

### **Front Cover:**

Open Cluster M-67, everyone's favorite target for determining photometric transforms,  
John C. Martin, Henry R. Barber Observatory, University of Illinois Springfield

### **Back Cover:**

SA-200 Grism spectrum of Wolf-Rayet star HD214419  
Forrest Sims, Desert Celestial Observatory

# **TABLE OF CONTENTS**

---

<b><u>PREFACE</u></b>	<b>vi</b>
<b><u>SYMPOSIUM SPONSORS</u></b>	<b>viii</b>
<b><u>SYMPOSIUM SCHEDULE</u></b>	<b>x</b>
<b><u>PRESENTATION PAPERS (IN ORDER PRESENTED)</u></b>	
<b>AUGMENTING TIME-LAPSE IMAGING RESULTS USING LITERATURE AND CATALOG DATA</b> <i>TOM POLAKIS</i>	<b>1</b>
<b>INTRODUCING FAST: FAST ACQUISITION OF STREAKED TARGETS</b> <i>DANIEL PARROTT</i>	<b>7</b>
<b>AUTOMATING ZEROPOINT PHOTOMETRY WITH FREeware</b> <i>WAYNE GREEN &amp; FRANK PARKS</i>	<b>16</b>
<b>ZENITH SKY BRIGHTNESS MEASUREMENTS NEAR BARNESVILLE, GA USA</b> <i>RICHARD W. SCHMUDE, JR &amp; TY CLARK</i>	<b>21</b>
<b>QUANTIFYING ISOCHRONE FIT PRECISION (POSTER)</b> <i>SOHPIA BHATTI, KAVI BIDLACK, NATHAN BOWMAN, &amp; KARTHIKEYA VATTEM</i>	<b>26</b>
<b>ASTROMETRY WITH A DSLR CAMERA. OBSERVATION PLANNING, IMAGE ACQUISITION, AND DATA ANALYSIS</b> <i>FABRIZIO PINTO</i>	<b>29</b>
<b>SOLAR SAIL PROPELLED CUBESAT AUTONAVIGATION IN DEEP SPACE: EXPERIMENTAL ASTEROID TARGETING WITH IPHONE AND DSLR CAMERA</b> <i>KIYMET YILDIR</i>	<b>39</b>
<b>CLARIFYING THE NATURE OF SOLAR CYCLES</b> <i>SARA MARTIN</i>	<b>45</b>
<b>SPECKLE TOOLBOX ORBITS ANALYSIS</b> <i>RUSS GENET, DAVID ROWE, MICHAEL-JAMES ELLIS, &amp; PAUL MCCUDDEN</i>	<b>46</b>
<b>ORBITAL ANALYSIS OF THE BINARY STAR WDS 17166-0027</b> <i>MICHAEL-JAMES L. ELLIS</i>	<b>50</b>
<b>SPECKLE ANALYSIS OF TEN CLOSE BINARIES FROM MT. WILSON</b> <i>BRADLEY BRUNGARDT, ELIAS FAUGHN, JOHN MAJOR, PAUL MCCUDDEN, ZAIDA WEEMS, &amp; KASSIOPEIA WEHLITZ</i>	<b>57</b>
<b>SPECKLE INTERFEROMETRY FOLLOW-UP TO NEWLY DISCOVERED GAIA ASTROMETRIC BINARIES</b> <i>MARK COPPER, RUSSELL GENET, DAVID ROWE, THOMAS SMITH, PAUL MCCUDDEN, &amp; MICHAEL-JAMES ELLIS</i>	<b>69</b>

<b>GAIA BINARY FOLLOW-UP WITH GEMINI SPECKLE INTERFEROMETRY</b> <i>ZACH HARTMAN, RUSSELL GENET, MARK COPPER, PAUL MCCUDDEN, MICHAEL-JAMES ELLIS, &amp; LOU JACKSON</i>	<b>76</b>
<b>IT HER, A MISCLASSIFIED ECLIPSING BINARY (POSTER)</b> <i>LAURENT CORP &amp; JEAN-BRUNO DESROSIERS</i>	<b>77</b>
<b>CCD PHOTOMETRIC MEASUREMENTS OF DY PEGASI</b> <i>DAVID BUATISTA</i>	<b>94</b>
<b>ZTF: DISAMBIGUATE VARIABLES THROUGH FOLLOW-UP</b> <i>ASHISH MAHABAL</i>	<b>96</b>
<b>OPTICAL SETI SEARCHES: AMATEUR'S INSIDE TRACK?</b> <i>RICHARD H. STANTON</i>	<b>97</b>
<b>THE O'CONNELL EFFECT IN ECLIPSING BINARY STARS</b> <i>ERIC CRAINE</i>	<b>104</b>
<b>NEW TECHNOLOGIES AND DANGEROUS QUESTIONS IN ASTRONOMY EDUCATION</b> <i>RACHEL FREED</i>	<b>107</b>
<b>AN OFF-THE-SHELF, FULLY-INSTRUMENTED RESEARCH OBSERVATORY FOR A RURAL COMMUNITY COLLEGE CONSORTIUM</b> <i>LOU JACKSON, RUSSELL GENET, ANN KNIGHTS, MICHAEL-JAMES ELLIS, ERIC BLACKHURST, CAMERON VITTIGLIO, &amp; PAUL MCCUDDEN</i>	<b>108</b>
<b>WIDEBAND PHOTOMETRY OF THE SEMI-REGULAR VARIABLE STAR RZ-ARIES</b> <i>RICHARD SCHMUDE, QASIM AHMED, REBECCA SMYLY, &amp; DENIS MARTINEZ</i>	<b>114</b>
<b>TIME SERIES ANALYSIS OF VARIABLE STARS IN SELECTED GLOBULAR CLUSTERS</b> <i>DOUGLAS WALKER</i>	<b>117</b>
<b>ANALYSIS OF SX PHOENICIS VARIABLE STARS IN THE OMEGA CENTAURI GLOBULAR CLUSTER</b> <i>DOUGLAS WALKER</i>	<b>136</b>
<b>DENEK AND THE ALPHA CYGINI VARIABLES</b> <i>JOYCE GUZIK, BRIAN KLOPPENBORG, &amp; JASON JACKIEWICZ</i>	<b>145</b>
<b>A LIFETIME OF TOTAL ECLIPSES</b> <i>JOHN MENKE</i>	<b>154</b>
<b>AZ CAS OBSERVATION CONCLUSIONS</b> <i>JOHN MENKE</i>	<b>158</b>
<b>SPECTROSCOPIC OBSERVATIONS OF THE 2024 ECLIPSE OF V695 CYG</b> <i>BOB BUCHHEIM</i>	<b>165</b>

## ***PREFACE***

---

Welcome to the 42nd annual Symposium of the Society for Astronomical Sciences. Thank you to our returning members and welcome to first time participants. We are grateful for your support and to be able to gather once again to share our interests and the fruits of our labor.

This year's agenda reflects the broad diversity of interests among SAS members, with papers covering photometry, spectroscopy, interferometry and astrometry; instruments ranging from eyeballs to CCDs and spectrographs; and projects ranging from education to citizen-science to a variety of astronomical research activities.

It takes many people to have a successful conference. The SAS Program Committee members are:

Robert Gill	Robert D. Stephens	John C. Martin
Wayne Green	Jerry Foote	Tony Rodda
Robert Buchheim	John Menke	

SAS Membership dues and Registration fees do not fully cover the costs of the Society and the annual Symposium. We owe a great debt of gratitude to our corporate sponsors for this year's Symposium: DC-3 Dreams Software, PlaneWave Instruments, Sierra Remote Observatories, Optec Optical and Electronic Products, and Sky & Telescope Magazine. Thank you!

We are grateful to the presenters, the attendees, and the community of practice in small-telescope research that is the heart of the SAS. We thank all of you for making the SAS Symposium one of the premiere events for professional-amateur collaboration in astronomy.

2024 May

## ***Symposium Sponsors***

---

The Society for Astronomical Sciences thanks the following companies for their participation and financial support. Without them, this conference would not be possible.



### **DC3 Dreams Software**

Developers of ACP Observatory Control Software

<http://www.dc3.com/>



### **PlaneWave Instruments**

Solving astronomical problems through the pursuit of the perfect telescope.

<http://planewave.com>



### **Sierra Remote Observatories**

World Class Remote Imaging and Data Acquisition from the Sierra Nevada Mountains

Unparalleled Seeing, Access and Support

<http://www.sierra-remote.com>



**Woodland Hills Camera & Telescopes**

Providing the best prices in astronomical products for more than 50 years.

<https://www.telescopes.net>



**Optec Optical and Electronic Products**

Helping Astronomers Measure The Stars Since 1979

<https://www.optecinc.com>



**S O F T W A R E   B I S Q U E**

*Superior imaging solutions for discriminating astronomers.*

---

**Software Bisque**

Superior imaging solutions for discriminating astronomers.

<https://www.bisque.com>



**Sky & Telescope Magazine**

The Essential Magazine of Astronomy

<http://www.skyandtelescope.com/>

## ***Symposium Schedule***

<b>Thursday June 20: Workshops</b>		
8:00	Registration	
	Morning Workshop	
9:00	Meteors and Orbits: The Global Meteor Network	Dr. Denis Vida
12:00	<i>Lunch Break</i>	
	Afternoon Workshop: Tricolor Imaging for Science	
13:00	Tri-Color Imaging for Science	John Hoot
15:30	AAVSO Perspective on Tri-color photometry	Dr. Brian Kloppenborg
16:00	<i>Welcome Reception</i>	

<b>Friday June 21: Technical Papers</b>		
	Registration	
8:00	Welcome	Bob Buchheim
8:15	Augmenting Time-lapse Imaging Results Using Literature and Catalog Data	Tom Polakis
8:40	Introducing FAST: Fast Acquisition of Streaked Targets	Daniel Parrott
9:05	Automating Zeropoint Photometry with Freeware	Frank Parks
9:30	Zenith sky brightness measurements near Barnesville, GA USA	Richard Schmude
9:40	<i>Sponsor Introduction</i>	
9:50	<i>Morning Break</i>	
10:10	Quantifying Isochrone Fit Precision (Poster)	Sophia Bhatti
10:20	Astrometry with a DSLR Camera. Observation Planning, Image Acquisition, and Data Analysis	Fabrizio Pinto
10:45	Solar Sail Propelled CubeSat Autonavagation in Deep Space: Experimental Asteroid Targeting with iPhone and DSLR Camera	Kıymet Yıldır
11:10	Clarifying the Nature of Solar Cycles	Sara Martin
11:55	<i>Sponsor Introduction</i>	
12:05	<i>Lunch Break</i>	
13:05	Speckle Toolbox Orbits Analysis	Russ Genet
13:30	Orbital Analysis of the Binary Star WDS 171666-0027	Michael-James Ellis
13:55	Speckle Analysis of Ten Close Binaries from Mt. Wilson	Bradley Brungardt
14:20	Speckle Interferometry Follow-Up to Newly Discovered Gaia Astrometric Binaries	Mark Copper
14:45	<i>Sponsor Introduction</i>	
14:55	<i>Afternoon Break</i>	
15:15	Gaia Binary Follow-up with Gemini Speckle Interferometry	Zach Hartman
15:40	IT Her, A Misclassified Eclipsing Binary (Poster)	Laurent Corp (RKB)
15:50	CCD photometric Measurements of DY Pegasi	David Bautista
16:00	ZTF: Disambiguate Variables Through Follow-up	Ashish Mahabal
16:25	Upgrading a 24-inch Cassegrain to Direct-Drive	Bruce Howard
16:35	Optical SETI Searches: Amateur's Inside Track?	Richard H. Stanton
17:00	<i>Evening Break</i>	
19:00	Panel Discussion: Role of Small Telescope Research in 2024 and Beyond	



## ***Symposium Schedule***

<b>Saturday June 22: Technical Papers</b>		
8:00	<i>Registration</i>	
8:30	Welcome	Bob Buchheim
8:45	The O'Connell Effect in Eclipsing Binary Stars	Eric Craine
9:10	New Technologies and Dangerous Questions in Astronomy Education	Racheal Freed
9:35	An Off-the-Shelf, Fully-Instrumented Research Observatory for a Rural Community College Consortium	Lou Jackson
10:00	<i>Sponsor Introduction</i>	
10:10	<i>Morning Break</i>	
10:30	Wideband Photometry of the Semi-Regular Variable Star RZ-Aries	Richard Schmude
10:55	Time Series Analysis of Variable Stars In Selected Globular Clusters (Poster)	Douglas Walker
11:05	Analysis of SX Phoenicis Variable Stars in the Omega Centauri Globular Cluster	Douglas Walker
11:30	Asteroid Occultation Timing – New and Improved	Steve Conard
11:40	<i>Sponsor Introduction</i>	
11:50	<i>Lunch Break &amp; Group Photo</i>	
13:05	Photometry of Near-earth Asteroid 439437 (2013 NK4)	Tom Polakis
13:15	Deneb and the Alpha Cygini Variables	Joyce Guzik
13:40	A Lifetime of Total Eclipses	John Menke
13:50	AZ Cas Observation Conclusions	John Menke
14:15	Spectroscopic Observations of the 2024 Eclipse of V695 Cyg	Bob Buchheim
14:40	Good Afternoon, and Good Luck	Bob Buchheim
16:00	<i>Closing Reception in Breakout Room</i>	



# Augmenting Time-lapse Imaging Results Using Literature and Catalog Data

*Tom Polakis*  
*Command Module Observatory (V02)*  
*121 W. Alameda Dr., Tempe, AZ 85282*  
*tpolakis@cox.net*

---

## Abstract

Time-lapse videos are commonly created with time scales ranging from minutes to hours, but creating useful time-lapse sequences for objects beyond our Solar System often requires decades for changes to be detectable. The best candidates for showing motion include nearby high-proper-motion stars, open clusters, planetary nebulae, and supernova remnants. In this work, images taken recently with a 32cm telescope in Arizona are compared with archive images from the turn-of-the-century photos or Palomar Sky Survey images from the 1950's and 1990's. Angular displacements measured from the image pairs and parallaxes from star catalogs are used to compute transverse velocities for nearby stars and supernova remnants. Proper motions found in these catalogs are used to determine open cluster membership. Published expansion rates for planetary nebulae are compared to those derived from the image pairs.

---

## 1. Introduction

Time-lapse imaging is a useful technique for visualizing slow-moving processes. Results are both aesthetically pleasing and informative. Due to the vast distances involved in astronomy, motions and changes in structure are typically imperceptible, despite the high velocities. Therefore, astronomical time-lapse videos require long observing intervals.

Nearly all of the time-lapse work done in astronomy involves the Solar System, featuring such phenomena as the sky moving over a landscape, solar prominences, and cloud motions on Jupiter. At distances outside the solar system, it becomes clear that the intervals between frames must be increased to years or decades in order to discern the extremely small angular motions.

Archive imagery exists for the entire sky in the form of sky surveys, and for particular showpiece objects as scanned photographs from the great observatories. In this work, these images were compared with those taken in recent years from Command Module Observatory, in Tempe, Arizona.

This project was undertaken mostly to relate a fascination with a dynamic universe, despite its static appearance during a human lifetime. Probing further, it was found that available catalogue data could be used to augment the time-lapse sequences. Transverse velocities, planetary nebula expansion rates, and open cluster membership are derived from the images, and described in this paper.

## 2. Images: Archived and Recent

The bulk of archive images were obtained using digitized images from the Palomar Sky Survey. Two survey generations were produced in the 1950's and 1990's. Scanned plates from the 48-inch Oschin Schmidt Telescope remain a valuable asset for researchers. For this work, the Digitized Sky Survey Plate Finder (STScI 2024) was used to locate and download regions of interest. Photographs with larger scale than Sky Survey scans were often found by image searches. The earliest of these were taken by telescopes at Lick, Yerkes, and Mount Wilson Observatories at the turn of the 20th century.

Recent images were all taken from Command Module Observatory (V02) in Tempe, Arizona, which houses a 32cm f/6.7 modified Dall-Kirkham telescope and an SBIG ST-6303 CCD camera. The site is urban, with a sky background that is more than 3 magnitudes above the natural level. Therefore, unfiltered images have greatly limited exposure times, and can reach only to magnitude  $V=19$  in the best conditions. Often, a narrowband Hydrogen Alpha filter was used to advantage on ionized objects.

Images taken with such different instruments have discordant plate scales and orientations, so registration of the image pairs always begins with reducing the size of the larger image to that of the smaller one. Even after resizing and rotating the frames to match, distortion across the images causes small differences in star positions, so software that performs an astrometric solution is required to produce an adequate match. In an attempt to make the image pairs as similar as possible, sharpness, brightness, and contrast is

matched to the “lowest common denominator” of the two images. After a suitable match between images is obtained, they are labeled with dates. In cases where motions are too subtle, arrows or gridlines are often added.

### 3. Catalog Data

The European Space Agency’s GAIA space telescope has produced a catalogue of 1.8 billion stars (DPAC 2024) – more than 1% of the Milky Way’s content. Fields have been imaged over multiple epochs with an astrometric precision of less than 1 milliarcsecond. The resulting catalog is queried at the VizieR Catalogue (2024) site. For this effort, the magnitudes, proper motions, and parallaxes were tabulated for objects of interest. Simple mathematical equations can be used to compute such stellar parameters as distances, transverse space velocities, and luminosities.

For objects other than stars, literature was consulted using queries of the Astronomical Data System site (ADS 2024).

### 4. Image Pairs

Obviously, time-lapse sequences are best viewed as video, and not well-suited for the format of a static paper. Attempts are made to show motions in the illustrations. A full gallery of deep-sky time-lapse sequences may be found at the author’s PBase site. [https://pbase.com/polakis/timelapse\\_deepsky](https://pbase.com/polakis/timelapse_deepsky)

#### 4.1 Barnard’s Star

With a distance of less than 2 parsecs and a high space velocity, Barnard’s Star (V2500 Oph) moves faster across our line of sight than any other. During a typical human lifetime, it will have moved roughly one quarter of a degree. This makes it an excellent target for showing its motion over a short interval.

Figure 1 is an overlay of two images taken at V02. Using astrometric solutions, the motion over a period of nearly 8 years was found to be 81.84 arcseconds. When converted to a proper motion in terms of milliarcseconds (mas) per year, a good agreement with the GAIA catalog values is shown, as shown in Table 1.



Figure 1. Overlaid images of Barnard’s Star

Date	RA	Dec	Proper motion (mas/yr)				
			Delta years	V02 East	V02 North	GAIA East	GAIA North
4/15/2016	17 57 47.66	04 44 25.1					
3/17/2023	17 57 47.30	04 45 36.7	7.88	-796.7	10352.0	-801.6	10362.4

Table 1. Proper motion of Barnard’s Star

#### 4.2 IC 1805 Foreground Stars

Nearby star-forming regions often show motions in time-lapse sequences spanning many decades. These motions are largely random, and their directions of movement are not intuitive based on the profiles of nebulous fragments.

IC 1805 is called the “Heart and Soul Nebula” due to its appearance in deep, wide-field images. Using a baseline of 68 years, no motions down to the arcsecond level were detectable in the image pair. This shouldn’t be surprising, since the nebula is 2.3 kpc away; motions amounting to a couple tenths of an arcsecond are too small to be evident at this image scale.

However, many foreground stars showed significant motion during the observing interval. Twenty-five of these stars with high proper motions are identified in Figure 2.

Of these 25 stars, 23 moved to the southeast, leading to the notion that they may be members of a common association. Coordinates of the foreground stars were entered into the GAIA DR3 catalog, using the VizieR interface, and the parallaxes and proper motions shown in Table 2 were returned. It is apparent that the values are too discordant for these stars to be associated.

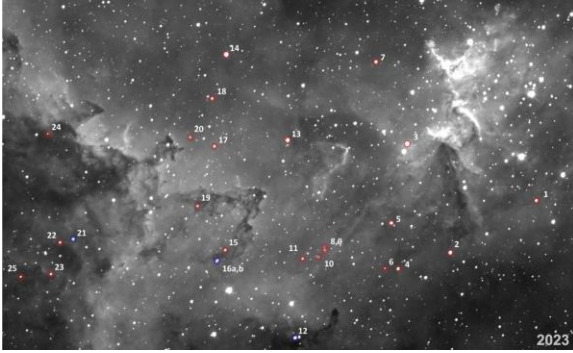


Figure 2. IC 1805 foreground stars

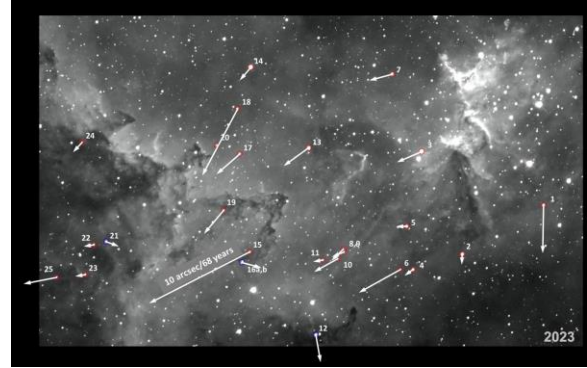


Figure 3. IC 1805 stars – angular proper motions

#	Dist (ly)	PM 68 yr (arcsec)
1	763	4.2
2	2641	0.8
3	946	2.3
4	1499	0.9
5	2828	0.8
6	524	4.2
7	727	2.2
8	4216	1.3
9	1854	1.4
10	574	2.3
11	1671	0.8
12	468	2.5
13	749	2.8
14	1200	1.6
15	278	10.0
16a	748	1.9
16b	746	1.9
17	983	2.7
18	183	6.5
19	450	2.7
20	--	--
21	952	1.1
22	5258	1.0
23	2974	0.5
24	2334	1.1
25	1094	3.1

Table 2. IC1805 stars - catalog data

The data table provided the information needed to create vectors that represent both angular and physical proper motions. They are shown with arrows and a scale represented by the largest arrow in Figures 3 and 4. Even the highest apparent proper motion is only 10 arcseconds in 68 years, while the fastest mover across our line of sight has a velocity of 107 km/s.

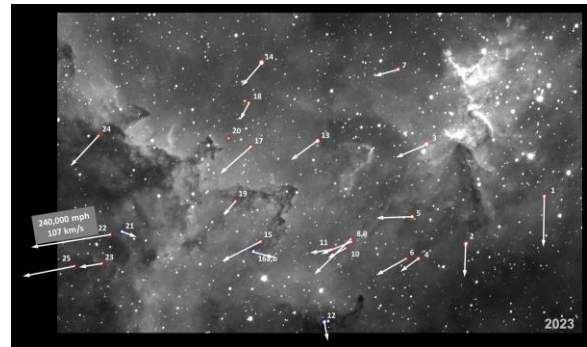


Figure 4. IC1805 stars – physical proper motions

The star extraction add-in StarXTerminator (RC Astro 2024) was used to remove all but the high proper motion stars, as shown in Figure 5. Knowing the apparent magnitudes and parallaxes, the absolute magnitudes are shown for comparison in the same figure. Absolute magnitudes of these nearby stars range from 1.6 to 9.0, or roughly one twentieth to 50 times as luminous as the Sun.

### 4.3 M44: Cluster motion and membership

At a distance of 187 pc, M44, the Beehive Cluster, is among the ten nearest open clusters. As such, it is an excellent candidate for showing its proper motion over a short observing interval.

Indeed, a pair of images spanning 70 years since 1954 contains dozens of bright stars near its center that move to the southwest. It is evident at a glance which stars are members of the cluster, all sharing the same proper motion. An image of the central region of M44 appears in Figure 6, with members and non-members of the star cluster highlighted.

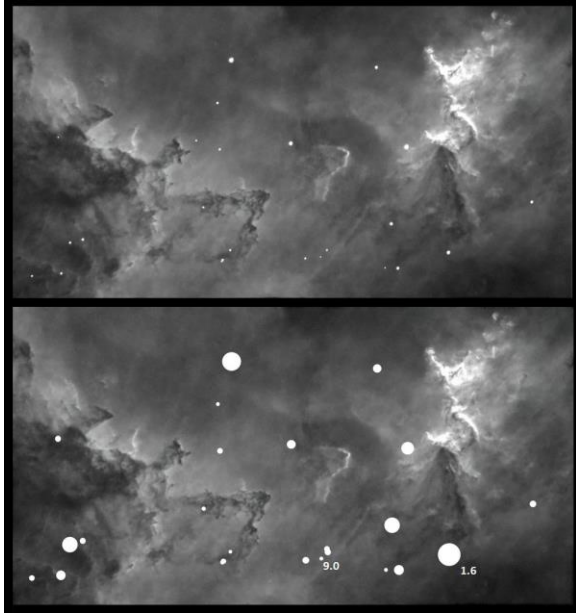


Figure 5. IC1805 apparent and absolute magnitudes

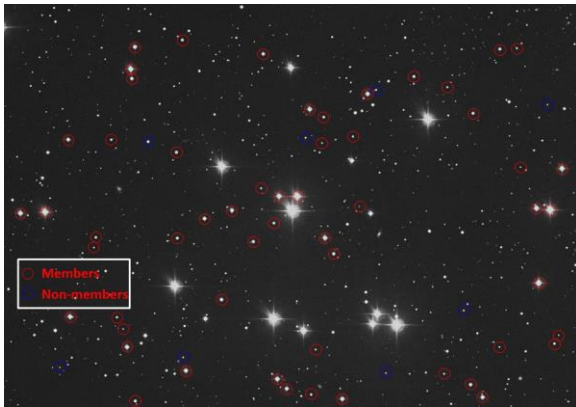


Figure 6. M44 cluster membership

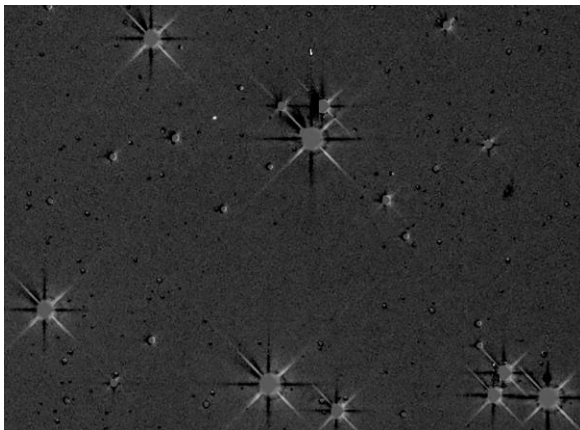


Figure 7. M44 difference image: 1954-2024

Obviously, it is difficult to illustrate motions in a static medium such as a science paper. One approach is a difference image, in which the earlier image is subtracted from the more recent image. In Figure 7, the V-shaped asterism is prominent, and moving stars in M44 appear as crescents “illuminated” in the direction of motion.

It was suspected that the cluster’s plotted diameter of roughly  $1\frac{1}{2}^\circ$  shown on charts is too small. GAIA DR3 was queried with the constraints of parallax between 5 and 6 milliarcseconds and proper motions in RA of -40 to -30 mas/year, and declination of -15 to -11 mas/year. A radius of  $3^\circ$  from its center was used. The query returned a total of 1017 stars matching these constraints. For comparison, identical queries run at several other locations turned up less than a half dozen stars. Hence, the 1017 stars are members of the Beehive.

By importing the 1017 star positions and magnitudes into a spreadsheet, a star chart could be created as a “bubble plot.” Figure 8 shows the true extent of cluster stars in M44. Note the “V” in the center of the chart. The diameter of the cluster is roughly 20 pc.

By overlaying an image on a star chart of only M44’s members, the cluster’s non-members become apparent. They are highlighted in Figure 9, which covers a  $1^\circ$  square field.

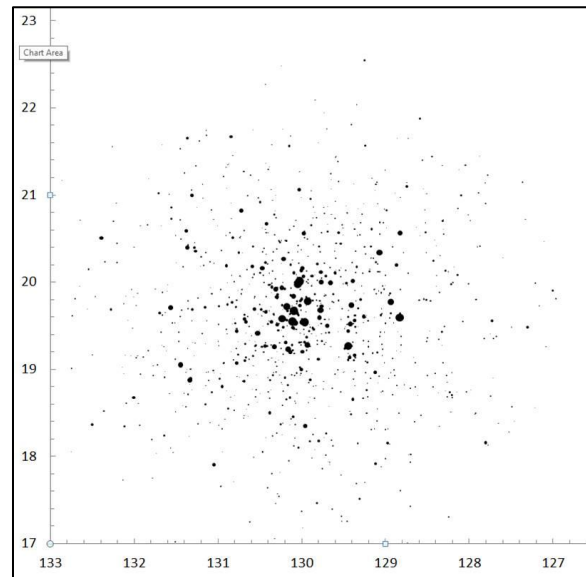


Figure 8. M44 member stars out to  $6^\circ$  radius

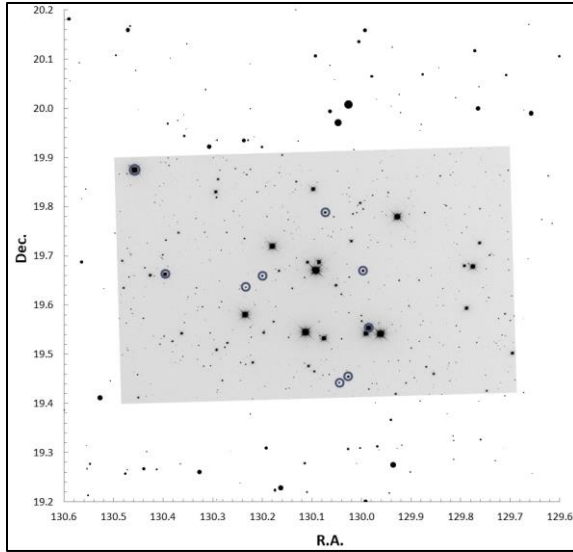


Figure 9. M44 image overlay showing non-members

Object	Dist.* pc	Scale		Year 1	Year 2	Defl. px	Edge V km/s	Spectro V* km/s	Factor
		arcsec/px	au/px						
M27	380	0.44	167	1899	2019	5	33	32	1.0

\* (2013) A&A 558, 78

Table 3. M27 computed expansion velocity.

#### 4.4 Expansion of Planetary Nebula M27

M27, the Dumbbell Nebula, is one of the closest bright planetary nebulae, located only 380 pc from the sun. Images of good quality exist from the turn of the 20<sup>th</sup> century. Such an image from 1899 was used to create an image pair spanning 120 years, shown in Figure 10.

Knowing the distance to M27, observing interval, and expansion in arcseconds from the images, we can estimate the lateral velocity due to expansion, and compare it to the spectroscopically determined velocity (Jacob et al. 2013). This is shown for M27 only in Table 3.

Since the deflection was measured with an integer number of pixels, it could be considered beginner's luck that the expansion velocity matched the published value so closely. Hence, an additional nine planetary nebulae that showed clear expansion were compared using this same method. Table 4 summarizes those results. In most cases, the agreement with spectroscopically determined expansion velocities is acceptable.

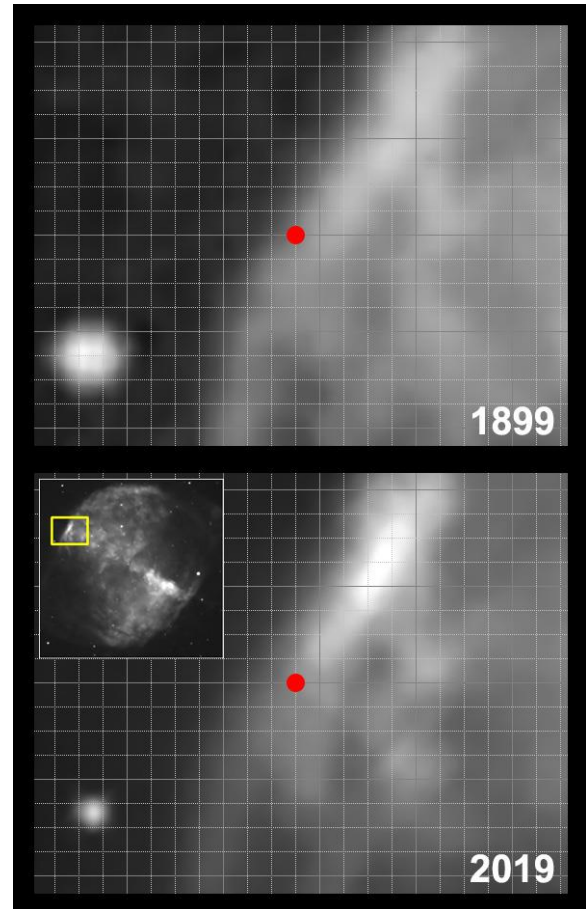


Figure 10. M27 expansion in 120 years

Object	Dist.* pc	Scale		Year 1	Year 2	Defl. px	Edge V km/s	Spectro V* km/s	Factor
		arcsec/px	au/px						
NGC 7293	220	1.47	322	1914	2015	4	60	21	2.9
NGC 246	500	0.90	448	1954	2019	1.5	49	35	1.4
NGC 7008	700	0.31	214	1914	2019	5	48	37	1.3
M57	700	0.35	242	1914	2015	3	34	22	1.5
NGC 1501	720	0.15	108	1914	2019	7	34	40	0.8
M97	760	0.80	608	1899	2019	1.5	36	34	1.1
JE 1	1150	0.85	980	1954	2018	1	73	24	3.0
NGC 7662	1260	0.11	140	1899	2019	4	22	27	0.8
NGC 7009	1450	0.11	160	1914	2019	3	22	25	0.9

\* (2013) A&A 558, 78

Table 4. Planetary nebulae expansion velocities

#### 4.5 Expansion of S/N Remnant M1

At a distance of 2 kpc, one would not expect to be able to detect motions in the Crab Nebula, even over a century of observing. However, supernova remnants move with velocities that are a couple orders of magnitude greater than typical velocities we associate with Milky Way objects. Figure 11 illustrates the position of a filament at three epochs. Since the pulsar is located at the center, it can be used for the 1054 epoch.

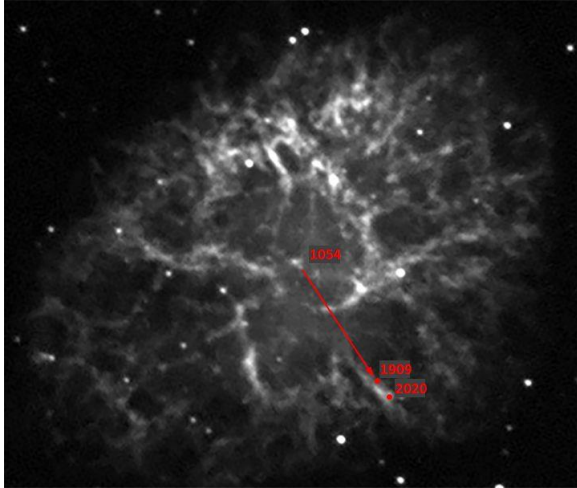


Figure 11. M1 expansion at three epochs

An archive image from 1909 was compared against one that was taken in 2020, and a deflection of nearly 14 arcseconds was measured. Both approaches were used to determine the expansion velocity of the Crab Nebula, and are summarized in Table 6.

Year 1	Year 2	Distance pc	Displacement arcsec	Angular rate mas/yr	Rate mph	Rate km/s
1054	2020	2000	107.9	111.7	2,363,694	1057
1909	2020	2000	13.9	124.9	2,643,601	1182

Table 6 Calculated expansion velocity of M1

The most recently published expansion velocity of M1 is 1250 km/s (Blair et al. (2023)), and these photographically determined values are in good agreement with that value.

## 5. Conclusions

Time-lapse sequences of objects outside the Solar System have proven to be an excellent visualization tool. Applying published catalog data to the images enhances the experience.

## 6. Acknowledgments

The author would like to collectively thank members of various Arizona astronomy clubs for their encouragement and useful suggestions. Jennifer Polakis is as good of a sounding board as one could hope for, showing remarkable patience with the author's enthusiasm for esoteric topics. Mike Wiles was helpful with reviewing and clarifying the manuscript.

## 7. References

ADS (2024). Astrophysics Data System Classic Form. <https://ui.adsabs.harvard.edu/classic-form>

Blair, W.P. & 5 co-authors (2023). "Expansion and Evolution of the Crab Nebula: A 23+ Year HST Perspective." HST Proposal Cycle 31, **ID17500**.

DPAC (2024). Data Processing and Analysis Consortium. <https://www.cosmos.esa.int/web/gaia/dpac/consortium>

Jacob, R., Schonberner, D., and Steffen, M. (2013). "The evolution of planetary nebulae VIII. True expansion rates and visibility times." *Astron. Astrophys.* **558**, 78-98."

RC Astro (2024). StarXTerminator. <https://www.rc-astro.com/software/sxt/>

STScI (2024). DSS Plate Finder. [https://archive.stsci.edu/cgi-bin/dss\\_plate\\_finder](https://archive.stsci.edu/cgi-bin/dss_plate_finder)

VizieR Catalogue (2024). VizieR search page. <https://vizier.cds.unistra.fr/viz-bin/VizieR>



# Introducing FAST: Fast Acquisition of Streaked Targets

Daniel Parrott  
tychotracker@gmail.com

---

## Abstract

The advent of modern CMOS cameras has enabled amateur astronomers to capture wide field images of the night sky with great detail. Many have utilized this new capability to aid in the search of minor planets, comets, and other moving objects including artificial satellites and debris. However, the larger sensors result in an increase in processing times. An optimal detection and tracking algorithm would allow for a turnaround time equal to or less than the amount of time it took to acquire the images. Since faster moving objects typically necessitate shorter exposures, the total acquisition time can be quite short. Additionally, due to the wide field, the algorithm should be able to robustly isolate, track, and identify the multiple objects that may pass through the field during the dwell time. Furthermore, as a number of these objects have rotating or tumbling motion, an ideal algorithm should tolerate high variability in brightness. A new detection algorithm, called Fast Acquisition of Streaked Targets (FAST), has been developed which aims to meet these criteria. As one example, it can process a set of 90 images, each 26 megapixels in size, in under 60 seconds, correctly identifying dozens of objects even in a crowded star field. As its name implies, it excels at detection of objects presenting a streaked profile, which can occur due to a combination of fast movement relative to the exposure times and plate scale. However, FAST can also detect objects having only a few pixels of streak, enabling it to quickly search a very wide range of possible motions. This paper describes the three parts that make up the overall algorithm: object detection, tracking, and identification. Finally, a number of datasets captured with various instruments will be presented for evaluation of the algorithm.

---

## 1. Introduction

There are a number of techniques to detect and track moving objects in a sequence of astronomical images. The conventional four frame technique involves capturing an image of a given field, waiting 20 minutes, returning to said field, and repeat until four images of that field have been captured. Moving objects can then be detected provided that they have sufficient signal-to-noise ratio (SNR) on each image (Denneau, 2013). Synthetic tracking (ST) is another technique which allows one to detect faint objects having a much lower SNR, as it operates on stacked images. In a blind search, ST processes thousands of stacked images, each exploring a different motion vector (Heinze, 2015). One downside to ST is that a robust implementation typically involves using the median stack, which necessitates that the object be present on at least 50% of the frames, which can be problematic if one has dwelled on a field for a long time with a narrow field of view. ST also becomes prohibitively time-consuming (or computationally demanding) when the motion of the object is sufficiently fast such that it imparts a streaked profile on the exposure, as motion rates must be explored on both axes of the search grid, resulting in an exponential increase in motion vectors for blind searches. Typically, this increase is mitigated for optimized surveys where the total time from first exposure to last is proportional to the speed of the object: a fast object

paired with a short dwell time can be identified with reasonable computation times. However, surveys would like to explore a wide range of motions, accommodating streaked objects, and for this a new algorithm has been developed: Fast Acquisition of Streaked Targets (FAST). The algorithm described in this paper encompasses detection, tracking, and identification of moving objects, including near earth asteroids (NEAs) and artificial satellites.

As one example, FAST can fully detect, track, and identify objects from a dataset of 90 exposures, each 26 megapixels in dimensions, in under 60 seconds, independent of object speed. It also accommodates large variability in object brightness and robustly isolates and tracks multiple objects in the same field, while other algorithms such as the Fast Radon Transform can have difficulties dealing with images that contain multiple streaked objects (Nir, 2018). Similar to ST, the FAST algorithm also operates well even in crowded star fields. Finally, FAST can also process objects having only a few pixels of streak, being able to detect very slow-moving objects alongside extremely fast-moving objects, as will be shown in one of the examples.

One application of FAST is to dwell on a field with a wide field instrument, such that any object that passes through the field during that time – even for just a few frames – will be detected. This makes it ideal for uncued searches of the GEO belt region or for blind detection of fast-moving asteroids. An added module, “Monitor Queue” has also been implemented to

further automate data processing so that an operator can leave the software unattended through the night.

## 2. Object Detection

At a most basic level, a detectable object imparts some sort of signal on an image. In the case of an object having a very low signal-to-noise ratio (SNR), this can present itself as an almost imperceptible fluctuation in a single pixel value on a single image. On the other end of the spectrum, an object having high SNR will contribute a vastly noticeable increase across multiple pixel values. One typical approach is to set a threshold corresponding to the “detection SNR” – that is, the minimum SNR that an object must have on a given image. As one extracts sources from an image, the SNR of each source is compared to this threshold, and those sources that are below the threshold are removed from further consideration. However, because the goal is to detect objects having motion, it is possible to take advantage of the fact that the pixel value will undergo a change in the provided dataset. One can then proceed to compute statistics for every pixel in the image, determining the average and standard deviation of each pixel. The signal of moving objects will therefore produce a new pixel value equal to the average plus some number of standard deviations. Therefore, an initial threshold requirement is that a detection pixel must have a value that is some number of sigmas away from the average pixel value spanning the images in the dataset.

### 2.1 Split Detections

Another aim of the algorithm is to be able to detect streaks even in crowded star fields. Figure shows an example of the Solar Dynamics Observatory (NORAD #36395) satellite passing through a crowded field.

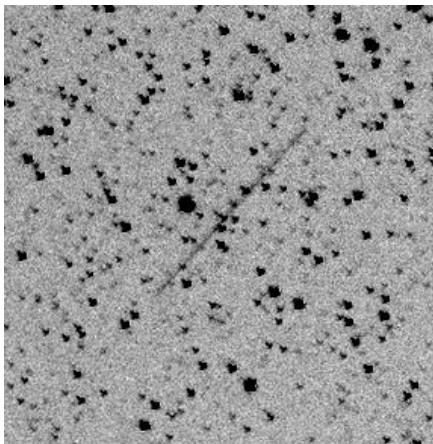


Figure 1: Streak in Crowded Star Field

As can be seen from this example, the streak passes in front of no fewer than six stars. The consequence of this is that because pixels occupied by stars typically have a higher noise variance than pixels of the background, the faint signal of the streak is unlikely to exceed the detection threshold of the star pixels, which means that rather than having one coherent detection, the streak will be broken up into several split detections.

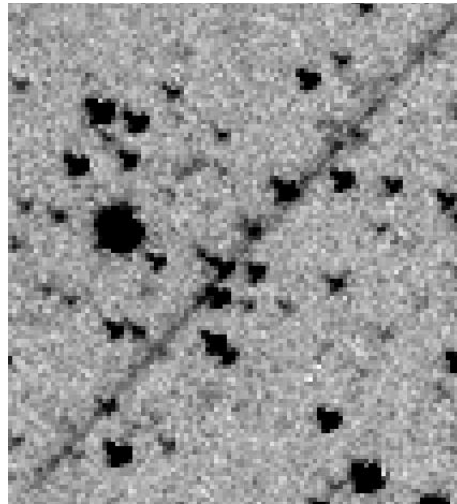


Figure 2: Streak at 4x Zoom

Figure shows the same streak at a higher zoom level for better inspection. Then, Figure shows what the streak looks like after having applied detection thresholds. The white background presents all pixels that failed to satisfy the detection threshold. Ideally, all pixels except those belonging to the streak would be in this white background, however, as can be seen there are some isolated clusters of noise that are visible throughout the image, outside the green rectangle.

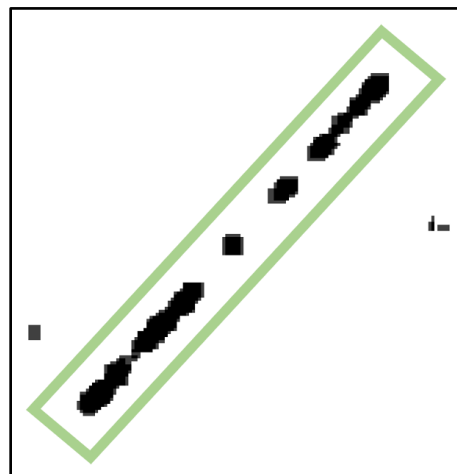
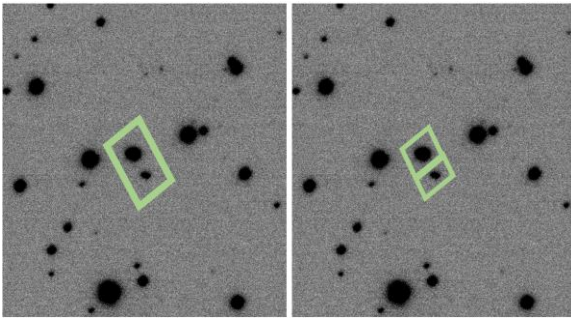


Figure 3: Streak with Detection Thresholds

The process of handling the split detections is rather straightforward: the algorithm iterates through all detections extracted from the image, and compares the endpoints of each detection to that of the endpoints of other detections. If any two pairings of endpoints are within some predetermined pixel proximity of each other, then the detections are merged into one. This “predetermined” proximity is therefore a configurable value that the end-user can optimize for their particular system. However, extensive analysis of multiple datasets across multiple instruments (having different plate scales, noise characteristics, etc.) has yielded an optimized value of 16 pixels that adequately merges nearly all split detections, while not over-enthusiastically merging independent detections.



**Figure 4: Falcon 9 Booster and IM-1 Lunar Lander.**

Figure shows an example of setting this parameter to 32 pixels, where there are two distinct objects: the fainter object being the Intuitive Machine’s IM-1 Lunar Lander (NORAD #58963), and the brighter object being the SpaceX Falcon 9 rocket booster (NORAD #58964) that launched it towards the Moon. The left side of the image shows how the two distinct objects were treated as one object when using 32 pixels as the proximity limit, while the right side shows how they are correctly classified as two distinct objects when using 16 pixels as the limit. Note that although these objects do not convey a recognizable streak – in fact they appear very much identical to the stars around them – they are nonetheless easily extracted by the algorithm as moving objects, showing that the algorithm is also capable of working with objects having minimal or almost no streak.

### 3. Tracking

After having generated detections for each image in the dataset, the next step is to identify tracks that comprise a series of two or more detections. Tracking is important for several reasons. First, it allows one to work with very faint detections that could likely be false detections. But by applying a tracker, the false detections will be eliminated because they (usually) do

not track consistently across multiple images. Secondly, a track allows one to determine the motion of the object, which is useful for identification and determining follow-up parameters. Finally, tracking allows one to isolate multiple objects that may appear in the same field, which happens regularly with wide-field instruments.

The FAST algorithm uses a 10-step tracking process:

1. Identify tracks
2. Update track motion
3. Score tracks
4. Sort tracks
5. Merge tracks
6. Centroid tracks
7. Merge tracks (second pass)
8. Compute track position – first image
9. Apply motion limits
10. Limit tracks

The first step, identifying tracks, initially involves matching detections from two consecutive images. The basic criteria here is that the two detections must have some level of similarity in their flux; if so, almost any pairing of detections can be considered a valid candidate track. Next, the tracker attempts to identify additional detections from subsequent images in the dataset. This time, the detections do not have to arise from consecutive images. However, there are limits in place on how much these additional detections are allowed to deviate from the initial track motion. For example, if the first two detections establish a speed of 5"/min, then a third detection should have a somewhat similar speed when matched with the second detection. The tolerance is also dependent on the exposure time and plate scale: for example, it is not uncommon for a highly streaked object to have a poor speed estimate from the initial two detections, so the algorithm will allow for a higher search window with subsequent detections. Position angle (direction) is also another matching parameter. For example, certainly it is not realistic for the subsequent detections to go in reverse direction from that of the initial two detections. In fact, it is possible to impose tighter constraints on the deviation from the initial direction, but again the tolerance will depend on how far apart the initial two detections are: if they are very close together, then the angle computation can have high uncertainty compared to detections that are farther apart. The candidate track is then established with a total of up to five detections. Tracks with fewer detections are still considered valid, but will have a lower score.

The second step is to update the motion of the established tracks. If a track is comprised of only two

detections, then its motion is already optimally computed. However, a track comprised of additional detections can have a more optimal motion computed if one uses the entire span of the track, especially for tracks of slow-moving objects.

The third step is to score tracks so that they can later be sorted. Track score is a key component to the usefulness of the tracker, as it should ideally only present tracks of real objects to the end-user while discarding or de-prioritizing the tracks that are likely to be false. At a high level, the scoring function looks at how many detections comprise the track, with more detections resulting in a higher score. It also looks at the consistency of detections, such as how much the detections deviate in flux. Another parameter is that if the track has a high speed, such that it should be expected to produce a streaked profile, then the score will be reduced if a detection has a shorter than expected streak length.

The fourth step is to then sort the tracks based on their computed track score. Tracks with high scores are ranked higher than those having a lower score. The sorting routine simply takes  $O(n \cdot \log(n))$  time to complete, where  $n$ =number of tracks identified.

### 3.1 Merging Tracks

The fifth step is to merge similar tracks together. This is a necessary step because tracks can have at most five detections, so multiple tracks may be established on an object that is detectable across more than five images. One might be tempted to say that two tracks are identical if they have the same speed and position angle. However, this metric alone is insufficient as multiple unique objects can have the same motion, as shown in Figure.

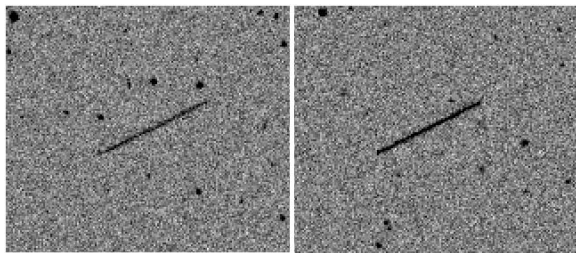


Figure 5: Left: COSMOS 2475; Right: COSMOS 2569

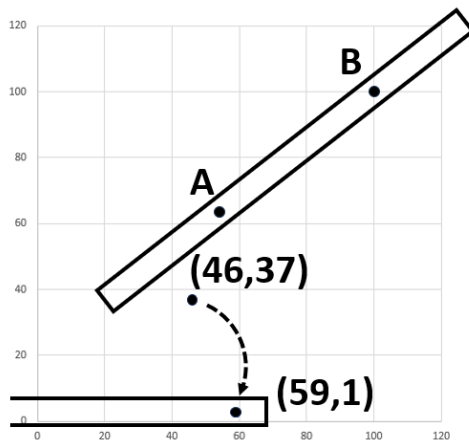
As Figure illustrates, two different objects can have nearly identical motion within the same dataset. In a dataset comprised of 30 images, COSMOS 2475 has a speed=2188"/min and PA of 26.5 degrees, while COSMOS 2569 has speed of 2211"/min and PA of 27.2 degrees. The difference in speed is around 1% and the difference in position angle is 0.7 degrees. Consider that it is not uncommon for an object to

exhibit a changing (non-linear) motion throughout a dataset, and it becomes clear that these differences are well within the tolerance that one would allow for a tracked object. Therefore, using motion by itself to determine if two tracks are that of the same object is not adequate. Instead, one must also determine if the detections on one track would be positioned in close proximity to the (integrated) positions of the other track at the same timestamps. Here again it is also necessary to determine the appropriate tolerances as a given detection may not have an exact centroid at the center of a streak; therefore, the algorithm adjusts the proximity tolerance according to the streak length. Even with this approach, it can still be a challenge to correctly identify tracks of the same object, particularly when a dataset spans enough time such that the object motion begins to exhibit curvature or noticeable deviation from a straight-line path. For most datasets, and especially those of surveys where the number and duration of exposures is optimized for a desired class of target, this is not a frequent issue.

As mentioned, two tracks will be merged if the detections from one of the tracks match up to the detections of the other track. Therefore, at a basic level one must be able to determine if two detections are a match. For detections arising from the same image (and therefore the same timestamp), no motion integration is necessary. However, for detections created from a separate set of images, having different timestamps, it is necessary to integrate their position according to the object motion. Once the positions of the two detections have been adjusted as necessary to be comparable to the same timestamp, the remaining work is to perform the actual comparison of the positions. One could do a simple distance computation, ala  $\sqrt{x^2+y^2}$ , yet doing so would not account for the uncertainty in object position along the length of the streak profile. Therefore, a better approach is to compare the position of one detection to a line segment centered around the position of the other detection. Since the line segment can (and often does) have rotation, the overall process involves the following steps:

1. Compute offset between the two detections, yielding  $X_0$  and  $Y_0$
2. Compute angle between track and CCD position angle
3. Rotate  $(X_0, Y_0)$  into a horizontal rectangle, yielding  $(X_1, Y_1)$
4. Compute dimensions of the horizontal rectangle
5. Determine if the transformed point  $(X_1, Y_1)$  falls inside the horizontal rectangle

The first step in the detection comparison is rather straightforward: one simply subtracts the expected position (integrated detection from track A) from the input position (current detection from track B). In other words, if the two detections have identical coordinates, the result is (0,0) – the origin. The second step is to compute the angle between the track position angle and the CCD (camera) position angle, also taking into account whether or not the view is flipped (if so, the angle is negated). Next, the third step is to rotate the offset point ( $X_0, Y_0$ ) into a horizontal rectangle, by subtracting 90 degrees from the angle computed in step 2 and applying the rotation matrix, yielding ( $X_1, Y_1$ ). The fourth step is to compute the desired bounds of the horizontal rectangle: this essentially acts as the matching tolerance. A longer exposure time or a faster object speed will produce a wider rectangle for the matching. Finally, the last step is to determine if the transformed ( $X_1, Y_1$ ) falls inside the computed horizontal rectangle. If so, then the two detections are considered a match. Otherwise, they are not a match and therefore it is likely that the two tracks to which they belong are not of the same object.



**Figure 6: Comparing Detections**

Figure shows how two detections are compared using a rotated rectangle for tolerance. Detection A is at position (54, 63) while detection B is at (100, 100). The offset ( $X_0, Y_0$ ) point is therefore at (46, 37), and upon rotation by the track position angle it is then positioned at (59, 1). Notice that after rotation there is practically no y-offset; rather, almost all of the delta is in the x-offset, allowing for one to now simply determine if the point resides inside a horizontal (rather than rotated) rectangle, which is a straightforward computation. For reference, the formula for computing ( $X_1, Y_1$ ) is shown in Figure.

$$\begin{aligned} x' &= x \cos(\theta) - y \sin(\theta) \\ y' &= x \sin(\theta) + y \cos(\theta) \end{aligned}$$

**Figure 7: Applying Rotation Matrix**

Having completed the first merge step of the tracking process, the next step of the tracker (6) is to centroid tracks. This process involves determining the speed of the track and computing its centroid appropriately. For slow-moving tracks, such as those having virtually no streak, the usual point spread function (PSF) fitting is performed to compute the centroid of each detection of the track. Otherwise, for tracks of objects having noticeable streak, the centroiding is presently determined by computing the midpoint of the streak bounds. Once the centroid of tracks has been determined, their motions (speed and position angle) are recomputed.

Step (7) of the tracking process is a second application of the merge process, as the previous step may have adjusted the motion of some tracks such that they could now be considered eligible for merging with other tracks.

Step (8) of the tracking process involves computing the position of each track as it would appear on the first image. This is a convenience routine for comparing tracks with known asteroids and comets that are integrated to the timestamp of the first image. However, for matching tracks with known artificial satellites, the more granular position information of each detection is preferred.

Step (9) of the tracking process involves applying motion limits to filter tracks that do not satisfy a user-defined lower- and upper-bound on speed and position angle. The user can toggle on/off the speed and position angle limits independently.

Finally, step (10) of the tracking process simply removes all tracks beyond a user-defined limit. Once tracking has completed, the resulting list of sorted, centroided, merged, and filtered tracks is returned to the user for inspection.

#### 4. Track Identification

While the previous process of tracking an object is able to transform raw detections into a set of tracks for the end-user, there is still an added step that can reduce the user workload: track identification. Nearly all artificial satellites are already known and catalogued, and approximately 90% of all asteroids are also catalogued. By matching tracks with known objects, the user is free to spend their time evaluating tracks that do not match up with any known object – these could be tracks of particular interest.

As mentioned previously in step (8) of the tracking process, it is possible to match tracks with known objects by integrating the database of orbital elements of minor planets to the timestamp of the first image. And since all tracks have a pre-computed position to that first image, all that remains is to compute the distance between that position and that of the integrated position of the minor planets. If the resulting distance is within some tolerance, a match is declared and the track is said to be associated with a known minor planet.

Similarly, the same can be done with artificial satellites, however a bit more care must be exercised because the fast motion of most satellites imposes a tighter tolerance on the delta time between an actual detection versus an integrated detection. In other words, one should use an actual detected position for matching, wherever it is possible to do so, rather than integrating (interpolating) to a common timestamp. Consequently, the elements of artificial satellites can be integrated to multiple timestamps across the dataset in order to ensure a good match.

## 5. Evaluation

A number of datasets have been collected to evaluate the performance of the FAST algorithm. These datasets include a variety of optical instruments and cameras. A typical implementation of the algorithm is to have it “stare” at the same region of the sky for an extended period, and typically processing 30 minutes worth of data at a time. This usually works out to around 100 images per dataset with each image having an exposure time of 10 seconds (depending on plate scale) and gap time of around 10 seconds between each exposure. While it is possible to supply the algorithm datasets having a dwell time of more than 30 minutes, track matching on artificial satellites could start to become suboptimal. Thus, an optimized survey would ideally capture multiple datasets throughout the night, each comprised of 30 minutes dwell time on a patch of the sky using a wide field instrument.

### Dataset #1:

Telescope: Samyang 135mm  
 Camera: ZWO ASI 2600MM (Sony IMX571)  
 Aperture: 65mm  
 Focal length: 130mm  
 Field of View: 621x415 arcmin (71.5 deg<sup>2</sup>)  
 Plate scale: 12"/pixel (at bin 2x)

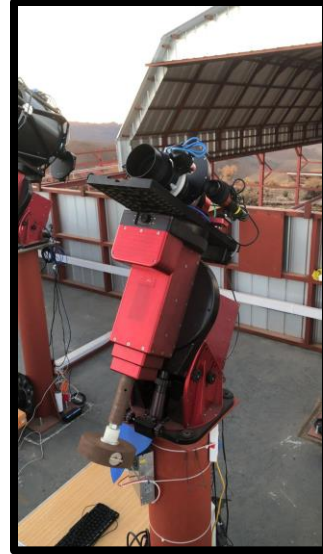


Figure 8: Samyang 135mm with ASI 2600MM (configuration from the iTelescope Network)

### Dataset characteristics:

Images: 57 images (each 3124x2088 pixels)  
 Exposure time per image: 3.00 seconds  
 Total Exposure time: 2.850 minutes  
 Total Dataset time: 14.083 minutes

### Results:

Tracks returned:  
 3 “High” confidence (3/3 real)  
 Detected two MEO objects and one LEO object  
 Processing time: 4 seconds

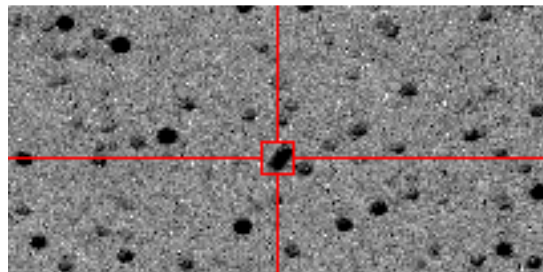


Figure 9: BREEZE-M DEB (TANK) (Speed=2092"/min)

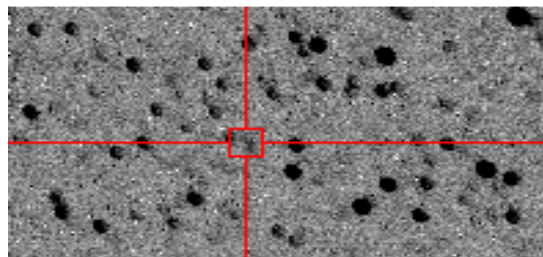


Figure10: COSMOS 2277 (GLONASS) (Speed=2274"/min)

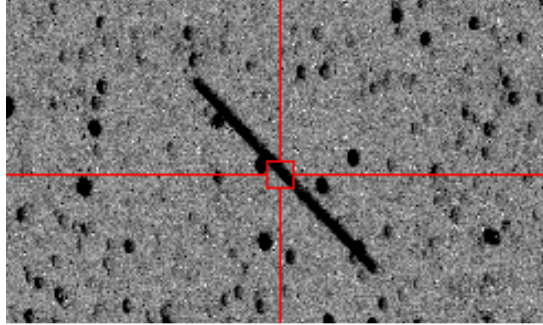


Figure 11: GONETS M 05 (Speed=29846"/min)

**Dataset #2:**

Telescope: Samyang 135mm  
 Camera: ZWO ASI 2600MM (Sony IMX571)  
 Aperture: 65mm  
 Focal length: 130mm  
 Field of View: 621x415 arcmin (71.5 deg<sup>2</sup>)  
 Plate scale: 12"/pixel (at bin 2x)

**Dataset characteristics:**

Images: 90 images (each 3124x2088 pixels)  
 Exposure time per image: 10.0 seconds  
 Total Exposure time: 15.00 minutes  
 Total Dataset time: 46.517 minutes

**Results:**

Tracks returned:  
 27 "High" confidence (27/27 real)  
 7 "Medium" confidence (5/7 real)  
 Processing time: 6 seconds

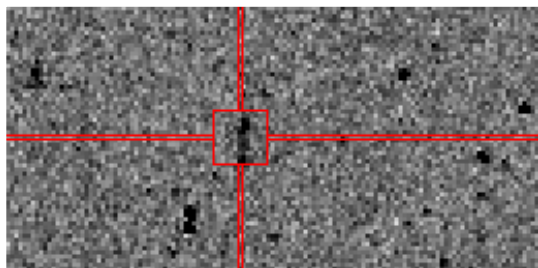


Figure 12: GSAT 6A

GSAT 6A (as well as all tracks here) was detected "blindly". It has a speed of 1450"/min and was found with no issue. In 2018 this same satellite was actually lost for a few days, following an orbit raising maneuver (Surendra, 2018).

**Dataset #3:**

Telescope: Takahashi Epsilon 180ED  
 Camera: ZWO ASI 2600MM (Sony IMX571)  
 Aperture: 180mm  
 Focal length: 500mm

Field of View: 160x107 arcmin (4.8 deg<sup>2</sup>)  
 Plate scale: 3.1"/pixel (at bin 2x)

**Dataset characteristics:**

Images: 90 images (each 3124x2088 pixels)  
 Exposure time per image: 10.0 seconds  
 Total Exposure time: 15.00 minutes  
 Total Dataset time: 27.183 minutes

**Results:**

Tracks returned:  
 11 "High" confidence (11/11 real)  
 1 "Low" confidence with 3 hits (1/1 real)  
 Processing time: 7 seconds

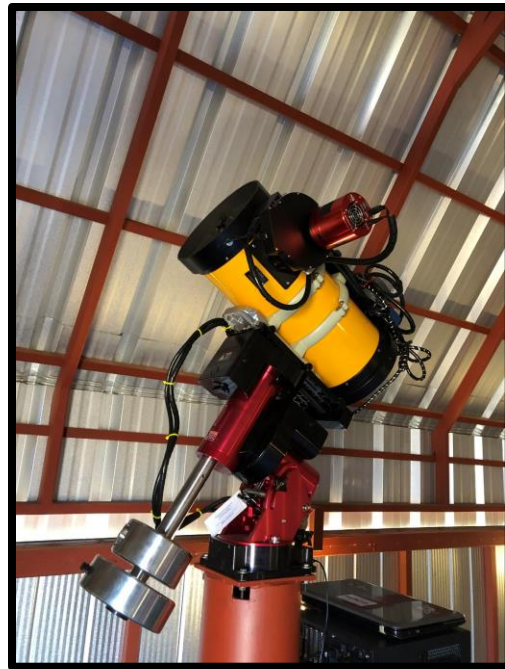


Figure 13: iTelescope T71 (Dataset #3)

As shown in Figure, this dataset includes an example of a track established on an object having high variability in brightness (Ariane 1 Deb). It was initially detected on image #30 in the sequence of 90 images. A second detection was also generated in the subsequent image (#31). However, the object rotation caused it to become fainter than the magnitude limit (approximately 16.5) on images 32-37. Then on image 38 the track was re-established, yielding a third detection and increasing track score. The motion of the track was 922"/min and position angle of 85 degrees.

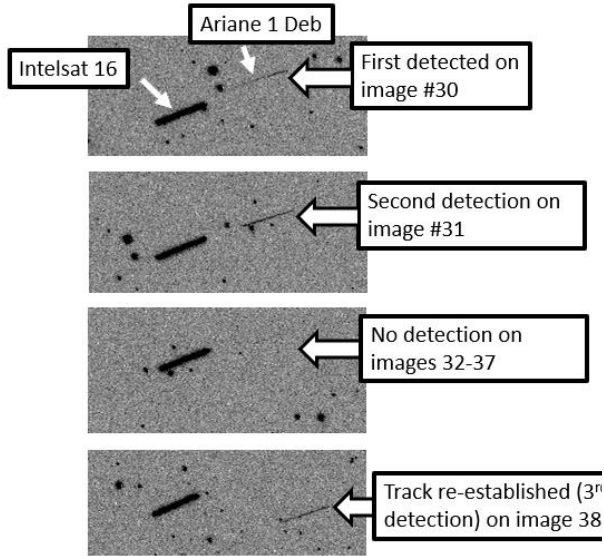


Figure 14: High Variability in Brightness

Num	Speed	PA	ObjNum	ObjName
1	956.13	123.5	23968U	ATLAS 2 CENTAUR ...
2	907.48	90.0	40664U	SKY MEXICO-1
3	1263.66	90.8	55683U	INMARSAT 6-F2
4	349.80	54.5	39169U	DELTA 4 R/B
5	901.20	106.4	22966U	SL-12 R/B(2)
6	901.85	89.4	36397U	INTELSAT 16
7	909.02	90.0	42692U	SGDC
8	900.79	89.2	37806U	COSMOS 2473
9	894.48	106.5	21759U	GORIZONT 24
10	431.70	87.3	27716U	ARIANE 5 R/B
11	901.04	87.2	39616U	AMAZONAS 4A
12	900.82	89.8	37826U	QUETZSAT 1
13	902.92	91.1	41866U	GOES 16
14	901.77	89.6	33373U	NIMIQ 4
15	933.67	93.6	32388U	HORIZONS 2
16	895.29	89.4	49818U	LDPE-1
17	787.90	96.5	---	---
18	900.94	88.5	40941U	ARSAT 2
19	898.12	89.9	38991U	STARONE C3
20	904.22	89.9	35873U	NIMIQ 5
21	880.76	91.6	44066U	S5 DEB
22	887.12	103.6	12089U	INTELSAT 502

Figure 15: Detection of Unknown Object



Figure 1: Motion of Track #17 (Courtesy of n2yo.com)

**Dataset #4:**

Telescope: Samyang 135mm  
 Camera: ZWO ASI 2600MM (Sony IMX571)  
 Aperture: 65mm  
 Focal length: 130mm  
 Field of View: 621x415 arcmin (71.5 deg<sup>2</sup>)  
 Plate scale: 12"/pixel (at bin 2x)

**Dataset characteristics:**

Images: 90 images (each 3124x2088 pixels)  
 Exposure time per image: 3.0 seconds  
 Total Exposure time: 4.500 minutes  
 Total Dataset time: 22.783 minutes

**Results:**

Tracks returned:  
 22 "High" confidence (22/22 real)  
 Processing time: 8 seconds

Dataset #4 has 22 tracks with "High" confidence. This dataset also shows an example of an "unknown" track (#17), that initially could not be matched to a known object. It has a speed of 788"/min, which is noticeably different from that of a geostationary satellite. Instead, it is a geosynchronous satellite with inclination of 5.6 degrees.

**Dataset #5:**

Telescope: 0.25m Ritchey-Chrétien  
 Camera: QHY42 (Gsense 400 CMOS)  
 Aperture: 250mm  
 Focal length: 2000mm  
 Field of View: 31x31 arcmin (0.267 deg<sup>2</sup>)  
 Plate scale: 2.25"/pixel (at bin 2x)

**Dataset characteristics:**

Images: 125 images (each 818x818 pixels)  
 Exposure time per image: 1.0 seconds  
 Total Exposure time: 2.083 minutes  
 Total Dataset time: 2.085 minutes

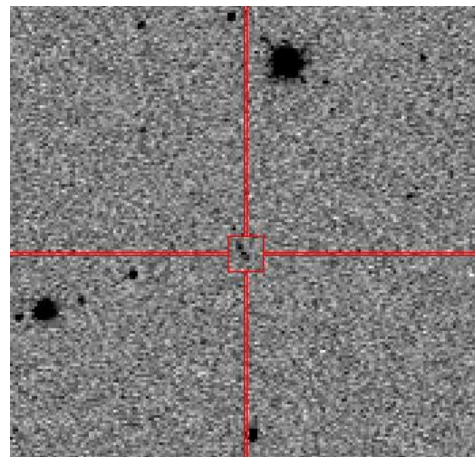


Figure 2: 2019 JH7 (Near Earth Asteroid)



This dataset shows an example of a tracked Near Earth Asteroid (NEA) found moving at 1145"/min, which is even faster than geostationary satellites at 900"/min. This indicated that it was indeed a close approach.

## 6. Future Enhancements

The FAST algorithm has been implemented into the Tycho Tracker software, which presently generates astrometry in MPC1992 (or alternatively ADES) format, consistent with report generation for astrometry of minor planets. However, for those seeking to use FAST for detection of artificial satellites, it can be desirable to generate reports in the Interactive Orbit Determination (IOD) format. This is a fairly straightforward feature to support and will be completed in the next revision. This will make the measurements compatible with those that are generally submitted to the SeeSat-L mailing list (Lewis, 1998).

## 7. Conclusion

The FAST algorithm is shown to quickly detect and identify moving objects in a series of images. It is robust in detecting objects with a streaked profile, as well as objects having high variability in brightness. When used in conjunction with a "Monitor Queue" tool that watches for incoming datasets, it can be greatly automated to process data from an entire night. Its ability to quickly match dozens of tracks with known objects allows one to easily spot unknown objects for follow-up.

## 8. Acknowledgements

I would like to thank the supporters of the Tycho software who have provided additional datasets used in refining and optimizing the algorithm: G. Privett, J. Jahn, A. Maury, G. Attard, D. Rankin, A. Francis, D. Bamberger, M. Holbrook, and many others.

## 9. References

- Denneau, L., et al. "The Pan-STARRS Moving Object Processing System." (2013). <https://arxiv.org/pdf/1302.7281.pdf>
- Heinze, A., et al. "Digital Tracking Observations Can Discover Asteroids Ten Times Fainter than Conventional Searches." (2015). <https://arxiv.org/pdf/1508.01599.pdf>
- Nir, G., et al. "Optimal and Efficient Streak Detection in Astronomical Images." (2018). <https://iopscience.iop.org/article/10.3847/1538-3881/aaddff/pdf>
- Surendra, S. "We now know the exact location of GSAT-6A communication satellite." (2018). <https://timesofindia.indiatimes.com/india/we-now-knows-exact-location-of-gsat-6a-communication-satellite-says-isro-chief/articleshow/63701803.cms>
- Lewis, G. "Interactive Orbit Determination (IOD) Version 0". (1998). <http://www.satobs.org/position/IODformat.html>

# Automating Zeropoint Photometry with Freeware

Wayne Green & Frank Parks  
Society for Astronomical Sciences  
[dxwayne@gmail.com](mailto:dxwayne@gmail.com)  
[fgparks@mac.com](mailto:fgparks@mac.com)

---

## Abstract

We automate the zeropoint reduction of astronomical CCD/CMOS photometric images using freely available Linux software tools. The tools include bash, Linux filters, SExtractor, PSFEx, Astrometry.net and PostgreSQL together with a few Python programs. This framework allows the practitioner to adjust the process to the special and peculiar circumstances of their sites and equipment. The code is available through GitHub for all to use.

---

## 1. Introduction

Reduction of photometric data starts with a choice of approaches. Common choices include differential vs zeropoint photometry and aperture vs Point Spread Function (PSF) extraction. References may be drawn from catalogs or may be synthesized as an "ensemble reference" (Bessell Honeycutt 1992 and references therein) We are going to restrict ourselves to the optical range of  $\lambda\lambda 3300\text{-}8600\text{\AA}$ . Programming, where practical, should always be platform agnostic. However, an increasing gulf is developing between Microsoft and other platforms. Here we use Linux (Unix), running on a small computer co-located on the Optical Tube Assembly (OTA). This allows most preliminary reduction steps to be performed very quickly and results may inform the next exposures of a program. We focus on open-source code packages.

The publication of data dictates the choice of reference catalog and approaches by the group's publisher. Catalogs vary widely and mixing and matching values from catalogs contributes to inaccuracies. The AAVSO (Mattei, 1989) maintains one of the oldest curated datasets, spanning over 113 years. The changes in technology across these data means color sampling of stars has varied widely. From visual observations (consistent except for eye response from aging of observers), photographic emulsions across several technology epochs; approaches to Photo-Electric-Photometry (PEP) using various sensors; and several generations of CCDs and now CMOS sensors all contribute to variations.

Photometric filter technology has evolved. The index of refraction and spectral characteristics of colored glass comes from the recipe of the glass and chemicals added to color the glass. Various glasses were sandwiched together to achieve the bandpass desired. Schott™ (The Schott Group, 2024) was a very popular source of glass for photometric filters. In the

1990's bi-refrangent filters were created with thin layers (thicknesses in fractions of wavelengths) of special material were combined to create a bandpass. Matching old filter requirements was never exact. The performance of filters varies batch-to-batch within a vendor; vendor-to-vendor; technology-to-technology. Filters were prone to color shifts due to aging. At the end of the day there is no perfect filter methodology.

Photometric filter technology has evolved. The index of refraction and spectral characteristics of colored glass comes from the recipe of the glass and chemicals added to color the glass. Various glasses were sandwiched together to achieve the bandpass desired. Schott(tm) (The Schott Group, 2024) was a very popular source of glass for photometric filters. In the 1990's bi-refrangent filters were created with thin layers (thicknesses in fractions of wavelengths) of special material were combined to create a bandpass. Matching old filter requirements was never exact. The performance of filters varies batch-to-batch within a vendor; vendor-to-vendor; technology-to-technology. Filters were prone to color shifts due to aging. At the end of the day there is no perfect filter methodology.

One of the critical elements of photometry is the filter set used, i.e. the Sloan's griz vs Johnson Cousins UBVRI filters. Transmission curves will vary in small details for a filter set between vendors, and transforms may be easily applied. The more variance the less accurate the transforms. Bessell (1992 and references therein) go into great detail about filter systems used in photometry.

Another critical element is the energy scale employed. Different filters were designed for different scales. Pogson (Pogson, 1856) laid the foundation of Vega Magnitude Standard (Tüg et al., 1977). Usually with the Vega system filters are described in terms of wavelength passbands. The AB magnitude system *m* (Oke and Gunn, 1983) uses a fixed energy and filters are described in terms of energy per frequency.

Caution needs to be exercised when mixing and matching magnitudes.

To account for filter differences, instrumentation variations and differences in air quality is managed using transformations. It is important to devote "engineering" time to maintain accurate transformations. One odd fact is the "color" of the sky changes with the phase of the moon. The phase of the moon is from 1, new to 14 full. For example see IRAF's (Fitzpatrick et al., 2024) kpno.dat where their V filter description is:

```
filter = "v "  
    extinction = 0.14  
    mag = 20  
    star = 36.2  
    sky0 = 21.8  
    sky1 = -0.0153  
    sky2 = -0.00838 sky + sky0 + sky1 + sky2  
    x phase2
```

The short answer is the methodology for shared data needs to be fixed in stone by the program and needs to be auditable. All raw data should be archived and retained.

Publishing accurate results is more important than how data is reduced. Error margins need be clearly understood and stated. To achieve accurate results requires diligent testing of the equipment to inform algorithms used during reduction. For example, a camera cooled to -10C will not have the same noise characteristics as one chilled to -20C. We encountered difficulties with reaching cooler temperatures and addressed this issue with new power supplies sufficient to requirements. Optics need to be cleaned and aligned. We do not rely on reports of efficacy of our equipment but choose to qualify the equipment ourselves.

This project employs zeropoint photometry using PSFs. The packages we rely upon include Ubuntu or Raspbian Linux, Astrometry.net, SExtractor/SExtractor++ (Bertin and Arnouts, 1996), PSFEx (Bertin, 2013), PostgreSQL(Stonebraker and Rowe,1986) with Q3C Koposov and Bartunov(2006) and Python3.8 (VanRossum and Drake Jr, 1995) or above. We use IRAF/PyRAF 2.17/2.18 on a Raspberry Pi mounted to the OTA. We require X11/R6 only to support IRAF needs.

The paper reports the large differences between Stetson and Landolt fields are due to the differences in the approach used by each study. Stetson used a PSF technique that was consolidated into the IRAF DAOPHOT/DAOPHOT2 system, where Landolt used a single detector with a 14-arcsecond aperture. Landolt's apertures admitted potential contaminating background sources.

## 2. Pipeline Overview

A so-called pipeline fixes a flow of information between packages and programs using a scripted or baked-in logic. Our testbed, called asolve, is a modular solution. This permits tweaking and changing the script for each new installation/instrument to meet requirements. The script requires variation in its algorithms for multi-channel sensors; CMOS sensors; differences in sky and filters, etc.

Open-source programs benefit from a large, interested community of users developing fast turn-around releases to correct errors. Many packages have active email forums and wikis.

Each version of our pipeline is managed with software version control in such a way that a full and complete audit of data reduction may be conducted at a later time. All raw data are retained.

## 3. Basic Reduction Steps

The basic steps vary. For a KAF 6803 sensor, we collect bias (zero) and dark frames in addition to flat fields for each filter. For newer chips like the KAF 16803, dark frames are found to have the same mean level as zero frames, but the variance increases with exposure. Experiments (Green and Sims, 2019) show that the variation is random for any given pixel. There is no way to make a mean value that does not potentially increase the noise for the pixel. Therefore, the dark data set is skipped. We find for CMOS sensors, binning is foolish. The sensor has no means to bin therefore any ideas about readnoise is moot. Pixel-to-pixel analysis and correction is best left to post-processing steps.

The usual image corrections and pixel corrections are made. The images are then platesolved using Astrometry.net using a plate scale, RA and Dec hints. For a number of images in one field, a special Astrometry.net configuration file is created to expedite solutions. The WCS corrected images are processed with sExtractor. The output file from sExtractor is converted to a csv file and further processed to remove any artifacts that are common with sExtractor. At this time, the csv file has the RA,Dec,flux,background and other information. The image's csv file is converted to PostgreSQL and added to the database. A special query is run, using QC3, to match the raw counts to magnitudes from the field's comparison stars. All stars are matched. From this a zeropoint magnitude is computed for each comparison star. These comparison star data are combined to create a zeropoint magnitude. The zeropoint allows all stars to be converted from ADU to magnitudes, together with error terms. A procedure built into PostgreSQL applies

the proper filter transforms. These data are recorded in the results table. The results table is then used to produce csv output suitable for post-processing and publication.

There are quite a few places where custom code is needed for these conversions.

## 4. Algorithms Used

A few equations help to understand the nature of magnitudes in general and zeropoint magnitudes in particular. The algorithm is used to determine the error statement for magnitudes is included.

Differential magnitude reduction does not use the zeropoint directly. Equation 1  $F^*$  and  $F_{comp}$  may be solved to convert the simultaneous observation into a magnitude:

$$\begin{aligned} m^* - m_{comp} &= -2.5 \log_{10} ( F^* / F_{comp} ) \\ m^* &= -2.5 \log_{10} ( F^* / F_{comp} ) + m_{comp} \quad (\text{eq 1}) \end{aligned}$$

Substituting a flux of 1 for  $F_{comp}$  :

$$\begin{aligned} m_{comp} - ZPT &= -2.5 \log_{10} ( F_{comp} / 1 ) \\ m_{target} &= m_{comp} + 2.5 \log_{10} ( F_{comp} ) - ZPT \end{aligned}$$

This allows gain corrected star ADU values to be converted directly into magnitudes. Ideally the ZPT magnitude would not change across the night but no night is perfectly photometric and the ZPT has to be calculated for each image. The output from SExtractor allows the database to evaluate background levels and detect gradients in an image.

References in the body text should use the name of the lead author plus a year, for example, Warner (2004). If there is more than one reference for a given author in the same year, use letters after the year, Warner (2004a). For multiple authors use something like Smith et al. (2006).

## 5. Key Files

The default.param of SExtractor allows extracting WCS RA/Dec together with x/y image position produced join database catalog to associate catalog stars with image star flux and statistics. See code repository<sup>1</sup> for examples of SExtractor default files.

The files default.sex, default.conv, default.nw and default.psfex for the PSFEx program. Each should be configured for each instrument. The instrument may then be passed to asolve to configure expectations for sextractor.

## 5.1 Astrometry.net

Linux uses soft links to include files in a directory without the need for copying the file. One may delete/replace soft-links at will. Windows shortcuts are actual files that must be opened, read, and acted upon. A master directory with the sets of index files is maintained. A separate directory with links to only the files needed at the platescale and locations for images for a particular site or instrument can be created. From these links an additional set of links to just the files needed for a particular RA/Dec field may be made. This greatly decreases the search time by Astrometry.net and allows for file protection and maintenance.

## 5.2 PostgreSQL

The PostgreSQL database, available as open source and commercially supported, first released in 1989, came from a collaboration between Professor Michael Stonebraker and sponsors including Defense Advanced Research Projects Agency (DARPA), the Army Research Office (ARO), the National Science Foundation (NSF), and ESL, Inc c (Stonebraker and Rowe, 1986). Currently at version 16.3, the environment supports many file types including JSON which is useful for storing FITS headers; blobs for binary and large text data; and uses several programming languages to customize features like Python and C/++. We use Sergey Kopusov's Q3C package (updated as recently as 5 months ago) for matching spherical coordinates, cone searches etc.

Drivers for PostgreSQL are available for TOPCAT allowing SAMP protocols to acquire data from over 25,000 catalogs in the Symbad Astronomical Database from Centre de Données astronomiques de Strasbourg (CDS) and other sources through the Aladin GUI interface or by direct ADQL queries.

PostgreSQL partitions databases with schema's where other open-source databases like MySQL and Maria reference between databases. The schema approach provides a high measure of security.

## 5.3 SExtractor, SExtractor++ and PSFEx

SExtractor and PSFEx are designed to support finding and classifying galaxies. It is very good at finding stars and digging out the counts for those

---

<sup>1</sup> <https://github.com/dxwayne/asolve.git>

sources. It is managed with a series of default parameter files that are customized for sites and equipment.

The output of sextractor is its own format. This requires a special script/program to convert the output of SExtractor into something more useful. Comma-separated-variable (csv) files are common between programs. One of the parameters is the VIGNET(n,m) command that extracts the pixels for each match to pass to PSFEx. PSFEx determines the best point-spread-function for each image. The result is disambiguated overlapping targets. It is best to acquire GAIA sources for each target area to the zeropoint magnitude to help identify targets or references that will be a problem. SExtractor's background extraction assists with stars that are embedded or projected against "texture" from nebulae or galaxies.

The goal is to filter the output of the SExtractor step looking for stars. While SExtractor was designed to locate and report on galaxies, it finds surprisingly large round things in an image, and sometime report phantom defections. Intelligent filtering is necessary.

Once flux and background is obtained the data are turned over to the last stage for processing using custom extensions for the PostgreSQL database.

## 5.4 Stating the Error Bars

In very general terms using Poisson statistics, noise of an observation goes as the square root of the signal. This is crude, and usually applies to counts (of photons) less than about 33. After 33 counts, Poisson statistics is very closely related to the Gaussian statistics. The Gaussian is often used because it has properties, especially with certain transformations, that makes computations quick and easy. As a general rule: a Signal-to-Noise-Ratio (SNR) of 100 means you want a count of 10,000 photons. The count has to be as recorded by the sensor.

Airmass attenuation is severe. For example, sunlight is measured at approximately 1350 Watts in space at the distance of Earth's orbit, but only around 1050 Watts makes it to the ground when the sun is at zenith and the atmosphere is clean. That is a 23 percent loss. Optics lose about 4 percent per surface, For a mirror, diagonal, two sides of a filter and a cover plate; assuming 95 percent reflection for the mirrors and around 98 percent for anti-reflection coated optics the total is  $.95^2 \times 0.98^3 = 0.84$ . The quantum efficiency for a CMOS sensor is about 60% in V-band for a total of  $0.84 \times 0.60$  or about 20 percent of the light makes it to the sensor. This changes with airmass. In general, an attenuation of 50 percent occurs at an telescope elevation angle of 30 degrees, meaning we are sensing 25 percent of the light. Losses along the way are difficult to quantify as the transparency of the

atmosphere varies widely. Chief causes are humidity, aerosols and carbon dioxide. Good reasons for space based telescopes.

It is easy to see that the Poisson rule is 'good enough'.

## 6. Derivation of Mathematical Relationships in Photometry

ADU for a star is a count of photons per unit time. The energy of a photon is  $E = h\nu$ , where  $h$  is Planck's constant, and  $\nu$  is the frequency giving an energy in cgs terms of [erg s]. The power is energy per unit time resulting in units of ergs. Power ratio of two energies, for electrical power expressed as decibels (dB) or  $\text{dB} = 10 \log_{10}(P1/P2)$ . The Pogson magnitude scales represents a power, but scaled in a way that the energy range seen by the naked eye covers a range of 100, broken down into 5 intervals giving 6 magnitudes. The constant used is -2.5 instead of the decibel scalar of 10. The minus sign makes dimmer targets have a larger number, and the 2.5 matches the power to the response sensitivity of the eye. In Pogson's paper, he works in natural logarithms. Using the log base conversion of shows why the value is 2.5 precisely:

$$\begin{aligned} \sqrt[5]{100} &= e^{\ln(100)/5} = 2.51204 \\ 0.4\bar{0} &= \log_{10}[e^{\ln(100)/5}] \\ \bar{0} &= \log_{10}[e^{\ln(100)/5}] \\ 2.5 &= \frac{1}{0.4} \end{aligned}$$

$$\text{Pogson Magnitude} = \log_{10} [\text{measured} / \text{reference}]$$

### 6.1 Platescale

This platescale equation 2 gives a good estimate of the vignette size in pixels for telescopes focal length and the night's seeing. It is also handy to determine the slit size in spectroscopy. Choossing a sextractor vignette value slightly larger is recommended.

$$\frac{206,264.8 [\text{arcsec/radian}]}{f[\mu\text{m}]} = \frac{\text{seeing}[\text{arcsec}]}{1[\mu\text{m}]} \quad \text{equation 2}$$

### 6.2 Expressing SNR

Noise, under a log relationship is pretty close at the 1 percent level. For noisier data this becomes more extreme

$$\begin{aligned} \text{mag} \pm \sigma_{\text{mag}} &= -2.5 \log \left( 1 + \frac{1}{S/N} \right) \\ 0.01080 &= -2.5 \log(1 + 1/100)(+1\text{percent}) \\ -0.01091 &= -2.5 \log(1 - 1/100)(-1\text{percent}) \\ 0.19795 &= -2.5 \log(1 + (20/100) + 20\text{percent}) \\ -0.24227 &= -2.5 \log(1 - 10/100)(-20\text{percent}) \end{aligned}$$

In practical terms, for a given signal  $S$  and a noise  $N$ :

$$C_0 = -2.5 \log_{10}(S \pm N) \\ -2.5 \log_{10}[S] \text{ with error } -2.5 \log_{10}(1 \pm N/S)$$

## 7. Conclusion

A pipeline is best viewed as a toolkit of basic routines that may be tailored and put together in unique ways to meet the needs of the instrumentation package. This needs to be considerate of site conditions (altitude, basic seeing, light pollution etc) and instrument conditions (entendu or throughput, color shifts (transformations) etc). This pipeline was designed to run, in real time, on the OTA for the instrument. This allows feedback to be computed and used independently of any master control system.

## 8. References

E. Bertin. PSFEx: Point Spread Function Extractor. Astrophysics Source Code Library, record ascl:1301.001, Jan. 2013.

E. Bertin and S. Arnouts. SExtractor: Software for source extraction. Astronomy and Astrophysics Supplement Series, 117:393–404, June 1996. doi: 10.1051/aas:1996164.

M. S. Bessell. Standard Photometric Systems. Annual Review Astron. Astrophys., 2005.

M. Fitzpatrick, V. Placco, A. Bolton, B. Merino, S. Ridgway, and L. Stanghellini. Modernizing IRAF to Support Gemini Data Reduction. arXiv e-prints, 2024.

W. Green and F. Sims. Parallax Angle and Instrumentation Issues for Small Telescope Spectroscopy. In 38th Annual Conference of the Society for Astronomical Sciences (SAS-2019), pages 97–108, June 2019.

R. K. Honeycutt. CCD Ensemble Photometry on an Inhomogeneous Set of Exposures. Publications of

the ASP, 104:435, June 1992. <https://ui.adsabs.harvard.edu/abs/1992PASP..104..435H>.

S. Kposov and O. Bartunov. Q3C, Quad Tree Cube— The new Sky-indexing Concept for Huge Astronomical Catalogues and its Realization for Main Astronomical Queries (Cone Search and Xmatch) in Open Source Database PostgreSQL. In C. Gabriel, C. Arviset, D. Ponz, and S. Enrique, editors, Astronomical Data Analysis Software and Systems XV, volume 351 of Astronomical Society of the Pacific Conference Series, page 735, July 2006.

J. A. Mattei. The AAVSO and its Variable Star Database. In G. A. Wilkins and S. Stevens-Rayburn, editors, IAU Colloq. 110: Library and Information Services in Astronomy, page 222, Jan. 1989.

J. B. Oke and J. E. Gunn. Secondary standard stars for absolute spectrophotometry. Astrophys. J., 266: 713–717, Mar. 1983. doi: 10.1086/160817.

N. Pogson. Magnitudes of Thirty-six of the Minor Planets for the first day of each month of the year 1857. Monthly Notices of the Royal Astronomical Society, 17:12–15, Nov. 1856. doi: 10.1093/mnras/17.1.12.

M. Stonebraker and L. Rowe. The design of postgres. ACM-SIGMOD Conference, 1986. The Schott Group. The schott group. WEB/URL, 2024. <https://www.schott.com/>.

H. Tüg, N. M. White, and G. W. Lockwood. Absolute energy distributions of alpha Lyrae and 109 Virginis from 3295 Å to 9040 Å. Astronomy & Astrophysics, 1977. <https://ui.adsabs.harvard.edu/abs/1977A&A....61..679T>.

G. Van Rossum and F. L. Drake Jr. Python tutorial: Centrum voor wiskunde en informatica amsterdam. The Netherlands, 1995

# Zenith Sky Brightness Measurements near Barnesville GA

*Richard W. Schmude, Jr.*  
*Gordon State College,*  
*419 College Dr. Barnesville, GA 30204*  
[\*schmude@gordonstate.edu\*](mailto:schmude@gordonstate.edu)

*Ty Clark*  
*Gordon State College,*  
*419 College Dr. Barnesville, GA 30204*  
[\*nc258055@gordonstate.edu\*](mailto:nc258055@gordonstate.edu)

---

## Abstract

This paper summarizes daytime and nighttime sky brightness measurements made mostly at the observer's zenith from Barnesville, GA (84.15° W, 33.05° N). The daytime sky brightens as the Sun's altitude increases. The daytime sky brightness is usually ~0.4 magnitudes per square arc second (mpsas) brighter during summer than at other times. This is probably caused by the haze that develops at that season. The sky brightness dropped  $10.0 \pm 0.3$  mpsas, at Dexter, MO, as a result of the April 8, 2024 total solar eclipse. The night sky brightness increased on October 28, 2023 as the full Moon's altitude increased. This work confirms earlier studies on how the Moon and Sun affect sky brightness.

---

## 1. Introduction

The sky brightens because of scattered sunlight and other sources of natural and human-made light sources. During the day, the Sun is the dominant source of light. Therefore, its altitude will control the sky brightness. Clouds and haze will also affect the sky brightness. Furthermore, the sky varies in brightness at different altitudes (Westfall, 1988). Therefore, I only report zenith sky brightness measurements here. Barentine (2022) has reviewed recent work related to the sky brightness.

In this study I have focused on daytime, twilight, and nighttime sky brightness. One objective of this study is to measure the daytime sky brightness at different times of the day and compare it to the sky brightness during a total solar eclipse. In this way, the brightness drop caused by the solar eclipse may be measured. A second objective is to carry out twilight measurements before sunrise and after sunset. A third objective is to measure the impact of the full Moon on nighttime sky brightness. With these objectives, the impact of lunar and solar eclipses on sky brightness is addressed. Afterwards, a comparison between the moonlit nighttime sky brightness and the sunlit daytime sky brightness is made to estimate the brightness of the Sun. Finally, a statement about future work is given.

## 2. Method and Materials

The writer used a Sky Quality Meter (SQM) with a narrow field of view (manufactured by Unihedron) to carry out his sky brightness measurements. The field of view is cone shaped. According to the manufacturer "The half width half maximum (HWHM) of the angular sensitivity is about  $10^\circ$ " (Unihedron Instruction Sheet, 2023). It also has an infrared blocking filter. The manufacturer's brochure also states, "the sensitivity to a point source  $\sim 19^\circ$  off-axis, is a factor of 10 lower than on-axis." This instrument measures brightness in units of magnitudes per square arc-second (or abbreviated as mpsas). This unit can be converted to others like the Candela/m<sup>2</sup> using proper transformation equations (Barentine, 2022). A Celestron neutral density filter was used in making sky brightness measurements during the day. This filter reduced the sky brightness by 2.98 magnitudes (or a factor of almost 16). This attenuation value was measured both with and without this filter near sunset.

The writer always held the SQM so that it was in a shadow so that direct sunlight (or moonlight) did not enter the detector. This was done because when the Sun was more than  $45^\circ$  from the Instrument's field of view, but was not blocked, the reading was brighter than when the instrument was in a shadow. Measurements made when the Sun's zenith angle was less than  $30^\circ$  were usually not made because the sky brightness exceeded the capacity of the instrument-filter combination.

In all cases, the sky brightness was taken near the zenith when that part of the sky was clear of clouds. In many cases, scattered clouds were present when I made measurements, but they were at least  $15^\circ$  away from the zenith.

Sunrise and sunset times are based on the NOAA ESRL Sunrise/Sunset Calculator (2024). The sunrise and sunset times are given to the nearest minute. During the time of sunrise and sunset the zenith sky brightness changes by 0.1 – 0.15 mpsas for each minute that passes. Therefore, any uncertainty in the sky brightness because of time is less than 0.1 mpsas. The time when the Sun altitude is  $6.0^\circ$  below the horizon is computed using the Sun coordinates and transit times in the JPL Horizons Ephemeris Generator (2024).

The two-sample t-Test for the difference between mean values is used in this study (Larson and Farber, 2006). Statistical tests are carried out at the 95 % confidence level.

### 3. Results

Several topics are described in this section that include daytime sky brightness, twilight sky brightness, the Moon’s effect on sky brightness, the effect of lunar and solar eclipses and the measurement of the Sun brightness. Finally, a statement about future work is given.

#### 3.1 Daytime sky brightness

Daytime zenith sky brightness measurements were made for most of a year. A sample graph of measurements made on March 20, 2024 is shown in Figure 1. The clear sky brightens as the Sun’s altitude rises. The brightness reaches a peak when the Sun transits the meridian – 16:44 UT on March 20 – (JPL Horizons Ephemeris, 2024). Afterwards, the sky dims as the Sun’s altitude declines. This diming is gradual and, hence, is difficult for the eye to detect over a few minutes.

The sky brightness may also be measured in terms of the Sun’s zenith angle. This is the angular distance between the Sun and the observer’s zenith. For Barnesville GA, the minimum solar zenith angle is  $\sim 10^\circ$  at the summer solstice and  $\sim 57^\circ$  at the winter solstice. The sky brightness increases as the zenith angle decreases. Figure 2 shows a graph of the zenith sky brightness plotted against the Sun’s zenith angle.

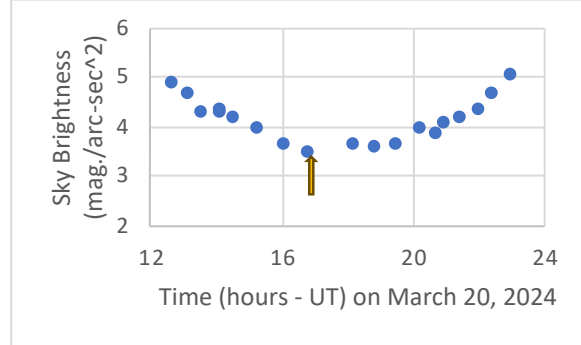


Figure 1: Sky brightness measured on March 20, 2024 from Barnesville, GA. the arrow is the time when the Sun transits the meridian.

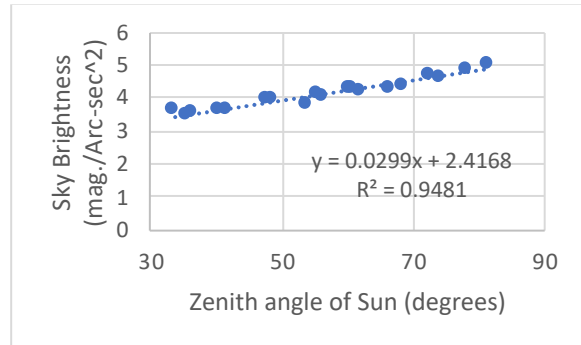


Figure 2: Sky brightness plotted against the solar zenith angle on March 20, 2024.

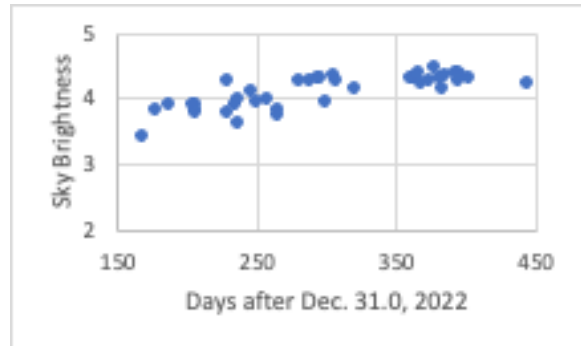


Figure 3: Sky brightness at a solar zenith angle of  $60^\circ$ .

One may also determine the sky brightness at a constant zenith angle throughout the year. A zenith angle of  $60^\circ$  is chosen because the Sun reaches this value in all seasons from Barnesville, GA. Therefore, the zenith sky brightness is measured when the Sun is  $60^\circ$  from the zenith. I measured this value by fitting sky brightness measurements made at various zenith angles for a specific day. Afterwards, these values were fitted to a linear equation. The desired value was then computed from this equation. A plot of the sky brightness at a zenith angle of  $60^\circ$  is shown in Figure 3 for different dates.



There is a brightening of  $\sim 0.4$  mpsas in Figure 3 during the summer months (168-270 days after Dec. 31.0, 2022). This is probably caused by the seasonal haze that is present on most clear summer days in Middle Georgia but disappears during fall.

Sky brightness measurements for several summer and fall/winter days were combined into two respective graphs. The points were fitted to linear equations with the results shown in Table 1. Essentially, the sky is  $\sim 0.4$  mpsas brighter during the summer than during the fall/winter based on the b values. This is probably because of the summer haze.

Season	m	b
summer	0.0268	2.28
fall/winter	0.0268	2.66

**Table 1: Sky brightness based on the equation  $y = mx + b$  where  $y$  is the sky brightness,  $m$  is the slope,  $x$  is the zenith angle of the Sun in degrees and  $y$  is the sky brightness at  $x = 0^\circ$ .**

In both time periods, the zenith sky brightness changes by  $0.0268 \text{ mag./arc-sec}^2$  per  $1.0^\circ$  change in the Sun's zenith angle.

### 3.2 Sky brightness during twilight

The sky brightness was measured at sunrise and sunset on several dates between June 17, 2023 and March 20, 2024. The mean sky brightness for sunrise is 7.45 (0.12, 41) mpsas where the numbers in parentheses are the standard deviation (in mpsas) and the number of measurements. The corresponding value for sunset is 7.49 (0.10, 35) mpsas. Based on the two-sample t-test, the sky brightness values for sunrise and sunset do not have a statistically significant difference. There does not appear to be a large (greater than 0.2 mpsas) seasonal trend in the sky brightness at sunrise/sunset.

The three stages of twilight (Civil, Nautical and Astronomical) occur when the Sun's altitude is  $0^\circ$  to  $6^\circ$ ,  $6^\circ$  to  $12^\circ$  and  $12^\circ$  to  $18^\circ$  below the horizon. The sky brightness was measured several times when the Sun altitude was at  $6^\circ$  below the horizon, which is the dividing point between civil and nautical twilight. The mean values (mpsas) for the morning and evening are 13.46 (0.23, 14) and 13.89 (0.15, 23), respectively. There is a statistically significant difference between the two mean values. The sky brightness was dimmer than 19 mpsas after astronomical twilight, and, hence, artificial lighting was not a significant source of the brightness. Therefore, the sky darkens by 6.44 mpsas between sunset and the end of civil twilight. This corresponds to a brightness drop of  $2.512^{6.44} = 377$ . Between the beginning of civil twilight and sunrise, the zenith sky brightens by 6.01 mpsas, which

corresponds to a factor of  $2.512^{6.01} = 254$ . These results are like those reported by Barentine (2022).

Based on a few measurements, the sky brightness is around 19.5 mpsas at my dark site when the Sun is  $12.0^\circ$  below the horizon. This value is probably influenced by natural and human-made light sources. The sky brightness when the Sun's altitude is more than  $18.0^\circ$  below the horizon is 20.1 to 20.2 mpsas at my dark sky locations.

### 3.3 Moon's impact on sky brightness

The Moon impacts the nighttime sky brightness. Unlike the Sun, the Moon's brightness changes with the phase angle. The sky brightness without a Moon is near 20.1-20.2 mpsas. With a Full moon (magnitude -12.6), the night sky brightens as the Moon's altitude rises. Results are plotted in Figure 4. On Oct. 28 (around 2:00 UT), the Moon's brightness ranged from -12.57 to -12.60 magnitudes (JPL Horizons Ephemeris Generator, 2024). The opposition surge on October 28 was negligible; see Kaydash et al. (2013). The results in Figure 4 are also consistent with Birriel and Adkins (2019). They report that the full Moon in January 2013, caused the night sky to brighten from 18.3 mpsas early in the evening to 16.1 mpsas later in the evening. The Moon had respective altitudes of  $15^\circ$  and  $65^\circ$ . Therefore, the sky brightened by 2.2 mpsas when the full moon's altitude increased from  $15^\circ$  to  $65^\circ$ .

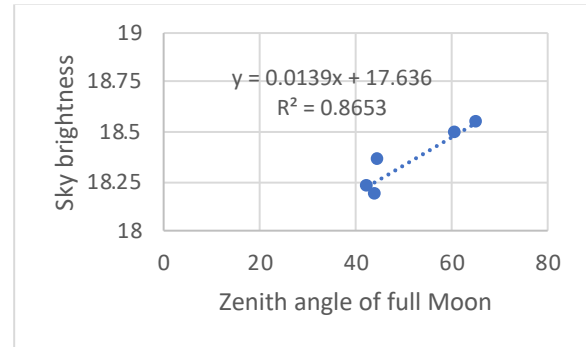


**Figure 4: Sky brightness on Oct. 28, 2023.**

### 3.4 Impact of Lunar Eclipse

Birriel and Adkins (2019) measured the sky brightness during the total lunar eclipse in January 2019. They report that the sky brightness (mpsas) dropped from 16.0 (U1) to 19.1 (U2). It remained at 19.1 mpsas until U3 and then rose to 16.6 mpsas at U4. (The terms U1 and U4 describe the time when the Moon first enters Earth's umbra to when it completely exits Earth's umbra. The terms U2 and U3 are when the Moon is first entirely inside Earth's umbra and the last instant when it is entirely in Earth's umbra.) They

report the Moon’s altitude was 56.2°, 66.8°, 71.9° and 67.9° at U1, U2, U3 and U4, respectively. Therefore, the Moon’s brightness drop of 10.2 magnitudes as a result of the total eclipse (Schmude, 2023) between U1 and U2 caused the sky brightness to change by 3.1 mpsas. Similarly, the sky brightness changed by 2.5 mpsas when the Moon went from U3 to U4. The authors report that thin clouds may have affected brightness measurements late in the eclipse.

### 3.5 Impact of solar eclipse

The zenith sky brightness during April 8, 2024 solar eclipse was measured at two different locations. In Barnesville, GA, the sky brightness (very thin clouds) dropped by 1.69 mpsas between first contact and at 19:05 Universal Time (UT) when 79 % of the Sun was covered by the Moon (or 21 % of the Sun is visible). This is close to the expected brightness drop (1.7 mpsas) when 21 % of the sunlight is reaching the sky. Ty Clark, in Dexter MO, measured the zenith sky brightness, using the same SQM that I used. He made measurements between 1:19 pm Central Daylight time (18:19 UT) to 1:58 pm Central Daylight time (18:58 UT). The results are plotted in Figure 5.

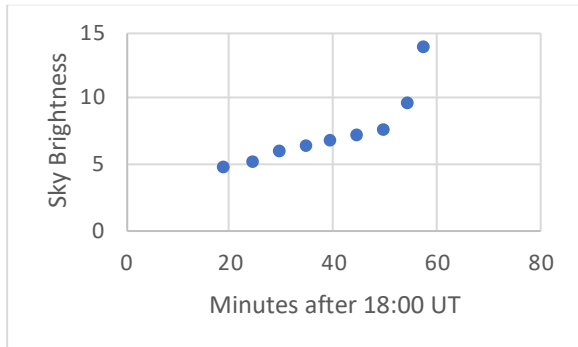


**Figure 5: Zenith sky brightness measurements, in mpsas, made on April 8, 2024 from Dexter, Missouri by Ty Clark.**

The sky brightness drop, as a result of the April 8, 2024, eclipse is now discussed. The sky brightness at 18:19 UT, was 4.50 mpsas but it had dropped to 13.77 mpsas one minute after totality. At 18:19 UT, the Sun was ~50% covered by the Moon in Dexter, since first contact was at 17:40 UT (Time and Date, 2024) and the eclipse had started at 18:57:02 UT (Great American Eclipse, 2024). The sky had already darkened by 0.75 mpsas and, hence, the sky brightness would have been 3.75 mpsas at 18:19 without the eclipse. Furthermore, the Sun’s altitude decreased by 2.4° between 18:19 UT and 18:58 UT. This would have led to a dimming of 0.06 mpsas based on Table 1. Therefore, the eclipse caused a drop of 13.77 – 3.75

– 0.06 = 9.96 mpsas or 10.0 mpsas. The estimated uncertainty is 0.3 mpsas.

Others have also measured the drop in sky brightness during a total solar eclipse. A few of these are summarized in Table 2.

Eclipse date	Brightness drop mpsas	Source
APR 8 2024	10.0±0.3*	Current work
AUG 21 2017	10	a
JUL 22 2009	7.4**	b
NOV 12 1966	8.55	c
NOV 12 1966	9.4*	d
JUN 8 1937	9.2	e
JUN 8 1918	9.4	f

\*very thin clouds \*\*cloudy skies

a Burns & Burnes (2018)

b Zainuddin et al. (2013)

c Dundekar (1968)

d Velasquez (1971)

e Velasquez (1971) his reference 13

f Velasquez (1971) his reference 17

**Table 2: Summary of a few brightness drops in sky brightness caused by total solar eclipses.**

One may see that the brightness drop of a total solar eclipse is on the order of 9-10 mpsas or a factor of 4000-10,000. Several sources (Dandekar, 1968), (Velasquez, 1971) and (Bruns & Bruns, 2018) show that the brightness dropped by a factor of 1.5 to 2 between U2 and mid-eclipse for the Nov. 12, 1966 event. The minimum duration of this eclipse was just under two minutes (TheSkyLive.com, 2024) and the 2017 eclipse lasted for just under three minutes (National Weather Service).

The sky brightness was measured at 18:58 UT from Dexter which was about one minute into totality. Therefore, the sky probably darkened after the first second of totality. Undoubtedly, the sky brightness drop for a six-minute total solar eclipse, at mid-eclipse, should be even larger than those during the middle the 1966, 2017 and 2024 eclipses. This may be part of the reason for the scatter in the data in Table 2. This should not be surprising since Schmude (2023) reports that the brightness of the totally eclipsed Moon dimmed as the Moon moved deeper into Earth’s umbra.

### 3.6 Measurement of Sun brightness

The difference in daytime and nighttime sky brightness are consistent with a Sun magnitude of  $-27.0 \pm 0.4$ . This is based on nighttime measurements made on October 28 and 29, 2023 from Hogg Mountain in Lamar County Georgia (one of my dark sky locations) and the daytime measurements

summarized in this study. The impact of the sky background on the sky brightness along with the brightness of the full moon were used in coming up with the Sun's brightness value. This result is consistent with the V-filter brightness of the Sun - 26.75 magnitudes (Livingston, 2000).

### 3.7 Future work

The write plans to undertake a thorough review of sky brightness at different times during previous total solar eclipses to learn how the sky brightness changes just before and during totality.

## 4. Acknowledgements

The writer would like to thank Carla Fredd for her assistance.

## 5. References

Barentine, J.C. "Night Sky Brightness Measurement, Quality Assessment and Monitoring." (2021). <https://arxiv.org/obs/2207.03551>.

Birriel, J.J. and Adkins, J.K. "Sky Brightness at Zenith During the January 2019 Total Lunar Eclipse." (2019). *JAAVSO*, **47**, 94-97.

Bruns, D.G. and Bruns, R.D. "Sky brightness and color measurements during the 21 August 2017 total solar eclipse." (2018). *Applied Optics*, **57** (16) 4590-4594.

Dandekar, B.S. "Measurements of the Zenith Sky Brightness and Color During the Total Solar Eclipse of 12 November 1966 at Quehua Bolivia." (1968). *Applied Optics* **7**, (4) 705-710.

Great American Eclipse (2024) at <https://www.greatamericaneclipse.com/missouri-2024-eclipse>.

JPL Horizons Ephemeris Generator (2024) at [https://ssd.jpl.nasa.gov/horizons/app.html#](https://ssd.jpl.nasa.gov/horizons/app.html#/).

Kaydash, V., Pieters, C., Shkuratov, Y. and Korokhim, V. "Lunar opposition effect as inferred from Chardrayaan-1 M<sup>3</sup> data." (2013). *Journal of Geophys. Res.: Planets*, **118**, 1221-1232, doi:10.1002/jgre.20098.

Larson, R. and Farber, B. "Elementary Statistics Picturing the World." Third Edition (2006). Pearson, Upper Saddle River, NJ.

Livingston, W.C. "Sun." (2000). in Allen's *Astrophysical Quantities* (Cox, A.N.-editor), Springer Verlag, New York, 341.

National Weather Service at <https://www.weather.gov/gsp/eclipse>.

NOAA ESRL Sunrise/Sunset Calculator at <https://gml.noaa.gov/grad/solcalc/sunrise.html>.

Schmude, R.W. Jr. "The January 21, 2019 Lunar Eclipse." (2023). *Georgia Journal of Science* **81**, Article 2. <https://digitalcommons.gaacademyu.org/gjs/vol81/iss2/2>.

TheSkyLive.com (2024) at <https://theskylive.com/solar-eclipse?id=1966-11-12>.

Time and date (2024) at <https://www.timeanddate.com/eclipse/in/@7163465?iso=20240408>.

Unihedron Instruction Sheet (2023). at [http://www.unihedron.com/projects/sqm-1/Instruction\\_sheet.pdf](http://www.unihedron.com/projects/sqm-1/Instruction_sheet.pdf).

Westfall, J.E. "How Bright The Sky?" (1988). *Proceedings of the Astronomical League (42<sup>nd</sup> National Meeting) Iowa Western Community College July 27-30, 1988*, 33-36.

Velasquez, D.A. "Zenith Sky Brightness and Color Change During the Total Solar Eclipse of 12 November 1966 at Santa Ines, Peru." (1971). *Applied Optics*, **10**, (6) 1211-1214.

Zainuddin, M.Z., Haron, S., Niri, M.A. et al. "Sky Brightness Condition During Total Solar Eclipse on July 22, 2009." (2013). *Middle-East Journal of Scientific Research*, **13** (2) 220-223.

# Quantifying Isochrone Fit Accuracy

*Sophia Bhatti*  
Stanford Online High School  
415 Broadway, Redwood City, CA 94063  
[sophiabhatti@gmail.com](mailto:sophiabhatti@gmail.com)

*Kavi Bidlack*  
Stanford Online High School  
415 Broadway, Redwood City, CA 94063  
[ksbidlack@gmail.com](mailto:ksbidlack@gmail.com)

*Nathan Bowman*  
Stanford Online High School  
415 Broadway, Redwood City, CA 94063  
[nathanlbowman@gmail.com](mailto:nathanlbowman@gmail.com)

*Karthikeya Vattem*  
Stanford Online High School  
415 Broadway, Redwood City, CA 94063  
[kkvattem@gmail.com](mailto:kkvattem@gmail.com)

---

## Abstract

Isochrone fitting, a method for determining star cluster parameters such as distance, age, reddening, and metallicity, has historically relied on visual procedures. In this project, an algorithm designed to enhance objectivity and quantify accuracy is introduced by providing a goodness-of-fit metric. The algorithm uses uncertainty-weighted residual calculations that balance computation speed and precision, in order to best evaluate an isochrone fit. The method is then validated via the comparison with manual isochrone fits of four open and four globular cluster isochrones using the Astromancer cluster fitting software.

---

## 1. Introduction

Previous methods used to quantitatively analyze isochrone fit include basic goodness-of-fit tests, the Mahalanobis distance, Bayesian inference (Eadie et al., 2022; Hernandez & Valls-Gabaud, 2006; Mints, 2008; Monteiro, 2010; Naylor & Jeffries, 2006; Perren & Piatti, 2015; Stenning et al., 2016; Valle et al., 2021, von Hippel et al., 2006). We developed a metric using residuals, or the distance between a given star in the cluster and the nearest point on the isochrone model. We gave higher weight to stars with a lower average photometric error, and then took the residual as a fraction of the maximum residual of the cluster to ensure a consistent scale.

## 2. Methods

To manually fit isochrones for comparison, the Gaia catalog was first queried through Astromancer,

which requires an initial RA and Dec radius that contains fewer than 5000 stars. Then, proper motion RA and Dec range, as well as distance, were narrowed to capture the regions of greatest density in proper motion space and distance space.

After applying these cuts, the Gaia, APASS, 2MASS, and WISE catalogs were queried for more stars (within the proper motion and distance cuts, but with a larger radius). Then, the isochrone was fitted manually; an example cluster is shown in Figure 1.

We wrote Python code to calculate the residuals. In our implementation, the uncertainties from each of the three filters are, similarly to the residuals, taken as a fraction of the maximum uncertainty. The Astromancer cluster fitting software gives the user the option to pick from which blue, red, and luminosity filters they want to use to analyze the cluster; for the analysis done in this paper the Gaia BP, Gaia RP, and Gaia G filters are used (Janzen, 2024).

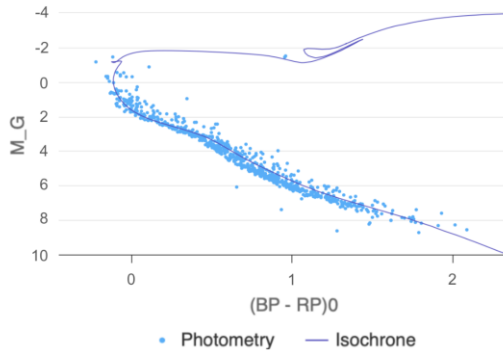


**Figure 1.** The manual isochrone fit for NGC 1912, an open cluster. Further details in Table 1. The vertical axis has been corrected for distance and the horizontal axis has been corrected for reddening.

### 3. Results

We fit eight clusters manually using Astromancer to find what we consider near-perfect fits, shown in Table 1 (Gaia Collaboration, 2023; Janzen et al., 2024). Literature values are displayed in bold (Hunt & Reffert, 2023; Pandey, 2007).

### 4. Acknowledgements

This work has made use of data from the European Space Agency (ESA) mission Gaia (<https://www.cosmos.esa.int/gaia>), processed by the Gaia Data Processing and Analysis Consortium (DPAC, <https://www.cosmos.esa.int/web/gaia/dpac/consortium>). Funding for the DPAC has been provided by national institutions, in particular the institutions participating in the Gaia Multilateral Agreement.

This research has made use of the WEBDA database, operated at the Department of Theoretical Physics and Astrophysics of the Masaryk University.

This research has made use of the VizieR catalogue access tool, CDS, Strasbourg, France (DOI: 10.26093/cds/vizieR). The original description of the VizieR service was published in 2000, A&AS 143, 23.

### 5. References

Eadie, G. M., Webb, J. J., & Rosenthal, J. S. (2022). Bayesian Inference of Globular Cluster Properties Using Distribution Functions. *The Astrophysical Journal*. 926. 10.3847/1538-4357/ac4494

Gaia Collaboration, C. Babusiaux, C. Fabricius, S. Khanna, et al. (2023) Gaia Data Release 3. Catalogue validation. *A&A* 674, pp. A32. <https://arxiv.org/abs/2206.05989>

Hernandez, X., & Valls-Gabaud, D. (2007). A robust statistical estimation of the basic parameters of single stellar populations – I. Method. *Monthly Notices of the Royal Astronomical Society*. 383(4), 1603-1618. <https://doi.org/10.1111/j.1365-2966.2007.12668.x>

Hunt, E. L., & Reffert, S. (2023). Improving the open cluster census. *Astronomy & Astrophysics*, 273, 1-31. <https://doi.org/10.1051/0004-6361/202346285> Janzen et al., 2024. Skynet Cluster Pro Plus: An Interactive Web Application for Stellar Astronomy Education. *Astronomy Education Journal* (in press).

Janzen et. al. (2024). Skynet Cluster Pro Plus: An Interactive Web Application For Stellar Astronomy Education. *Astronomy Education Journal*, *in press*.

Mints, A., & Hekker, S. (2018). Isochrone fitting in the Gaia era. *Astronomy & Astrophysics*. 618, 1-15. <https://doi.org/10.1051/0004-6361/201832739>

Monteiro, H., Dias, W. S., & Caetano, T. C. (2010). Fitting isochrones to open cluster photometric data. *Astronomy & Astrophysics*, 516, 1-17. 10.1051/0004-6361/200913677

Naylor, T., & Jeffries, R. D. (2006). A maximum-likelihood method for fitting colour-magnitude diagrams. *Monthly Notices of the Royal Astronomical Society*. 373, 1251-1263. 10.1111/j.1365-2966.2006.11099.x

Pandey, Anil K., Sharma, S., Upadhyay, K., Ogura, K., Sandhu, T. S., Mito, H., Sagar, R. (2007). Stellar Contents of Two Intermediate Age Clusters: NGC 1912 and NGC 1907. *Publications of the Astronomical Society of Japan*, 59(3) 547–558, <https://doi.org/10.1093/pasj/59.3.547>

Perren, G. I., Vázquez, R. A., & Piatti, A. E. (2015). ASteCA: Automated Stellar Cluster Analysis. *Astronomy & Astrophysics*. 576, 1-29. 10.1051/0004-6361/201424946

Stenning, D. C., Wagner-Kaiser, R., Robinson, E., van Dyk, D. A., von Hippel, T., Sarajedini, A., & Stein, N. (2016). Bayesian Analysis of Two Stellar Populations in Galactic Globular Clusters. *The Astrophysical Journal*. 826. 10.3847/0004-637X/826/1/41

Valle, G., Dell’Omodarme, M., & Tognelli, E. (2021). Goodness-of-fit test for isochrone fitting in the Gaia era. *Astronomy & Astrophysics*. 649, 1-15. <https://doi.org/10.1051/0004-6361/202140413>

von Hippel, T., Jefferys, W. H., Scott, J., Stein, N., Winget, D. E., DeGennaro, S., Dam, A., & Jeffery, E. (2006). Inverting Color-Magnitude Diagrams to

Access Precise Star Cluster Parameters: A Bayesian Approach. *The Astrophysical Journal*. 645. 10.1086/504369

Name	Type of cluster (open or globular)	PM RA $\pm$ uncertainty (mas/yr)	PM Dec $\pm$ uncertainty (mas/yr)	Distance $\pm$ uncertainty (kpc)	Distance (kpc)	Age (log years)	Metallicity (solar)	Reddening (mag)	Radius (deg)	Number of Stars	Velocity Dispersion (mas/yr)
NGC 1912	open	1.54 $\pm$ 0.33	-4.45 $\pm$ 0.32	1.16 $\pm$ 0.20	1.04	8.4	-0.15	0.33	0.20	731 <sup>1</sup>	0.14
Literature		<b>1.545 <math>\pm</math> 0.404<sup>1</sup></b>	<b>-4.430 <math>\pm</math> 0.386<sup>1</sup></b>	<b>1.085<sup>1</sup></b>	<b>1.071<sup>1</sup></b>	<b>8.431<sup>1</sup></b>	<b>-0.100<sup>2</sup></b>	<b>0.235<sup>1</sup></b>	<b>0.673<sup>1</sup></b>	<b>1041<sup>1</sup></b>	
NGC 2453	open	-2.27 $\pm$ 1.03	3.30 $\pm$ 0.77	1.71 $\pm$ 1.31	2.49	9.2	-0.6	0.46	0.16	247	0.41
Literature		<b>-2.338 <math>\pm</math> 0.191<sup>1</sup></b>	<b>3.434 <math>\pm</math> 0.232<sup>1</sup></b>	<b>4.031<sup>1</sup></b>	<b>4.058<sup>1</sup></b>	<b>8.086<sup>1</sup></b>	<b>0.31<sup>1</sup></b>	<b>0.392<sup>1</sup></b>	<b>0.306<sup>1</sup></b>	<b>212<sup>1</sup></b>	
NGC 4103	open	-6.38 $\pm$ 1.00	0.06 $\pm$ 0.71	1.84 $\pm$ 1.60	1.37	7.45	-1.1	0.4	0.42	2779	0.41
Literature		<b>-6.207 <math>\pm</math> 0.356<sup>1</sup></b>	<b>0.185 <math>\pm</math> 0.357<sup>1</sup></b>	<b>1.898<sup>1</sup></b>	<b>1.893<sup>1</sup></b>	<b>7.472<sup>1</sup></b>	<b>0.02<sup>1</sup></b>	<b>0.289<sup>1</sup></b>	<b>0.279<sup>1</sup></b>	<b>435<sup>1</sup></b>	
NGC 6583	open	1.29 $\pm$ 0.32	-0.07 $\pm$ 0.49	2.21 $\pm$ 2.00	2.04	9	0.45	0.51	0.2	4506	0.11
Literature		<b>1.329 <math>\pm</math> 0.315<sup>1</sup></b>	<b>0.0784 <math>\pm</math> 0.347<sup>1</sup></b>	<b>2.241<sup>1</sup></b>	<b>2.265<sup>1</sup></b>	<b>8.794<sup>1</sup></b>	<b>-0.81<sup>1</sup></b>	<b>0.690<sup>1</sup></b>	<b>0.287<sup>1</sup></b>	<b>341<sup>1</sup></b>	
NGC 6715	globular	-2.75 $\pm$ 0.67	-1.16 $\pm$ 1.38	28.11 $\pm$ 10.83	23.13	9.45	-1.25	0.29	0.29	300	0.17
Literature		<b>-2.675 <math>\pm</math> 0.324<sup>1</sup></b>	<b>-1.386 <math>\pm</math> 0.277<sup>1</sup></b>	<b>19.971<sup>1</sup></b>	<b>13.871<sup>1</sup></b>	<b>8.194<sup>1</sup></b>	<b>-0.11<sup>1</sup></b>	<b>1.063<sup>1</sup></b>	<b>0.182<sup>1</sup></b>	<b>1221<sup>1</sup></b>	
NGC 6121	globular	-12.43 $\pm$ 1.73	-19.12 $\pm$ 1.61	1.63 $\pm$ 0.94	2.51	10.2	-1.7	0.44	0.05	3689	0.61
Literature		<b>-12.515 <math>\pm</math> 1.348<sup>1</sup></b>	<b>-19.014 <math>\pm</math> 1.268<sup>1</sup></b>	<b>1.771<sup>1</sup></b>	<b>1.751<sup>1</sup></b>	<b>9.886<sup>1</sup></b>	<b>-0.44<sup>1</sup></b>	<b>0.206<sup>1</sup></b>	<b>0.365<sup>1</sup></b>	<b>22191<sup>1</sup></b>	
NGC 6366	globular	-0.32 $\pm$ 0.67	-5.12 $\pm$ 0.67	2.76 $\pm$ 1.62	3.13	10.15	-1.25	0.81	0.9	3036	0.25
Literature		<b>-0.333 <math>\pm</math> 0.541<sup>1</sup></b>	<b>-5.164 <math>\pm</math> 0.493<sup>1</sup></b>	<b>3.547<sup>1</sup></b>	<b>3.583<sup>1</sup></b>	<b>9.674<sup>1</sup></b>	<b>-0.64<sup>1</sup></b>	<b>0.728<sup>1</sup></b>	<b>0.181<sup>1</sup></b>	<b>3753<sup>1</sup></b>	
NGC 6266	globular	-4.88 $\pm$ 1.21	-2.94 $\pm$ 1.35	5.75 $\pm$ 2.67	5.91	10.05	-1.9	0.64	0.42	2878	0.49
Literature		<b>-4.966 <math>\pm</math> 0.897<sup>1</sup></b>	<b>-2.946 <math>\pm</math> 0.782<sup>1</sup></b>	<b>5.549<sup>1</sup></b>	<b>6.397<sup>1</sup></b>	<b>8.129<sup>1</sup></b>	<b>-0.56<sup>1</sup></b>	<b>1.003<sup>1</sup></b>	<b>0.377<sup>1</sup></b>	<b>1288<sup>1</sup></b>	

**Table 1. Manual isochrone fit values and literature values. Uncertainties for proper motion from literature values were found by taking three standard deviations. Literature radii are tidal radii. Manual fits were performed in Cluster Astromancer (<https://astromancer.skynet.unc.edu/cluster>) using Gaia DR3 Catalog data.**

# Astrometry with a DSLR camera. Observation planning, image acquisition, and data analysis

Fabrizio Pinto

EKOSPACE and Department of Aerospace Engineering, Izmir University of Economics

Teleferik Mahallesi, Sakarya Cd. No: 156, 35330 Balçova/Izmir, Türkiye.

fabrizio.pinto@ieu.edu.tr

---

## Abstract

In this paper, we shall consider Digital Single Lens Reflex (DSLR) cameras as tools for the extraction of useful astrometric data by means of scientific digital imaging techniques. Our goal is to offer information useful to carry out research complementary to what is well-known to be possible in the field of DSLR photometry. The author has been pursuing the remarkable potential of digital imaging for pedagogical purposes in classical dynamics since the early days of widely available CCD cameras. One overarching goal is the adoption of strategies allowing the researcher to proceed with minimal cost but without excessively compromising data quality. Hence the camera discussed will be a relatively old Canon 500D, enhanced by a variable zoom lens and relatively inexpensive, but absolutely indispensable, hardware additions. The camera is mounted on a fixed tripod, without equatorial tracking. For the same reasons, all software used is either Free Open Source Software (FOSS) or, in very few, but important cases, legally available freeware not available as open source. Also, the laptop used is an HP Pavilion running under Windows 8. These choices are made to demonstrate the feasibility to turn almost any aging DSLR camera into a small but effective ground-based astronomical observatory. In addition to sample workflows used by the author in university class settings — leading from image acquisition, to stacking and to orbit determination — we shall provide results from CCD sensor computer simulations for centroid position error analysis and estimation.

---

## 1. Introduction

Writing in the pages of *Scientific American* over four decades ago, Kristian and Blouke (1982) subtitled their contribution as follows:

“Microelectronic technology has presented astronomers with a sensitive new radiation detector that is expected to improve the accuracy of many crucial observations.”

This may have been an understatement. In the years following the invention of the earliest semiconductor Charge Coupled Devices (CCDs) by Boyle and Smith (1970) at Bell Laboratories, the “astronomical push” (McLean 2008) to put the new technology at the service of cutting-edge imaging has been unrelenting. Starting with Jim Janesick’s first successful attempt to image the Moon with a 100×100 CCD coupled to his own 8-inch telescope (McLean 2008), the invention of digital camera sensors revolutionized all those subfields of scientific research that require image acquisition and analysis. One obvious direction of sensor development has been growth in size and complexity, exemplified, for instance, by the Near-Infrared Camera aboard the James Webb Telescope (Burriesci 2005). However, remarkable progress has also occurred in the opposite direction, motivated by the runaway growth of the “SmallSat” industry and its inexhaustible need for miniaturization. This is exemplified by recent images

of the Earth acquired by the 2 mm-sized TRISAT-R CubeSat camera from an altitude of approximately 6,000 km (ESA 2023).

Another interesting area of research and development (R&D) has been that of applications of commercial DSLR cameras in astrophysical and in space engineering. One unsurprising factor driving such investigations is the appeal of a relatively low price compared to that of typical scientific-grade CCD cameras (Jensen 2015), quite effectively illustrated by such quantitative figures of merit as “photons per dollar” (see Hoot 2007, Table 1). Other features that make the choice of these devices attractive and possibly even competitive include, for instance, the ability to acquire simultaneous multicolor images, at the cost of having to carry out transformations from the *RGB* Bayer matrix color spectral response of the DSLR sensor to the known Johnson filter transparency (Hoot 2007, Vitek 2012, Park et al. 2016a, Zhang 2017). Connected to price appeal is the possibility to use a large battery of wide field of view (FOV) DSLR cameras to monitor the sky in “patrol” activities, such as in the search for artificial satellites and debris (Park 2013, Park 2016b, Skuljan 2015, 2016, and 2017).

Generally speaking, a reasonable literature search by the present author seems to indicate the existence of a significantly larger number of references on accurate DSLR photometry (Kloppenborg 2012, Blackford 2016) as opposed to those on DSLR astrometry. To clarify our definition, *stellar*

astrometry is of course generally well represented as it is routinely carried out as the necessary “pre-requisite of precise photometry” (Zhang 2017), including in the above cited DSLR photometric measurements. However, astrometric studies of objects *in motion* with respect to astrometric standard stars, including asteroids, comets, and spacecraft, appear to be less numerous. For instance, although DSLR photometry practitioners can rely on such authoritative and widely used resources as the *Eclipsing Binary Observing Guide* (Pickard 2011) by the British Astronomical Association and the fascinating *AAVSO DSLR Observing Manual* (Blackford 2016), equivalent resources on solar system and spacecraft DSLR astrometry are, to the best of this author’s knowledge, less widespread, at least in the form of comprehensive manuals. Informative resources attesting the growing interest in the general field of DSLR astronomical imaging are those by Ashley (2015) and Buchheim (2015).

In addition to bone fide research carried out by means of DSLR cameras, either employed as tools for data acquisition or as objects of engineering tests, digital imaging technology has also radically transformed science pedagogy. The author has explored such a potential in physics and astronomy education at all levels, from secondary school to the graduate level, since the early days of commercial CCD cameras (Pinto 1995a, 1995b, 1996, and Rest 1996, Pinto 2022). This interest continues in the age of remarkably sensitive phone cameras and far more sophisticated DSLR cameras.

The motivations for this conference paper follow naturally from the considerations presented above. Very small spacecraft (generally referred to herein as “SmallSats”) require an understanding of the technological capabilities of ever smaller cameras. A relative dearth of literature on DSLR astrometry has led this author to exploring various regimes in which such devices might be useful. The opportunity to incorporate digital image acquisition and analysis within the syllabi of astronomy, astrophysics, and space engineering classes has required an ongoing effort to prepare explanatory materials in this area. Finally, original research in this field, with the opportunity to collect data otherwise unavailable by other means, is indeed possible. Work by the author on asteroid astrometry is available in the open-source literature (Pinto 2022) and shall not be replicated here. A repository of representative DSLR images taken with various lenses, including some at the prime focus of a 90 mm Meade ETX90, is in the Community Photos section of the EarthSky website (Pinto 2024b). Student theses on autonomous optical navigation by small digital cameras in deep space supervised by this author are available at the Zenodo repository

maintained by CERN (Karaaliler 2022 and Sivasli 2023) and those results as well shall not be repeated here (see also Yildir 2024, these Proceedings). In what follows, we shall concentrate on sketching our ongoing efforts in the area of DSLR astrometry of artificial satellites by analyzing an example with emphasis on the pedagogy of orbital mechanics of objects in Earth orbit.

## 2. The sample activity

As an exercise, we consider the computation of the orbit of the Chinese Space Station (Tiangong, 天宫,) from measurements obtained by analyzing digital images of a “pass” of that vehicle over the western Aegean coast town of Izmir, Türkiye. As a practical matter, this student activity may or may not include image acquisition, that is, the calibrated image files may be either provided by the instructor or acquired by students, depending on the class being taught, student knowledge levels, equipment available, logistics, location, and personal interest. This pedagogical approach parallels a related exercise guiding students through asteroid identification by digital “blinking” of DSLR images, followed by data preparation in the “80-column” (“punch-card”) Minor Planet Center (MPC) format, and ending with the calculation of the *heliocentric* orbit of the object (Pinto 2022). In general, encouraging students to obtain their own images has been found to lead to further insights during discussions. For instance, since members of a class may be scattered over a geographical area larger than 40 km during the week and objects in low earth orbit (LEO) may typically reach altitudes as low as 300-400 km, the parallax effect ( $\sim 0.1$  rad) is quite apparent even visually, providing a striking illustration of the three-dimensionality of space through a depth perception typically unavailable in astronomy. Furthermore, parallax measurements also afford a direct calculation of the distance from the observer, which is of independent research importance.

### 2.1 Hardware

The equipment employed to obtain the results discussed herein consists of a Canon 500D, in this case coupled to a zoom lens of focal length (18-55) mm, assembled on a sturdy tripod head and operated without tracking. The camera in question is not expected to be identical for every student, and an effort is presently being made to allow students to carry out their observations by using other DSLR cameras available, as well as with their smartphones or tablets. This presents its own challenges since different brands



or models have different hardware and software features, which must be known to the instructor in order to design feasible and mutually compatible activities. One example of such issues is the fact that some brands release the temperature of the sensor in the metadata of any image (EXIF file) whereas others keep that information proprietary; similarly it is not always clear from the product literature whether the time of creation of the image file represents the beginning of the exposure, the end, an average, or a later time when the file is downloaded to a memory storage device. In the last few years, student experiences were reported using a Canon 350D, a Nikon D3100, and an iPhone 11 (for the latter two see Yildir (2024, these Proceedings).

In order to avoid vibrations, the camera is commanded either by its internal timer, or, again depending on the class details, it may be connected to a laptop for use by more advanced users. Among very desirable hardware additions is an external power source connected, for instance, to a wall outlet, which was in use in the present project.

## 2.2 Software

Consistently with the choice of DSLR cameras as a cost reducing tool, the author follows a policy of avoidance of pay-walled software for all class activities. This does not mean that proprietary, closed source software is never used, so long as legally free versions are available. The most typical examples are the Free Wolfram Engine (WFE) for developers (Mathematica language), which is freely available but not open source (McLoone 2019, Wolfram 2019); other examples are the proprietary camera control software, and, depending on student preference, reference managers programs such as Mendeley (free but now closed source), which may be replaced by Zotero (free and open source software, that is, FOSS) or equivalent. All data obtained from images is eventually collected into a Jupyter Notebook designed for the activity (see that available for asteroid orbit determination in Pinto (2022)); all such information can be analyzed by accessing any available kernels (such as the Wolfram Free Engine) and plots can be produced. In order to provide students with an experience reporting scientific data, a brief report written in LaTeX and slides for a presentation are also required.

Information regarding all needed software tools is available at various public project components stored in the Open Science Framework (OSF) instructor account (<https://osf.io/tehp2/>). The starting point of this journey for students without FOSS/freeware experience is the installation of *Freeplane* (<https://sourceforge.net/projects/freeplane/>), an app

needed to open a mindmap file listing many FOSS/freeware tools. Also needed is the note-taking app *Joplin* (<https://joplinapp.org/>), capable to support a subset of LaTeX commands. Once these two tools are installed, students can proceed to install any other tools they wish by downloading instructions from the available OSF Wikis and Files.

An effort is being made to consider the needs of students using either Mac OS or Linux, although these represent a very small minority. In particular, a program is underway to deploy the Linux operating system more widely within my classes at all levels. In the last few years, several activities have required the students to become familiar with *Cygwin* (<https://www.cygwin.com/>), which was reported by students to be hassle-free. On the other hand, the *Oracle VM Virtual Box* (<https://www.virtualbox.org/>) was given a less positive reception due to heavy memory demands on the system. A few enterprising students reported that they were far happier to just install a Linux distribution such as Ubuntu, possibly as a dual boot with Windows (Akkaş 2020). In these cases, Linux has been used to run SExtractor (Bertin 1996) and NASA 42 ), so far only available for Linux (<https://github.com/ericstoneking/42>).

In order to ensure that all students – even those without the latest laptop models available – can carry out the required projects, the author tests all activities on an older laptop running Windows 8, although most users run Windows 10 or 11. Because of the approach described in this section, all software tools mentioned herein are assumed to be FOSS, except the Wolfram Free Engine (WFE).

## 3. Observing

It is obvious to this author that most students approach sky imaging with almost no knowledge of the process to be followed to acquire images of scientific value. Indeed, very few students have handled an actual full-featured camera, especially on Manual settings. In this respect, there appears to be a curriculum gap between very advanced, highly mathematical orbital and celestial mechanics courses and contact with observational reality. The experience of observing any satellite directly represents almost a “culture shock” to many students, often met with audible surprise both at the difficulties and at the possible rewards. Without wanting to appear condescending, this moment of transition between a computer screen and physical reality may be very frustrating for first-time observers, who may benefit from interaction with more senior and experienced student peers.

### 3.1 Preparations

Although this will be obvious to professionals, students must be encouraged to carry out detailed planning activities to ensure that any observation yields scientifically useful results.

### 3.2 Charting

For an activity such as the observation of a spacecraft, after checking the weather forecast, this will consist of logging into websites that provide user-friendly predictions of passes at the exact location of the observer. A widely used resource is Heavens-Above (<http://heavens-above.com/>). A more comprehensive analysis must be obtained from such apps as the planetarium program *Stellarium* (Zotti 2019), with the *Satellites* plug-in enabled (<https://stellarium.org/>). Upon updating to the latest known two-line element (TLE) information (also available from *Celestrak* at <http://celestrak.org/>; see Vallado 2012), tools of this type allow planning of the orientation of the camera sensor within the sky map, pointing of the camera-head, exposure timing, as well as of the exact placement of the tripod at the observation site. Further sophistication can be achieved by making use of the *Stellarium* scripting engine (Zotti 2024).

### 3.3 The event

The event imaged is the appearance (or “pass”) of the Tiangong over Izmir on 10 April 2024. During this opportunity, by using the historical TLE data available from *Celestrak*, the spacecraft can be seen to have emerged from the shadow of the Earth at 2024-04-10T02:13:04 UTC (notice that Türkiye at UTC+3 does not observe daylight savings time). A few seconds later (T02:13:14), the object became fully visible upon exiting the penumbra. The average of these two times corresponds to the time provided by Heavens Above for the exit from the shadow (T02:13:08) within  $\pm 1$  s. The altitude reached a maximum of approximately  $78^\circ$  before declining and falling below  $10^\circ$  at T02:16:35. The expected apparent magnitude was predicted to peak at approximately +1.6 and to fall to +3 towards the end of the event. The distance from the observatory at maximum height was 385 km.



Figure 1. Stellarium chart showing the track of the Tiangong amongst the constellations during the pass (negative, or inverted display). The blue rectangle is the Canon 500D sensor field of view (FOV). The light and dark green curves crossing the field from bottom right to top left are the umbra and penumbra of the Earth, respectively. In red, the segment of the satellite track from its exit from the umbra to the field edge (compare this view to Fig. 4).

### 3.4 Synchronization

Synchronization of the camera to atomic time is indispensable, and indeed timing accuracy remains one of the great challenges for orbit determination at the pedagogical level. This can *approximately* be achieved by synchronizing the laptop to atomic time and then connecting the camera to the laptop to synchronize the two. Since the internal laptop clock is notoriously inaccurate, it is good practice to synchronize the camera just before the observation starts. Depending on the brand, this can also be achieved by using an external GPS unit. Synchronization to such a website as *Time-is* is expected (<https://time.is/about>) to provide an accuracy of  $\Delta t \approx \pm(0.02-0.1)$  s, depending on Internet connection and computer performance. Since the circular orbital speed in LEO is  $v_c \approx 7$  km/s, at an altitude  $H = 700$  km directly overhead, the maximum position uncertainty,  $v_c \Delta t = 0.7$  km, translates into an angular uncertainty of  $\Delta \theta = v_c \Delta t / H = 0.001$  rad  $\approx 200$  arc sec. This is comparable to, and possibly greater than, the resolving power as determined either by the Rayleigh criterion ( $\Delta \theta_{Ray} \approx 1.22 \lambda / D$ ) or pixel size  $\Delta \theta_{pix} \approx 2 d / F$  (Pinto 1995a, p. 440), where  $D$  is the entrance pupil after considering the f-ratio used (typically 5.6),  $d$  is the pixel size, and  $F$  is the focal length. These simple

considerations illustrate the importance of accurate time-keeping in this type of problem, as opposed, for instance, to asteroid observation in deep space.

It may be useful to prepare the camera settings before starting the observation. Obviously, this requires switching all features to Manual. In our case, we used f/5.6 and experimented with the highest setting of ISO 12800 (without any noise reduction-feature enabled). This is not available by default and must be activated by the user (Revell 2010, p. 206).

### 3.5 Focusing

One of the most critical, and often underestimated, tasks is proper focusing. This is a long discussion, especially as it pertains to stellar photometry (see the extensive treatment in Blackford (2016)). For the purposes of this astrometric project, we shall assume that the students are instructed to bring stellar images to “pinpoint” size either by hand (as done in the case of this report) or, possibly, by software control of electronic lenses. Regardless of the details, this process is found to take a longer time than students expect, and special warnings must be given about “focus creep” during the observing run, as well as to any unwanted focus shifts when flat field frames are taken (Sec. 3.8). In practice, it is found that, with the Canon 500D, one can take advantage of the Magnify Image button in Live View to assess far more effectively the size of star images on the sensor. In order to cause such images to appear on the LCD display, it is necessary to switch to as much as 30 s exposure. If even that is insufficient, extremely distant lights may have to be used.

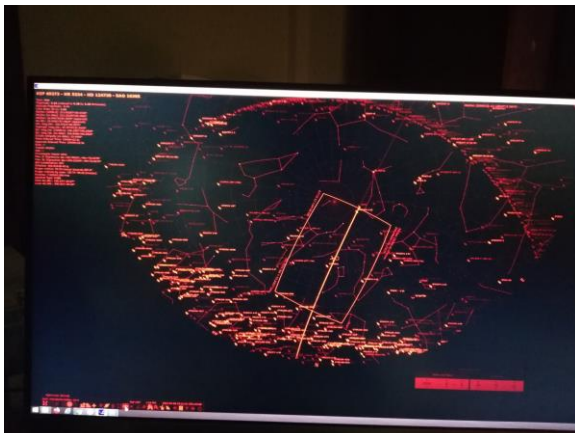


Figure 2. Stellarium in night mode for field identification.

### 3.6 Camera alignment and orientation

It is the experience of the author that student contact with the sky in a setting other than that of a professional astronomical observatory is not devoid of challenges. If the camera is mounted on a tripod and not piggybacked on a computer-controlled telescope, the responsibility to identify the relevant region of the sky that the spacecraft will cross is entirely upon the observer. In this sense, bringing a laptop with *Stellarium* running in night mode may be enormously helpful. In addition, or as an alternative, smartphone apps with dimmed out screens may make this process simpler. It must be recalled that, quite often, satellites in LEO not in a retrograde orbit will travel in a direction opposite that of celestial objects during the night, thus contributing to confusion with some students. Using the *Stellarium* sensor definition properties, it is possible to make a reasonable plan of action as to the orientation of the camera. Additional problems to consider may be related to the height of the satellite above the horizon. For instance, if the spacecraft appears near the zenith, it is surprisingly difficult to access the LCD display unless the tripod is set as high as possible.

The best practice is to take as many test shots as needed to ensure that the camera is ready well ahead of time. Some considerations are in order. It is relatively simple to bring into view as many stars as needed for a final alignment verification with exposures in the 5-10 s range.

However, such exposures will be *single* shots, which the Canon 500D takes approximately 2 s after the shutter release button is pressed. Once all is confirmed, allowance must be made for the rotation if the Earth will before the shots are taken. Also, in this project, the Canon 500D was set to take bursts of 10 shots with 1 s exposure without computer control, for maximum simplicity. It is crucial to remember to make this last-moment setting change from single shots to bursts after the camera is considered focused and aligned. Since bursts are taken by the camera after approximately 10 s, this longer delay must be factored in to plan the exact moment to depress the release button.

Most tasks described so far can be carried out by camera control software, such as DigiCamControl (<https://digidcamcontrol.com/>) with the added benefit of the Astronomy tab and scripting. In this project, however, all imaging was carried out by depressing the release button and waiting for the default delay.



Figure 3. The Canon 500D on its tripod during setup.



Figure 4. The first 6 tracklets of the 10-image burst commencing at time T02:13:11:61 (Set 1). Notice a defect in the stacking at tracklet #1 (barely visible). Corona Borealis is visible at the bottom left. The initial range is  $\approx 390$  km.

### 3.7 Image acquisition

As the camera carries out the 10-image burst, it has been observed that the last shot is appreciably delayed with respect to the previous ones. This may be due to the downloading of large RAW files. Importantly, following the burst, the task of image file writing to the memory card requires approximately 2 minutes. During this time, no imaging is possible. Hence the two sets of data used herein are two 10-image bursts separated by a time gap.

### 3.8 Calibration frames

Immediately following image acquisition, the observer proceeds by taking three sets of 50 images each for dark frames (lens capped, no setting change), bias frames (lens capped, exposure at 1/4000 s), and flat field frames. These are taken upon returning indoors by imaging a large computer screen showing a uniformly white canvas, without any focus change, and with exposures such as to not saturate the image

(typically this means exposures in the 1/800 s to 1/2500 s).

### 3.9 Stacking and astrometric calibration

In order to obtain images of the spacecraft in motion as trails superimposed to the night sky, we use DeepSkyStacker (DSS). It is not uncommon for some frames to be rejected by DSS and experience leads to the settings needed to retain as many frames as possible. The output produced by DSS is typically a 32-bit TIFF color file, which is transformed to 16-bit by using, for instance, GIMP (<https://www.gimp.org/>). The DSS output file, named by default Autosave, is then uploaded to the “blind” astrometric calibration program *Astrometry.net* (Lang 2009), accessible online (<http://nova.astrometry.net/>). If a successful plate solution is obtained, *Astrometry.net* will return a report along with a fully calibrated, 8-bit FITS image file (new-image.fits).

This new image file can be downloaded and opened in the astrometric stacking program *ASTAP* (<http://www.hnsky.org/astap>) to provide *ASTAP* with the initial coordinates of the center of the image, scale, and orientation, needed by *ASTAP* to achieve its own plate solution. The workflow including *Astrometry.net* and *ASTAP* may require fine-tuning due to the extremely short focal lengths involved. Both applications offer options to successfully treat most cases we have encountered.

The final product of this process is an image showing the spacecraft 1 s tracklets over the sky, astrometrically calibrated so that the celestial coordinates of the tracklets can be determined (see Fig. 4 and 5).



Figure 5. The second 10-image burst, commencing at time T02:14:40:07 (Set 2). Notice a defect in the stacking at tracklet #6 (barely visible) and the delayed image of the 10<sup>th</sup> tracklet at far left. The length of the tracklets is smaller than in Fig. 4 due both to increased range ( $\sim 750$  km) and perspective. The bright star just above the center right is Altair ( $\alpha$  Aql).

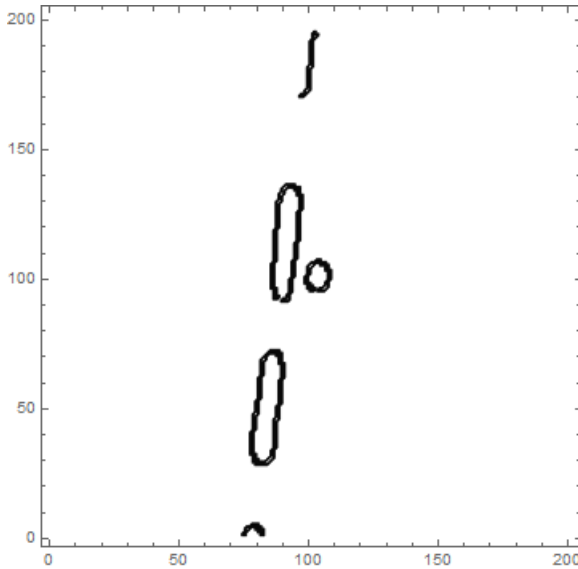


**Figure 6. Successful edge detection for the identification of satellite tracklets in the Mathematica language. The instruction used is EdgeDetect, with an appropriate fine-tuning of the needed parameters (pinto 2024a). Notice the challenge presented by the image of the star  $\iota$  CrB - 14 CrB on the right of the central tracklet (compare Fig. 4, 3<sup>rd</sup> tracklet from the right, where the same star is visible).**

#### 4. Measurements

The first step in obtaining measurements of the coordinates of the spacecraft as a function of time is to read out the Metadata files of every light frame to collect the Create Date entry, containing the time at which the image was taken. I useful FOSS app to collect all such information from the CR2 RAW format files created by the Canon 500D is Metadata++.

Once such information is prepared in a text file, the coordinates of the tracklets must be measured directly from the calibrated and stacked FITS image. As also done in the previously cited asteroid activity (Pinto 2022), the option exists to measure such coordinates by hovering the mouse on a prominent feature of the tracklets and ready out the Right Ascension and Declination at the bottom right of the *ASTAP* screen. Clearly, this measurement is for orientation only and it cannot be considered rigorous, despite its pedagogical value. The results made available here were indeed obtained by estimating the coordinates of the beginning of every tracklet manually. This process may also have value to determine orbits very quickly if an approximate estimate is needed for the price of a measurement error.

The fast identification and accurate determination of the coordinates of satellite tracklets is in fact an ongoing research topic (Park 2013, Park 2016b, Skuljan 2015, 2016, and 2017).

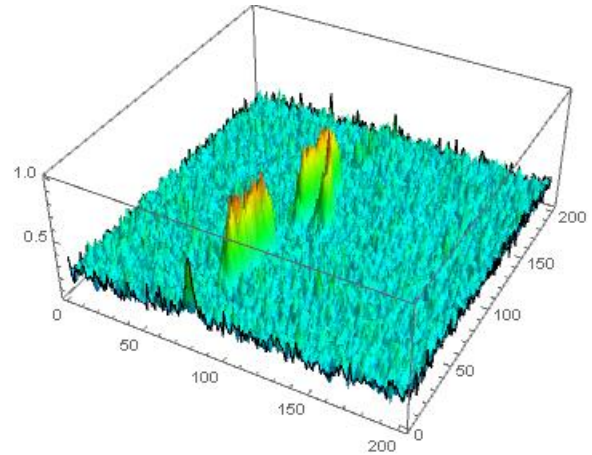


**Figure 7. The tracklets identified by edge detection in Fig. 6, shown here in a 3D plot of the pixel readout, normalized to the highest pixel value, which is set equal to unity. The effect of noise is apparent even in such more easily identifiable tracklets.**

Such research is aimed at the identification of satellite tracks in astronomical photographs and the fastest and most accurate algorithms to compute satellite orbits in nearly real time from that limited information. After candidate tracklets have been identified, a tracklet fitting function, equivalent to the Point Spread Function (PSF) familiar from stellar astrometry, must be adopted to determine the tracklet coordinates.

In our group, we have been experimenting with the machine vision capabilities made available by the Wolfram Free Engine (Mathematica language) to identify satellites tracks (Akkaş 2020). Some results can be seen in Figs. 6 and 7, and full analysis with details shall be reported in a forthcoming publication. The Mathematica instructions to obtain such results can be found in the Jupyter Notebook available as Supplementary Materials of this paper (Pinto 2024a).

Further insight is offered by Fig. 7, showing the noise present in the digital images. It must be appreciated that, although the magnitude of even such a large spacecraft as the *Tiangong* is relatively large (i.e. although the object is bright), it is moving very rapidly across the sensor. A rough estimate shows that the radiation received from the *Tiangong* is deposited over a number of pixels  $\approx 20$  times that of the star visible in both Figures ( $\iota$  CrB - 14 CrB). For this reason, although the *Tiangong* was predicted to have an apparent magnitude  $\approx +2$  and the star  $\iota$  CrB - 14 CrB has only an apparent catalog magnitude  $m \approx +5$  (SIMBAD: 16 01 27.61835231089 +29 50 49.1872027369), that is, three magnitudes fainter, they appear to produce similar pixel readouts in Fig. 7 (i.e.,  $(100^{1/5})^3 \cong 16$ , as roughly expected). In other words, the signal to noise ratio,  $S/N$ , of satellite tracklets is drastically affected by rapid motion of these objects

amongst the stars and its effect on tracklet coordinates must be carefully assessed.

One important refinement of the measurements obtained is the differential atmospheric refraction, which is neglected in this report.

## 5. Orbit calculation

The procedure to obtain an estimate of the TLE from the coordinates thus measured starts with reformatting the time and celestial coordinates, along with the coordinates of the observer, into the IOD (Interactive Orbit Determination) format introduced by George D. Lewis. Although this can be done manually, the IOD Entry 1.2 app available at the website maintained by Marco Langbroek (Langbroek 2024) is quite useful. Once the IOD file is ready, it can be processed by the ELFIND program for a first estimate of the TLE, followed by a more detailed analysis by means of SATFIT. The details of this procedure, along with download links, are available at the website maintained by Scott Campbell (Campbell 2024). The results found are shown in Fig. 8.

## 6. Conclusions

The results obtained through this relatively simple DSLR activity are encouraging, particularly regarding the values of the TLE for the inclination (error  $\approx 0.01\%$ ), Right Ascension of the ascending node (error  $\approx 0.2\%$ ) and the mean motion (error  $\approx 2\%$ ). The eccentricity, although consistent with a nearly circular orbit, has a large relative error; the argument of the perigee and the mean anomaly are clearly unreliable. A study is presently being carried out to determine whether such errors may be due to timing inaccuracies and also what the effect of a manual estimate of the tracklet coordinates might be. The increase in sophistication required to achieve better accuracy will have to be weighed against the potential pedagogical benefit. Results will be presented in upcoming reports.

```

THE GUI: INITIAL VIEW HELP
-----CELESTRAK-----
CSS (TIANHE) HISTORIC 2024-04-09T16:37:07 GMT
1 48274U 21035A 24100.81744799 .00017308 00000+0 17358-3 0 9997
2 48274 41.4672 140.8588 0008508 357.1074 2.9716 15.65067909168393
CSS (TIANHE) HISTORIC 2024-04-110T00:16:33 GMT
1 48274U 21035A 24101.13650447 .00017660 00000+0 17695-3 0 9994
2 48274 41.4672 138.9045 0008463 359.4723 0.6107 15.65079759168446
CSS (TIANHE) HISTORIC 2024-04-110T09:27:53 GMT
1 48274U 21035A 24101.51936946 .00016785 00000+0 16831-3 0 9995
2 48274 41.4672 136.5594 0008377 2.2221 357.8655 15.65091404168502
-----
1 48274U 24101.09351933 0.00000073 00000-0 50000-4 0 03
2 48274 41.4594 139.1475 0129257 100.7960 16.6251 15.33244115 08
-----

```

Figure 8. The first three entries represent the TLE files at three epochs encompassing the date and time of the observation. The last entry shows the preliminary report obtained from ELFIND and SATFIT.

## 7. Supplementary materials

All raw data used in this project is available as Supplementary materials (Pinto 2024a). For practicality due to the large data volume, neither the individual calibration nor the individual light frames are stored therein but only the masters and the final calibrated frames. Individual raw frames are available from the author upon reasonable request.

## 8. References

Akkaş, A. Büyükbayram A., and Milan B., “Digital image analysis for ground-based fast object detection and for interplanetary spacecraft autonomous optical navigation,” (2020). *Thesis, unpublished*.

Bertin, E. and Arouts, S., “SExtractor: Software for source extraction,” (1996). *A&AS* **117**, 393-404.

Blackford, M., *The AAVSO DSLR Observing Manual* (AAVSO, Cambridge, MA, 2016).

Boyle, W. S. and Smith, G. E., “Charge Coupled Semiconductor Devices,” (1982). *Bell Syst. Tech. J.* **49**, 587-593.

Burriesci, L. G., “NIRCam Instrument Overview,” (2005). *Proc. SPIE* **5904**, *Cryogenic Optical Systems and Instruments XI*, 590403, J. B. Heaney and L. G. Burriesci, Eds. (25 August 2005).

Campbell, S. *Satellite Orbit Determination*: <http://sat.belastro.net/satelliteorbitdetermination.com>, 111 July 2012, Accessed: 1 May 2024.

ESA, “Earth Through a 2-mm Lens From a 6,000 km Orbit,” *SciTechDaily*: <https://scitechdaily.com/earth-through-a-2-mm-lens-from-a-6000-km-orbit/>, 10 November 2023, Accessed: 7 May 2024.

Hoot, J. E., “Photometry With DSLR Cameras,” (2007). *The Society for Astronomical Sciences 26th Annual Symposium on Telescope Science*. Held May 22-24, 2007 at Big Bear, CA. Published by the Society for Astronomical Sciences.

Jensen, T. J., *Budget Astrophotography. Imaging with your DSLR or Webcam* (Springer Science+Business Media, New York, 2015).

Karaaliler, H., Akan, Y., Demirbağ, D. L., and Macit, İ., “Autonomous optical and inertial navigation of solar-sail propelled CubeSat class spacecraft during targeting missions to asteroids and minor moons,”

- (2022). *Zenodo*. <https://doi.org/10.5281/zenodo.7032367>.
- Kloppenborg, B. K. “A Demonstration of Accurate Wide-field V-band Photometry Using a Consumer-grade DSLR Camera,” (2012). *JAAVSO*, **40**, 815-833.
- Kristian, J. and Blouke, M., “Charge-coupled devices in astronomy,” (1982). *Sci. Am.* **247**, 67-74.
- Lang, D, et al., “Astrometry.net: Blind astrometric calibration of arbitrary astronomical images,” (2009). *Astron. J.*, **139**, 1782-1800.
- Langbroek, M. *Astronomical Software*: <https://langbrom.home.xs4all.nl/software.html>, 19 June 2020, Accessed 1 May 2024.
- McLean, J. S. *Electronic Imaging in Astronomy* (Springer, Berlin, 2008).
- McLoone, J., “Why Wolfram Tech Isn’t Open Source—A Dozen Reasons,” (2019). *News, Views, and Insights*: <https://blog.wolfram.com/2019/04/02/why-wolfram-tech-isnt-open-source-a-dozen-reasons/>, 2 April 2019. Accessed: 8 May 2024.
- Park, S.-Y., et al. “Development of a Data Reduction Algorithm for Optical Wide Field Patrol ( OWL ) II: Improving Measurement of Lengths of Detected Streaks,” (2016a). *JASS* **33**, 2211-227.
- Park, W., et al., “Photometric Transformation from RGB Bayer Filter System to Johnson-Cousins BVR Filter System,” (2016b). *Adv. Space Res.* **57**, 509-518.
- Pickard, R., *Eclipsing Binary Observing Guide* (British Astronomical Association, London, 2011).
- Pinto, F., “CCDs in the Mechanics Lab & A Competitive Alternative? (Part I),” (1995a). *Phys. Teach.*, **33**, 436-441.
- Pinto, F., “CCDs in the Mechanics Lab & A Competitive Alternative? (Part II),” (1995b). *Phys. Teach.*, **33**, 520-524.
- Pinto, F., ““Can Apples Fall Upwards?” Astronomy for Students and Their Teachers at the Merle A. Starr Observatory,” (1996). *Bull. Am. Astron. Soc.*, **28**, 958.
- Pinto, F. “Introduction to asteroid detection, centroid characterization, and orbit determination,” (2022). *Zenodo*. <https://doi.org/10.5281/zenodo.7006675>.
- Pinto, F. “Astrometry with a DSLR camera. Observation planning, image acquisition, and data analysis. Supplementary materials,” (2024a). Accessed: 7 May 2024. Retrived from the OSF: [https://osf.io/4b73a/?view\\_only=423dfdccbd0845cc9e1385df50a25cb9](https://osf.io/4b73a/?view_only=423dfdccbd0845cc9e1385df50a25cb9)
- Pinto, F. *EarthSky Community Photos: Fabrizio Pinto*: [https://ecp.earthsky.org/?filter\\_1\\_3=Fabrizio&filter\\_1\\_6=Pinto&mode=all](https://ecp.earthsky.org/?filter_1_3=Fabrizio&filter_1_6=Pinto&mode=all) , (2024b). Accessed: 7 May 2024.
- Rest, A., “Calibration of a CCD Camera and Correction of its Images,” (1996). *Thesis, unpublished*.
- Revell, J., *Canon Rebel T1i/500D. From snapshots to Great Shots* (Peachpit Press, Berkeley, CA, 2010).
- Sivashi, A. O., Köse, B., and Gürhan, E., “Autonomous Optical and Inertial Navigation of a Solar-sail Propelled CubeSat Class Spacecraft Targeting Mars and its Moons,” (2023). *Zenodo*. <https://doi.org/10.5281/zenodo.8188984>.
- Skuljan, J., “Trial Firefly - Building a Space Situational Awareness Capability at the Defence Technology Agency,” (2015). DTA Report 402 NR 1683 (Defence Technology Agency, Auckland, New Zealand, 2015).
- Skuljan, J., “Automated astrometric analysis of satellite observations using wide-field imaging,” (2016). *Advanced Maui Optical and Space Surveillance Technologies Conference (AMOS)*
- Skuljan, J., “QuadCam - a quadruple polarimetric camera for space situational awareness,” (2017). *Advanced Maui Optical and Space Surveillance Technologies Conference (AMOS) held in Wailea, Maui, Hawaii, September 19-22, 2017*.
- Vallado, D. A. and Cefola, P. J., “Two-line element sets – Practice and use,” (2012). In *Proc. 63rd International Astronautical Congress, Naples, Italy, 1-5 October 2012* (IAF, IAC-12-A6.6.11).
- Vítek, S. and Blažek, M., “Notes on DSLR photometry,” (2012) S. Guziy et al., Eds., in *Second Workshop on Robotic Autonomous Observatories, ASI Conference Series 7*, 231-238.
- Wolfram, S., “Launching Today: Free Wolfram Engine for Developers,” (2019). *Steven Wolfram Writings*: <https://writings.stephenwolfram.com/2019/05/launchi>

[ng-today-free-wolfram-engine-for-developers/](https://www.wolfram.com/language/learn-today-free-wolfram-engine-for-developers/),  
Accessed: 21 May 2019.

Yıldır, K., “Solar Sail Propelled CubeSat Autonomous Navigation in Deep Space: Experimental Asteroid Targeting With iPhone and DSLR Cameras,” (2024). (these *Proceedings*).

Zhang, M., et al., “Precision Multiband Photometry with a DSLR Camera,” (2017). *Pub. Astron. Soc. Pac.* **128**, 035001.

Zotti G. et al., “The Simulated Sky: Stellarium for Cultural Astronomy Research,” (2019). *JSA*, **6**, 221-258.

Zotti G. and Wolf, A., Eds., *Stellarium 24.1 User Guide* (stellarium.org, 2024).



# Solar Sail Propelled CubeSat Autonomous Navigation in Deep Space: Experimental Asteroid Targeting With iPhone and DSLR Cameras

*Kıymet Yıldır*

*Faculty of Engineering, Department of Aerospace Engineering  
Izmir University of Economics*

*Fevzi Çakmak, Sakarya Cd. No:156, 35330 Balçova/İzmir, Türkiye  
kiymet.yildir@std.ieu.edu.tr*

---

## Abstract

Solar sail missions in deep space are expected to require special navigational considerations due to relatively large stochastic disturbances over extremely long, very low-level thrusting time periods. This paper presents early experimental results on beacon asteroid detection — part of an undergraduate thesis project on realistic autonomous optical navigation simulations of small spacecraft propelled to Mars by a solar sail. Such a mission offers additional technological challenges, given the mass and volume limitations upon the design of the imaging subsystem, which affect the maximum magnitude of beacon asteroids detectable at very long range. Here we discuss observations carried out with an iPhone 11 camera and a Nikon D3100 DSLR camera, both on a tripod and operated in parked mode, without equatorial tracking. The workflow was adapted from that used in our university classwork and designed for asteroid orbit calculation by means of commercial digital cameras, appropriately modified to solve the classical inverse problem of the determination of the position of the observer. A discussion will be presented of the centroid coordinate observational errors for both imaging systems and of error propagation to the spacecraft dynamical state estimates. This analysis will yield a first estimate of the mass penalty corresponding to a required gain in the detectable asteroid apparent magnitude. A software data pipeline from onboard data acquisition to the final spacecraft navigational solution will be presented. Next steps in the implementation of the approach discussed in this thesis in an operational environment shall be considered.

---

## 1. Introduction

Nowadays deep space missions are the most improving section in the space industry. Interplanetary missions and asteroid mining are two of example for deep space missions. Propulsion motors is not efficient and not usable regarding the needed fuel amount. Regarding communications and navigation, particular challenges apply throughout the mission. The distance of the spacecraft from the ground stations may be problematic due to time. In this conference paper, the optical navigation subsystem of a mission targeting Mars and its Moons will be considered (Zengin et al. 2023). With this approach, beacon asteroids and comets are used for calculating the position of the spacecraft. The main focus of this paper will be asteroid and comet detection with an iPhone (Odenwald 2023) and a Nikon D3100 DSLR camera. For asteroid and comet targeting and detection, the decision was made to only make use of Free Open Source Software (FOSS) and other tools licensed as freeware although, possibly, not yet open sourced (Pinto 2022).

## 2. Methodology

### 2.1 Observation Planning

The first step in observation planning is knowledge of available equipment and geographical location. As far as equipment, a critical piece of information for observation planning is the maximum apparent magnitude reachable. To determine such maximum t magnitude, observations must be made to detect relatively faint whose magnitude is known from existing catalogs. With that knowledge, it can be assumed that celestial objects with lower magnitudes (i.e. brighter) than that maximum value, can be detected in the image. In this project, data are obtained from the website *theskylive.com* and the FOSS planetarium program *Stellarium*, combined with data from observations.

### 2.2 Observations

During the observations, attempts were made to minimize both the human and environmental effects on the equipment. To stabilize the camera, a tripod was used and during image acquisition, the camera was connected to a computer, via the app

‘digiCamControl’. By this procedure, pictures were taken without any physical human intervention. By these methods, vibrations can be prevented, and the correct timing can be achieved by synchronizing both the camera and the computer have synchronized with atomic clock time provided by the time.is app.



Figure 1 Observation setup example. (DSLR Camera)



Figure 3 Observation setup example with the author. (iPhone Camera)

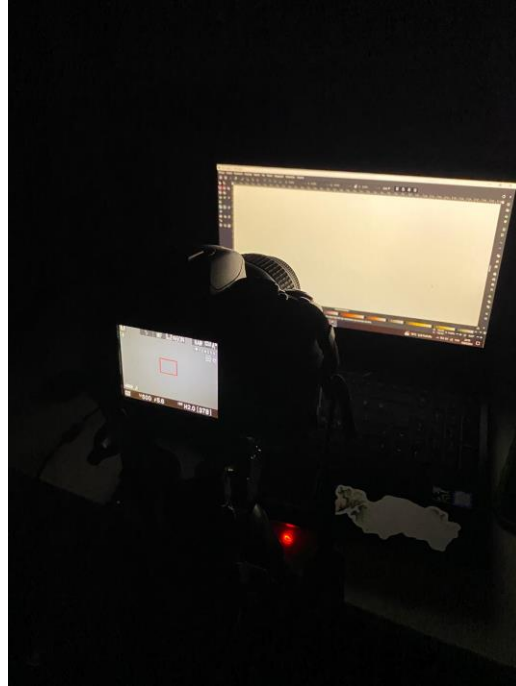


Figure 3 Flat frame setup example. (DSLR Camera)

Image calibration for all acquired images is of course necessary. Without calibration, dust, for example, may affect the results as also uncontrolled temperature of the sensor. (see Sec. 2.3).

## 2.3 Data Processing

In this Section, we consider the workflow leading from raw, uncalibrated light images to the final science frame by using calibration frames.

### 2.3.1. Dark Frames

The camera pixels gather a signal proportional to the exposure duration even in the absence of light (Armin 1996). The random flow of electrons within the semiconductor is the cause of this dark or thermal count. The dark pixel reading needs to be determined in order to accurately calibrate a raw image accurately.

Temperature has an impact on dark frames in addition to exposure. As a result, the dark frames need to be taken at the same temperature as the light images.

The requirements are as follows: the dark exposure must match the exposure of the image, the camera lens must be fully dark and covered, and the dark frames must be taken at the same temperature as the light images.

### 2.3.2. Flat Frames.

The flat frame is a map of the relative sensitivity of each detector pixel, whereas the flat calibration accounts for variations in the camera sensitivity and aberrations in the telescope field of view. These frames are produced by imaging a surface that is uniformly lit.

Because of the very short exposures involved, temperature has no appreciable bearing on flat frames. Thus, the flat calibrations are relatively portable.

The entire area in front of the camera must be uniformly illuminated; this can be a full white screen, full white paper, etc. (Armin 1996).

### 2.3.3. Bias Frames.

The bias frame is an error caused by camera charge. When the camera gets active a signal has starts, therefore there might be an error in this signal.

Bias also affected by temperature too. The temperature of the surroundings and the temperature of the sensors effects the charge of the camera.

For taking bias, camera lenses need to be closed and then the shortest exposure must have been selected, then the bias can be taken.

### 2.3.4. Light Frames.

Light frames are the raw images themselves, that is, the actual images of celestial objects.

In this paper, 50 images were taken for each of them. The exposure for both light and dark frames is 1 second. The ISO value of the camera is 12800, although, under particular circumstances, the ISO was chosen as 6400. All raw light images are stacked after calibration (Armin 1996).

### 2.3.5. Stacking Process by DeepSkyStacker (DSS)

Astrophotographers all around the world use DeepSkyStacker, a well-liked and effective stacking tool, which is free and accessible in 12 languages (Ashley 2015).

It is a free and open-source tool for stacking astronomical photos in relation to calibration frames and star rotation. As stated in previous sections, frames are used in the calibration procedure.

When the stacking process is completed, DSS automatically saves a “.tif” file, also if wanted the stacking process's info can be saved as a “.txt” file. For the data process the “.fits” file is needed. So, in this paper, GIMP was used for changing the “.tif”

file to the “.fits” file. Here is in the figure 4 output of DSS can be seen as an example.

### 2.3.6. Astrometry.net

The algorithm accessible at this website carries out astrometric image calibrations. Following the calibration and stacking in DSS, images are sent to Astrometry.net for plate solving. That method allows one to determine the precise position of the photo as well as its celestial coordinates in the sky. The details of the “blind calibration approach” are clarified by Lang (Lang et al. 2010), where further details are found.

As can be seen from figure 5 *astrometry.net* provides a reliable calibration and also marks important celestial objects and it calculates the center Right Ascension (RA) and Declination (Dec) values of the image, so that way position calculation of any object can be carried out.



Figure 4 DSS output.



Figure 5 Astrometry.net output.

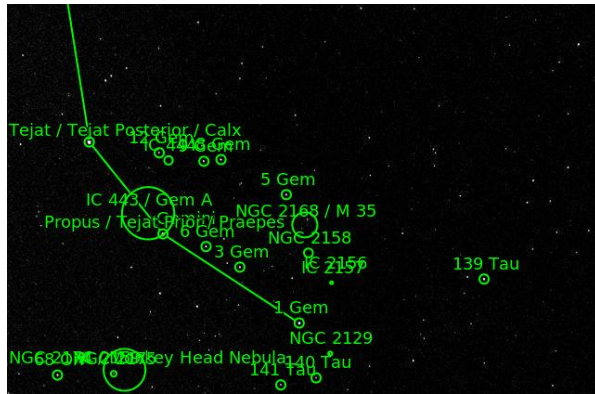


Figure 6 Astrometry.net output for a particular cropped area.

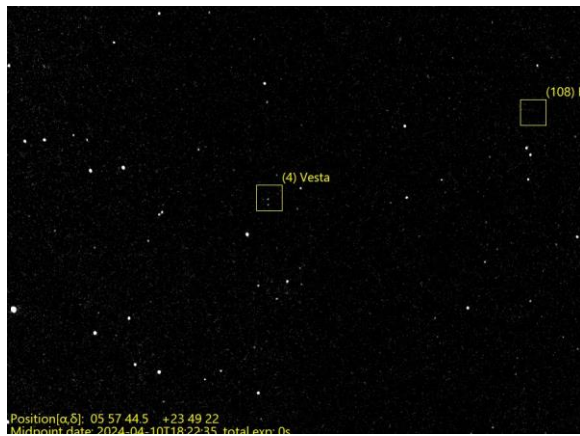


Figure 7 ASTAP Output for a particular cropped area with marked asteroids.

### 2.3.7. Astrometric Stacking Program (ASTAP)

One Free Open-Source Software tool that can stack images and determine RA-Dec values is called ASTAP (Astrometric Stacking Program). ASTAP was utilized in this research project to obtain the RA-Dec values of the objects. Astrometry.net performed the astrometric calibration computations prior to ASTAP, such as determining the image center as RA-Dec values. That calibration allows ASTAP to compute the RA-Dec of each pixel. In this paper, ASTAP was used to obtain the celestial coordinates of asteroids and comets. ASTAP also aids in locating asteroids and comets when the observation date is included in the fits header.

As can be seen from figure 7, one of the main objects of this paper is represented by the objects at the center of the square provided by ASTAP.

The overall workflow executed for this paper is shown in figure 8.

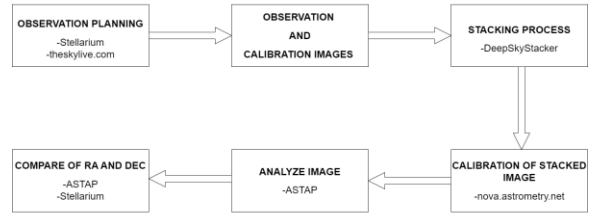


Figure 8 Workflow (Sketched via diagrams.net).

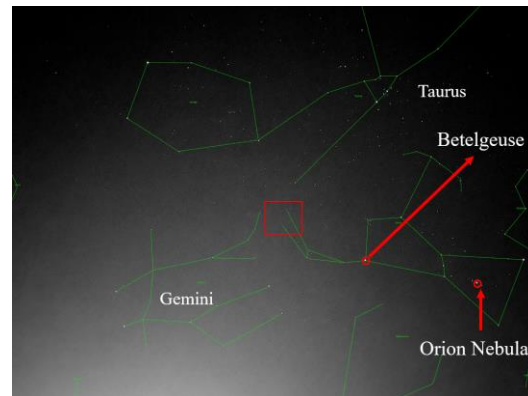


Figure 9 Final image (iPhone Camera).

In the last part of the workflow, a comparison with the data that comes from pictures and the data that comes from *Stellarium* (data based on NASA JPL) has been made. This is the part that is going to be used in the optical navigation part as the next step. The aim is to make the optical navigation calibrations and prove that.

## 3. Results

In this paper, 2 celestial objects were studied, the asteroid (4) Vesta and the comet 12P/Pons-Brooks. These objects are going to be used in simulated optical navigation as beacon celestial objects.

### 3.1 Vesta Detection with an iPhone 11's Camera

While these observations were made, Vesta had a magnitude approximately equal to +6 thus, being visible even with a smartphone camera.

For a CubeSat mission, a small camera is necessary due to the small surface area mass required. For that reason, detecting an asteroid with a smartphone camera is a capstone for a CubeSat mission that is going to use optical navigation.

Figure 9 is an output image from astrometry.net astrometric calibration. As can be seen, there is a square in a particular area. Vesta is located at the center of the red rectangle.

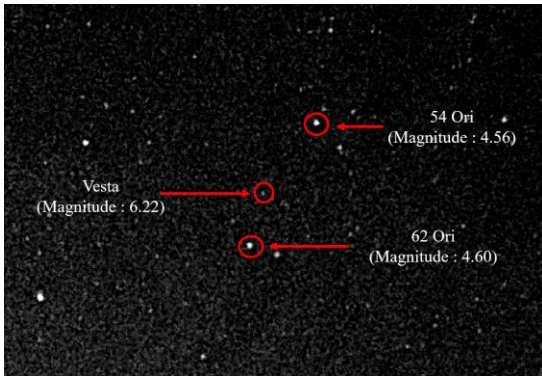


Figure 10 Red rectangle area in the previous image. (iPhone Camera).



Figure 10 Zoomed image of figure 5. (DSLR Camera).

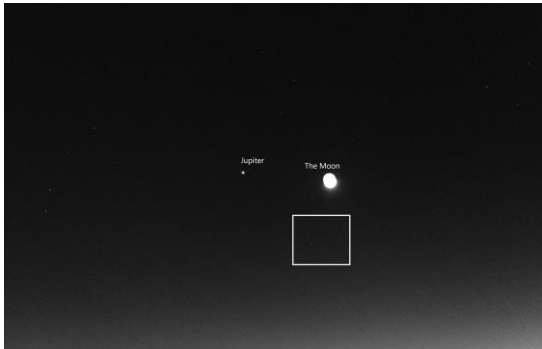


Figure 11 Final image for 12P/Pons-Brooks. (DSLR Camera).

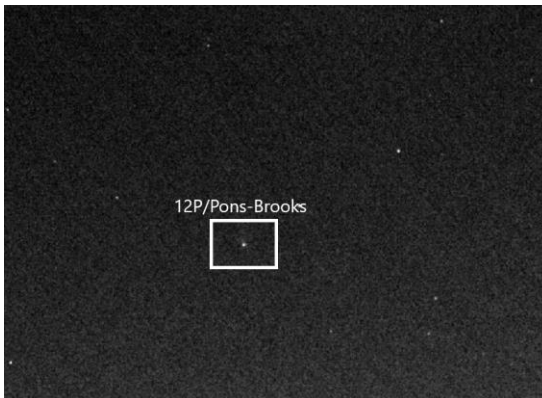


Figure 12 Squared area that zoomed. (DSLR Camera).

As the next step concerning that scientific final image, the position calculation of Vesta is going to be made, and then again respect to that position the CubeSat's position is going to be calculated.

Expected Coordinates:

6h 02m 43.25s,  
+20° 25 ' 02.2''

Measured Coordinates:

6h 19m 26.88s,  
+20° 55 ' 19.1''

### 3.2 Vesta Detection with a Nikon D3100 DSLR Camera

While the observations with the DSLR camera were made, Vesta had a magnitude around +8, which is beyond the iPhone 11's detection limit. A zoomed area around Vesta is shown in Fig. 11.

The same process is going to be applied in this image.

Expected Coordinates:

6h 12m 43.37s,  
+24° 45 ' 19.0''

Measured Coordinates:

6h 12m 03.03s,  
+24° 44 ' 27.9''

### 3.3 Comet 12P/Pons-Brooks Detection with a Nikon D3100 DSLR Camera

While the observations were made, comet 12P/Pons-Brooks had a magnitude of around +4 making even the tail of the comet visible in the final science frame (figs. 12-13).

The same calibration workflow described previously is applied in this image to investigate the possibility to use comets as well as optical navigation beacons.

Expected Coordinates:

2h 49m 28.62s,  
+16° 57 ' 41.7''

Measured Coordinates:

2h 49m 39.46s,  
+17° 02 ' 24.5''

## 4. Conclusions

Following the workflow we discussed, science frames were produced. These images show beacon

celestial objects to carry out optical navigation for a CubeSat mission. In this paper, we demonstrated the remote detection of two such beacon celestial objects by means of a phone camera and a small DSLR camera. These experimental results, in agreement with the expected ephemeris positions, show that a small camera can be used for autonomous optical navigation in deep space missions.

## 5. Acknowledgments

I would like to thank Dr. Fabrizio Pinto for his continuous supervision during my thesis and for providing the tripod. Thanks, are also due to my colleague, Ms. Ayten Pamuk, for providing the Nikon D3100 DSLR camera. I recognize the DeepSkyStacker (DSS) and Astrometric Stacking Program (ASTAP) communities for promptly answering all my questions. I also acknowledge the developers of the Free Wolfram Engine in the Mathematica language for making this important tool available to Jupyter Notebook users. Finally, thanks are due to Mr. Jay Trimble (NASA Ames), Mission System Manager of the VIPER Lunar Rover, for providing early feedback and constructive criticism about the results presented above.

## 6. References

C. Zengin, C. Oral, I. E. Ozer, T. Turhan, “Trajectory design and flight dynamics of a solar-sail propelled CubeSat class spacecraft targeting Mars and its moons” (2023). doi:10.5281/zenodo.8191968. URL <https://zenodo.org/record/8191968>

D. S. Odenwald, *A Guide to Smartphone Astrophotography* (NASA, Washington, DC, 2020).

F. Pinto, “Introduction to asteroid detection, centroid characterization, and orbit determination” (2022). doi:10.5281/zenodo.7006675.

URL <https://zenodo.org/record/7006675>

R. Armin, *Calibration of a CCD Camera and Correction of Its Images* (Master's thesis, 1996).

J. Ashley, *Astrophotography on the Go. Using Short Exposures with Light Mounts* (Springer, Switzerland, 2015). doi: 10.1007/978-3-319-09831-9

Gimp, <https://www.gimp.org/>. (accessed on 05.03.2024)

Astrometry.net, (accessed on: 05.03.2024) <https://nova.astrometry.net/explore>

D. Lang, D. W. Hogg, K. Mierle, M. Blanton, S. Roweis, “Astrometry.net: Blind astrometric calibration of arbitrary astronomical images”, *Astron. J.*, 139 (5) (2010) 1782–1800. doi:10.1088/0004-6256/139/5/1782.

I. M. Hazal Karaaliler, Yagiz Akan, Deniz Lena Demirbag, “Autonomous optical and inertial navigation of solar-sail propelled CubeSat class spacecraft during targeting missions to asteroids and minor moons” (2021). doi: 10.5281/zenodo.7032366 URL <https://zenodo.org/records/7032367>

A. O. Sivasli, B. Kose, E. Gurhan, “Autonomous Optical and Inertial Navigation of a Solar-sail Propelled CubeSat Class Spacecraft Targeting Mars and its Moons” (2022). doi: 10.5281/zenodo.8188983 URL <https://zenodo.org/records/8188984>

F. Pinto, “CCDs in the mechanics lab—A competitive alternative?”, *Phys. Teach.*, 33, 436-441 (PartI) (1995). doi:10.1119/1.2344260.

M. Blackford, “AAVSO DSLR Observing Manual” Version 1.4 (American Association of Variable Star Observers, Cambridge, 2016).

# Clarifying the Nature of Solar Cycles

*Sara F. Martin*

*Helio Research, La Crescenta, CA 91214*

---

## **Abstract**

The concept of solar cycles has been extended and altered by research papers showing every solar cycle is 22 years long. They begin and end with 4-7 years of small active regions without sunspots. Sunspots only occur during 9-14 years close to the middle of each of the 22-year solar cycles. Two latitude bands of active regions in each solar hemisphere have opposite polarity orientations. The bands are offset from each other in latitude by about 30 degrees and in time by 11 years. This led to previous thinking that the durations of all solar cycles were approximately 11 years. Within the context of this updated concept of solar cycles, the talk will include (a) how active regions and sunspots develop from elementary bipoles, (b) why sunspots are shallow, (c) the roles of filaments in solar cycles, and (d) how solar cycles reverse polarity every 11 years.

---

# Desmos and Speckle Toolbox Analysis of WDS 21001+0731

*Russell Genet*  
Eastern Arizona College  
Fairborn Institute  
610 E. Tahoe Vista Circle  
Payson, AZ 85541  
[RussellGenet@FairbornInstitute.org](mailto:RussellGenet@FairbornInstitute.org)

*David Rowe*  
PlaneWave Instruments  
1375N Main Street  
Adrian, MI 49221  
[drowesmi@aol.com](mailto:drowesmi@aol.com)

*Michael-James Ellis*  
Payson High School  
Eastern Arizona College  
301 S. McLane Road  
Payson, AZ 85541  
[michael.ellis@pusd10.org](mailto:michael.ellis@pusd10.org)

*Paul McCudden*  
Colorado Mountain College  
1275 Crawford Avenue  
Steamboat Springs, CO 80487  
[pmccudden@coloradomtn.edu](mailto:pmccudden@coloradomtn.edu)

---

## Abstract

The known binary WDS 21001+0731 (KUI 102) was observed via speckle interferometry on 2023.4899 with the 1.5-meter telescope at Mt. Wilson Observatory. Bispectrum analysis with the Speckle Toolbox provided a position angle of  $180.8^\circ$  and a separation of  $0.246''$ . Desmos graphical analysis of the apparent orbit showed that observations made since the last published orbit in 2014 were systematically deviating from the published orbit. A new Speckle Toolbox routine, Orbits, obtained revised orbital elements.

---

## 1. Observations

WDS 21001+0731 (KUI 102) was first discovered to be a double star by Gerard P. Kuiper (1934) using the 36-inch refractor and filar (visual) micrometer at Lick Observatory. This bright binary (6.23 mag F1 primary, 8.13 mag secondary) has a reported period of 58.4 years. The first speckle observation was made in 1979 by Hal McAlister (McAlister & Hendry 1982) on the 4-meter telescope at Kitt Peak National Observatory. To date there have been 32 speckle observations (not counting the recent speckle observation at Mt. Wilson Observatory reported in this paper). Many of these speckle observations were on the 4.0- and 3.5-meter telescopes at KPNO and the historic 100-inch telescope at Mt.

Wilson Observatory that Edwin Hubble used to discover the size and expansion of the universe.

The recent speckle interferometry observation of WDS 21001+0731, reported for the first time in this paper, was obtained on the 1.5-meter telescope at Mt. Wilson Observatory (MWO) on the night of June 28, 2023 (JD 2023.490). The observational equipment and techniques have been described by Faughn et al. (2023). The Speckle Toolbox (STB) was used to reduce the observations (Rowe & Genet 2015, and Harshaw et al. 2017). The STB reduction screen is shown in Figure 1. Note that the separation was  $0.246''$ , while the on-sky position angle was  $179.21^\circ$  which was subtracted from  $360^\circ$  to provide the final position angle of  $180.79^\circ$ .



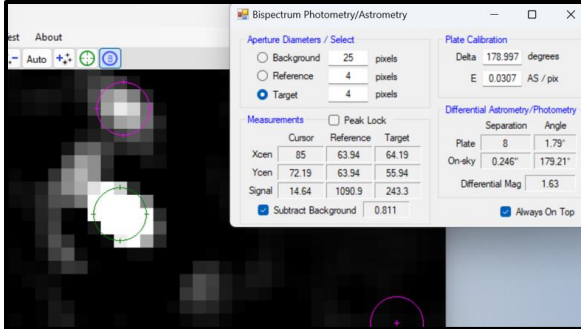


Figure 1: Speckle Toolbox reduction of WDS 21001+0731.

## 2. Desmos 6<sup>th</sup> Orbit Apparent Ellipse

With the position angle and separation from the MWO observation obtained with STB, the next portion of the analysis utilized Desmos, an online graphing calculator. Desmos is used in geometry, algebra, and calculus classes at many high schools and colleges. Student binary star analysis is facilitated by their familiarity with Desmos and its ability to visually portray the analysis. The Desmos graph for this analysis can be accessed at

<https://www.desmos.com/calculator/iknqxd1qw9>

The first step in the Desmos analysis was to paste in, as a Desmos background, the orbital plot of WDS 21001+0731 as calculated by Hartkopf and Mason (2014) from the *Sixth Catalog of Orbits of Visual Binary Stars* (Matson et al. 2023), hereafter the *6<sup>th</sup> Orbit Catalog*. The background plot was then rotated, scaled, and translated as detailed by Genet et al. (2024) and shown in Figure 2.

The U.S. Naval Observatory kindly provided a list of all published observations of WDS 21001+0731 from their Washington Double Star Catalog (hereafter the WDS Catalog). The position angles and separations of 10 past observations were entered into Desmos from the WDS text file. Except for the discovery observation, Kui1934, the other nine were all speckle interferometry observations; seven of them already plotted as large blue dots on the 6<sup>th</sup> Orbit background plot. The Desmos points appear as smaller red dots inside of the large blue dots in Figure 2. Rather than adding the Desmos points for all the past speckle observations, seven were chosen that were somewhat evenly spaced along the orbit. Two recent observations, Tok2018 and Tok2021, were not included on the background plot and were added as Desmos points, seen respectively as smaller orange and red dots. Finally, the June 2023 speckle observation at Mt Wilson Observatory, MWO2023, was added in as a light blue solid point.

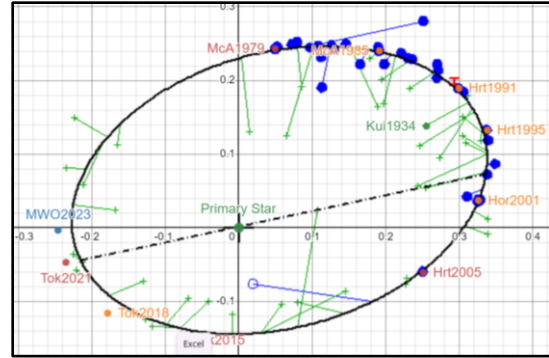


Figure 2: Background calibration plot and added Desmos observational points and labels.

The next step in the analysis was to create a Desmos ellipse that matched as closely as possible the 6<sup>th</sup> Orbit apparent background ellipse. For an ellipse not centered on the origin and not coincident with the x axis, as is our case, one can use the general parametric equations for an ellipse in the Cartesian plane:

$$x = (h + a \cos t)(\cos q) + (k + b \sin t)(-\sin q) \text{ and}$$

$$y = (h + a \cos t)(\sin q) + (k + b \sin t)(\cos q)$$

where:

- a is the semi-major axis
- b is the semi-minor axis
- h is the translation along the major axis
- k is the translation along the minor axis
- q is the angle of the ellipse major axis with respect to the Desmos x axis
- t is a parametric variable

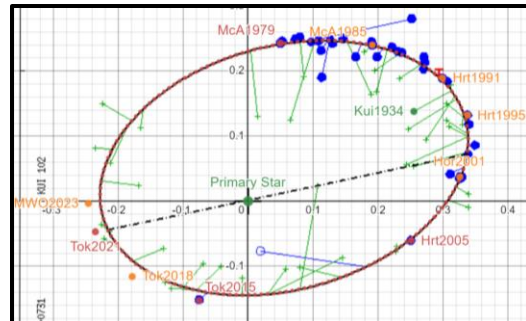


Figure 3: Match of the apparent Desmos and 6<sup>th</sup> Orbit ellipses.

The five Desmos apparent ellipse parameters were iteratively adjusted until the Desmos ellipse (small red dots) overlaid the black 6<sup>th</sup> Orbit ellipse. The quite exact overlay is even more obvious when magnified.

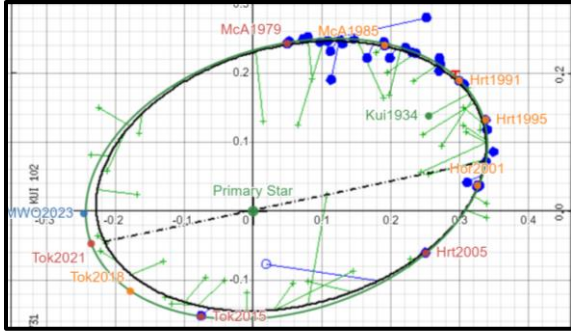


Figure 4: The new apparent ellipse (green line).

### 3. New Apparent Ellipse

A new Desmos apparent ellipse (green line in Figure 4) was created to best fit to the nine past speckle observations. Emphasis was placed on shaping the ellipse to match the last three Tokovinin observations, Tok2015, Tok2018, and Tok2021, while also matching the other speckle observations. Adjusting the five Desmos apparent ellipse parameters to get a best fit was an iterative process that required magnification of various portions of the ellipse during the iterations. It was clear from this apparent ellipse that a new set of orbital elements for the true orbit would better describe the orbit of this binary star.

### 4. Observational Accuracy

One possible approach to estimating the accuracy of binary star observations is to compare them with linear interpolated values from the annual ephemerides in the 6th Orbit Catalog. For longer period binaries with well-established orbits and slowly changing position angles and separations, new observations often closely match the interpolated ephemerides values.

However, the orbit of short period binaries can have significant curvature over a one-year period, making linear interpolation problematic. Furthermore, orbits that are not Grade 1 may contain significant errors. Finally, the catalog orbits are optimized for best fit across all observations over the entire orbit, while estimating the accuracy of a new observation might benefit from placing more emphasis on a comparison with recent high-quality observations—often those made after the orbital elements were estimated.

Andrei Tokovinin’s speckle interferometry observations on the Southern Astrophysical Observatory (SOAR) 4.1-meter telescope are of consistent high accuracy. If a new ellipse goes through several of Tokovinin’s recent SOAR observations with high precision and is also a good fit to earlier speckle observations, then how well Tokovinin’s observations agree with each other, and how far MWO

observations depart from the new ellipses can be an indication of consistency of Tokovinin’s observations as well as providing an estimate of the accuracy of the Mt. Wilson Observation.

Figure 5 shows the three most recent published Tokovinin observations of which two, Tok2018 and Tok2021, were not included in the 6th Orbit plot. Also shown is the MWO2023 observation.

Desmos can provide the distances the individual observations are located from the best ellipse. Movable point P2 is placed over the observation, while P1 is placed at the perpendicular to the ellipse. Desmos automatically calculates the distance. In Figure 6, each major grid line is 1.0 milli-arcseconds (mas), while the minor grid lines are 0.2 mas. The MWO2023 observation deviated 2.74 mas from the ellipse. Tok2015 and Tok2021 had very low deviations, while Tok2018 had the largest deviation at 0.46 micro arcseconds.

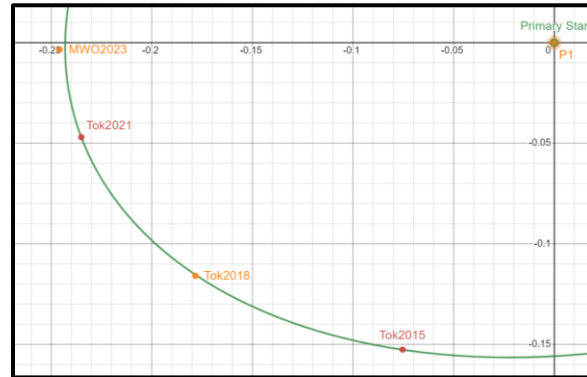


Figure 5: Three recent Tokovinin observations on the 4.1-meter SOAR telescope in Chile make a useful comparison for this year’s MWO2023 1.5-meter observation at Mt. Wilson Observatory.



Figure 6: Deviation of the Mt. Wilson Observatory observation from the new apparent ellipse.

### 5. New Orbital Elements

The newly developed *Orbits* routine in STB was used to derive revised orbital elements. The past observations supplied by the Naval Observatory from

the WDS Catalog were read in along with the MWO2023 observation. At this point, all the observations were included and equally weighted. The Weighted Root Mean Square Deviation (WRMSD) of the observations from the Hartkopf and Mason (2014) published orbit was calculated by Orbits as 40.88 mas.

Although we did not know the observational weights used in the 2014 analysis, the Orbits display suggested that the large number of less accurate visual observations inside the 2014 orbit might have biased the calculated orbit to be smaller than post 2014 more accurate speckle observations suggested it should be. Since the orbit is now reasonably covered by speckle observations, we simply gave non-speckle, non-space telescope observations in Orbits a zero weight and derived a new orbit which produced a WRMSD of 8.78 mas, a significant improvement. However, the revised orbit appeared slightly small, due most likely to the four largest off-orbit deviations all being on the inside of the orbit. These four and their inside deviations were: McA1982 19.52 mas, Bag1990 14.28 mas, Doc 2000 25.86 mas, and Gii2012 15.49 mas.

With these four observations removed, the final revised orbit is a good fit to all the remaining speckle (and space telescope) observations. The final WRMSD was 5.84 mas. Since all the remaining observations were weighted equally (weight of 1.0), the RMS deviation of the observations from the calculated orbit was also 5.84 mas. The MWO2023 observation deviated 1.64 mas from the calculated orbit. The final revised orbital elements are shown in Table 1.

Parameter	Value	Units
Period	59.65	years
Semimajor Axis	0.3073	arc seconds
Eccentricity	0.2732	n/a
Inclination	128.75	degrees
Long of Acc. Node	193.64	degrees
Time at Periastron	1957.357	date
Long. Of Periastron	314.54	degrees

**Table 1: Revised orbital elements.**

## 6. Conclusion

Both Desmos and Speckle ToolBox Orbits are useful tools for analyzing binary star orbits. Observations of WDS 21001+0731 made since its orbital elements were last derived (including our observation reported in this paper) suggested that a new orbit would provide a significant improvement. Speckle ToolBox Orbits provided these revised orbital elements.

## 7. Acknowledgements

The United States Naval Observatory supplied past observations from their *Washington Double Star Catalog*. The background plot was from the *Sixth Catalog of Orbits of Visual Binary Stars*. Gravic Inc. kindly provided travel funds for students to attend the run at Mt. Wilson Observatory. Rachel Freed, Reed and Chris Estrada, Nick Hardy, Leon Bewersdorff, Joseph Burch, Paul McCudden, Tom Smith and others either generated the target lists or managed the observations. Thomas Meneghini, the Director of the Mt. Wilson Observatory, and his staff provided support during the observation run. We thank Eastern Arizona College, the Fairborn Institute, Payson High School, Colorado Mountain College, and PlaneWave Instruments for their support.

## 8. References

- Faughn, E., J. Major, & P. McCudden. "Speckle Astrometry of WDS 18181-0120." (2023). *Journal of Double Star Observations*, **19**, 420.
- Genet, R., P. McCudden, & M. Ellis. "Desmos Graphical Analysis of Binary Stars — A Tutorial with HU 481 (WDS 16212+2259) Example." (2024). *Journal of Double Star Observations, in press*, **20**, 264.
- Harshaw, R., D. Rowe, & R. Genet. "The Speckle Toolbox: A Powerful Data Reduction Tool for CCD Astrometry." (2017). *Journal of Double Star Observations*, **13**, 52.
- Hartkopf, W. & B. Mason. (2014). *IAU Information Circular on Double Stars*. 184, 1.
- Kuiper, G. "Six New Bright Close Binaries." (1934). *Publications of the Astronomical Society of the Pacific*, **46**, 359.
- Matson, R., S. Williams, W. Hartkopf, & B. Mason. . *Sixth Catalog of Orbits of Visual Binary Stars*, U.S. (2023). Naval Observatory, Washington,DC. <http://www.astro.gsu.edu/wds/orb6.html>
- McAlister, H. & E. Hendry. "Speckle Interferometry Measurements of Binary Stars VII." (1982). *Astrophysical Journal Supplement*, **49**, 267.
- Rowe, D, & R. Genet. "User's Guide to PS3 Speckle Interferometry Reduction Process." (2015). *Journal of Double Star Observations*, **11** (1s), 266.

# Orbital Analysis of the Binary Star WDS 17166-0027

Michael-James L. Ellis  
 Fairborn Institute  
 PO Box 1656, Tonto Basin, AZ 85553  
 MichaelJamesEllis@FairbornInstitute.org

## Abstract

A position angle of  $30.92^\circ$  and a separation of  $0.635''$  for the Binary Star WDS 17166-0027 was obtained from a speckle interferometry observation at Mt. Wilson Observatory using the 1.5-meter telescope on 2023.49. The currently published orbit of WDS 17166-0027 does not include four additional published observations: Wasson 2016.34 (Speckle), Serot 2017.51 (CCD), and Tokovinin 2019.38, and 2021.33 (hrcam). Desmos and Speckle Toolbox Binary Star Orbits analysis of WDS 17166-0027 with the addition of these five observations yielded significant changes to the orbital elements, which are provided.

## 1. Introduction

In June of 2023, students, instructors, and astronomers at Mt. Wilson Observatory conducted new speckle interferometry observations of the binary star WDS 17166-0027.

To analyze the published and newly acquired observation of WDS 17166-0027, the Desmos Graphical Analysis process, Genet et al. (2024), and Ellis et al. (2024) was used in conjunction with Speckle Toolbox Orbits (STBO), Rowe & Genet (2015), and Harshaw (2017).

The resolved apparent orbit from Desmos and STBO, as well as the orbital elements found through STBO, were compared with the apparent orbital plot, shown in Figure 1, and the orbital elements from the USNO Sixth Catalog of Orbits of Visual Binary Stars (6th Orbit Catalog), Table 1, Matson et al. (2023), to determine if a new orbit was warranted.

## 2. New Observation

The Known Binaries Program, Hardy et al. (2023), was conducted by a team of students, and instructors; as well as, amateur and professional astronomers, Faughn et al. (2023). The program involved performing speckle interferometry observations on 50 close binary stars in June of 2023 at the Mt. Wilson Observatory (MWO) using the 1.5-meter telescope.

Among the 50 binaries observed, WDS 17166-0027 was observed on 2023.492. The reduction for this observation was completed using the Speckle Toolbox, and a nearby single reference star, which resulted in a position angle of  $30.92^\circ$  and a separation of  $0.635''$ .

In addition to the MWO2023.49 observation, four additional published observations were not included in the U.S. Naval Observatory's apparent orbital plot. These four observations (Wasson 2016.34, Serot 2017.51, and Tokovinin 2019.38, and 2021.33) are shown in Table 2.

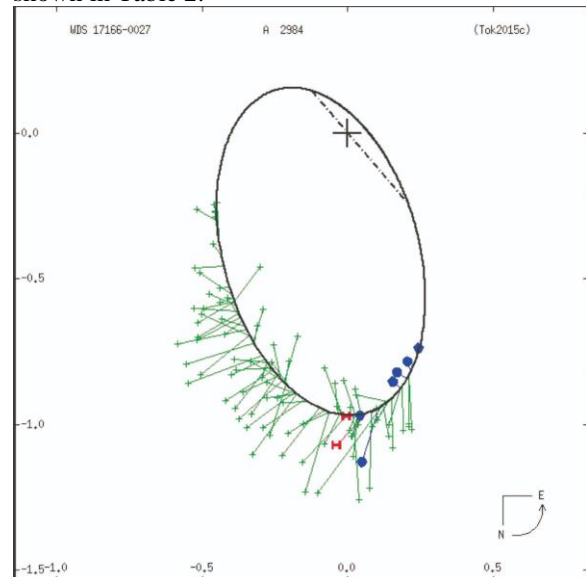


Figure 1. The orbital plot of WDS 17166-0027 from the 6th Orbit Catalog.

ORBITAL ELEMENTS: WDS 17166-0027 (A 2984)								
P	a	i	Node	T	e	omega	G	Reference
140.76 y	0.959 a	65.1	220.5	1890.53 y	0.866	287.5	3	Tok2015c
+/- 023	0.008	0	0	0.36	0.003	0		

Table 1. Orbital Elements as they appear in the 6th Orbit Catalog.

Observation Date	Position Angle	Sep. arcsec	Reference code	Tech. code
2016.337	21.37°	0.772	Wss2018	S
2017.512	22.3°	0.72	Stj2018b	C
2019.380	24°	0.7059	Tok2020e	St
2021.330	26.7°	0.6768	Tok2022f	St

**Table 2. Data for additional observations from the WDS historical data table.**

### 3. Desmos Analysis

The Desmos analysis employs a visual average of the micrometer observations, with a preference for aligning with the first observation made on 1915.54, Aitken (1918). The Desmos apparent orbit is also weighted more heavily towards speckle interferometry observations, as they tend to exhibit a higher degree of accuracy. The Hipparcos 1991.25 observation, which was the initial speckle observation for WDS 17166-0027, and the Tokovinin observations are recognized for their precision and were given the most weight among the speckle observations for this analysis.

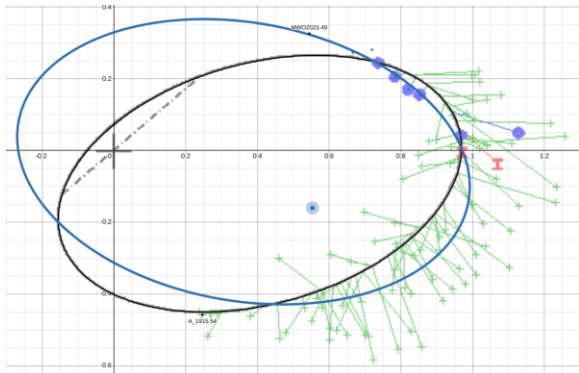


**Figure 2. Desmos apparent orbit (blue) over published orbit from 6th Orbit Catalog.**

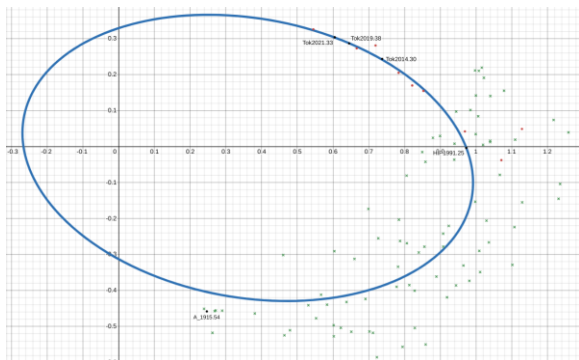


**Figure 3. Desmos plot with speckle observations in red, micrometer observations in green, and visually weight observations in black.**

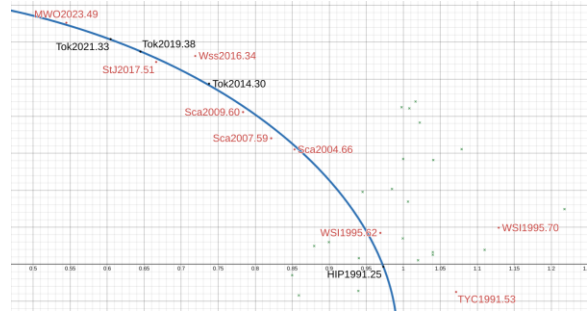


**Figure 4. Close-up of speckle observations in Figure 3.**

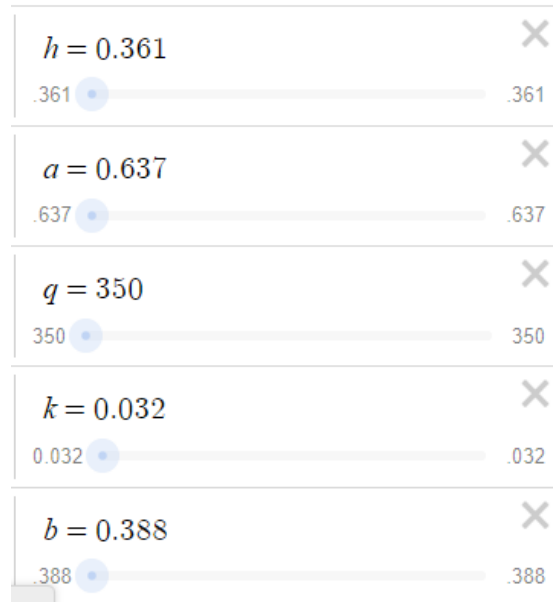


**Figure 5. Desmos apparent orbit ellipse measurements**

This Desmos analysis can be accessed at <https://www.desmos.com/calculator/qzxjz2agpy> after creating a free account at desmos.com.

### 4. STBO Analysis

Speckle Toolbox Orbits (STBO) allows the USNO's historical text file of binary star observations to be directly imported into the program as described by Genet et al. (2024). When selecting "Read Observation File," the program opens the computer files for upload. Once the file is uploaded, it automatically plots all the published observations and the USNO orbit based on the orbital elements reported in the historical data. Additional observations not included in the historical data can be added by selecting "Add Custom Observation File."

The "Add Custom Observation File" option was not used to add the 2023.49 Mt. Wilson observation for this particular analysis. Instead, the observation

was added to the USNO text file before uploading it to STBO.

When the 'Optimize' function is selected within Speckle Toolbox Orbits, the apparent orbit undergoes a refinement process based on all available observations. This program continually refines the orbit and generates a set of orbital elements as the Weighted Root Mean Square Deviation (WRMSD) approaches a minimum. Upon reaching a plateau, where the reduction in the WRMSD slows to near cessation, the optimization process may be stopped.

In the optimization process, different weights can be assigned to groups of observations based on their respective observation techniques. Additionally, individual observations can be selectively omitted from consideration.

In an attempt to optimize the refined orbit and minimize the WRMSD, a weight needed to be assigned to certain observations, and individual observations needed to be excluded from the optimization. To achieve this as objectively as possible, micrometer (visual) observations were analyzed separately from the others to determine a weight for the non-micrometer observations. This was because accurate micrometer observations are typically more difficult to achieve; however, the viability and importance of these observations cannot be dismissed. The observation types and their technique codes associated with WDS 17166-0027 are as follows.

- C = CCD or other two-dimensional electronic imaging
- Hh = Hipparcos
- Ht = Tycho
- Ma = micrometer with refractor
- Mb = micrometer with reflector
- Mc = Comparison image micrometer
- S = speckle interferometric technique
- Sq = Mt. Wilson speckle interferometric
- St = Tokovinin "hrcam"
- Su = USNO speckle

The non-micrometer observations (C, Hh, Ht, S, Sq, St, Su) were then disabled by deselecting the "Use?" box next to each technique code, Figure 6. Consequently, the optimizer was executed based solely on micrometer observations (Ma, Mb, Mc) to obtain the orbital parameters. After a few minutes of running the optimizer, no significant change was observed in the weighted root mean square deviation. Thus, the optimizer was stopped. The WRMSD for the micrometer-only observations was recorded as 112.88 milliarcseconds (mas), Figure 7.

Latest	Code	Num	Weight	Use?
2023.49	Sq	1	1	<input type="checkbox"/>
2021.33	St	3	1	<input type="checkbox"/>
2017.51	C	1	1	<input type="checkbox"/>
2016.34	S	4	1	<input type="checkbox"/>
2008.54	Ma	72	1	<input checked="" type="checkbox"/>
2004.52	Mb	8	1	<input checked="" type="checkbox"/>
1995.7	Su	2	1	<input type="checkbox"/>
1991.53	Ht	1	1	<input type="checkbox"/>
1991.25	Hh	1	1	<input type="checkbox"/>
1964.45	Mc	2	1	<input checked="" type="checkbox"/>

Figure 6. Screenshot of STBO technique selection.

Read Observation File		WDS	17166-0027
DD	A 2984	Observations	95
Add Custom Observation File			
Orbital Parameters			
Period	150.98	yrs	<input checked="" type="checkbox"/>
Semi-major axis	0.9836	AS	<input checked="" type="checkbox"/>
Eccentricity	0.8725		<input checked="" type="checkbox"/>
Inclination	57.1	deg	<input checked="" type="checkbox"/>
Long. of Acc. Node	249.7	deg	<input checked="" type="checkbox"/>
Time at Periastron	1905.153	year	<input checked="" type="checkbox"/>
Long. of Periastron	278.39	deg	<input checked="" type="checkbox"/>
Optimizer Gradient Coefficient	0.003		
Optimizer Random Coefficient	0.0003		
Stats		WRMSD (mas)	
Optimize	1 / 16100	112.88	

Figure 7. Screenshot of STBO DATA table after first micrometer-only optimization.

To further reduce the WRMSD, any observations with a distance greater than  $2\sigma$  ( $2\sigma = \text{WRMSD} * 2 = 112.88 \text{ mas} * 2 = 225.76 \text{ mas}$ ) were excluded from a second optimization. The distance of individual observations from the apparent orbit can be seen by right-clicking on the observation, Figure 8. If the distance is greater than  $2\sigma$ , "Don't Use in Optimizer WRMSD" can be selected to exclude the observation from optimization.

The iterative procedure of eliminating observations with values greater than  $2\sigma$  and re-optimizing was repeated until no observations with values exceeding  $2\sigma$  could be identified.

After removing the first observations greater than  $2\sigma$  (B\_1960b, LBU1987a, and Hei1998), a second optimization was performed with the new dataset. The second optimization resulted in a WRMSD of 103.63 mas, and three observations over  $2\sigma$  (Fur1937, Pop1977b, and Zul1983). The Third optimization produced a WRMSD of 95.91 mas and two observations with a distance greater than  $2\sigma$

(VBs1954, and Ary1994), and the fourth optimization resulted in a WRMSD of 91.51mas, and a single observation greater than  $2\sigma$  (Wor1967b).

After conducting five optimizations and thoroughly vetting observations with sigma values of two or greater, the resulting weighted root mean square deviation was 89.26 mas, Figure 9. No observations with  $\sigma$  values greater than two were included in the final micrometer observation set. A total of nine observations were withheld from the data set, resulting in a total of 73 observations included in the micrometer-only optimized data set.

After completing the optimization process with the micrometer observations, the process was repeated with the non-micrometer observations, Figure 10.

The first two optimizations (WRMSD 46.953 mas, and 27.044 mas) each yielded one observation with a distance greater than  $2\sigma$  WS11999b, and Tyc2000e respectively.

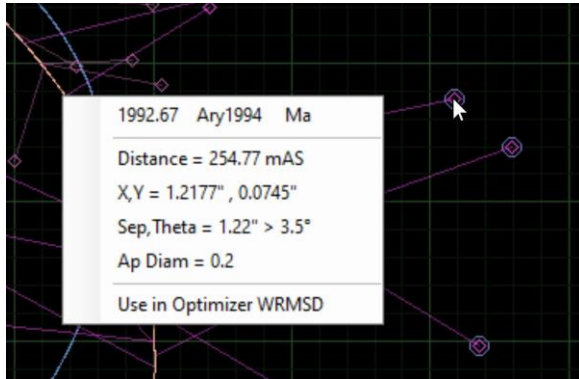


Figure 8. Example of right-clicking on an observation in STBO for the data table.

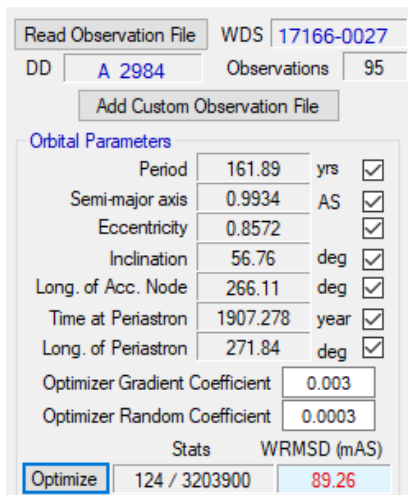


Figure 9. Screenshot of STBO DATA table after final micrometer-only optimization.

Technique Codes				
Latest	Code	Num	Weight	Use?
2023.49	Sq	1	1	<input checked="" type="checkbox"/>
2021.33	St	3	1	<input checked="" type="checkbox"/>
2017.51	C	1	1	<input checked="" type="checkbox"/>
2016.34	S	4	1	<input checked="" type="checkbox"/>
2008.54	Ma	72	1	<input type="checkbox"/>
2004.52	Mb	8	1	<input type="checkbox"/>
1995.7	Su	2	1	<input checked="" type="checkbox"/>
1991.53	Ht	1	1	<input checked="" type="checkbox"/>
1991.25	Hh	1	1	<input checked="" type="checkbox"/>
1964.45	Mc	2	1	<input type="checkbox"/>

Figure 10. Screenshot of technique selection non-micrometer observation.

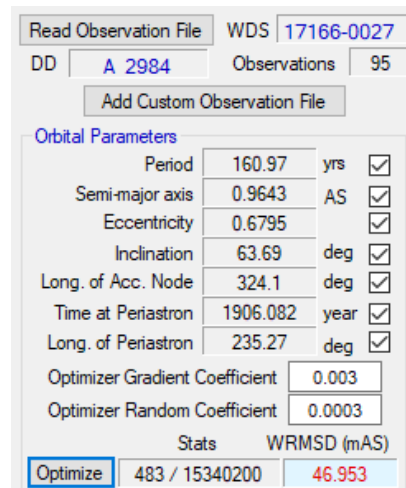


Figure 11. First optimization of non-micrometer observation.

After three optimizations of the non-micrometer observations, no further observations were found to have a distance of  $2\sigma$  or more. The final weighted root mean square deviation for the remaining 11 observations was 13.99 mas, Figure 12. No observations with  $\sigma$  values greater than two were included in the final non-micrometer observation set.

Following the optimization of the two groups of observations, micrometer, and non-micrometer, the non-micrometer observations were weighted. First, a WRMSD ratio was determined by dividing the WRMSD of the first dataset by the WRMSD of the second dataset ( $89.26\text{mas}/13.99\text{mas} = 6.38$ ). Second, a ratio for the number of observations was determined ( $73/11 = 6.64$ ). Finally, the weight was computed by multiplying the two ratios ( $6.38 * 6.64 = 42.36$ ). This weight was subsequently applied to all the non-micrometer observations, and the technique codes were enabled, Figure 13.

Technique Codes				
Latest	Code	Num	Weight	Use?
2023.49	Sq	1	42.36	<input checked="" type="checkbox"/>
2021.33	St	3	42.36	<input checked="" type="checkbox"/>
2017.51	C	1	42.36	<input checked="" type="checkbox"/>
2016.34	S	4	42.36	<input checked="" type="checkbox"/>
2008.54	Ma	72	1	<input checked="" type="checkbox"/>
2004.52	Mb	8	1	<input checked="" type="checkbox"/>
1995.7	Su	2	42.36	<input checked="" type="checkbox"/>
1991.53	Ht	1	42.36	<input checked="" type="checkbox"/>
1991.25	Hh	1	42.36	<input checked="" type="checkbox"/>
1964.45	Mc	2	1	<input checked="" type="checkbox"/>

Figure 13. Weighted observations.

Read Observation File WDS 17166-0027

DD A 2984 Observations 95

Add Custom Observation File

**Orbital Parameters**

Period	155.8	yrs	<input checked="" type="checkbox"/>
Semi-major axis	0.6399	AS	<input checked="" type="checkbox"/>
Eccentricity	0.605		<input checked="" type="checkbox"/>
Inclination	34.73	deg	<input checked="" type="checkbox"/>
Long. of Asc. Node	184.73	deg	<input checked="" type="checkbox"/>
Time at Periastron	1893.187	year	<input checked="" type="checkbox"/>
Long. of Periastron	339.86	deg	<input checked="" type="checkbox"/>
Optimizer Gradient Coefficient	0.003		
Optimizer Random Coefficient	0.0003		

Stats WRMSD (mAS)

Optimize 1 / 31000 40.565

Plot Original Apparent Ellipse

Get Starting Values from CSV File

**Ephemeris and Apparent Ellipse**

Epoch 2024.483 years Generate

Distance PtoS (rho)	0.619	AS
Angle (Theta)	31.56	deg
Ell. Center (x)	0.371	AS N
Ell. Center (y)	-0.079	AS E
Semi-major Axis	0.632	AS
Semi-minor Axis	0.424	AS
Eccentricity	0.741	
Rotation of Ellipse	-5.9	deg

Figure 14: Final orbital elements obtained through Speckle Toolbox Orbits analysis, and the proposed new orbital elements for WDS 17166-0027.

Following the application of a weight of 42.36 to technique codes C, Hh, Ht, S, Sq, St, and Su, the optimizer was executed using the remaining 73 micrometer and 11 non-micrometer observations. The resultant Speckle Toolbox analysis produced new orbital elements, Figure 14.

Upon completion of both the Desmos and Speckle Toolbox Orbits analyses, a comparison was conducted between the two. Subsequently, the STBO plot was imported into Desmos for further evaluation, Figure 15. Though Desmos lacks the in-depth orbital analysis capability of Speckle Toolbox Orbits, most notably the ability to provide new orbital elements, Desmos is a visually appealing and intuitive application. It allows for the simultaneous comparison of multiple ellipses (apparent orbits) and offers enhanced readability. Using the Desmos plot to verify observations on a Cartesian plane with respect to the STBO plot adds to the validity of the STBO plot. To improve the legibility and identification of observations for comparison, the first historical observation A\_1915.54, and the most recent observation MWO2023.49, have been marked with black dots. The green x's indicate micrometer observations, the red x indicates Hipparcos, the blue dots indicate all other non-micrometer observations and the red circles indicate all observations that are not included in the STBO optimizer, Figure 16.

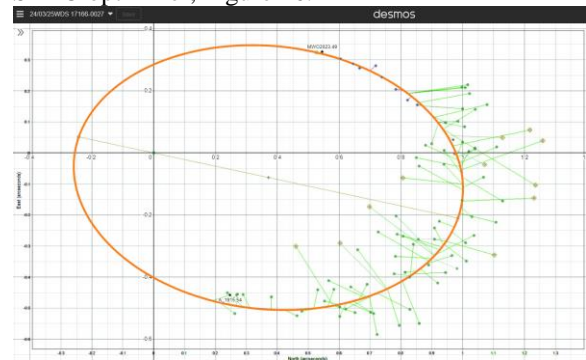


Figure 15. Speckle Toolbox Orbits plot imported into Desmos.

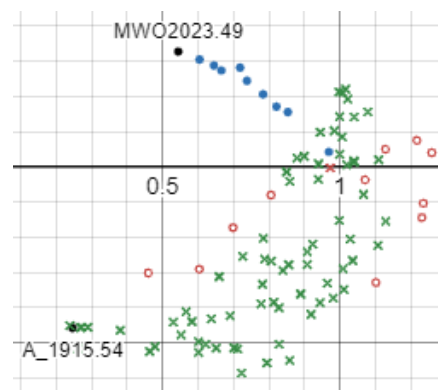


Figure 16. Observations on the Desmos plot.



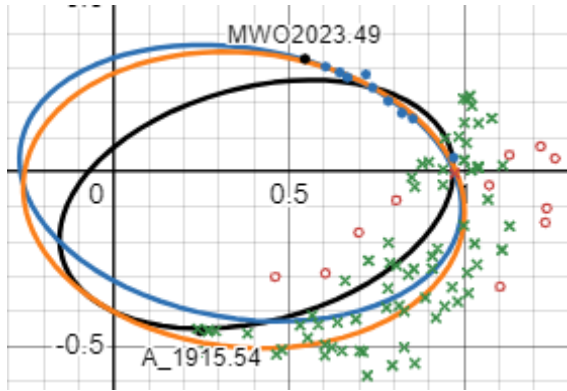


Figure 17. Three orbits plotted in Desmos USNO; black, Desmos visual orbit; blue, STBO orbit orange.

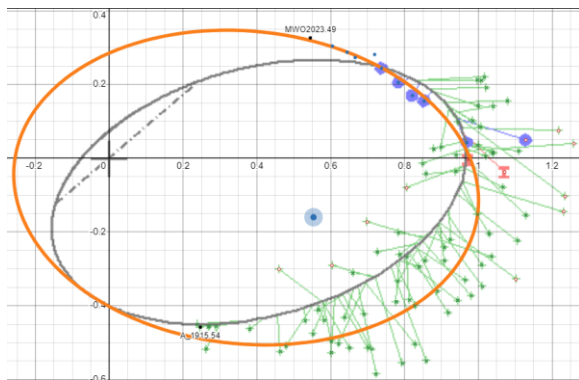


Figure 18. STBO orbit orange over USNO orbit black.

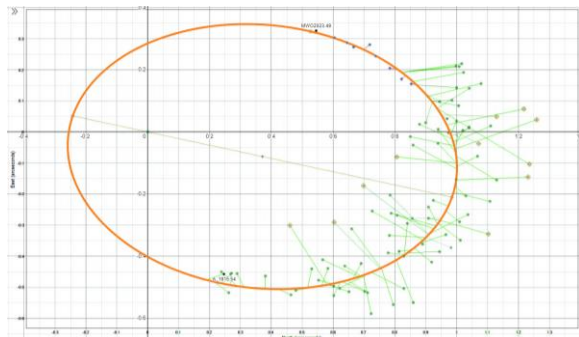


Figure 19: Proposed orbit for WDS 17166-0027.

To do a visual comparison of the STBO, Desmos, and USNO orbits, the ellipses for all three were added to the Desmos Cartesian plane. To differentiate between the three orbits the USNO orbit was plotted in black, the Desmos visual orbit was plotted in blue, and the STBO orbit was plotted in orange, Figure 17.

## 5. Conclusion

The examination of binary star WDS 17166-0027 reveals that there is a need to update the presently published orbit in the USNO Sixth Catalog of Orbits

of Visual Binary Stars to reflect the previously unpublished 2023.49 Mt. Wilson observation, which yielded a position angle of  $30.92^\circ$  and separation of  $0.635''$ . Additionally, there are the 2021.33 and 2019.38 Tokovinin, 2017.51 Serot, and 2016.34 Wasson observations, which are not currently reflected in the published orbit, Figure 18.

Based on the weighted root mean square deviation, the Speckle Toolbox approach used to resolve the orbit for WDS 17166-0027, omits observations from the optimization process, Table 3, and provides a weight for the historically more accurate observations. As such, the Speckle Toolbox analysis is the more objective approach and provides the recommended orbital elements, Figure 19.

It is important to note that there are some subjective aspects to both the Desmos analysis and the Speckle Toolbox Orbits analysis. This paper presents two apparent orbits, both of which have their respective validity. To truly affirm any proposed orbit for this binary star, it will require an additional 40-50 years of observations.

Micrometer Observations				
Observation Date	Reference Code	Distance (mas)	Sigma	Tech. code
1933.53	Fur1937	222.67	2.15	Ma
1944.31	VBs1954	198.67	2.07	Mb
1958.44	B_1960b	234.49	2.08	Mb
1963.46	Wor1967b	183.34	2.01	Ma
1976.34	Pop1977b	232.18	2.24	Ma
1981.482	Zul1983a	208.8	2.01	Ma
1985.71	LBu1987a	240.07	2.13	Ma
1992.67	Ary1994	198.81	2.07	Ma
1997.61	Hei1998	277.64	2.46	Ma
Non-Micrometer Observations				
1991.53	TYC	62.7	2.32	Ht
1995.70	WSI1999b	127.94	2.72	Su

Table 3. Observations redacted from the optimization process in chronological order based on the date of observation.

## 6. Acknowledgments

The United States Naval Observatory supplied past WDS 17166-0027 observations from their Washington Double Star Catalog. The background plot was from the Sixth Catalog of Orbits of Visual Binary Stars. Dave Rowe's Speckle Toolbox and the Desmos graphing calculator were used for the reduction and analysis. The Institute for Student Astronomical Research (InStAR) purchased time on the 1.5-meter telescope at Mt. Wilson Observatory where the new speckle interferometry of WDS 17166-





0027 was made. Gravic Inc. provided travel funds for students to attend the run. Rachel Freed, Reed Estrada, Chris Estrada, Nick Hardy, Leon Bewersdorff, Joseph Burch, Paul McCudden, Tom Smith, and others helped organize the run and manage the observations. Thomas Meneghini, the Director of the Mt. Wilson Observatory, and his staff provided support during the run. Thanks also to Payson High School, Eastern Arizona College, and the Fairborn Institute for their support of this analysis. Special thanks to Russ Genet for all his support and assistance.

## 7. References

- Aitken, R.G., "One Hundred New Double Stars: Twenty-Fourth List." (1918) Lick Observatory Bulletins 306, University of California Press Berkeley, 9, 134.
- Ellis, M., D. Holland, H. Kinnick & R. Genet. "Desmos Analysis of the Binary Star CHR 259 (WDS 15496-0326)." (2024). *Journal of Double Star Observations*, 20, 114.
- Faughn, E., J. Major, & P. McCudden. "Speckle Astrometry of WDS 18181-0120." (2023). *Journal of Double Star Observations*, 19, 420.
- Genet, R. "Speckle Interferometry of close Visual Binaries." (2015) *Journal of Double Star Observations*, 11, 183.
- Genet, R., P. McCudden, & M. Ellis. "Desmos Graphical Analysis of Binary Stars — A Tutorial with HU 481 (WDS 16212+2259) Example." (2024). *Journal of Double Star Observations*, in press, 20, 264.
- Genet, R., D. Rowe, M. Ellis, & P. McCudden. "Desmos and Speckle Toolbox Orbits Analysis of WDS 21001+0731" (2024), this proceedings.
- Hardy, N., L. Bewersdorff, D. Rowe, R. Genet, R. Wasson, J. Armstrong, S. Dixon, M. Harris, T. Smith, R. Freed, P. McCudden, S. Rajkumar, M. Davis, C. Giavarini, R. Snyder, R. Wolly, M. Calvin, S. Cotton, & M. Rabin. Automated Speckle Interferometry of Known Binaries: With WDS 12274-2843 B228 as an Example. (2023). *Journal of Double Star Observations*, 19, 106.
- Harshaw, R., D. Rowe, & R. Genet. "The Speckle Toolbox: A Powerful Data Reduction Tool for CCD Astrometry." (2017). *Journal of Double Star Observations*, 13, 52.
- Matson, R., S. Williams, W. Hartkopf, & B. Mason. Sixth Catalog of Orbits of Visual Binary Stars. (2023). U.S. Naval Observatory, Washington, DC. <http://www.astro.gsu.edu/wds/orb6.html>
- Rowe, D., and R. Genet. "User's Guide to PS3 Speckle Interferometry Reduction Process." (2015). *Journal of Double Star Observations*, 11, 266.

# Speckle Analysis of Ten Close Binaries from Mt. Wilson

Bradley Brungardt   
Colorado State University, Ft. Collins, CO  
[bradley.brungardt@colostate.edu](mailto:bradley.brungardt@colostate.edu)

Elias Faughn , John Major , Paul McCudden , Zaida Weems, Kassiopeia Wehlitz   
Colorado Mountain College, Steamboat Springs, CO

---

## Abstract

A set of ten known WDS binaries were chosen for varied orbital characteristics and reliable recent speckle measurements from a total of 53 observed using the historic 60 inch telescope at Mt Wilson Observatory in June, 2023. They were then analyzed with Speckle Toolbox and its new Orbits subroutine, along with Desmos commercial software. All ten showed  $\rho$  and  $\theta$  that were consistent with previous measurements and with orbit models published in the 6th Orbit catalog. Orbital fits created by optimizing previous and current speckle data only showed modest variations from published orbits. The results confirm the value of large-aperture data combined with open-source software in the hands of first-time researchers.

---

## 1. Introduction

Many binary systems exhibit separations too small to be measured visually, which makes measurement of stellar masses difficult and complicates our understanding of their period, orbital paths, and other qualities. Atmospheric effects limit our opportunities to observe such targets, and often result in inaccurate measurements. Fortunately, these atmospheric effects can be significantly mitigated by employing Speckle Interferometry (Labeyrie 1970), a process by which hundreds or thousands of short-exposure images are “stacked” and then processed by specialized software to effectively “freeze” the distortion caused by poor seeing conditions (Harshaw et al, 2017). This method can be used by both large-aperture and even amateur instruments to effectively measure the separation and position angle of stars otherwise unresolvable by other means.

The historic 60" Mount Wilson telescope was used in June of 2023 to gather data on 53 targets selected from a list combining the WDS catalog with the 6th Orbit Catalog and Ephemerides (McCudden, et al, 2022). The list parameters included the following:

- RA between 13:30h and 21:30h
- Dec from -25 to +90 degrees
- Primary magnitude from 7 to 12
- Delta magnitude less than 1.5
- Nominal separation between 0.1" and 1.5"
- Period less than 200 years
- # of speckle observations 100 or fewer
- Speckle observations in the last 5 years
- Grade 1-4

Of the original 53 targets, ten were chosen for analysis. Data from four reference stars were also collected, based on their confirmed non-binary nature and being within ten degrees of at least one target system.

Taken as a group, the ten targets represent a wide range of parameters (See Table 1). The closest system is located at 33.21 ly, while the furthest lies at 466.66 ly, and is nearly 14x as distant. One has been observed 270 times since 1862, while another two have been measured less than a dozen times since 1991. Their spectra range from A5 V to M, and their periods are between 5 and 154.2 years. All feature speckle measurements within the last 10 years, and 8 of 10 include traditionally reliable and precise measurements from Tokovinin, and all but one target (WDS 17119-0151) has Hipparcos data (Söderhjelm, 1999). This diversity within the original selection parameters was useful to test our measurement, analysis, and display tools across different types of binary systems. Our objective was to apply these tools to a selection of stars that exhibited a variety of periods, historical data available, spectral class, and other characteristics.

## 2. Equipment and Methods

Data was taken between 2023.488 (June 25th, 2023) and 2023.492 (June 28th, 2023) using the historic 60-inch telescope at the Mount Wilson Observatory. The telescope was equipped at the bent Cassegrain focus with a ZWO ASI 6200MM Pro camera, fitted with an Astronomik ProPlanet 642 BP 2850002585 (IR) filter with a midpoint transmission at 750 nm. Each double star and reference star

captured had one five-second exposure and 500 20-millisecond exposure images. Table 2 lists the selected binary pairs and the dates that the images were captured, along with the reference stars used for each observation, chosen from nearby HD catalog stars.

Using Platesolve, one 20-second image of the periphery of M13 was taken each night for a plate solution. The results provided the plate rotation angle and image scale, which were used to calibrate Speckle Toolbox. Results are shown in Table 3.

The stars and their reference stars were reduced using Speckle Toolbox (STB) (Rowe, 2017), with an ROI pixel size of 128 for all, except 19487+1504, which used a 256-pixel reduction when the 128-pixel images were unsolvable. A sample reduction from STB is shown in Figure 1.

### 3. Data

Table 4 displays the measured mean  $\rho$  and mean  $\theta$ . Each author measured the  $\rho$  and  $\theta$  of their star pairs five times for a 128-pixel image. Mean  $\rho$  and mean  $\theta$  represent the average of all of those measurements. Those observed on two consecutive nights underwent this process twice, and Table 4 shows the average of all ten measurements in that case. It is important to note that  $180^\circ$  must be subtracted from each measured  $\theta$  to account for the reflection of the image due to mirrors within the telescope, which has been accounted for in the table.

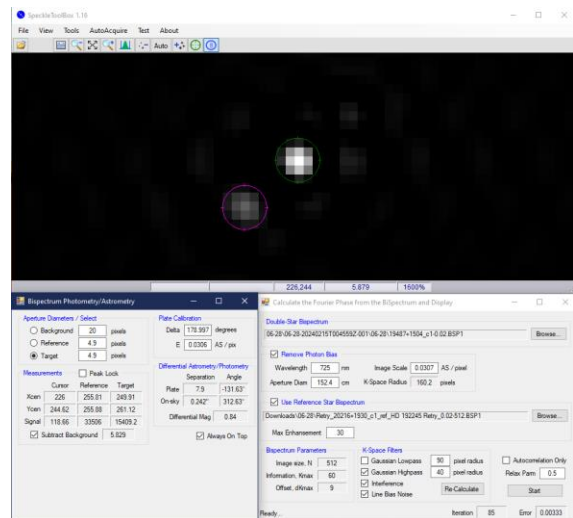


Figure 1: Sample Bispectrum Image from Speckle Toolbox of WDS 18558+0327 showing the star pair, the display parameters screen, and the photometry/astrometry measurements screen

## 4. Discussion

STB’s new Orbits routine was used to reoptimize the orbits of all ten pairs using only speckle data and the current data point, and the results were imported into the commercial software Desmos, converting orbital parameters to x,y coordinates (Genet, 2024) and then plotted. The origin of the graph represents the primary star’s position. The results are shown in Figure 2. The USNO published data and orbit are also shown. All speckle observations were weighted equally, some observations with obvious  $180^\circ$  position angle errors were corrected, and clear outliers were also excluded. In these plots, North is to the right and East up for each, and the units are arcseconds. The solid yellow line is the 6th Orbit catalog published orbit, and the green dotted line is our reoptimized speckle-only orbit. Our observations are labeled MWO 2023. The weighted root mean squared deviation (WRMSD) of the reoptimized orbits were calculated by STB and compared to those calculated using all published data. Results are shown in Table 6.

Our values align well with historic measurements and extrapolated 6th Orbit Ephemerides. In the case of 20306+1349, two very different orbital solutions are posted by the USNO. Our observation matches the Doc2021e orbit more closely. Future observations are needed to improve the grade of this pair’s orbit. Figure 2 shows 20306+1349 with both the Doc2021e and Tok2019h orbits plotted.

## 5. Conclusions

Speckle techniques using STB on the 60-inch Mt Wilson telescope easily measured separations down to nearly 0.1 arcseconds. Our measurements and orbital elements match closely those published in the 6th Orbit Ephemerides Catalog. The reoptimization employed in STB using only speckle and our data resulted in more precise orbits with smaller WRMSD values. These orbits only deviated slightly from the USNO published orbits, perhaps also because the reoptimization included more recent observations made since the USNO published orbital ephemerides. Our tools performed accurately across close binary targets with varied characteristics. In addition, Desmos proved to be an easy-to-use, clear, and legible means of displaying data. Desmos also was able to accurately represent  $\rho$  and  $\theta$  measurements and multiple orbital paths for comparative analysis.

The use of open-source software like STB alongside observations made by large apertures allows for any interested party to effectively make accurate

measurements and to evaluate the previously calculated orbits using more recent observations. STB's Orbits routine allows for including or excluding particular observations and weighting them differently. This allows for new orbit fits to be tested and evaluated. Desmos is an intuitive and easily accessible tool to use for modeling orbits using values determined using the STB Orbits routine and has the advantage of being familiar to many high school and community college researchers.

## 6. Acknowledgements

This research has made use of the Washington Double Star Catalog maintained at the U.S. Naval Observatory.

This work used the SIMBAD service operated by Centre des Données Stellaires (Strasbourg, France), biblio-graphic references from the Astrophysics Data System maintained by SAO/NASA

This research made use of the Stelle Doppie database, maintained by Gianluca Sordiglioni.

The authors are grateful to the Colorado Mountain College Foundation for supporting student travel and research

Thanks to Rachel Freed and the Institute for Student Astronomical Research for funding instrument time at MWO, and to Tom Menighini and MWO staff.

Thanks to Dave Rowe for Speckle Tool Box 10.02 and his development of the Orbits routine.

## 7. References

Genet, R., McCudden, P., Ellis, M. (2024) Desmos Graphical Analysis of Binary Stars — A Tutorial with

HU 481 (WDS 16212+2259) Example. *The Journal of Double Star Observations*, 20(2), p. 264-274

Harshaw, R., Rowe, D., & Genet, R. (2017) The Speckle Toolbox: A Powerful Data Reduction Tool for CCD

Astrometry. *The Journal of Double Star Observations*, Volume 13, Number 1, January 1, 2017

Labeyrie A. (1970) Attainment of Diffraction Limited Resolution in Large Telescopes by Fourier Analysing Speckle Patterns in Star Images. *Astron. & Astrophys.* 6, 85-87.  
<https://adsabs.harvard.edu/pdf/1970A%26A.....6...85L>

McCudden, P., Genet, R., Willie, E, Dugan, L., Risin, S. (2022) Known Binaries Excel Spreadsheet. *The Journal of Double Star Observations*, Volume 18, Number 4, October 1, 2022.

Scardia M., Jean-Louis Prieur, L. Pansecchi, Josefina Ling, R. Argyle, et al. (2021). Orbital elements of double stars: BU 453 AB, A 819 AB, STT 406, BU 367 AB. 2021, pp. Circulaire N° 205. hal-03741127

Söderhjelm, Setaffan. Visual binary orbits and masses post Hipparcos. *Astronomy and Astrophysics*, v. 341, p. 121-140 (1999)  
<https://articles.adsabs.harvard.edu/pdf/1999A%26A...341..121S>

WDS	$\theta$ ( $^{\circ}$ )	$\rho$ ( $''$ )	Date First Observed	Total # of Observations	# of Speckle Observations	Period (yrs)	Distance (ly)	Spectral Class
17119-0151	7.1	0.596	1948.69	27	8	$34.49 \pm 0.11$	33.21	M
17293+2924	65.4	0.583	1902.371	101	15	89	77.51	K2
17533+2459	78.9	0.394	1901.60	118	14	38.09	159.97	G8 V
17584+0428	354.1	0.255	1934.5	30	20	$14.717 \pm 0.05$	142.26	K8
18558+0327	313.2	0.177	1910.48	96	23	$154.2 \pm 9.7$	466.66	A5 V
19243+2032	124.1	0.286	1991.25	9	8	60	393.01	F6 V
19487+1504	47.7	0.237	1907.51	84	9	$88.1 \pm 1.3$	445.62	F5 V
19490+1909	141	0.14	1862.62	270	76	23.24	255.06	A1 V
19598-0957	109.2	0.239	1887.66	96	68	$4.867 \pm 0.004$	72.42	F8 V
20306+1349	319.3	0.157	1991.25	11	10	95	297.62	F8

**Table 1. USNO Historic Data for Observed Double Stars**

WDS	6/25 (2023.481)	6/27 (2023.486)	6/28 (2023.489)	reference star
17119-0151	x			HD154186
17293+2924	x		x	HD164506
17533+2459			x	HD164506
17584+0428			x	HD164506
18558+0327			x	HD174487
19243+2032		x	x	HD185530
19487+1504		x	x	HD350318
19490+1909			x	HD192245
19598-0957		x		HD187532
20306+1349		x		HD193723

**Table 2. Target pairs with Date(s) Captured and Reference Stars**

Night	Pixel scale (")	Plate rotation angle (°)
6/25	0.0307	94.22
6/27	0.0306	179.048
6/28	0.0306	178.98

**Table 3. Plate solutions for each night**

Target (Discoverer code)	# of Nights Observed	$\rho$ ("	Standard Deviation of $\rho$	$\theta$ (°)	Standard Deviation of $\theta$
17119-0151 (LPM629)	2	0.608	0.00546	14.580	0.43038
17293+2924 (A351)	2	0.582	0.00309	65.940	0.33659
17533+2459 (A235)	1	0.399	0.00197	78.700	2.90793
17584+0428 (KUI84)	1	0.245	0.01160	357.383	1.22404
18558+0327 (A2192)	1	0.153	0.00989	307.005	0.89229
19243+2032 (HDS2752)	2	0.302	0.157	118.533	0.09502
19487+1504 (A1658)	2	0.235 (256px)	.00290 (256px)	48.353 (256px)	0.37276 (256px)
19490+1909 (AGC11)	1	0.136	0.00812	140.240	1.31292
19598-0957 (HO276)	1	0.228	0.00650	92.132	2.53317
20306+1349 (HDS2932)	1	0.166	0.00299	330.068	2.23729

**Table 4 - Reduced Data**

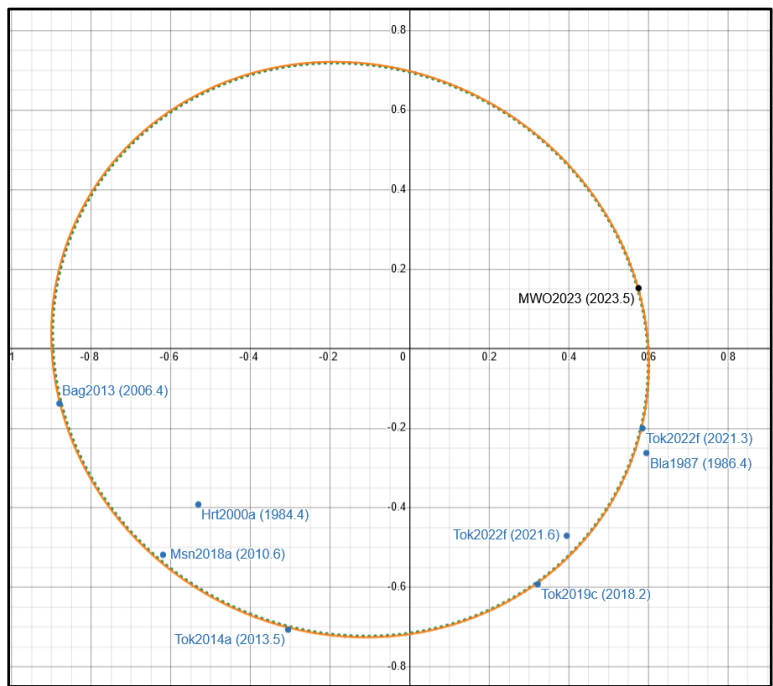
WDS	Our $\rho$ (")	Our $\theta$ (°)	6th Orbit Ephemeris linear extrapolated rho (")	6th Orbit Ephemeris linear extrapolated theta (°)
17119-0151	.595	14.822	0.597	14.671
17293+2924	.581	66.168	0.577	65.8
17533+2459	0.398	78.879	0.397	79.5
17584+0428	.277	357.720	0.253	356.3
18558+0327	.163	310.440	0.180	311.1
19243+2032	.299	118.944	0.287	118.7
19487+1504	.237	48.361	.237	45.9
19490+1909	.132	137.554	.124	137.0
19598-0957	.238	91.973	.212	89.1
20306+1349	.169	331.035	.158	326.2

**Table 5 - New data compared to 6th Orbit Catalog extrapolated data**

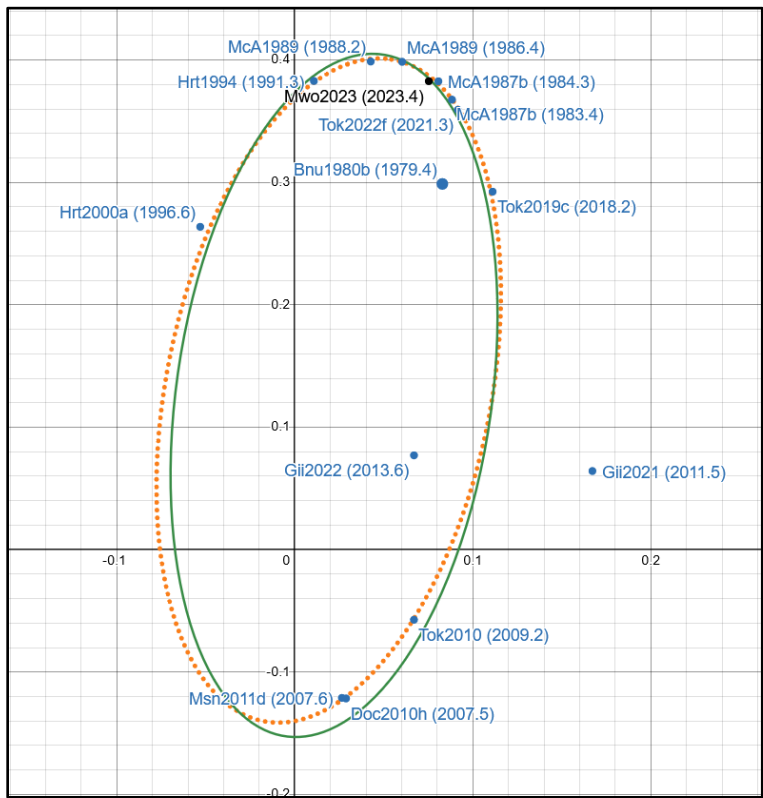
WDS	WRMSD Before (")	WRMSD After (")
17119-0151	159.805	57.028
17293+2924	109.588	9.396
17533+2459	45.583	28.012
17584+0428	75.803	19.943
18558+0327	60.567	12.254
19243+2032	19.332	4.771
19487+1504	27.642	5.663
19490+1909	119.866	40.637
19598-0957	135.216	27.964
20306+1349	11.463	7.534

**Table 6. WRMSD of each binary pair orbit fit before and after the exclusion of non-speckle data**

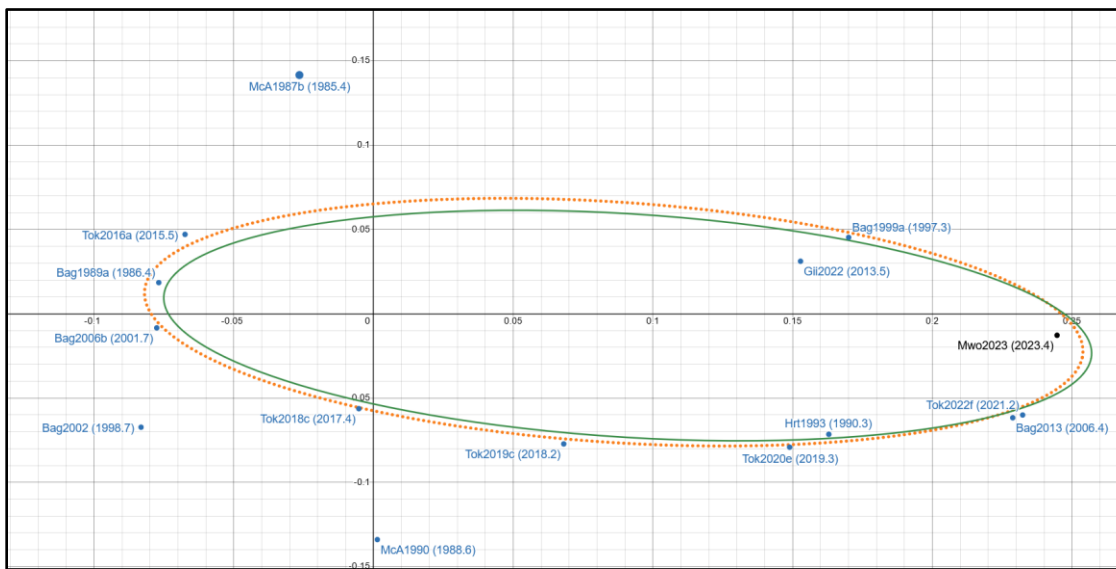
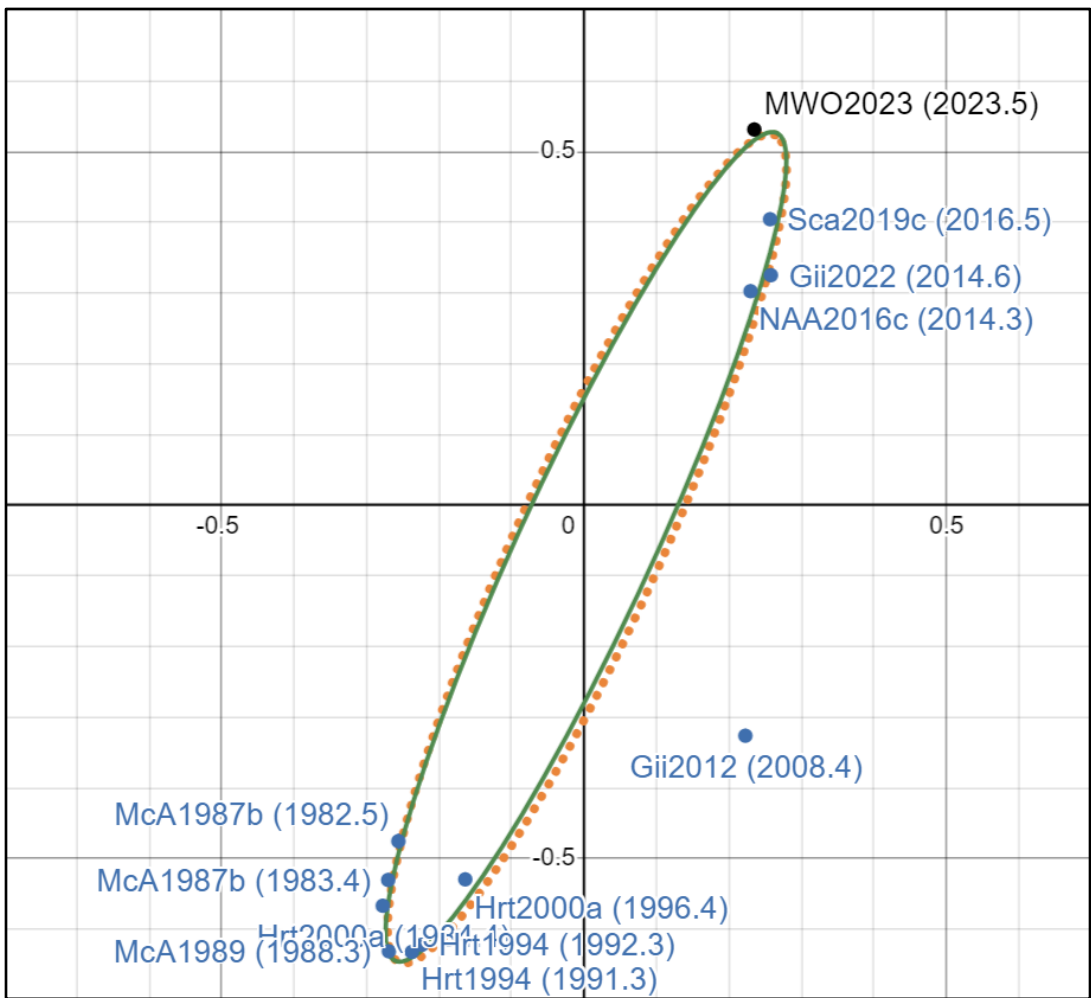


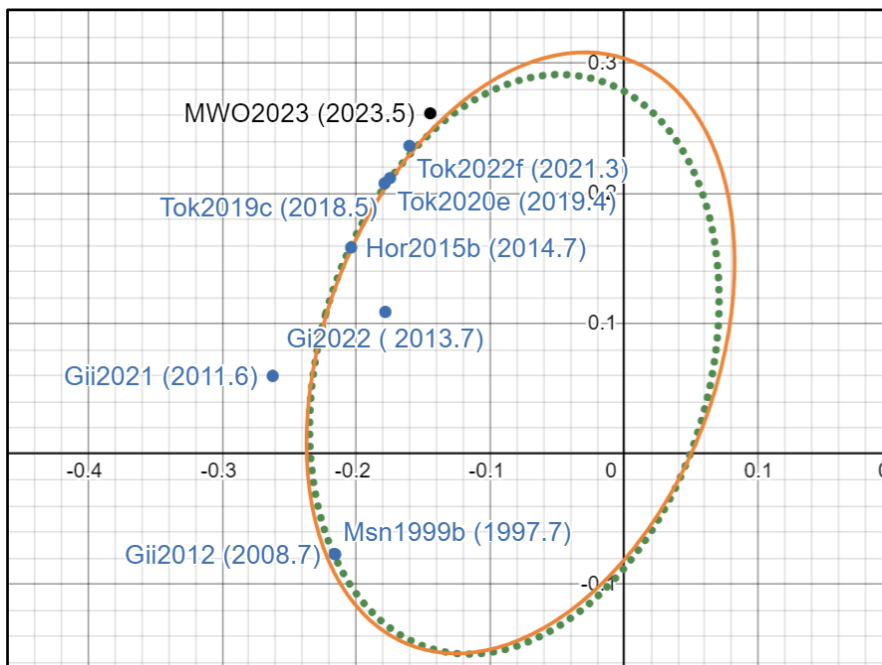
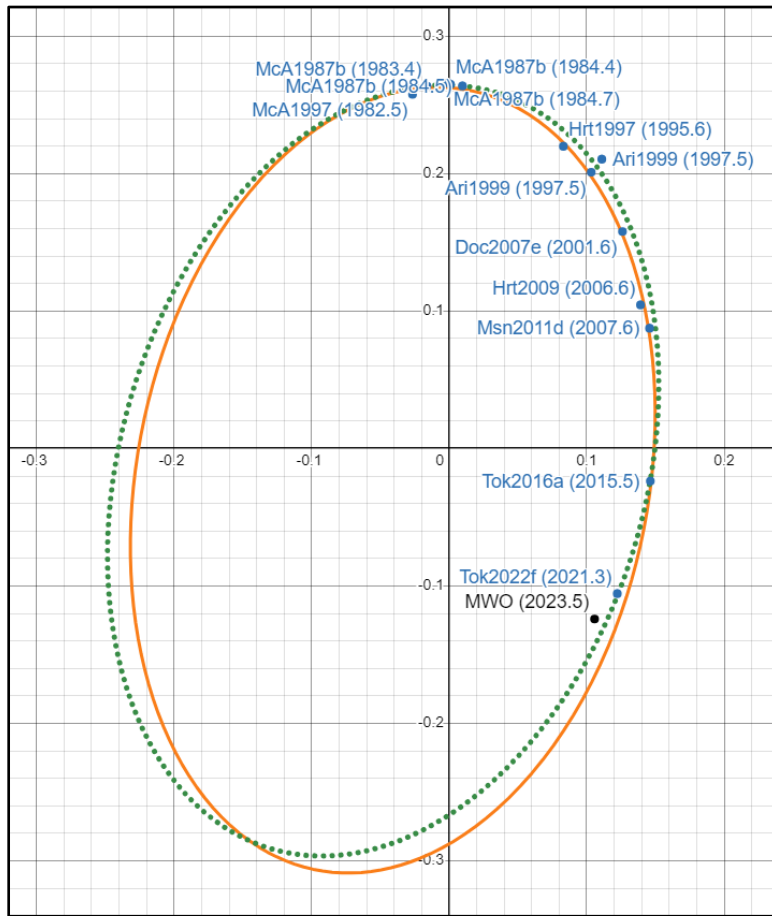


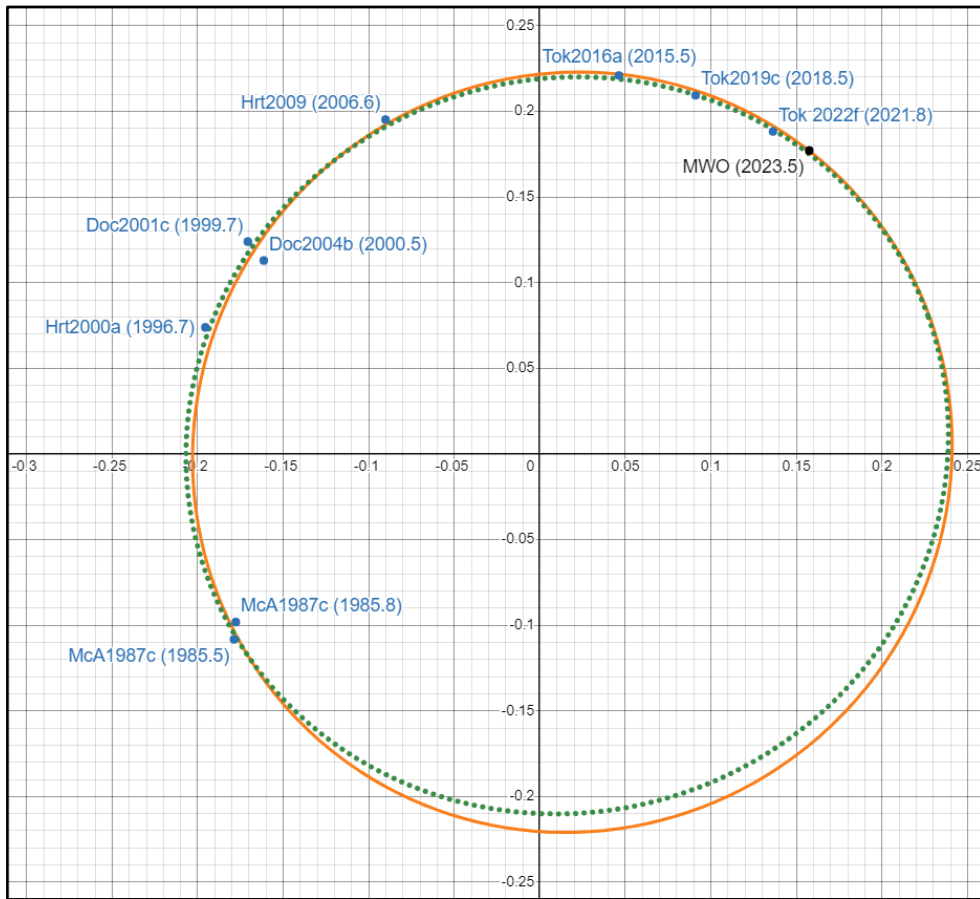
17119-0151



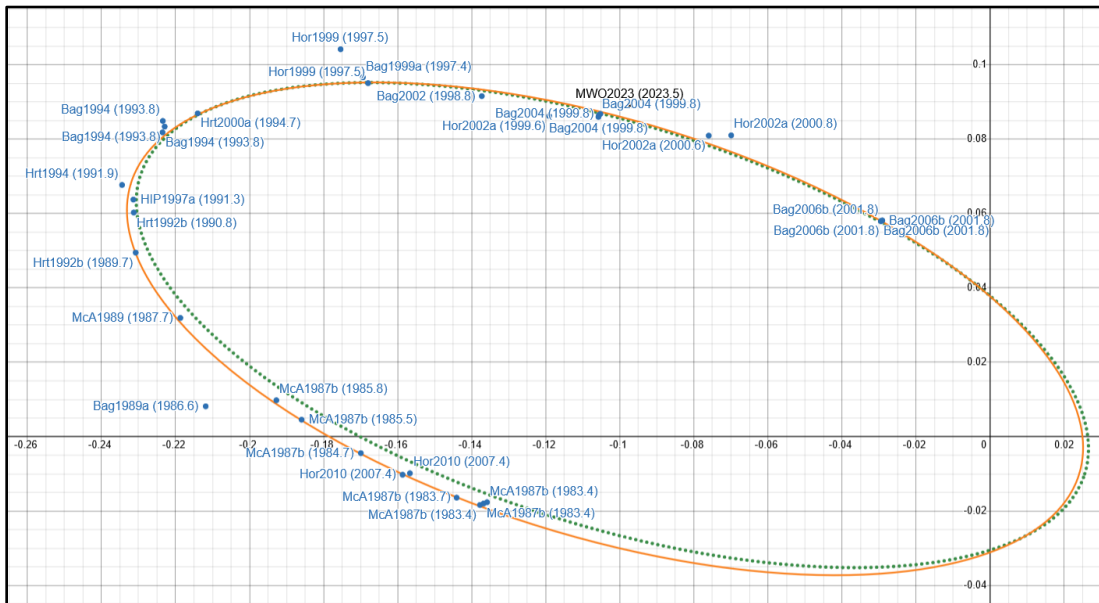
17533+2549



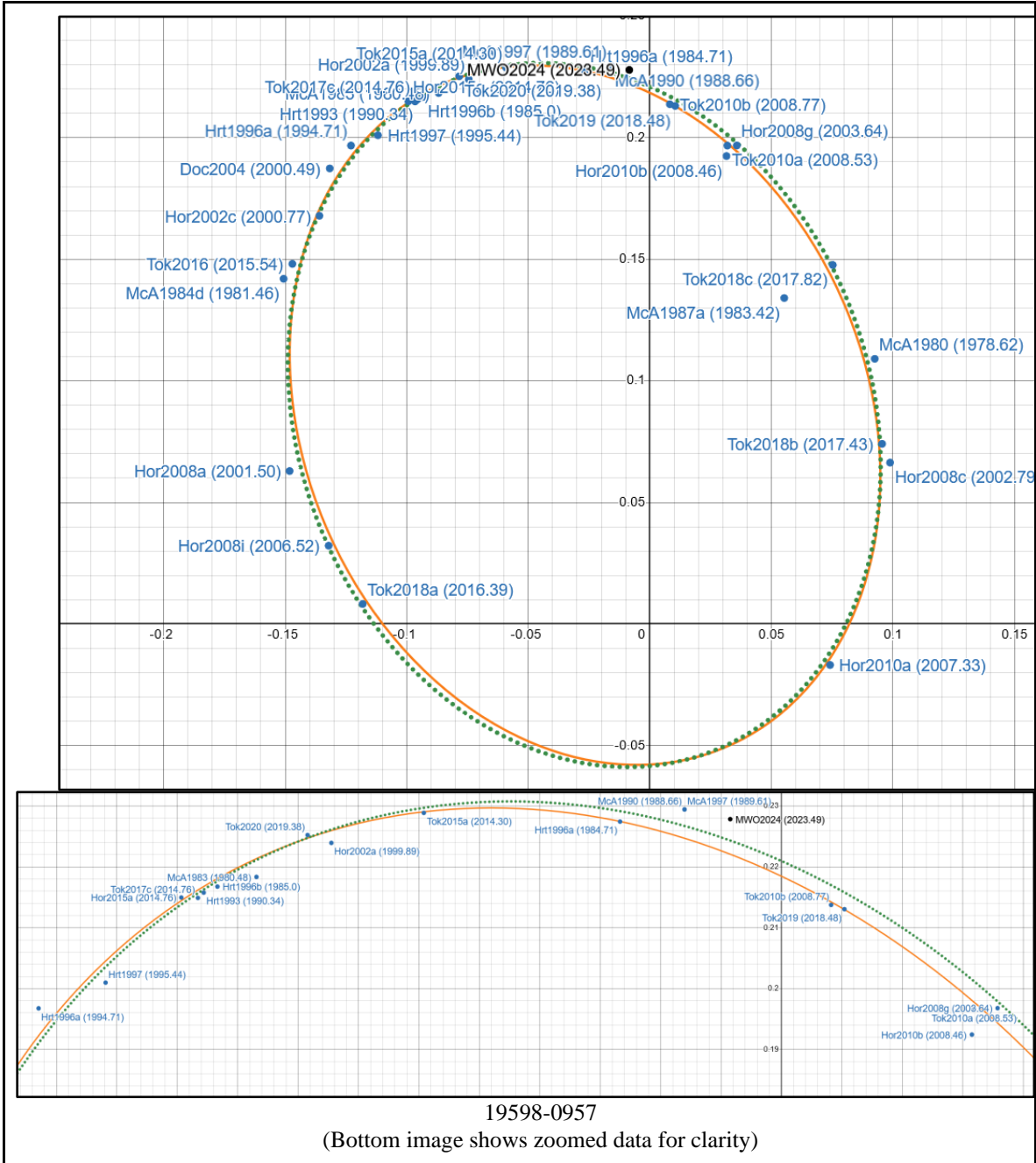




19487+1504



19490+1909



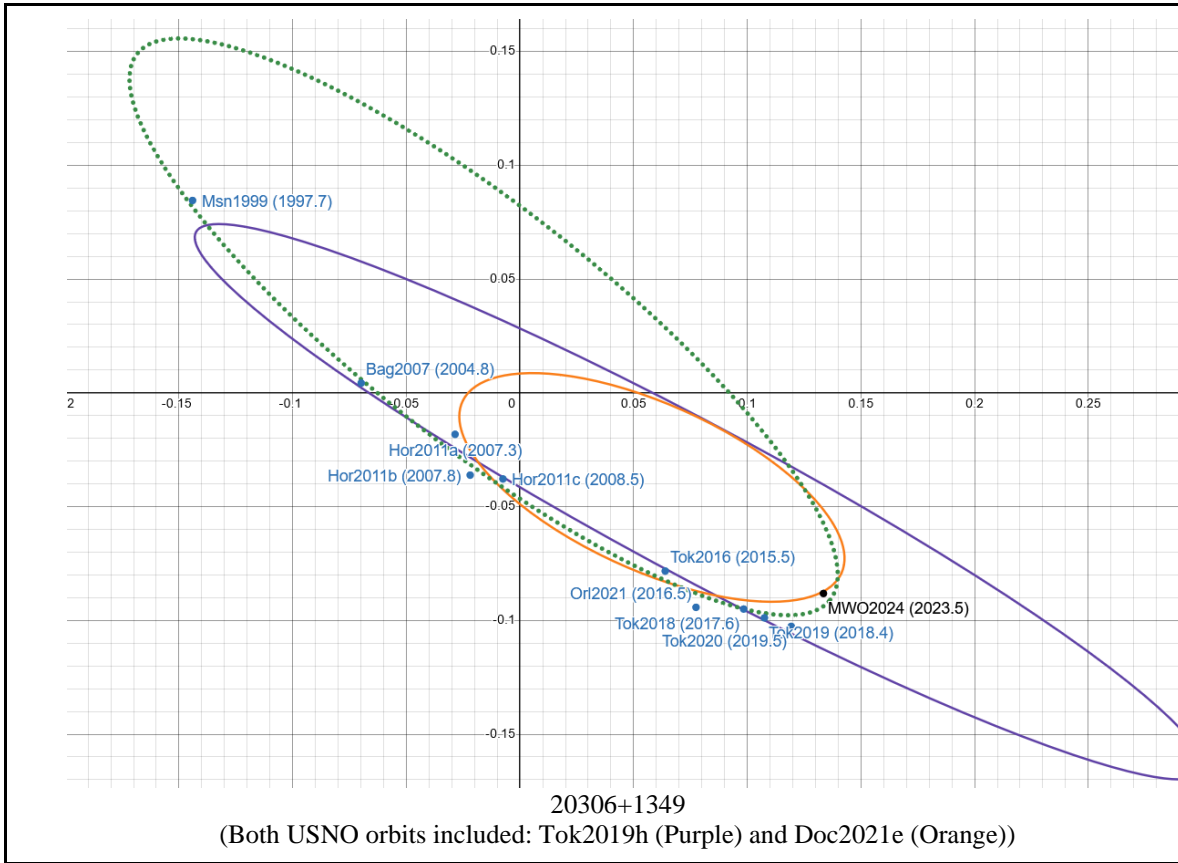


Figure 2: Reoptimized orbits in green (dotted) with published USNO orbits in orange (solid), plotted with Desmos. Current measurement labeled "MWO 2023" Scale in arcseconds.

# Speckle Interferometry Follow-Up to Newly Discovered Gaia Astrometric Binaries

*Mark Copper*  
*Magdalena Transit Observatory*  
*PO Box 1272*  
*Magdalena, NM 87825*  
*MLCopper@gmail.com*

*Russell Genet*  
*Eastern Arizona College*  
*Fairborn Institute*  
*610 E. Tahoe Vista Circle*  
*Payson, AZ 85541*  
*RussellGenet@FairbornInstitute.org*

*David Rowe*  
*PlaneWave Instruments*  
*1375N Main Street*  
*Adrian, MI 49221*  
*drowesmi@aol.com*

*Thomas Smith*  
*Dark Ridge Observatory*  
*Weed, NM*  
*michael.ellis@pusd10.org*

*Paul McCudden*  
*Colorado Mountain College*  
*1275 Crawford Avenue*  
*Steamboat Springs, CO 80487*  
*pmccuden@coloradomtn.edu*

*Michael-James Ellis*  
*Payson High School*  
*301 S. McLane Road*  
*Payson, AZ 85541*  
*michael.ellis@pusd10.org*

---

## Abstract

Gaia, the European Space Agency telescope launched in 2013, has gathered data on over 1 billion objects—mostly stars within our galaxy. Subsequent photometric analysis of the 3<sup>rd</sup> Data Release (DR3) identified 4,115,743 stars that appeared as unresolved single stars and yet were suspected of having multiple components due to apparent departure from linear proper motion. Of these stars 504,394 have been verified as binary stars, dubbed “astrometric binaries” since unresolved. They were divided into four subcategories based on the motion of their photocenters: (1) variable acceleration binaries, (2) constant acceleration binaries, (3) binaries for which an orbit could be calculated, and (4) binaries with apparent motion induced by a photometrically variable component. When the non-single star candidates identified by Gaia were crossed with the Washington Double Star Catalog, 2791 were also found in the WDS. A significant number of these are observable via speckle interferometry with “smaller” telescopes, especially if one includes the 1.5- and 2.5-meter telescopes at Mt. Wilson Observatory as smaller. The remainder provides a rich catalog for possible newly resolved pairs. Nearly half of the 2791 WDS pairs are marked “dubious” by WDS, but confirmation by Gaia suggests they could profitably be revisited. Just over a hundred

binaries have orbits delineated both in the 6<sup>th</sup> orbital catalog and Gaia DR3 which could provide for refined orbit calculation methods. Finally, Gaia will run out of propellant mid-2025, so the acceleration binaries which have periods longer than  $\sim 10$  years will only be partially covered. Ground-based speckle interferometry observations can help fill the gap until another Gaia-like astrometric telescope is launched, probably decades in the future.

---

## 1. Introduction

This paper continues a line of binary star studies made possible by the cross matching of historical data from the Washington Double Star catalog with data newly published from the Gaia satellite. One of us (Rowe) cross matched the entire WDS catalog with Gaia's DR2 leading to an analysis distinguishing gravitationally bound binaries from optical doubles in the WDS catalog [6].

Later, with data from Gaia EDR3, El-Badry [4] and others found a million binary stars. Then the Gaia DR3 team (DPAC) [5] announced the determination of over half a million non-single stars (NSS) including 166,500 astrometric orbits, far surpassing the 235 astrometric orbits from the Hipparcos mission [7] and the 3655 orbits in the WDS 6th orbital catalog (<https://crf.usno.navy.mil/wds-orb6>).

The astrometric orbits may be of interest to astronomers with meter class telescopes because they are not Gaia resolved orbits. If these binaries can be resolved with ground observation, that provides a metric separation when combined with accurate parallax measurement. That, in turn, gives the combined mass of the system. Now suppose that an accurate ratio of the astrometric ellipse semimajor axis to the relative ellipse semimajor axis is available. Then if a relation of luminosity to mass can be inferred, it follows that an estimate of individual masses can also be made.

The constant and variable acceleration NSS could also be of interest to double star enthusiasts. Any of these stars that can be resolved on the ground will have already exhibited sufficient motion to invite orbit estimates, especially when a longer baseline of observation can be established. This is especially true if the astrometric accelerations can complement position measurements.

The second point the Gaia DR3 team makes about its NSS determinations is that they are very conservative. That is, a single star designation was retained for most of the NSS candidate stars, but the classification of NSS was quite rigorous. That is to say, statistically speaking, there are many more close visual double stars among the 4 million NSS candidates that await discovery. Perhaps a closer look at Gaia DR3 statistical measures could lead to establishing guidelines for automated surveys. We discuss this briefly in Section **Error! Reference source not found.**

Outside the category of Gaia DR3's NSS candidates are the "partially resolved" binaries. These stars were explicitly excluded from the NSS pool but constitute fertile ground for new discoveries. The Gaia DR3 team specified three such excluding measures: multi-peak observations, elongated observations, and dispersed observations where the effective red and blue binning were inconsistent with the intensity of the green light detection. Instead of using these statistics to eliminate astrometric NSS candidates, they can be used to indicate candidates for new visually resolved star discoveries.

Finally, as El-Badry [3] points out, Gaia DR3 proper motion data can be collated with Hipparcos proper motion data to flush out proper motion anomalies. Anomalies derived from the longer timeline between Hipparcos 1991 observations and Gaia 2016 observations which were not detected over the Gaia mission life would indicate longer period binaries and wider separations of relatively close systems, hence prime targets for further investigation.

So basically, there are two ways smaller telescope researchers can work with Gaia DR3 data. With access to 1.5-meter aperture telescopes and larger, like those at the Mt Wilson Observatory, and with access to fast, sensitive cameras, computing power and sophisticated computational techniques like speckle interferometry, researchers (including students and citizen scientists) can actually extend Gaia's spatial resolution, possibly even to the extent of resolving Gaia non-single stars and Hipparcos/Gaia proper motion anomalies. Even smaller telescopes, using speckle interferometry, can investigate the partially resolved binaries detected by Gaia. Also, the longer timeline available to ground based observations will allow follow up on satellite discoveries, perhaps even to proposing orbits for acceleration and partially resolved binaries.

## 2. RUWE and Non-Single Stars

Stars for which successive position measurements do not satisfactorily align with uniform motion across the sky are candidates for unresolved multi-star systems. The statistic for measuring such failure is called "Renormalized Unit Weight Error" or RUWE and is derived from the residuals from fitting the single star model. The ESA team takes  $RUWE > 1.4$  as the cut-off a multi-star object.

The "partially resolved" multiple stars are those for which additional statistics indicate multiplicity but



which are not fully resolved by the satellite. Three criteria are used:

- Multi-peak
- Elongation
- Smear

“Multi-peak” stars include stars which are not fully resolved but exhibit multi-mode PSF’s such as double stars at the Rayleigh limit, while “elongated” stars include stars just closer than the Sparrow limit. Both multi-peak and elongation statistics are available in Gaia DR3.

“Smear” is a bit different and is derived from the blue and red photometric CCDs as well as the astrometric CCDs (see Figure **Error! Reference source not found.**). Because light is dispersed by prisms, an extended source may appear singular to the lower resolution blue and red photometric instruments but be sufficiently resolved in the higher resolution instrument so that its light will be dispersed over more pixels than a single source would be and thus be detected as a dimmer source. Hence such a disparity,  $|C^*| < 1.645\sigma_{C^*}$  in the Venn diagram, Figure **Error! Reference source not found.**, is used as an additional criterion for exclusion from the NSS category.

If any of these three criteria indicate partial resolution, the star is put aside for later analysis in DR4 or DR5.

If a star shows no visual sign of multiplicity and yet has elevated RUWE, its apparent “wobble” may fit one of the astrometric binary star models. There are four astrometric binary model classes.

- **variable acceleration binary**
- **constant acceleration binary**
- **binary with astrometric orbit**
- **variable induced movement**

Of the 4 million plus such candidate stars observed by Gaia, just over half a million fit one of the models. Such stars were classified as astrometric non-single stars. The single star classification of the remaining 3.5 million stars was retained (see Figure 3).

We would like to know whether any of the astrometric binary stars can be resolved visually by ground-based telescopes, possibly by relatively small telescopes via speckle interferometry. Separations would have to be tight, of course, since the 1.48-meter Gaia satellite mirror detected no visual indication of multiplicity.

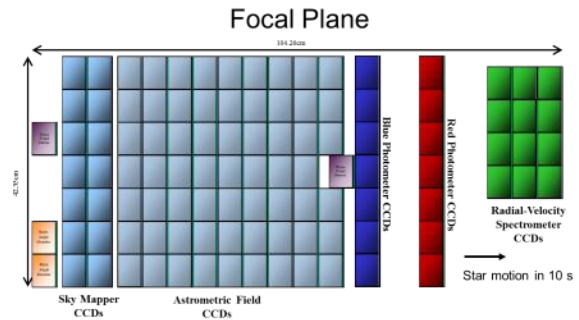


Figure 1: Gaia instrument schematic from [2]

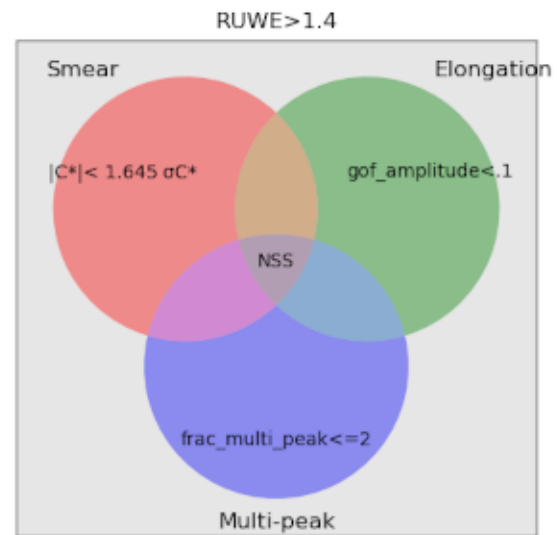


Figure 2: Candidates for unresolved non-single stars (NSS)

## 2.1 Gaia Astrometric Orbits

When the Gaia non-single stars with orbital solutions is cross matched against the WDS catalog, there are about 100 matches. When the same Gaia stars are cross matched against the 6th orbital catalog, there are 42 matches.

Since the Gaia orbits are computed on the basis of the apparent wobble of a single star, the Gaia orbits don’t measure actual separation between the two components. Having a measure of the angular separation between components from the WDS catalog together with Gaia’s parallax measurement indicates the distance between the components and hence their mass. Going the other way, there are about 60 WDS pairs which now have an orbit calculated.

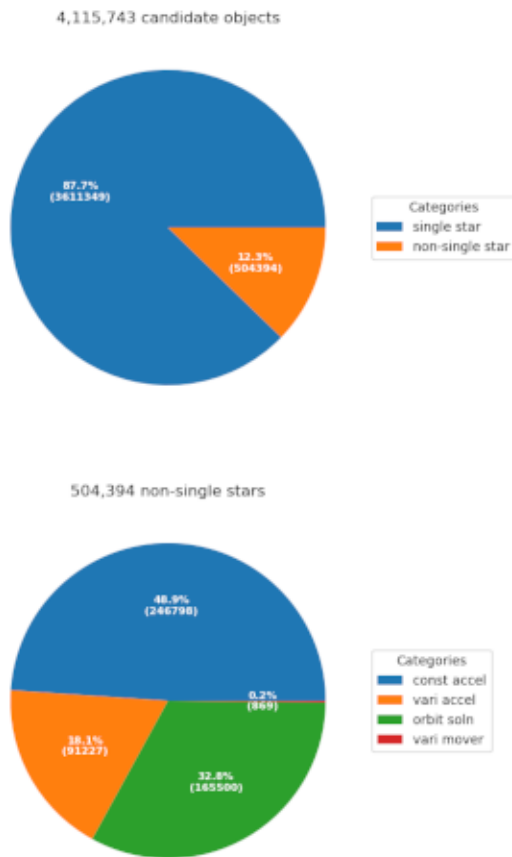


Figure 4: Distribution of Gaia DR3 non-single stars

## 2.2 Gaia Acceleration Solutions

There are 338,215 stars that are classified by Gaia as non-single stars that lack an orbit computation but which nevertheless fit a model in which the proper motion of the star deviates from uniform motion at a fixed rate or at a uniformly changing rate. Some 380 of these stars are also listed in the WDS catalog.

## 2.3 Gaia elevated RUWE single stars

There were over 4 million Gaia observed stars that appeared single but whose progress of positional measurements were noisy enough that they were investigated as possible astrometric double stars. After investigation, a single-star designation was retained for 3.6 million.

Of the 4 million NSS candidate stars, 2789 of them also appear in the WDS catalog as actual double stars. That is to say that while only ~12% of the NSS candidates were ultimately categorized as multiple stars, ~17% of the 2789 WDS stars in the candidate

category also appeared in the NSS categories. This suggests, modulo several caveats, that the group of 3.6 million NSS candidate stars for which the single star designation was retained might still be relatively rich in multiple stars and thus possible targets for ground-based follow-on investigation. After all, if the elevated RUWE is real and not instrument error, there must be some physical cause for the wobble.

3.6 million is still a large pool, even for automated acquisition, but the parameters used to isolate the published astrometric binaries can be modified in order to concentrate follow up checks on the targets at the periphery of the accepted non-single stars. The Gaia group documentation gives three parameters: RUWE, goodness of fit, and significance. RUWE is a general statistic, so it is possible to restrict a search to RUWE considerably larger than the 1.4 threshold for candidacy. Goodness of fit (a sort of  $\chi^2$  test) and significance (a sort of SNR test) could also be loosened. These statistics are explained in detail by Halbwachs et al [5]. El-Badry [3] has pointed out that radial velocity uncertainty might also be an indicator of wobble and hence of a companion.

Such stars, if they are binary stars, would be very close doubles. But just as Gaia has multiplied the field of stars observed by Hipparcos in the 1990's, so too has technology advanced for modest-aperture ground-based telescopes. Larger aperture telescopes, higher QE, faster cameras, more powerful computers, and the dissemination of speckle interferometry algorithms have all enabled ground-based observers to detect closer binary systems. Even if only elongation of such systems are detected by smaller telescopes, they can be referred to larger telescopes for further observation.

## 3. Proper Motion Anomaly

Renormalized unit weight error (RUWE) measures a star's departure from rectilinear motion (great circle motion along the celestial sphere). At lower levels it might just be random noise but at larger values it reflects the effects of force applied. For Gaia, however, these departures take place only over the life of the mission. Stars that take dozens of years to complete their orbits might not register their gravitational effects in RUWE.

Of course, this is just what binary astronomers are quite familiar with: accuracy issues aside, if three observations do not lie on the same great circle, there is a force responsible. With Hipparcos and Gaia satellites, measurements of position have been precise enough to get a proper motion (PM) reading over the life of the mission. If Hipparcos and Gaia measurements can be calibrated, that would provide a

25-year interval between PM measurements. If the same star observed by Hipparcos around 1991 and then by Gaia around 2016 registers a significantly different PM, one observation to another, then a force is involved. If a force is involved, astronomers may already have reported it, or it may be a previously undetected double. Of course, "significant difference" should eliminate most but not all false candidates due to measurement noise.

One researcher, Brandt [1], has indeed correlated Hipparcos and Gaia PMs, providing a window into nearly a quarter-century of PM deviations. If Brandt's data is screened for maximum proper motion anomaly (PMA), it turns out that in fact many have already been detected by double star astronomers. Take, for example, all the stars with PM measured in both Hipparcos and Gaia and order them by projected PM (i.e. divide PM by parallax) and use the same criteria as with Gaia NSS to discard partially resolved multiple stars, that is, just as in Figure **Error! Reference source not found.** but with RUWE criterion replaced with PMA. Then take the top 5%. This comes to 4618 stars. Cross match with WDS catalog, and about 400 WDS entries match. Caveat: many of these doubles are so wide that the secondary would have been easily resolved. So, the large PMA might indicate a close-in companion that ground-based smaller telescopes cannot split. Nevertheless, the frequency of WDS matches is 10-fold that for Gaia's NSS.

Perhaps elevated PMA alone is enough of a hint of multiplicity to merit further ground-based observations.

#### 4. Partial Resolution

Although the diffraction limit of the Gaia detector lies below 0.1 arcsecond, the proportion of double stars fully resolved in Gaia's DR3 falls below 100% for angular separations less than 1 arcsecond. However, multiplicity of stars not fully resolved by Gaia may yet be indicated by Gaia statistics. Such stars can then be further investigated by ground-based meter class telescopes. For example, El-Badry [3] notes that "Most pairs with separations wider than  $\sim 0.2$  arcsec have `frac_multi_peak`  $> 0$ ". This can be turned around and Gaia DR3 be searched for stars where `frac_multi_peak` (Figure **Error! Reference source not found.**) is allowed to exceed 2, that is, sources for which greater than 2% of good scans recorded multiple local flux maxima.

There are quite a few of these multiple maxima. If the search is narrowed to sources with G-magnitude within, say, the very narrow range between 10.0 and 10.1 magnitudes, 5050 stars are found. El-Badry also notes that some of these stars are already members of

fully resolved pairs with separations up to 2.5 arcseconds or so, and, indeed, 308 of the 5050 correspond to WDS binaries with separations between 1.0 and 2.5 arcseconds. Nevertheless, 607 (12%) of these 5050 sources match WDS binaries with separations less than 1 arcsecond. Of course, even these might already have been resolved by Gaia (see El-Badry [3] Figure 2, upper panel). In this case, though, a search of El-Badry et al [4] turns up 198 resolved binaries where the combined G-magnitude of the pair lies between 10.0 and 10.1. All but 13 of the El-Badry pairs are recorded in the WDS catalog. That is, Gaia DR3 fully resolved  $\sim 30\%$  of WDS known binary stars with separations less than 1 arcsecond.

So even in this small tranche there are  $\sim 4000$  possible undiscovered double stars, none of which are in the Gaia non-single star candidate list, and none of which are in the WDS catalog. To refine the search for visual doubles, this class might be ranked by `frac_multi_peak` or by various combinations of RUWE, excess BP/RP dispersion and isotropy indicated in Figure **Error! Reference source not found.**. Indications of proximity and radial velocity variance could also provide helpful filters.

Pushing this example a little further, consider just the elongation factor, `gof_amplitude`. It is weakly positively correlated with `frac_multi_peak`, 0.33, but slight enough to add information and thus some filtering. (cf. Figure **Error! Reference source not found.**).

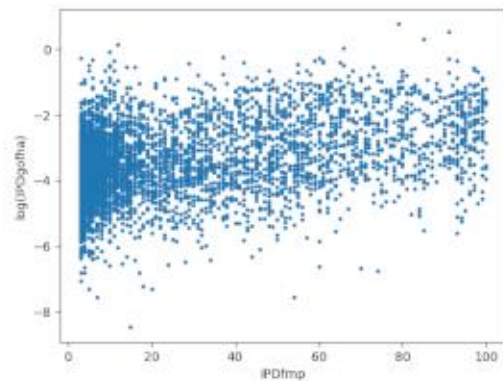
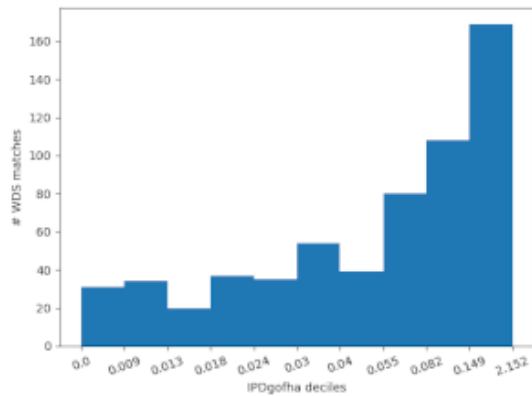


Figure 4: Weak correlation between IPDfmp and IPDgofha



**Figure 5: Density of WDS binaries against IPDgofha values**

Simply partitioning the `gof_amplitude` values into deciles, one sees that the higher values correspond to higher density of WDS doubles. Hence one might guess that higher `gof_amplitude` values are indicative of greater chances of being multiple in general, and that the Gaia team was justified in using the statistic to control for partially resolved double stars. (cf. Figure **Error! Reference source not found.**)

All this is to say that a program to search for new double stars with meter class telescopes can be fashioned from Gaia DR3 indicators of partial resolution.

## 5. Data Sources

The information from the Washington Double Star catalog cited here originates with observations contributed by astronomers over the years and collated and published online with public access by the US Naval Observatory (<https://crf.usno.navy.mil/wdstext>). The Naval Observatory has also uploaded the WDS catalog to the Strasbourg astronomical Data Center (<https://cds.unistra.fr/>) where it is available through the VizieR library (<https://vizier.cds.unistra.fr/viz-bin/VizieR>). The European Space Agency publishes data from both the Hipparcos and Gaia satellites online with free public access on their websites (<https://gea.esac.esa.int/archive/>) as well as VizieR. Brandt [1] uploaded his catalog to VizieR. El-Badry et al [4] made their catalog available to the public at CERN's zenodo.org.

## 6. Data Access Tools

Tools for accessing the data published by the Naval Observatory, CERN and the ESA, either directly or through VizieR, are provided in Python

modules Numpy, PyVO and Astropy. The modules themselves use the table access protocol (TAP) and the astronomical data query language (ADQL) curated by the International Virtual Observatory Alliance (IVOA). ADQL is a version of SQL modified to facilitate astronomy-related queries. All these resources and tools get strung together in a short Python script for a view. For example, the PMA view can be diagrammed as in Figure **Error! Reference source not found.**

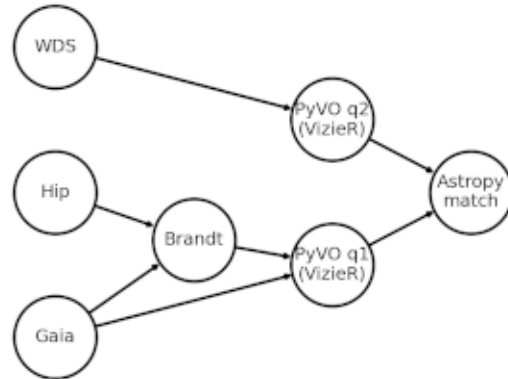


**Figure 6: Work flow for comparing Hipparcos/Gaia proper motion anomaly detection with WDS known binary stars**

It should be said that the data libraries offer several interfaces, and this provides flexibility to the access method. For example, one of us (Smith) uses TopCat and Gaia Archive Advanced Query to find and download data for further processing with spreadsheets.

## 7. Conclusion

Astrometric satellite data, principally from Gaia but also from Hipparcos, provide new sources of data for the investigation of multiple stars. New tools have been developed to access this data and collate it with historical data. Historical data not only provides a longer timeline for binary star evolution but can also serve as statistical samples from the larger pool of multiple stars revealed by Gaia. The limited resolution and timeline of the satellites can be complemented by ground-based observations, providing opportunities for study with modest aperture telescopes combined with newly developed cameras and speckle interferometric techniques.

## 8. Acknowledgements

Mark Copper would like to thank all the people that create the data, make it available to the public,

create the free tools to access it, and even support access by the general public with help desks that really do help. Amazing. We all thank Eastern Arizona College, the Fairborn Institute, Gravic Inc., Payson High School, and Colorado Mountain College for their support.

## 9. References

- [1] Timothy D. Brandt. The Hipparcos-gaia catalog of accelerations: Gaiaedr3 edition. *The Astrophysical Journal Supplement Series*, 254(2):42, June 2021.
- [2] <https://www.cosmos.esa.int/web/gaia/focal-plane>
- [3] Kareem El-Badry. Gaia's binary star renaissance, 2024.
- [4] Kareem El-Badry, Hans-Walter Rix, and Tyler M Heintz. A million binaries from Gaia eDR3: sample selection and validation of Gaia parallax uncertainties. *Monthly Notices of the Royal Astronomical Society*, 506(2):2269–2295, 02 2021.
- [5] Jean-Louis Halbwachs, Dimitri Pourbaix, Frederic Arenou, Laurent Galluccio, Patrick Guillout, Nathalie Bauchet, Olivier Marchal, Gilles Sadowski, and David Teyssier. Gaiadata release 3: Astrometric binary star processing. *Astronomy & Astrophysics*, 674:A9, June 2023.
- [6] Richard Harshaw. Gaia dr2 and the washington double star catalog: A tale of two databases. *Journal of Double Star Observations*, 14(4):734–740, October 2018.
- [7] L. Lindegren, F. Mignard, S. Söderhjelm, M. Badiali, H. H. Bernstein, P. Lampens, R. Pannunzio, F. Arenou, P. L. Bernacca, J. L. Falin, M. Froeschlé, J. Kovalevsky, C. Martin, M. A. C. Perryman, and R. Wielen. Double star data in the HIPPARCOS Catalogue. *Astronomy & Astrophysics*, 323:L53–L56, July 1997.

# Gaia Binary Follow-up with Gemini Speckle Interferometry

*Zachary Hartman  
NOIRLab, Gemini North*

*Russell Genet  
Fairborn Institute*

*Mark Copper  
Magdalena Transit Observatory*

*Paul McCudden  
Colorado Mountain College*

*Michael-James Ellis  
Payson High School*

*Lou Jackson  
Eastern Arizona College*

---

## Abstract

By the time Gaia's mission is completed, it will have provided high-quality orbital elements of close astrometric binaries with periods less than 10 years, most of them new discoveries. However, binaries with periods longer than 10 years would benefit from additional ground-based astrometric observations. Some overlap between the ground and space observations while Gaia is still operating would help assure continuity between the two sets of observations. Instructors and students at several community colleges and high schools are launching a Gaia binary follow-up program with automated speckle interferometry observations on a 1.0-meter PlaneWave Instruments telescope at the El Sauce Observatory in Chile's Atacama Desert, as well as in-person speckle observations with the 1.5- and 2.5-meter telescopes at Mt. Wilson Observatory. These observations will provide follow-up for binaries with apparent separations down to  $\sim 100$  mas. To provide coverage below 100 mas (down to  $\sim 30$  mas), we are applying for Gemini Fast Turnaround (FT) observing mode time with the Alopeke speckle interferometry system on Gemini North. Alopeke provides simultaneous coverage in two narrow bands centered at 562 and 832 nm. The FT observing mode allows users to convert an idea into data much more quickly than the regular semester process. Approximately 10% of the time at both Gemini North and South is currently available for the FT program. While FT proposals do not need to be urgent, they do need to propose good, short, self-contained projects that will result in publication. Students may participate in the program under PhD supervision. All program participants are required to review several other FT proposals; a good experience for students. If this pilot Gemini FT Gaia follow-up project results in student team published papers, we may ask for modest additional time.

---

# IT Her, A MISCLASSIFIED ECLIPSING BINARY

*Laurent CORP*  
BAA-SAF-AAVSO-T60  
e-mail: [astro.laucorp@orange.fr](mailto:astro.laucorp@orange.fr)

*Jean-Bruno DESROSIERS*  
BAA-SAF-AAVSO-SAS-GSNST  
e-mail: [jbd@omsj.info](mailto:jbd@omsj.info)

---

## ABSTRACT

Here we describe the collaboration between 2 amateur astronomers located on two different continents, one in Europe (France) and the other on the American continent (Canada-Quebec) to observe and analyze the star IT HER. This collaboration started in 2021, the advantage is that observations can be done continuously and can cover a period of twelve consecutive hours. The observed star required more attention because the references did not agree with the observations. Here we reveal the result of our observations, discoveries and findings.

---

## 1. INTRODUCTION

The first step was to collect as much documentation on each star in order to establish a file and compare the already existing literature with our observations. Then we also agreed that once the good weather arrived, observing would be the priority and that later, during the cold season, the work of compilation and analysis would be done. The choice of target stars was made in order to be able to make the most of the stars available during the favorable months. Observations of stars in the constellation Virgo began at the beginning of spring, then others were chosen in the constellations of Hercules, Ophiuchus, Delphinus, Andromeda and Pegasus.

Towards the end of the 2022 season, one of these stars was causing a problem, which we found as references and documentation did not match with what we had observed. So we thought it was a mistake and of course, checked everything. But subsequently, in our research we found observation reports, particularly in the AAVSO VSX database, which stated that our star IT Her was wrongly classified, which prompted us to further our research.

## 2. The IT Her star

Interest in this star was sparked by its classification, with it being classified as RR Lyrae (General Catalog of Variable Stars (Samus+ 2007-2011)).

Stars of this type are relatively old and pulsating stars, called population II stars, therefore showing low metallicity. The B-V color indices vary from +0.14 at maximum to +0.45 at minimum, a spectral type

ranging from A8 to F7 and an absolute magnitude approaching 0.6 to 0.7.5.

Their mass is about half the Sun and they are rich in helium. They climbed the branch of the Red Giants, displayed the helium flash, then reached the Horizontal Branch. There, they have reached the zone of instability where they undergo pulsations. From their position in the instability band of the HR diagram, these stars have an effective temperature of 6,100 K to 7,400 K, therefore just a little hotter than the Sun\* .

However, the apparent magnitude of IT Her is between 12.4 and

12.8, (RA 18:45:46.41 and DEC:25;19;59.4 in J2000)

Its spectral type is A5IIIvar, according to the AAVSO catalog VSX.[1] We are therefore normally considering a star of spectral type "A" and which mainly displays Balmer lines (Hydrogen), this based on the work of Cecilia Payne(1925) which is also based on the work of the astronomer Meghnad Saha on the ionization of stellar atmospheres. A type A5 star should also display an average surface temperature of 8,310 Kelvin and an absolute magnitude close to 2.4, according to tables from the University of Northern Iowa.

In this same AAVSO catalog, we note that the IT Her star is an EW type eclipsing binary whose two components fill their Roche lobe and have a very ellipsoidal shape. They are contact binaries, because they are in touch. It should be noted that the two components may have different masses, but since they are in contact, they will have the same temperature. IT Her has a period of 0.339395 day (8.1455 h) again according to the

AAVSO VSX.

The Gaia archive site[9] indicates a distance of 365.0779 parsec which gives us a distance of 1190.5190319 light years. IT Her is therefore in our Milky Way and denotes radial velocity of  $V(\text{km/s}) - 16.65559$ .

The observatory's O-C ephemeris website SOHURA

Astronomical Observatory indicates that this star is listed as RR

Lyrae of type RRc under the id 400237 400237 IT Her 18h 45m 46.4s 25o 19' 59" |RRC| 12.9 0.226038 and announces a change in the O-C of the star.

Our primary observations did not match some of these descriptions, so we decided to study it in more depth.

### 3. Observation locations

1st instrumentation: Pic du Midi (France)[2]

The Pic du Midi observatory is located in France in the Pyrenees at an altitude of 2,887 meters. This Mecca of French astronomy is home to several telescopes dedicated to Sun, planets and exoplanets observation.

Amateur astronomers can have - if they request it to the T60 Association - a 50 cm diameter telescope to carry out their own observations.

The model is a CDK 20 Planewave installed on a NOVA 120 mount built by Alcor-System.

Optical type: Dall-Kirkham with a 508 mm mirror and a focal length of 3,454 mm (F/6.8) reduced to F/4.5 with a focal reducer.

The camera is a ZWO ASI 6200 MM whose photosites measure 3.8 micron pixels, 9600 x 4800 pixels. Sloan g' and r' filters complete the camera. The field is 53' by 35'. Sampling: 0.22 sec. arc/pixel, each image weighs 50 MB in 2x2 binning

2nd instrumentation: OMSJ (Mont St-Joseph Observatory, Quebec-Canada)

Located in Quebec, on Mount St-Joseph, right in the middle of the world's first dark sky reserve, the OMSJ (Mont St-Joseph Observatory) benefits from a particular darkness, since the mountain hides the light pollution from the west and the trees, that from the northeast (Lac-Mégantic).

In addition, it is located nearly 600 meters above sea level. This advantageous position makes it a suitable place for observations under one of the most beautiful skies because the entire environment of the Mont-Mégantic region, famous for its professional observatory, is protected in order to preserve the sky quality (see: ricemm.org).



Figure 01 - The 50 cm telescope of the Pic du Midi Observatory



Figure 02 - The two parallel telescopes of OMSJ

Two telescopes set in parallel on a CEM120 mount (Ioptron), the first is dedicated to "standard" photometry (ED127 APO-Triplet Scope - 127 mm diameter and 952 mm focal length F/7.5 (Explore Scientific), camera CCD SBIG ST8, filters CV, B, V, Rc, Ic, HA, OIII, SA200). Field (FOV): 1.95 arcsec/pixel.

The second telescope is dedicated to spectroscopy as well as deep sky imaging and tracking, (Schmidt-Cassegrain 355 mm in diameter with F/6.3 focal reducer or 2463 mm focal length; Alpy 600 with a resolution of 600 rpm, 23 micron slot. Also, LowSpec-1800 and Star'ex - 2400. Other CCD and CMOS instruments and cameras are in development and will be available for both science and astrophotography to meet needs and make the observatory as versatile as possible.



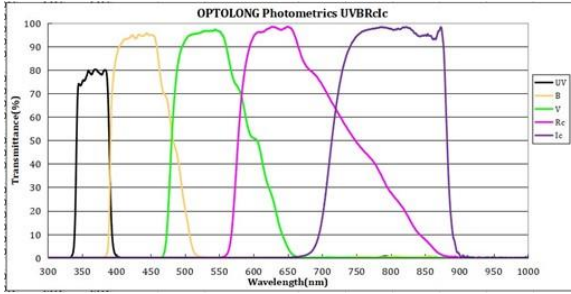


Figure 03 - Filters U, B, V, Rc, Ic

#### 4. Filters used during observations:

##### 4.1 Johnson/Cousins filters, Optolong (OMSJ)

Photometric filters Johnson/Cousins are the culmination of several years of research. This system of "bandpass" filters was introduced in the 1950s-1970s by the American astronomers Horld Lester Johnson and William Wilson Morgan. It is one of several photometric systems which, including the system of Bessell filters, developed in the 1990s and finally established itself as one of the standards, with the integration of Rc and Ic filters whose bandwidths have been adapted to today's CCD-CMOS cameras and adopted by numerous observatories and associations such as the AAVSO. (Bessel2005ARAA43p293).

In classic photometry, the U filters are rarely used unlike all the others, particularly the B and the V which are used to find the color index (B-V) ((Sekiguchi et al (2000)) which offers an approximation of the temperature of the star and thus its classification. The fact that the Rc and Ic filters approach the infrared also makes them very useful because tables have been set up to evaluate, among other things, the degree of luminosity of a star, for example symbiotic stars. Note that the filters used (Optolong brand) have also been adjusted for CMOS cameras.

##### 4.2 SLOAN type filters (Pic du Midi):

The SLOAN filters originate from one of the most spectacular monitoring projects of an American observatory. The "SDSS Project".

These new filters were created with the advent of the "Sloan Digital Sky Survey" (SDSS) project. The 2.5-meter telescope located at Apache Point in New Mexico (United States) is equipped with a very special camera, equipped with 30 SITE/Tektronix 2048 x 2048 CCDs (24 micron pixels). The photometric detectors are set up in a focal plane in six columns of five CCD

sensors and provide constant tracking to scan the sky and create three-dimensional maps " the most detailed of the Universe ever made".

As these filters are very defined and do not overlap, some researchers have obtained them in order to carry out other photometric researchers which requires very tight photometric bands. From there, the system became more and more popular. There is still a certain reluctance to use it due to the sustainability of the data (data history). Long-term photometric monitoring of stars requires persistence and stability of the equipment. If there is a change, it will inevitably be reflected in the consistency of the data.

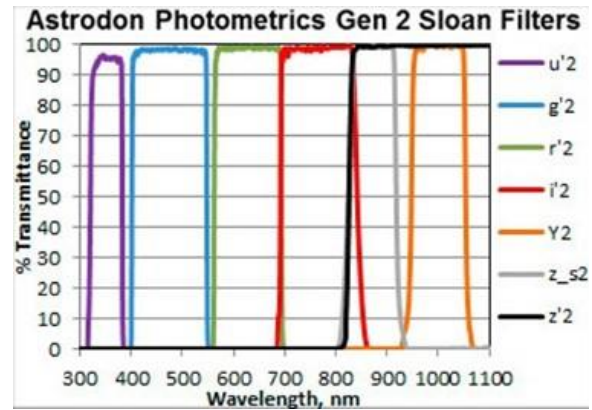


Figure 04 - Sloan Filters

#### 5. Table of reference stars:

We investigated to find a few more stars with an ideal average B-V between 0.5 and 0.85.

NOMS	RA	DEC	B-V
HD 336946	18:46:33.33	25:06:50.6	0.57
TYC 2112-1510-1	18:45:19.66	25:10:11.0	0.74
TYC 2112-1473-1	18:45:03.44	25:07:14.7	0.52
TYC 2112-956-1	18:45:26.08	25:29:14.00	0.65

Table 1

#### 6. Observations and photometric data

Our data comes from two sources: our observations and those of the TESS satellite [19] (see next paragraph)

Our observations: We carried out 8 nights of observations, including two in France and six in Quebec.

### 6.1 In France :

At the 50 cm telescope of the Pic du Midi Observatory, two nights of observations were carried out in July 2022 and July 2023 on this star. The average exposure time was 60 seconds. using a Sloan r' filter.

### 6.2 In Quebec :

Average exposure time with the ED127: 100 sec. in V, 200 sec. in B, 65 sec. in R, 70 sec. in Ic The reduction software used is: Maxim DL version 5.23 and 6.26 (George 2000).

On the spectroscopic side, the combined images of the Alpy 600, which is equipped with an Atik-414ex camera, a very sensitive Titan guiding camera, and the mount offering long-term exposure tracking, make it possible to obtain sufficient signal for the magnitude of the star as well as a view of the star from 3,800 to 7,420 Angstrom.

## 7. Table of observations

Table 2 is attached at the end of the paper.

## 8. Temperature index (B-V) calculated according to the method suggested by Sekiguchi et al (2000) [17]

Table 3 is attached at the end of the paper.

Through our combined photometric observations from the two observatories, we noted that the measurements obtained by the B-V carried out suggest to us that the temperature of the star would be around 4,868 Kelvin, which corresponds to a star of spectral type "K", which n is not consistent with that of a spectral type A5IIIvar (around 8310 K), as indicated by certain databases [11].

It should be noted that these calculated temperatures are only one element in order to be able to base our analyzes and thus validate other observation parameters.

## 9. O-C

The O-Cs make it possible to show the difference between the observed moment and the calculated moment during the primary and secondary minima. The minimum moments were calculated using the

MAVKA software (Andrych 2020), the symmetric polynomial method giving the best result. Our measurements also show that the O-C do not have the same value depending on whether we observe a primary or secondary minimum, in the latter case it is weaker. The original minimum moments come from (Kreiner 2004). The graph below shows us a decrease in O-C from 2017 after several years of stability (2005-2015). Following our observations, we were also able to complete the O-C diagram on the Sahoro Astronomical Observatory website.

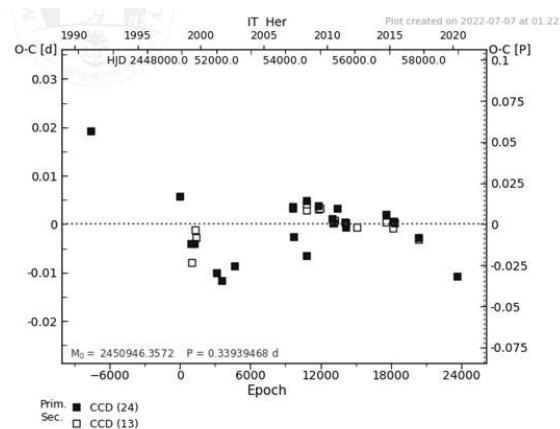


Figure 5 - O-C over the period 1990 - 2022 <https://www.as.up.krakow.pl/minicalc/HERIT.HTM> The website tells us:  $HJD_{min} = 2452500.1175 + E \times 0.33939351$

## 10. Light and reference curves - TESS satellite [18]

One of the possible advantages today is to complement and validate our observations, with observations carried out by satellites such as TESS, Gaia[9].

Using the Peranso[8] analysis software (Vanmuster, 2016), we imported data from several satellites and the TESS satellite offered the best choice with two ranges temporal, i.e. from June 4, 2021 to July 23, 2021 and then from July 9 to August 5, 2022. We immediately notice the regularity of the curves.

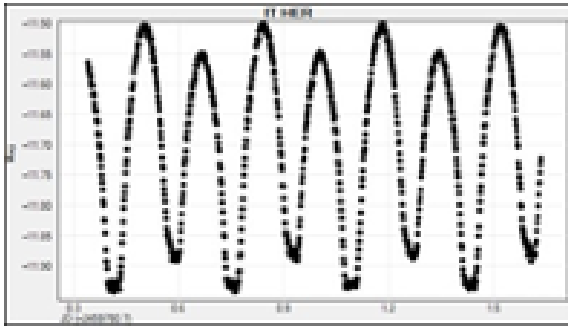


Figure 6 - TESS light curves

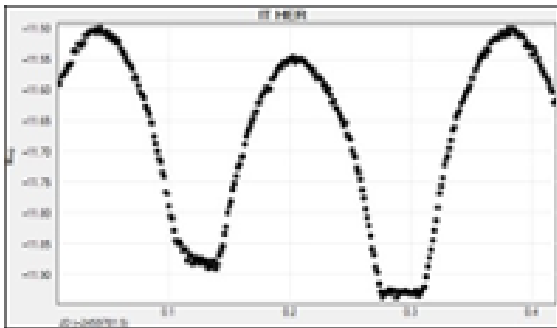


Figure 7 - Detail of the typical light curve

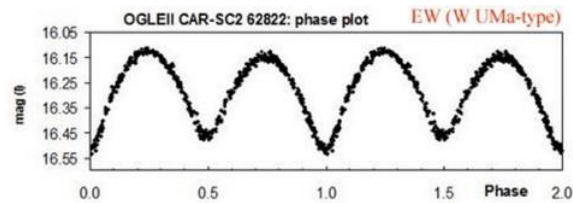


Figure 8 - Courtesy of the AAVSO

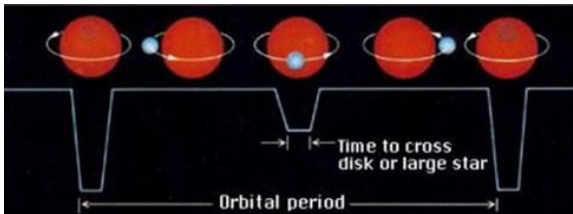


Figure 9 - Courtesy of the AAVSO

It is by enlarging that we notice “plateaux” in the minima, which is a particularity of this star, which leads us to the hypothesis that this star could have components of different masses. These being due to the transit time of one body past another is an indication of marked difference between the components forming a binary star.

## 11. Phase and Period:

The phase of the binary star (point between a primary or secondary minimum and the next maximum) was estimated to be 2.16 hours from our observations and also by importing data from the TESS satellite which was subsequently analyzed with the Peranso software (Vanmuster, 2016).

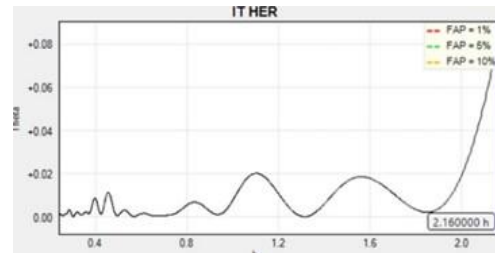


Figure 10 - phase diagram

In its nomenclature on the star and on its research site, the TESS18 satellite, as well as the AAVSO database, indicate a period which would be 0.33934 days, or 8.1455 hours. From our observations, we confirm this displayed value.

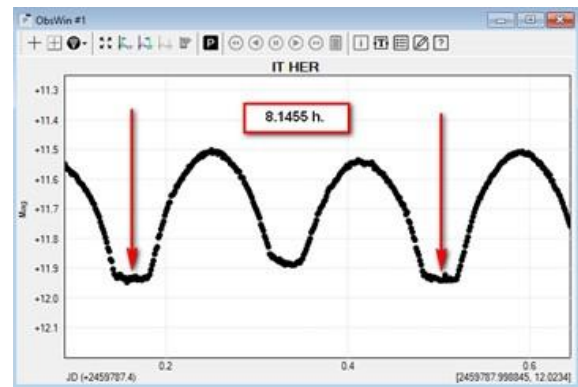


Figure 11 - Full period of IT Her

## 12. Other items found:

Another fact discovered during our reference and validation research: in the star file in the AAVSO VSX database, an image of the IT Her curve dating from 2007-09-29 01:04 UTC from ASAS -3 and observation of NSVS already proved on this date that the star could be an EW type binary but since then, there have not been many observations:

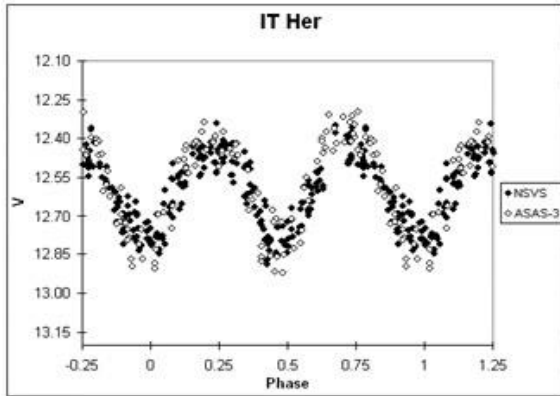


Figure 12 - Full period of IT Her  
["https://www.aavso.org/vsxdocs/15048/133/ITHerEW.gif"](https://www.aavso.org/vsxdocs/15048/133/ITHerEW.gif)

In the same entry in the VSX database of the star: "[https://www.aavso.org/vsx/index.php?view=detail.to\\_poid=15048](https://www.aavso.org/vsx/index.php?view=detail.to_poid=15048)" There is a comment from 2006-12-10 from an observer named Patrick Wils: "EW, not RR". In our research to better understand the curves of our star as well as its particularities, we found a few stars which have a light curve similar to our observations, including V566 OPH. Thanks to the StarLightPro10 3D simulator software available on the site: ("<http://www.midnightkite.com/index.aspx?URL=Binary>"), we were able to get a "visual" of the reason for the significant "flat" in the observed light curve of this star, during the star's minimums as well as a visual of what the star might look like. The solution seems to lie in the difference in the star's two components' masses.

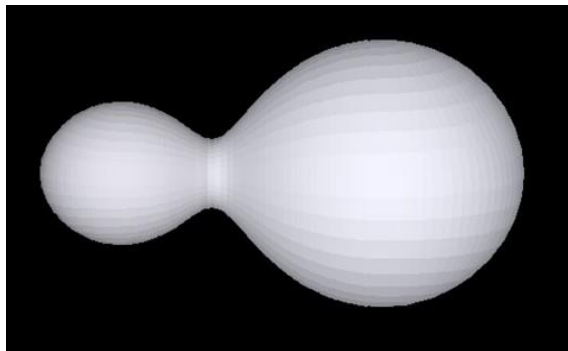


Figure 13 - 3D simulation

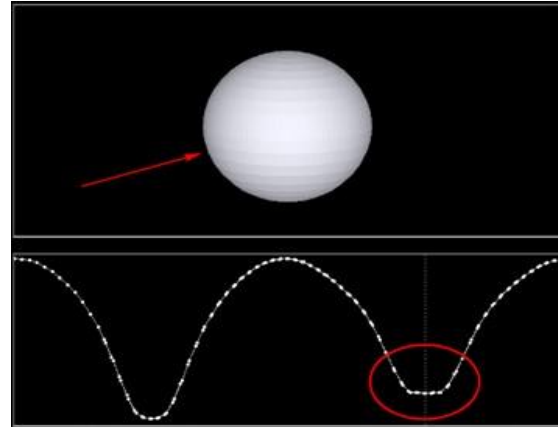


Figure 14 - Phase where the spectra were taken

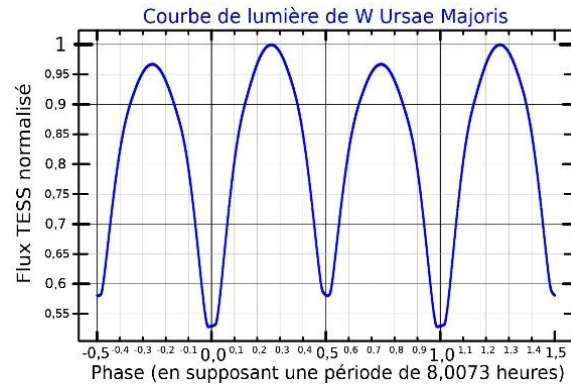


Figure 15 - Light curves of the star W Ursae Majoris exported from TESS.

The curves obtained from our observations of IT Her, are reminiscent of that of a binary very famous for the classification group that it represents, the "EW", W Ursae Majoris which, moreover, has a period of 0.3336 days, or 8 hours 23 seconds, which is very similar to IT Her.

Here on the other hand, the CDS informs us of a radial speed of -29.60 Km/s., which is higher than that the front site for IT Her is -16.02 Km/s. This point is important and must be refuted or confirmed by instruments of with greater diameter than ours.

### 13. Spectroscopy :

One of our references specified that IT Her was a type A5 star. As already discussed in the introduction of this document, one of the specificities of type "A" stars is the appearance of Balmer lines and therefore of hydrogen. This is due to the ionization of hydrogen atoms which are very active at 10,000 degrees Kelvin.

Hydrogen electrons are particularly active between temperatures between 6,000K and 40,000K,

which means that type "A" stars in particular demonstrate Balmer lines, namely H alpha, beta, gamma, delta, epsilon and zeta.

To compare with our star IT Her, during our reference searches we discovered, among other things, that on the "site research of Gaia", the spectrum displayed did not correspond to the reference literature either. In the raw spectrum of IT Her, hydrogen lines were not very present, but other elements found led us down a path.

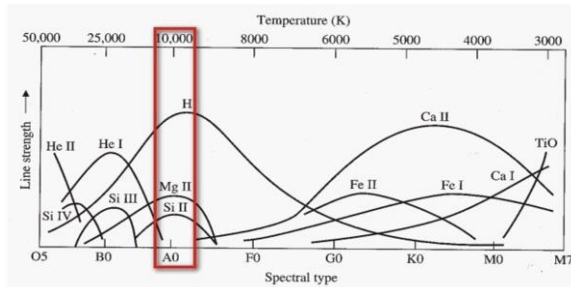


**Figure 16 – Line strengths as a function of plasma temperature or Payne curves.**

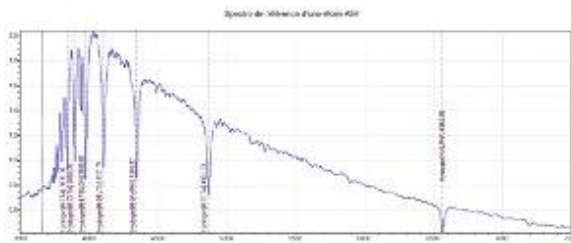


**Figure 17 - Reference spectrum of an A5V star**

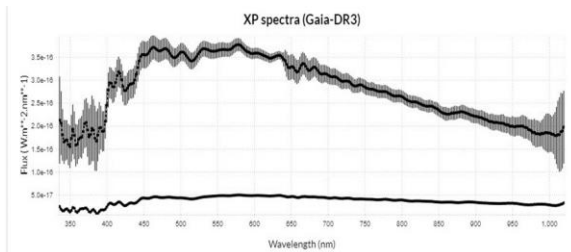


**Figure 18 - Spectrum from GAIA DR3- BP/RP (XP)**

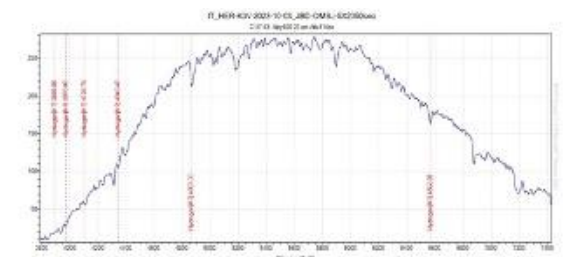


**Figure 19 – Calibrated raw spectrum of IT Her with localization of Balmer lines.**



**Figure 20 – IT Her spectrum with instrumental correction and location of Balmer lines which are very active.**

After some searches for reference stars as well as based on observations collected in photometry, we noticed several similarities between the reference spectrum presented by Gaia (XP- (300-1000 nm) and a reference spectrum of the type spectral-K3V

From there, we decided to observe the star in spectroscopy, first at wide field using an Alpy 600 to allow us to verify the correct spectral type of the star and this, in at least two different phases of the binary (see next section). With an Atik 414ex CCD camera, we have an average dispersion of 3.460444 Å/px.

Two nights with favorable skies then occurred, namely October 3, 2023 (2023-10-03) and October 4, 2023 (2023-10-04). The star having an average “V” magnitude of 12.4 to 12.6, to obtain a sufficient signal, 5 exposures of 2,350 sec. (5 times 38 min 20 sec) were made the first evening and 4 X 2,400 sec (4 times 40 min) the day after.

## 14. Compilation of two nights of “wide field” spectroscopy observations:

Figure 21 is placed at the end of the paper.

Representation of the compilations of these two nights: we can already see marked differences in the wavelengths 4310 (Fe3) 4390.03 (Na1), 4392.81 (Na2), 5167.30 (Triplet Mg), 5577.34 (O1) and 6592.91 (Fe1), which may indicate phases of the binary and therefore different elements between the two bodies.

This star of variable magnitude (12.4-12.8) has already demonstrated to us, in photometry by average B-V indices, a spectral type suggesting a 'K' type star (3,500 to 5,249 Kelvin) as well as by the hydrogen bands not very present, the presence of neutral metals, but also by traces of carbon, traces of titanium oxides. In addition, the presence or rather almost the absence of calcium Ca1 (3933.66 and 3968.47 Å) also leaves us to think of a colder surface temperature.

These values would all need to be revalidated at higher resolutions as well as with further observations. In the spectra of the night from 2023-10-03 to 2023-10-04, we noticed some traces of titanium oxide (TiO),

(4537.23 and 4589.95) as well as several changes in the lines over the hours, which may confirm significant differences between the two components of the star.

We even notice marked changes over the hours of exposure, around several lines including the 4312 line which splits, 4871.32 (Fe1), 5569.62 (Fe1), 5875.62 (He1), 6380.77 (N4), 6538.78 (Ca3) as well as several others. Remember that the star has an orbit estimated at only 8.1455 hours, so the changes can be very rapid and that, given the sensitivity of the spectroscope and the magnitude of the star, the introduction of parasitic noise into the signal is possible.

Further follow-up observations must be made to validate the possible cyclicity of the spectral changes between the two components of the star.

Figure 22 is placed at the end of the paper.

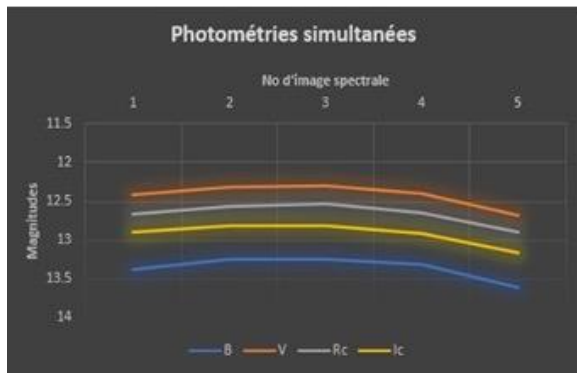


Figure 23 – simultaneous BVRI light curves

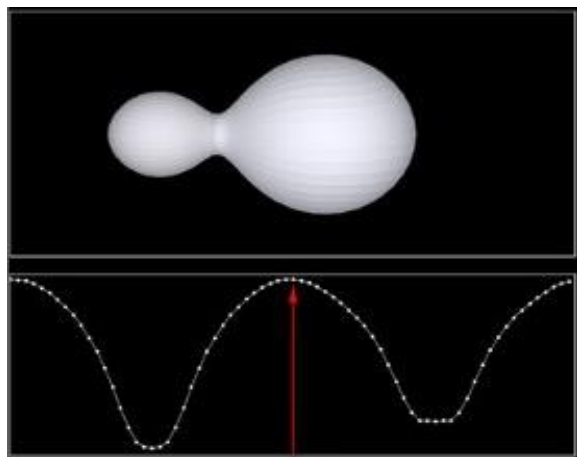


Figure 24 - Phase where the spectra were taken

As elements of these changes, in the spectra of the night from 2023-10-04 to 2023-10-05, this time, the marked absence of titanium oxide suggests to us a temperature undoubtedly higher than 4,400 Kelvin (F5), because it is at this level that the Tio disappears

(Stars and Their Spectra3, James B. Caler, p109, 5.1). So the idea that the two bodies of the star are different is materialized as much in their masses, but also in their temperatures and their compositions which seem to differ. As the masses are different, their stellar developments and stages are surely somewhat different too. On the other hand, as these stars are in close contact, their Roche lobe must also share their temperatures as well as the matter of the two celestial bodies.

The same phenomenon of differences between the same lines was also noticed the next day (2023-10-04), between the 2,400 sec (40 min.) exposures, but this time, also in a few other new lines. Here again, we notice changes in a few main lines over the hours. More observations are therefore required before establishing anything. But already, we are certain that this star is not one of spectral type "A".

Figure 25 is placed at the end of the paper.

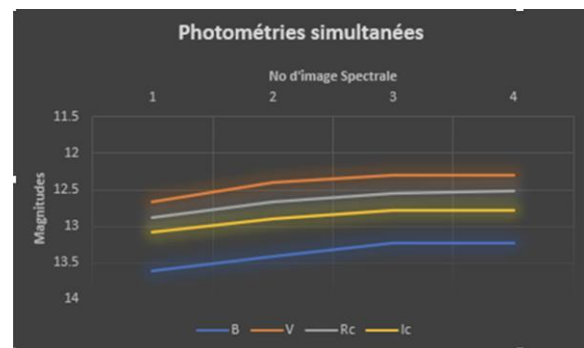


Figure 26 – Simultaneous BVRI light curves

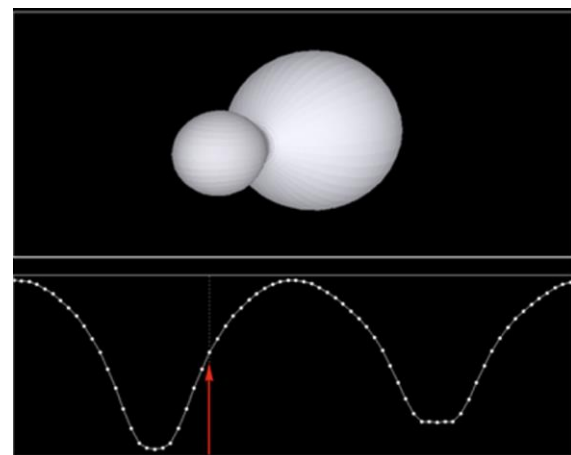


Figure 27: Phase where the spectra were taken

Figure 28 is placed at the end of the paper.

To ensure this and thus have a general idea of the changes, we divided the two profiles by themselves in

order to obtain two graphs (suggestion from Mr. David Valls-Gabaud, University of Cambridge). By juxtaposing them on the same graph, the lines offer graphs of which several points are almost mirrored. Where the points meet it indicates a change, the rest of the analysis involves finding the material that is affected.

In the changes highlighted by this process of dividing profiles (Figure 28), we mainly find iron (Fe1, Fe3), calcium (Ca1, Ca2), carbon (C3), sodium (Na2), nitrogen (N3), sulfide (S2) and helium (He1), but also titanium (Ti1, Ti3). These latter elements perhaps suggest to us a colder spectral classification than we thought. Of course, we must not forget that here, we are working at low resolution ( $r=600$ ) with a dispersion of  $3.358392 \text{ \AA/px}$ .

## 15. Simulation 3D

The only simulation we found is the one from this study :

"<https://ui.adsabs.harvard.edu/abs/2022sas..conf..16H/abstract>"

- Modeling Binary Stars Using Gaia Parallax (SAS-John Hoot, 2022)

From the data made available to us and the parameters from the article cited above, we carried out the following simulation show in Figure 30 and 31 using the Binary Maker 3.0 software (Bradstreet and Steelman, 2002).

Note on the light curve in Figure 29 that the maxima are not at the same height (O'CONNELL effect), this being due to the presence of spots (equivalent to sunspots) on one of the stars or to the presence of dust around the system.

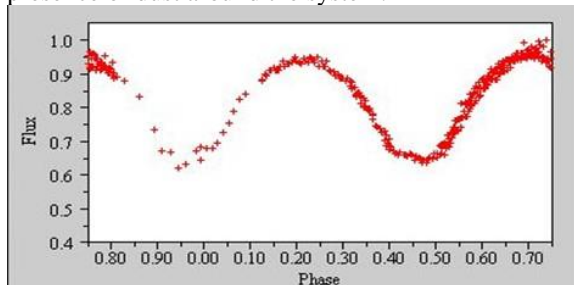


Figure 29 - V-band light curve obtained from our observation data

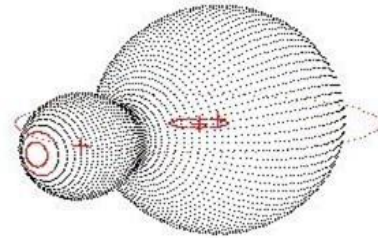


Figure 30 - 3D model

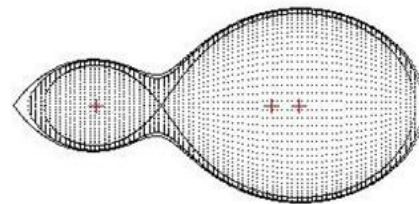


Figure 31 - Outline

The 3D modeling was obtained from light curve data (see figure 14 - Light curve of 2023-20-04). We see very clearly the mass ratio as well as the presence of a spot on the second star.

Figure 31 shows the barycenter of the system as well as highlighting the exchanges between the two stars and the common envelope.

Note that there then exists around each star a special surface, which is the one which is in contact (at the Lagrange point L1) with its centered counterpart. We call this part: Roche surface, and the volume it contains, the Roche lobe.

Here are the parameters used to carry out the simulation:

Mass ratio: 6.25

According to Gaia, we have IT Her A (secondary star):

0.34059461664501695 and IT Her B (primary star):

2.7219529361897408

Tilt:  $81^\circ$

Temperature:  $5,399^\circ$

Period: 0.3392 day

Even if this modeling remains imperfect, it allows us to know how this system is constituted and concretizes our hypothesis from the beginning.

0.39

## 16. Discussions

Through our observations and analyses, we note that the IT Her star is indeed not an RR Lyrae (CDS, Simbad, GCVS), but rather an EW type eclipsing binary. The curves that we collected as well as those from the TESS18 satellite demonstrate this very well. Furthermore, according to the literature, RR Lyrae are generally positioned at the center of the instability band, opposite type A to F stars.

Once again, according to our observations and analyzes carried out both in photometry and in spectroscopy, this star is classified much more in colder temperatures, of the order of 5,000 Kelvin, which would make it a “K” type star (RR Lyrae Stars4, Horace A. Smith, Cambridge Astrophysics Series, p 1).

Furthermore, the spectra and photometric observations made by Gaia9 and TESS18 are in agreement with our observations. This way we can even locate IT Her in an H-R diagram, which brings us into the main sequence area, which also matches our observations.

During our searches for existing documentation on this star, we noted that the AAVSO VSX database contained 6 sources of documentation on the star and that the Strasbourg CDS was not left out, with no less than 22 documentation sources.

Several of these sources were bulletins from "Commission 27 and 42 of the IAU information bulletins on Variables Stars", others came from observatory observation reports dating back as far as 1992 and stipulating that the star IT Her was indeed a star of type RR Lyrae. Subsequently, our research also discovered other more recent documents which stipulated that the star was indeed an EW and their light curves are similar to ours as well as that imported by the TESS satellite.

We leave as references the documents cited at the end of this document.

## 17. Conclusion

In summary, particularly in photometry, our observations lead us to a W type star Ursae Majoris, EW, a contact binary both for its light curve and its short period. In spectroscopy, we notice in the changes

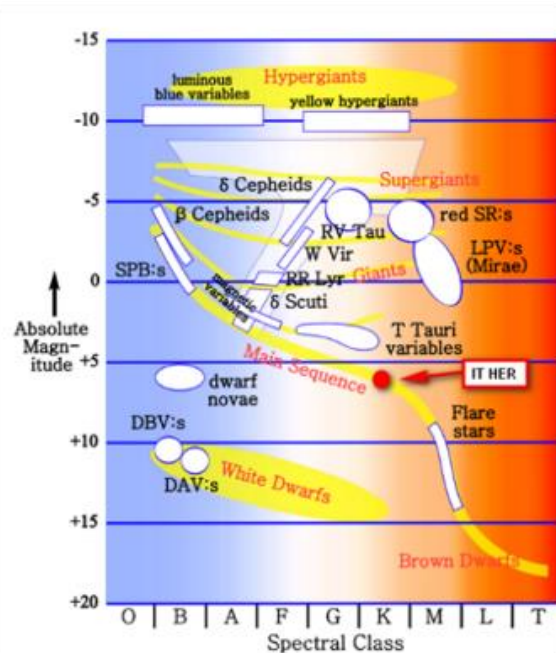


Figure 32 – Approximate location of the star IT Her according to our observations. HR diagram of variable stars, courtesy of the AAVSO

of Ca1 and Ca2, but in less intense quantities, Fe1 and Fe2, Na2, in short, we notice "metals" present in the stars much colder than the "A" type stars. Following this publication and other observations, requests for corrections will be made according to the protocols of each database. For now, we propose a spectral classification between K3 and K4, since we assume that the binary star is still in the main sequence and that the average temperatures match our observations. But the fact of having noticed traces of triple ionized titanium oxide (Ti3) on our spectra, but also Ti1, encourages us to continue observations in order to better identify this star. This is why we also suggest to continue spectrophotometric observations in 2024, particularly during minimums, which would allow us to isolate spectra of a single star from the binary. Other spectral observation projects, this time at high definition, are also planned in order to verify the radial velocities, which would then allow us to go further in our calculations of individual masses and other information with a view to carrying out a projection of the star in more complete 3D. It is important to mention that long series of observations during the same nights are important to ensure the quality of the curves. A review of this research also leads us to the conclusion that, even in professional catalogs and databases, there are sometimes errors. But also, there are changes in the stars. We know that nothing in the universe is immutable, everything changes,



particularly binaries. As professional observatories are expensive and cannot ensure long-term monitoring, and often, only passionate amateurs can, even with their small telescopes, make interesting follow-ups and validate what we sometimes think is "the truth". Luckily, professional astronomers are also there and some are available to help us learn and advance our passion. They are precious, because then it becomes an "astronomical" subject!...

## 18. Acknowledgements

- Martine Castets, co-observer during the missions in 2022 and 2023, without whom the observations at the Pic du Midi Observatory would not have been possible.

- David Valls-Gabaud (Paris Observatory - University of Cambridge) and - Yves Grosdidier (University of Sherbrooke) for proofreading and sound advices in both photometry and spectroscopy.

- Malhar Kendurkar, DAO (Dominion Astrophysical Observatory), GSNST (Global SuperNovae Search Team) with his many wise advices during the second reading.

- Manon Bouchard for the final corrections of French and English version of this document

## 19. References

\* It is important to note that the database VSX is not a bibliographic source as SIMBAD or the ADS. VSX will only list references that have been used to revise the information of the VSX record.

[1]- AAVSO/VSX : "IT Her data sheet"

[2] - Association T60: association which manages the 50 cm telescope at [1]'Pic du Midi Observatory: "<http://astrosurf.com/t60/>"

[3]- "Stars and Their Spectra, James B. Kaler, Cambridge University Press."

[4]- "Spectral Atlas for Amateur Astronomers, Richard Walker, Cambridge."

[5]- "Stellar Spectral Classification, Richard O. Gray and Christopher J. Corbally."

[6]- "RR Lyrae Stars, Horace A. Smith, Cambridge Astrophysics Series."

[7]- "Modeling and Analysis of Eclipsing Binary Stars, Andrej Prsa, AAS."

[8]- "Peranso software" Paunzen, E., Vanmunster, T., 2016, Peranso - Light Curve and Period Analysis Software. *Astronomische Nachrichten* 337, 239-246.

[9]- "Gaia Single source research": <https://gaia.ari.uni-heidelberg.de/singlesource.html>

[10]- "StarLightPro 3D Binary Simulator software": <https://gaia.ari.uni-heidelberg.de/singlesource.html> : <http://www.midnightkite.com/index.aspx?URL=Binary>

[11]- "Stars Statistiques from the University of Northern Iowa "

[12]- The spectra were processed using the software "BASS Project" (Basic Astronomical Spectroscopy Software), John Paraskeva, as suggested in chapter 7 of the manual « Spectral Atlas for Amateur Astronomers, Richard Walker, Cambridge ».

[13]- "COMMISSIONS 27 AND 42 OF THE IAU INFORMATION BULLETIN ON VARIABLE STARS" Number 5945

[14]- K. D. Andrych, I. L. Andronov, L. L. Chinarova. MAVKA: "Program of Statistically Optimal Determination of Phenomenological Parameters of Extrema". Parabolic Spline Algorithm and Analysis of Variability of the Semi-Regular Star Z UMa. *Journal of Physical Studies* 24(1), Article 1902 [10 pages] (2020) | ADS

[15]- "Binary Maker 3"

[16]- "Kreiner, J. M. 2004, *Acta Astron.*, 54, 207"

[17]- "A Study of the B-V Colour Temperature Relation" Sekiguchi et al (2000).

[18]- "Luxorion"

[19]- "Data from the TESS satellite" (Transiting Exoplanet Survey Satellite)

[20]- "Bob Nelson's O-C files, 2016" [21]- "Physical Nature and Orbital Behavior of the Eclipsing System UZ Leonis"

[22]- G.Pojmanski, *Acta Astronomica* 52, 397, 2002. 2002AcA....52..397P [23]- "ROTSE All-Sky Surveys for Variable Stars. I. Test Fields"

[24]- "P.Ahnert, KVBB N24, 1941.1941KVeBB...6....4A"

[25]- "COMMISSIONS 27 AND 42 OF THE IAU INFORMATION BULLETIN ON VARIABLE STARS Number 6123"

## 20. References CDS Strasbourg :

"2018AJ....156..241H" [ D ,1] Astron. J., 156, 241-241 (2018/November-0) A first catalog of variable stars measured by the Asteroid Terrestrial-impact Last Alert System (ATLAS). HEINZE A.N., TONRY J.L., DENNEAU L., FLEWELLING H., STALDER B., REST A., SMITH K.W., SMARTT S.J. and WEILAND H.

[] "2016IBVS.6164....1N" IAU Inform. Bull. Var. Stars, 6164, 1 (2016/March-0) CCD Minima for Selected Eclipsing Binaries in 2015. NELSON R.H.

"2015IBVS.6152....1H" [] IAU Inform. Bull. Var. Stars, 6152, 1 (2015/October-0) BAV-Results of observations - Photoelectric Minima of Selected Eclipsing Binaries and Maxima of Pulsating Stars. HUBSCHER J.

"2014MNRAS.441..715G [ D ,1]" Mon. Not. R. Astron. Soc., 441, 715-725 (2014/June-2) A mid-infrared study of RR Lyrae stars with the Wide-field Infrared Survey Explorer all-sky data release. GAVRILCHENKO T., KLEIN C.R., BLOOM J.S. and RICHARDS J.W.

"2013AN....334..860A [ D ,1]" Astron. Nachr., 334, 860 (2013) Eclipsing variables: Catalogue and classification. AVVAKUMOVA E.A., MALKOV O.Yu. and KNIAZEV A.Yu.

"2012IBVS.6010....1H [ D ]" IAU Inform. Bull. Var. Stars, 6010, 1 (2012/January-0) BAV-results of observations photoelectric minima of selected eclipsing binaries and maxima of pulsating stars. HUBSCHER J., LEHMANN P.B. and WALTER F.

"2011BAVSM.215....1H [ D ,1]" Berliner Arbeitsgemeinschaft fuer Veraenderliche Sterne - Mitteilungen, 215, 1-15 (2011) BAV-Results of observations - Photoelectric minima of selected eclipsing binaries and maxima of pulsating stars. HUEBSCHER J.

"2011BAVSR..60....9M [ O ]" BAV Rundbrief, 60, 9 (2011/March-0) IT Her - ein W-UMa-Stern mit periodenaenderung. MAINTZ G.

"2011IBVS.5984....1H [ D ,13]" IAU Inform. Bull. Var. Stars, 5984, 1 (2011/April-0) BAV-results of observations photoelectric minima of selected eclipsing binaries and maxima of pulsating stars. HUBSCHER J.

"2009AJ....138..466H [ D ,1]" Astron. J., 138, 466-477 (2009/August-0) Automated variable star classification using the Northern Sky Variability Survey. HOFFMAN D.I., HARRISON T.E. and McNAMARA B.J.

"2009IBVS.5874....1H [ D ]" IAU Inform. Bull. Var. Stars, 5874, 1 (2009/January-0) BAV-results of observations photoelectric minima of selected eclipsing binaries and maxima of pulsating stars. HUBSCHER J., STEINBACH H.-M. and WALTER F.

"2007IBVS.5802....1H []" IAU Inform. Bull. Var. Stars, 5802, 1 (2007/October-0) Photoelectric minima of selected eclipsing binaries and maxima of pulsating stars. HUEBSCHER J.

"2006MNRAS.368.1757W []" Mon. Not. R. Astron. Soc., 368, 1757-1763 (2006/June-1) A catalogue of RR Lyrae stars from the Northern Sky Variability Survey. WILS P., LLOYD C. and BERNHARD K.

"2004AcA....54..207K [ D ,1]" Acta Astron., 54, 207-210 (2004) Up-to-date linear elements of eclipsing binaries. KREINER J.M.

"2003CoSka..33...38P []" Contr. Astron. Obs. Skalnaté Pleso, 33, 38-70 (2003) Catalogue of the field contact binary stars. PRIBULLA T., KREINER J.M. and TREMKO J.

"2003IBVS.5438....1D []" IAU Inform. Bull. Var. Stars, 5438, 1 (2003/July-0) 162-nd list of minima timings of eclipsing binaries by BBSAG observers. DIETHELM R. "2001IBVS.5027....1D []" IAU Inform. Bull. Var. Stars, 5027, 1 (2001/February-0) Times of minima of eclipsing binaries from ROTSE1 CCD data I: named variables. DIETHELM R.

"2000AJ....119.1901A [ D ,1]" Astron. J., 119, 1901-1913

(2000/April-0) ROTSE all-sky surveys for variable stars. I. Test fields. AKERLOF C., AMROSE S., BALSANO R., BLOCH J., CASPERSON D., FLETCHER S., GISLER G., HILLS J., KEHOE R., LEE B., et al.

"1999IBVS.4663....1D [T ]" IAU Inform. Bull. Var. Stars, 4663, 1-2 (1999/January-0) New CCD-lightcurve and improved elements of IT Herculis. DIETHELM R.

"1996AJ....112.2769S []" Astron. J., 112, 2769-2785 (1996) The Behlen Observatory variable star survey. IV. SCHMIDT E.G. and SETH A.

"1992JAVSO..21...16R []" J. Am. Assoc. Variable star obs., 21, 16-19 (1992/June-0) CCD observations of short-period variables at Middlebury College RATCLIFF S.J. and COLLINS J.M.

<u>Dates</u>	<u>Phenomenon Observed</u>	<u>Instrument</u>	<u>Epoch of Minimum</u>	<u>O-C</u>	<u>Sources</u>
22/07/2022	Min. primary	T50	2459763.4684	- 0.0173	G Samolyk JAAVSO 51
27/08/2022	Min. secondary	OMSJ	2459819.6358	- 0.0110	This study
02/09/2022	Min. → Maximum	OMSJ	Not calculable		
18/05/2023	Min. sec. → Maximum	OMSJ	2460083.6847	- 0.0118	This study
09/07/2023	Min. secondary	T50	2460148.5127	- 0.0189	G Samolyk JAAVSO 52
12/07/2023	Max.	OMSJ	Not calculable		
03/10/2023	Max. →/Minimum	OMSJ	Not calculable		
04/10/2023	Max.	OMSJ	Not calculable		

**Table 2. Table of Observations**

	PHOTOMETRY			Surface Temperature
Date	B	V	B-V	Cal. Moy.
T-50-2022-07-02		12.34		
OMSJ-27/08/2022		12.49		
OMSJ-02/09/2022	13.56	12.43	1.13	4600
OMSJ-18/05/2023	13.33	12.43	0.90	5062
OMSJ-19/05/2023	13.55	12.53	1.02	4820
T-50-2023-07-09		12.88		
OMSJ-12/07/2023		12.36		
OMSJ-03/10/2023	13.41	12.44	0.97	4921
OMSJ-04/10/2023	13.33	12.37	0.96	4936
Temp. average::				4868 Kelvin

Table 3: Calculated average surface temperatures of the star.

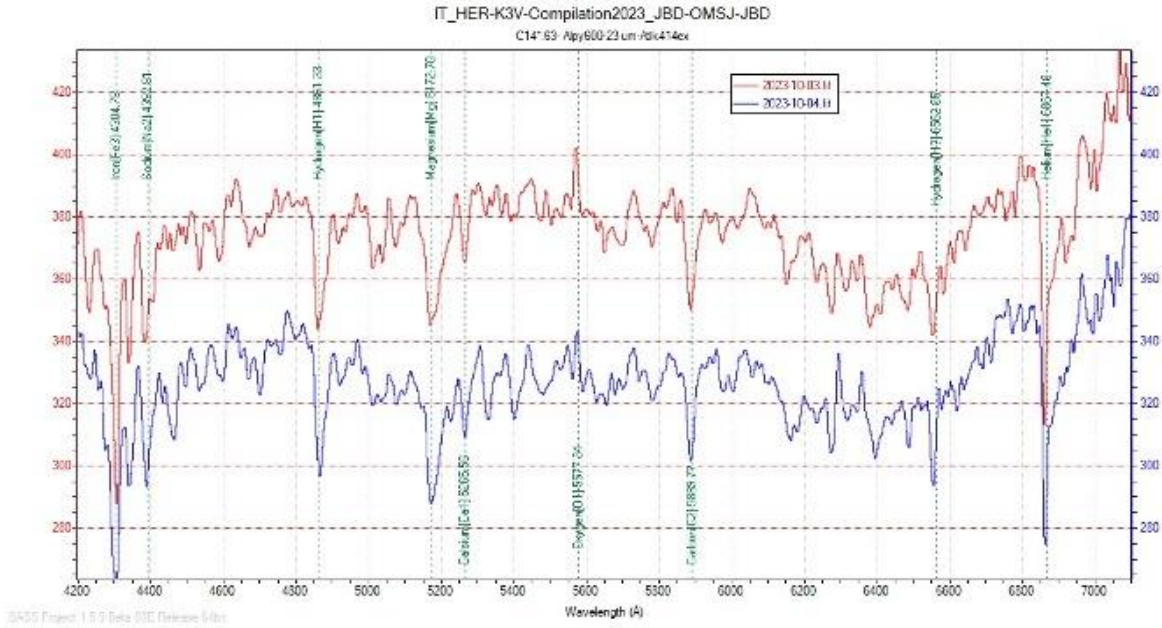


Figure 21 – Compilation of 2023-20-03 and 2023-10-04

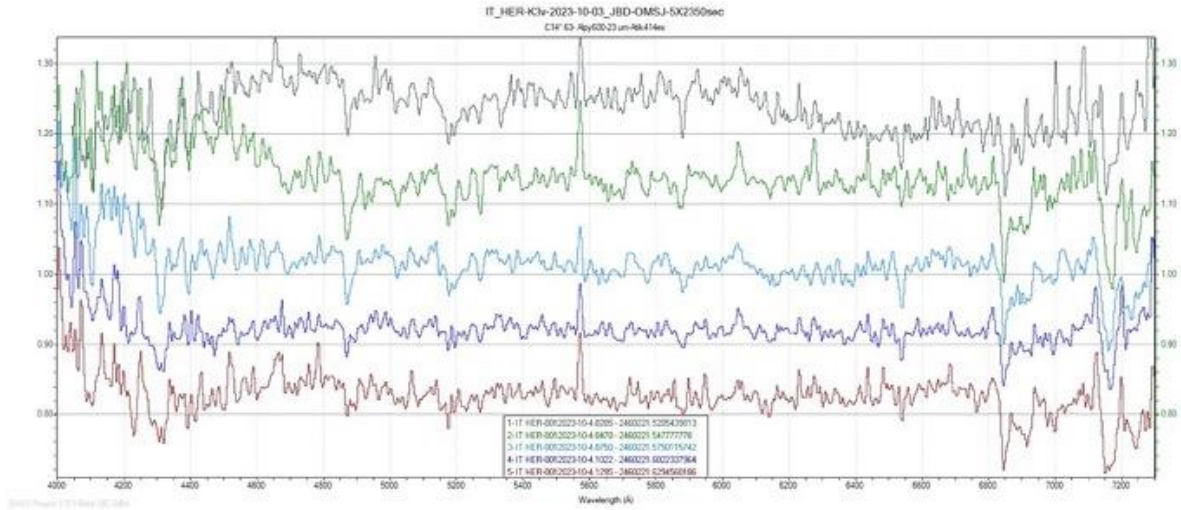


Figure 22 – Compilation of spectra carried out during the night of 2023-10-03 to 2023-10-04

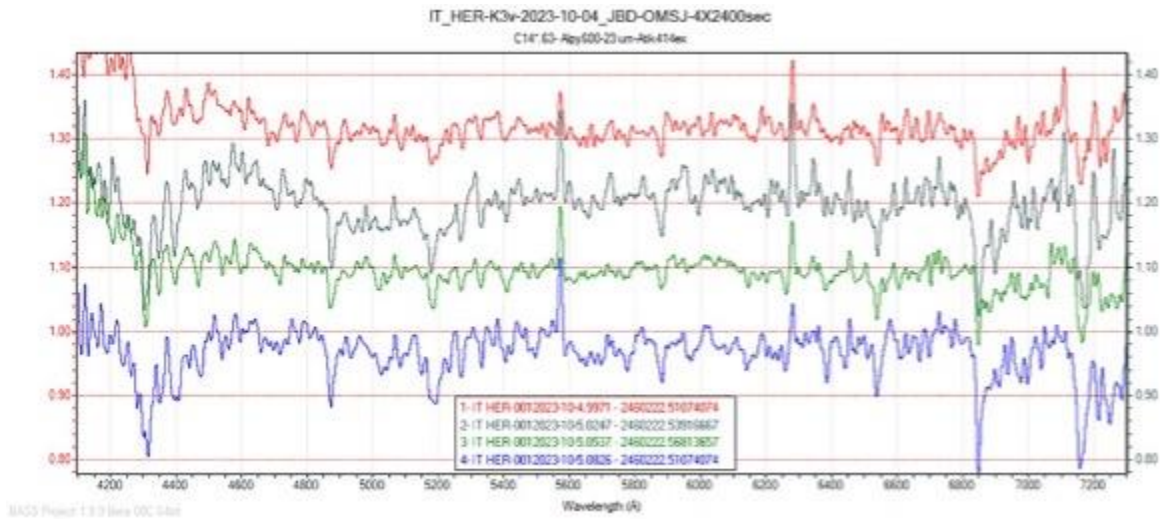


Figure 25 – Compilation of spectra taken during the night from 2023-10-04 to 2023-10-05

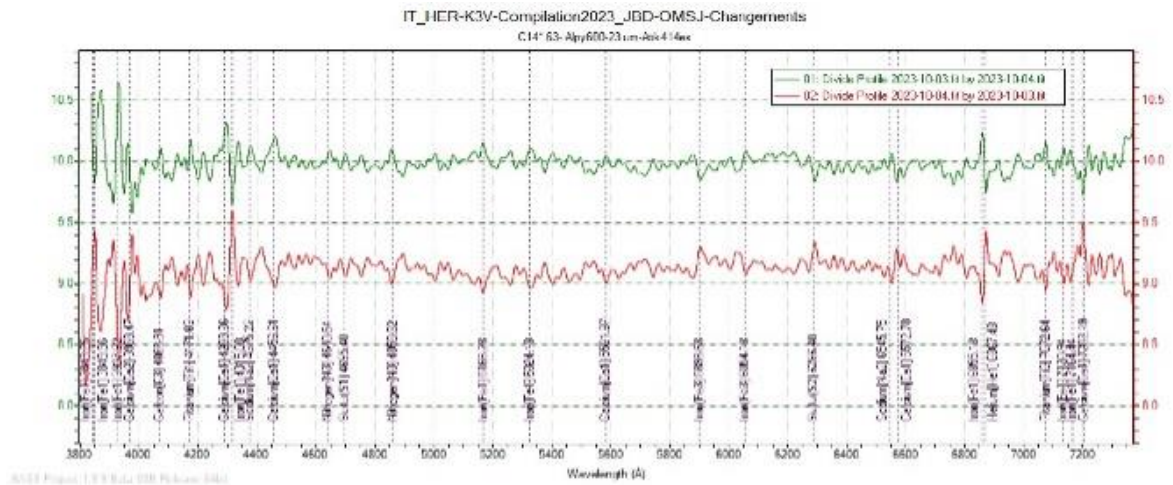


Figure 28 – Graph showing the changes between the profiles of 03 and 04-10-2023.

# A Period Analysis of DY Pegasi, an SX Phoenicis Star

David Bautista

Mt. San Antonio College

1100 N Grand Ave. Walnut, CA 91789

dbautista24@mtsac.edu

---

## Abstract

Presented here are the CCD photometric measurements of the SX Phoenicis star DY Pegasi taken on three separate nights of observation over the course of two months. These photometric measurements were then calibrated, aligned, and measured the change in flux of DY Peg relative to stable comparison stars through the program AstrolmageJ. The lightcurves generated from each night then had their periods measured to provide a range in period to compute a refined period of 0.073308 days through the program VStar. An Analysis of Variance, or ANOVA, test was also performed on VStar returning a p-value less than 0.000001 indicating statistical significance in addition to visually evaluating how well the computed period fit the collated data by generating a phase plot through VStar. Although the difference is minimal, the computed period of 0.073308 days does differ from the well-established period of 0.0729261 days but the overall shape of the lightcurve remains consistent with rapid increase and a more gradual decrease in flux. Further observations from multiple institutions are necessary in order to carefully monitor the period of DY Peg to corroborate this observed increase in period or perhaps any other changes.

---

## 1. Introduction

DY Pegasi (DY Peg) is a known SX Phoenicis star, a type of variable star considered to be the  $\delta$  Scuti stars of Population II and old disk population (L.J. Li and S.B. Qian 2010). SX Phe stars tend to display high amplitudes over a short period, typically smaller than 0.08 days (ibid). DY Peg in particular has a magnitude range of 10.00-10.56V over a period of 0.0729261 days with a right ascension of 23:08:51.19 and a declination of +17:12:56.0 according to the American Association of Variable Star Observers (AAVSO 2023). The reason behind DY Peg's cyclical change in magnitude is the result of a periodic expansion and contraction due to the imbalance between DY Peg's radially inward gravitational force and the outward force produced by nuclear fusion.

Since the initial discovery of DY Peg's variable nature by Morgenroth in 1934, the period of DY Peg has been the subject of numerous studies and remains one of 13 known field SX Phe stars (J. N. Fu et al 2009). Additionally, DY Peg is also believed to have a companion though the identity of this companion remains the subject of debate. The two most likely identities of this companion are a brown dwarf (L.J. Li and S.B. Qian 2010) or a hot white dwarf (H.-F. Xue and J.-S. Niu 2020). By continuing to study the magnitude range and period of DY Peg, more information can be ascertained that may lead to a more comprehensive understanding behind the evolution

and behavior of SX Phe variable stars.

## 2. Observations

Over the course of seven weeks, from October 11th through November 22nd, three nights were taken to gather photometric data on the target star DY Peg from the Mt. San Antonio College Observatory in Walnut, California. The equipment used to collect photometric data on DY Peg consisted of the Mt. SAC Observatory's 406.4 mm Meade RCX400 Schmidt-Cassegrain telescope with a focal length of 3251 mm. The camera model used was the SBIG STL 6303-E, a charge-coupled device that has a gain of 1.4 e-/ADU, a readout noise of 13.5 e-, and a dark current of 0.3 e-/pix/sec. However, in order to account for the introduction of noise from operating the camera shutter or from maintaining an open shutter during longer exposures, a set of calibration frames were taken at a temperature of -9.8 degrees Celsius and applied during the processing stage. For each night of observation, a series of nine frames was taken for each type of calibration frame: three second flat frames with a light panel and a Johnson V filter, 40 second dark frames, and bias frames. Afterwards, a series of 115–120 light frames of DY Peg were taken with the Johnson V filter and an exposure of 40 seconds, with each observation session lasting around two hours.

After a complete observation session, the light frames are then aligned, inspected for unwanted sources of light, have the calibration frames applied,

and analyzed using aperture photometry with the program AstroImageJ. Before analyzing every calibrated light frame, four comparison stars within the star field around DY Peg were selected through the use of the Aladin Sky Atlas and confirmed to be stable stars through the SIMBAD Astronomical Database. See Table 1 for the list of chosen comparison stars.

AstroImageJ then used the stable comparison stars and measured the difference in the relative flux of DY Peg relative to the comparison stars for every light frame to create a light curve. However, since the light from these comparison stars must travel through different amounts of air as the observation night progresses, the flux of each comparison star was detrended. See Figures 1 and 2.

Label	Comp Star ID	Right Ascension	Declination
C2	HD 218587	23:09:05.051	+17 08 20.76
C3	GSC 01712-01246	23:08:40.548	+17 08 14.41
C4	GSC 01712-00542	23:08:51.523	+17 10 49.15
C5	TYC 1712-1110-1	23:09:21.601	+17 09 22.03

**Table 1.** A table of the comparison stars used.

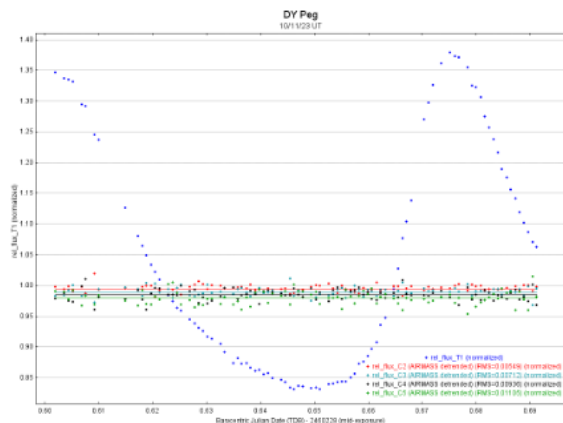


**Figure 1.** Lightcurve of DY Peg October 11th, 2023.

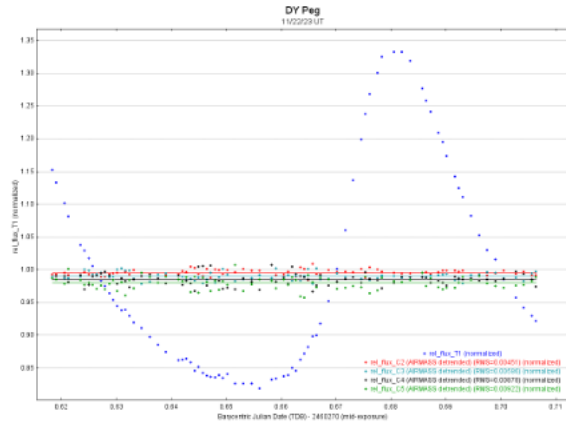


**Figure 2.** Lightcurve of DY Peg November 22nd, 2023.

The resulting Measurements file from each night of observation was opened using the Notepad program and loaded into an Excel spreadsheet. The individual spreadsheets of data from each night of observation were compiled into a new spreadsheet by loading the Barycentric Julian Date, the relative flux of DY Peg, and the relative flux error from each night in chronological order. The spreadsheets of data from each individual night were read by the VStar (Benn, D. 2012) program to obtain an overall mean for the period. The spreadsheet containing the organized data from every night can be analyzed by VStar in tandem with the mean of the period to get a refined period. The newly determined period's fit to the overall data was tested by creating a phase plot and applying the new period's value. Finally, an Analysis of Variance, or ANOVA, test was performed to determine the statistical significance of the calculated period measurement.

### 3. Results

The data gathered from each night of observation were analyzed through the use of VStar to determine the period of DY Peg for their respective night. The periods of three individual nights were averaged to calculate an overall mean period of 0.074236667 days. However, in order to obtain a more accurate measurement of the period a Date Compensated Discrete Fourier Transform with period range was applied to account for the amount of time between each night of recorded data. The parameters used were a low period of 0.072 days and a high period of 0.076 with a resolution of 0.000001 days, which re-turned a period value of 0.073308 days. See Figure 3.



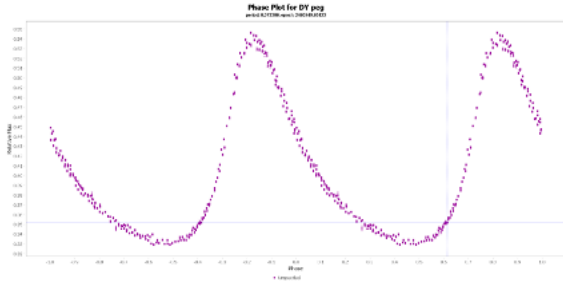


**Figure 3. DY Peg phase plot 0.073308 day period.**

To evaluate how well the new calculated period fits the data from every night, a phase plot was made with the new period applied as seen in Figure 3. Furthermore, an ANOVA test was also performed and returned a p-value less than 0.000001 meaning the period measurement is statistically significant. The computed period of 0.073308 days is larger than the reported period of 0.0729261 days according to AAVSO (AAVSO 2023).

#### 4. Conclusions

Upon visual examination, the light curve of DY Peg as seen in Figure 1 and Figure 2 has a steeper incline when approaching a peak, indicating that DY Peg increases fairly quickly in flux. However, DY Peg shows a more gradual decrease in flux when approaching a minimum and remains at a lower flux for longer before rapidly increasing again. As previously mentioned, the determined period of 0.073308 for DY Peg is marginally larger than the commonly reported period of 0.0729261. The determined period was computed from very recent data while the aforementioned accepted period of DY Peg was reported from 2009. In order to confirm or contradict the computed period, additional observations must be made from other institutions in order to establish whether or not the period of DY Peg has in-creased. By making additional observations, a more comprehensive model can be made for the overall behavior of other SX Phe type stars,

specifically how the period of SX Phe stars may change over time. Additionally, other observational methods are necessary in order to identify the companion for DY Peg. Currently, one possible identity of this companion is most likely a brown dwarf of around  $0.028 M_{\text{Sun}}$  at an orbital inclination of 90 degrees (L.J. Li and S.B. Qian 2010). The other possible identity of this companion could be a hot white dwarf due to the detection of  $\alpha$ -elements calcium, sulfur and an excess of carbon through spectroscopic observations of DY Peg, these elements cannot be generated by a brown dwarf throughout its evolutionary history (H.-F. Xue and J.-S. Niu 2020). Future observations must have more precise photometric observations, spectroscopic observations, and observations within the infrared spectrum to rule out either possibility of the companion object's identity.

#### 5. Acknowledgements

This research has made use of the International Variable Star Index (VSX) database, operated at AAVSO, Cambridge, Massachusetts, USA. This research has made use of the Aladin Sky Atlas, operated at CDS, Strasbourg, France. This research has also made use of the SIMBAD astronomical database, operated at CDS, Strasbourg, France.

#### 6. References

- American Association for Variable Star Observers 2016, The International Variable Star Index, **v1.1**, 140.144.129.16
- J. N. Fu, et al. 2009, *PASP*, **121**, 87
- L.J. Li and S.B. Qian. 2010, *AJ*, **139**, 2639
- H.-F. Xue and J.-S. Niu. 2020, *ApJ*, **904**, 5
- Benn, D. 2012, *JAAVSA*, **40**, 852

# ZTF: Disambiguate variables through follow-up

*Ashish Mahabal, ZTF, Caltech*

---

## Abstract

The Zwicky Transient Facility (ZTF) has been publishing classifications for the Northern sky from its observations with the 1.2m Oschin telescope in the  $g/r/i$  bands. Hundreds of points over the last few years provide fertile ground for computing many statistical features. We use XGBoost and DNNs on these features for our classifications. While we get many secure classifications leading to excellent science, there are also a large number of sources whose classification stays ambiguous. Targeted observations of these over a period can help disambiguate their classifications and help push the boundary of our understanding and towards completeness of populations. There is also the possibility of discovering rare outliers - either within a class, or an entire new subclass. A fraction of these sources are bright enough to be within the reach of small-telescopes. We describe the entire process and point to resources and code that will enable researchers to pick subsets of such objects to get additional observations. This also has a potential impact on future surveys like Rubin/LSS

---

# Optical SETI searches: Amateur's inside track?

Richard H. Stanton  
Jet Propulsion Laboratory, retired  
1429 Shay Road, Big Bear City, CA 92314  
rhstanton@gmail.com

---

## Abstract

The absence of any confirmed signal from extraterrestrials, despite 60 years of searching, can be attributed to two possibilities: (1) the Earth may not have received any signals we are capable of detecting, or (2) we were simply not looking when detectable signals passed by. Given the sporadic nature of SETI searches to date, particularly in optical wavelengths, the door is wide open to the second possibility. Amateur astronomers equipped with 8" or larger telescopes, capable of finding and tracking bright target stars, could help fill this gap. A telescope equipped with a fast photometer has the potential of finding a SETI signal when no one else is looking. The author has conducted a number of such searches over the past decade, finding numerous "signals" from airplanes, satellites, meteors, sky flashes, and also two interesting "strange" signals. This paper describes a fast photometer designed for these searches using readily available commercial technology. Both the hardware design and the author's search approach are described, in addition to plots typical search results. Since no one can prove what approach aliens might be using to communicate with us, amateur searches looking for signals in fast time-series photometry might well be the first to discover the SETI signal that continues to elude professionals

---

## 1. Introduction

Searches for signals that could be attributed to extraterrestrial intelligence (SETI) began using radio frequencies in the 1960s (Drake) and have continued to emphasize this approach to this day. Searches in optical wavelengths have mostly sought nanosecond pulses that would momentarily outshine the host star, as proposed by Schwartz & Townes (1961) and pursued by Howard (2015) and others. The absence of a successful detection of any signal to date has not diminished enthusiasm for finding new and better ways to search (Tarter et al 2009). Newer pursuits in the visible and near-infrared include mining existing data from major observatories for any signs of extraterrestrial activity (Tellis & Marcy 2017) and proposing dedicated observatories to enable fast, all-sky optical searches (Wright 2020).

With all this activity by SETI scientists, one might feel that there is little room for amateurs to participate in the search. Professional astronomers have the access to large telescopes, sophisticated instrumentation and knowledgeable collaborators who push them to ever increasing insights and discoveries. But since there have been no confirmed SETI discoveries, all current insights *could be wrong!* Perhaps one doesn't need a large radio telescope or sophisticated electronics capable of detecting nanosecond light pulses. What if there are clear signals that could be discovered using simple time-series photometry, but none have been found since no observations were recorded when they occurred? If

that were true, amateur astronomers with their superior numbers of telescopes and clear nights might have the advantage. Suppose that it would take an average of 100,000 hours of searching to find one unambiguous optical signal. This might be accomplished in as little as five years if 200 amateurs around the world each contributed 100 hours of observations per year. In contrast, professionals dedicating 50 nights per year in ten different observatories would require 20 years for a discovery.

This paper describes one path available to amateurs interested in joining this search. Beginning with the "habitable" target stars that can be reached by amateur-size telescopes, the focus shifts to describing a system capable of generating the fast stellar photometry needed (§2). A brief description is given of the author's program that searches these data for "signals" (§3), followed by a few examples of the many fascinating targets found flying over our heads at night (§4).

A key element of this approach is the use of photon counting to achieve low noise, high bandwidth digital data that can be noiselessly re-binned to any needed time resolution. The critical parts of this design, including photomultiplier (PMT) modules, a pulse counting PC board and various mechanical and optical components are readily available from commercial suppliers. Each search involves staring at a target star and recording a time-series of fast photometry that might include a brief signal sent by the star's inhabitants. Since we have no *a priori* knowledge of the time structure of a possible signal,

the generated time-series data are searched for both pulses and periodic variations using the Fast Fourier Transform. Starting with a fast sample rate enables searches over several orders of magnitude in time resolution. Both the data acquisition and subsequent search processes are described, each benefitting tremendously from the capability of modern personal computers.

## 2. Observation approach

### 2.1 Available target stars

Probably the best stars to focus on are those similar to our Sun, a G2V main sequence star. Rather than concentrate only on stars of this spectral class, Turnbull and Tartar (2002) generated a catalog of nearby “habitable stellar systems” over a range of spectral types, called HabCat. Figure 1 summarizes the number of targets listed in this catalog vs. visual magnitude. The top curve gives the number of available HabCat stars as a function of visual magnitude for the entire sky. A somewhat smaller number is available if one is restricted to declinations north of  $-20^\circ$  (lower curve). While some 5000 stars can be seen with the eye ( $V=6$ ) only about 80 of these are in HabCat and even fewer ( $\sim 50$ ) are north of  $-20^\circ$  declination. This number increases rapidly if one includes stars of 7th magnitude ( $\sim 275$ ) or 8th magnitude ( $\sim 1450$ ).

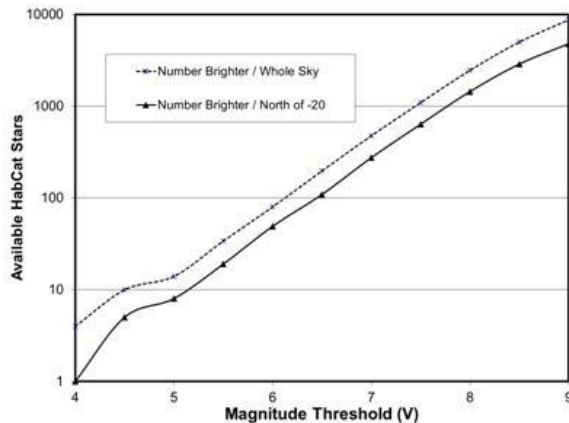


Figure 1. Available target stars vs. magnitude

### 2.2 Photon count rates

The photon count rate expected as a function of star magnitude and telescope aperture is plotted in Figure 2, for a broadband spectral response system. Many signals can be easily detected with a count rate of 100,000/s, depending on several factors. A slowly varying signal ( $<50\text{Hz}$ ) is more likely to be affected by

atmospheric scintillation than by counting statistics, so a lower count rate is fine. At higher frequencies ( $>200\text{Hz}$ ) the atmosphere is often “frozen out”, leaving counting statistics as the limiting noise source. Since this noise is the square root of the count rate, the signal-to-noise ratio improves as a larger telescope is used, increasing the photon rate. Note that a rate limit of 3,000,000/s is suggested since the counting rate becomes increasingly non-linear as the photon pulses overlap. These tubes will be damaged if exposed to room light levels while powered, but the brief appearance of a bright meteor has never resulted in measurable damage in the author’s systems, even when the count rate briefly saturates at 20 million counts per second.

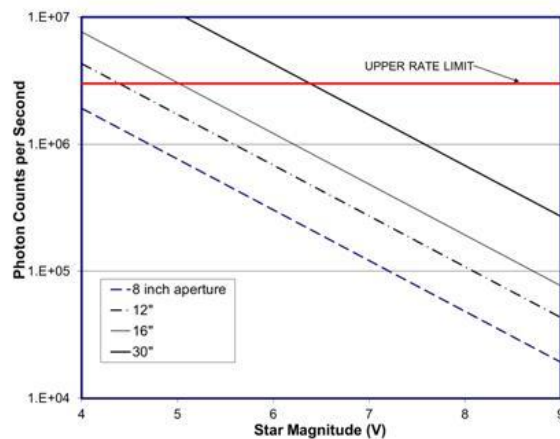


Figure 2. Photon count rate vs. telescope aperture

The conclusion from these figures is that even an 8-inch aperture will have hundreds of candidate stars to observe at a count rate of 100,000/s or more. Larger telescopes can reach many more stars, some at significantly higher count rates. Moonlight and sky background generally add little to the starlight signal since they are more diffuse than the incoming starlight. This implies that nights of good seeing that are too bright for deep sky observing can often be used for SETI searches.

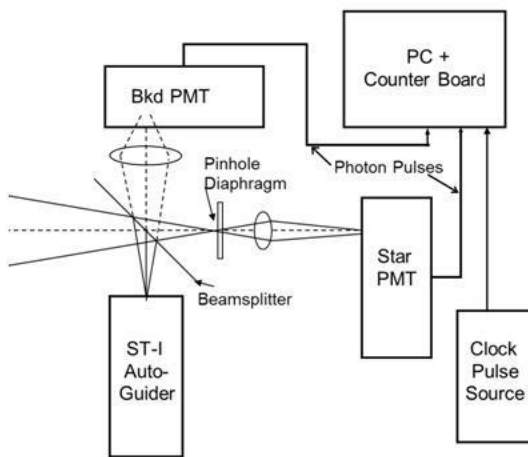


Figure 3. Basic 2-channel system

### 2.3 Photometer

The 2-channel photometer schematic in Figure 3 is a simplified version of the 3- and 4-channel systems used by the author Stanton (2015). This simplification allows most of the star's light to be directed into a single channel, maximizing its measured photon rate. The second channel (Bkd), measures light from a disk of sky immediately surrounding the target star, reflected by the shiny metal around the pinhole. This Bkd signal can be extremely helpful in determining whether a detected signal originated from the target star or from something else. The author also uses simultaneous photography of a one-degree field around the target star during observations to help identify nearby targets. Although sometimes very helpful, this additional capability is not required for the basic system.

Light entering the photometer first encounters a beamsplitter that directs 10 to 20% to the autoguider. I use an SBIG ST-i for the guide function. Since these are no longer manufactured, any autoguider compatible with the telescope control system should work. Note that the entire system, PMTs, diaphragm, relay optics and autoguider form an integrated, rigid structure, assuring that the calibration between the autoguider coordinates and the light incident on the PMTs remains fixed. After passing through the beamsplitter, light is focused on the pinhole diaphragm. I use a relatively large diaphragm, 41arcsec diameter, to avoid modulating the star's light due to tracking wander. Pinholes mounted on supporting disks are available in a variety of sizes. Light reflected around the pinhole is focused on the second PMT to measure the sky background (Bkd).

While this reflection is not of optical quality, it provides a good measure of background field immediately surrounding the diaphragm.

Photon pulses from both PMTs are routed to a single counter board in a dedicated PC with solid state drive. I use 50' BNC cables to conduct the individual photon pulses from the telescope to the counting system in a separate building. An oscillator chip and a few digital chips can provide the clock pulses—no need to purchase an expensive pulse generator. A single 10 kHz clock pulse terminates the count samples for all channels simultaneously. This means that all observations accumulate count samples 100 $\mu$ s long regardless of whether the observation is looking for extraterrestrial signals, monitoring an eruptive variable star or simply measuring a star's brightness and color! This may seem irrational, but the fact that all data are integer counts measured without any analog electronics (no amplifiers or A/D conversion) implies that they can be noiselessly added together to create new time series with resolution any multiple of 100 $\mu$ s. The computer and counter board may be working harder than necessary to produce files when this resolution is not needed, but they don't complain. Having extra time resolution available when it is needed can be invaluable.

#### 2.3.1. Commercially available components

Previous systems using earlier versions of the counter board and computers with mechanical hard drives occasionally crashed unexpectedly, particularly when bright stars were observed. The present system has never experienced such a failure in over five years of operation, even when three of the four channels are generating pulses at several million counts per second.

An important aspect of this design is that it can be assembled using commercially available components:

1. **Photomultiplier modules:** Hamamatsu H8259-2 photon counting modules incorporate photomultiplier tube, high-voltage supply and preset pulse amplifier/discriminator in a small 4x5x10cm box. Connect 5V and you have photon pulses!

2. **Counter board:** National Instruments NI 6612, inserted in a Dell XPS computer with solid-state "hard drive". NI software stores count samples in the drive, which are then automatically transferred to several files after each observation (this takes some time, but can be done in parallel with the next observation). This system has never crashed during an observation (but does fail if you forget to turn on the PMT module power or clock pulses!)

3. **Optical and mechanical parts:** Edmund Optics has a wide range of compatible mechanical components, lenses, diaphragm, filters, beam-splitters

and housings that provide essentially all the components for the author's three- and four-channel systems. The only custom parts needed have been the interfaces to the telescope focuser and to the photomultiplier modules. A selection of these components and two Hamamatsu PMT modules are shown in Figure 4.

### 3. Searching for signals

The following discussion shifts to experience with the author's system, a four-channel photometer (colors Y, B, CLR and Bkd) pictured in Figure 5. The photometer is located at the prime focus of a 30" Obsession Dobson modified for closed-loop tracking using a ServoCat and ST-i autoguider. It should be emphasized that a 30-inch telescope and a four-channel photometer are NOT needed to achieve data that is entirely adequate for optical SETI searches.



Figure 4. Typical system components

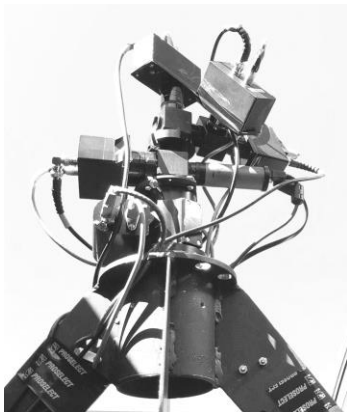


Figure 5. 4-channel photometer at focus of 30" scope

### 3.1 Data processing

Analyzing the large quantity of data generated is not as daunting as might appear. A single program was written to search these data and generate a one-page summary of everything found that might be of interest.

The program proceeds treating all channels identically, including Bkd:

1. Bin the original time-series into six new series, each with samples four times longer than its predecessor. This produces 7 time-series for each channel with 100 $\mu$ s to 0.4096s samples.

2. Search each series for pulses (positive and negative) and save the two largest for each bin level

3. Convert each series into a frequency spectrum using the Fast Fourier Transform and multiple 50% overlaps to reduce noise

4. Eliminate atmospheric power using a running average and search each spectrum for the two largest peaks

5. Summarize everything found versus bin level in a single page summary for each star

6. Generate additional files for display, such as a plot of all data at one second resolution for a "quick look", power spectra both before and after removal of atmospheric power, and 6.4ms binned data that can be easily plotted for a closer look at possible signals.

All this processing takes place automatically and fairly quickly. A run analyzing a night's data of four stars = 3360s x 4 channels x 10,000points/s x 4 stars = 537.6 million data points, typically takes less than 10 minutes processing time on a standard Dell XPS computer.

The most challenging part of this process comes next (Stanton 2019). Since any part of the original series can be examined at any desired time resolution, one is tempted to look at each detected pulse to see if it is interesting. This can be very time-consuming. The opposite extreme is to decide that nothing is very interesting and possibly ignore a real signal. The strange pulses in Figure 11 were originally written off as "birds". It wasn't until nearly five years later, when another similar signal was found, that it became clear that these pulses could not have been made by birds. One needs to be cautious since some of the most interesting signals are often easy to ignore.

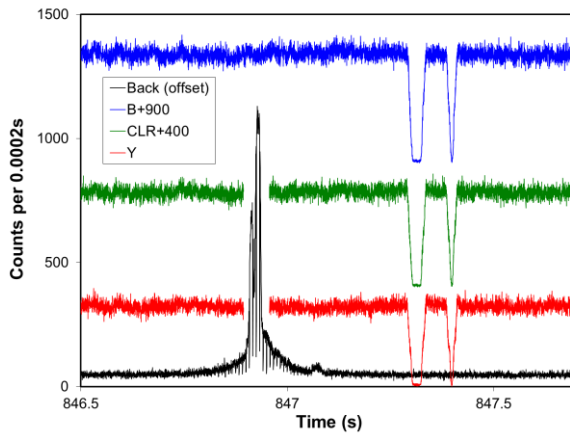


Figure 6. Airplane passage

#### 4. Typical “signals”

The following figures show a few of the myriad of “signals” that appear in the night sky. Figure 6 shows a typical airplane passage where both the wing and stabilizer completely block out the target star’s light. As is usually the case, the Bkd channel picks up one or more of the planes lights during the passage. The Bkd signal has been offset in time for clarity. Note that none of this intense flash is picked up in the color channels, as is usually the case. Since signals such as these distort both the time and frequency searches, the search program is re-run using sections of the time-series that don’t contain the airplane passage.

Figure 7 illustrates the passage of an illuminated satellite directly through the 41arcsec diaphragm and surrounding Bkd field. These events are becoming more common with the huge number of satellites being launched (60,000?) for worldwide internet. The satellite first produces a signal as it passes through the Bkd field that then disappears as the satellite enters the diaphragm. This type of signal also upsets the automatic search program and is avoided in the search process.

Figure 8 shows a Perseid meteor passing through the Bkd field and diaphragm at  $\sim 30^\circ/s$ . The traces have been offset in time for clarity. If a small object moves from the Bkd channel to the diaphragm, the Bkd signal is usually about 5% of the sum of the three star channel’s response, as in Figure 7. But the peak Bkd intensity in Figure 8 is much brighter than this, implying that only a portion of the meteor’s light was captured in the diaphragm. This might be due to a near miss or perhaps the size of the meteor fireball was larger than the diaphragm. Note also that both traces fade “slowly” due to a fading vapor train.

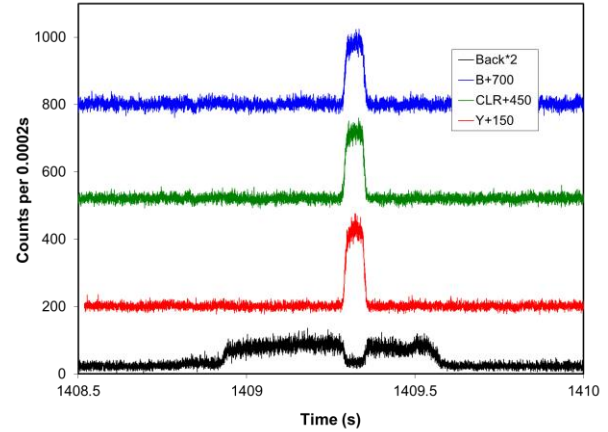


Figure 7. Satellite central passage through photometer

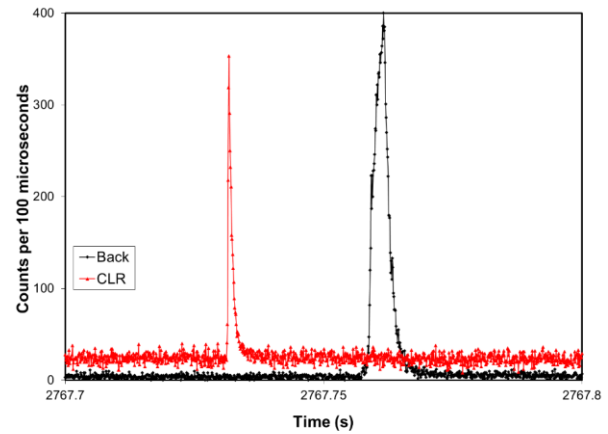


Figure 8. CLR & Bkd channels of Perseid meteor

Figure 9 illustrates the power of seeking signals in the frequency domain. This spectrum of the Crab Pulsar was calculated using its B-channel time-series signal of 59 photons per second against a background (skylight, moon and nebula) of 6000/s. Although there was no chance of detecting this signal in the time domain (without *a priori* knowledge of its frequency), it is clearly visible in this spectrum, calculated by summing 731 individual, noisy spectra. The spectrum shows that a 29.64Hz signal is present with many harmonics, indicating a waveform that deviates significantly from a sinusoid.

Once the fundamental frequency is determined using the spectrum, it is possible to display the signal in the time domain by adding up 70,000 time-slices, each corresponding to one rotation of the pulsar. After some iteration to get the exact frequency, the final light curve emerges (Figure 10). Note that its non-sinusoidal shape is clear, even though the peak amplitude of the curve is only 0.3 photons per 0.5ms above the background.

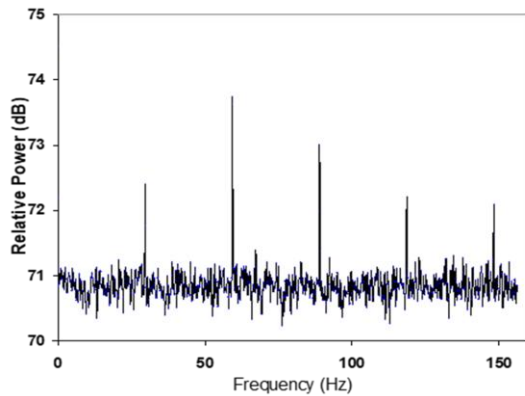


Figure 9. Crab Pulsar Spectrum

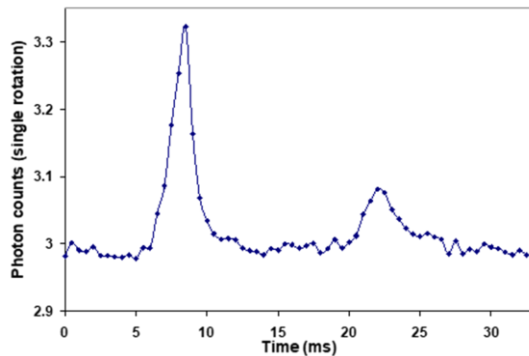


Figure 10. Crab Pulsar time-domain waveform

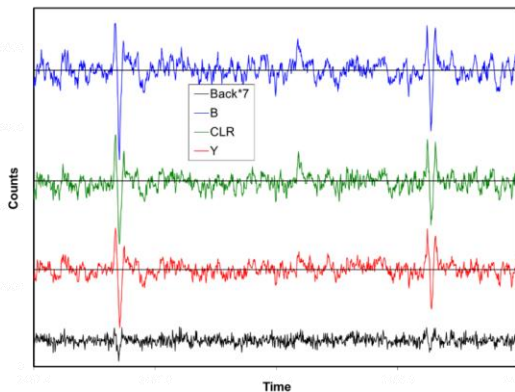


Figure 11. Strange pulses in the light of HD217014

The final example, Figure 11, shows two strange pulses that have not yet been fully explained. These pulses were first seen in 2019 and largely ignored until a very similar event was detected observing a different star in 2023. A separate paper is planned to describe these signals and possible explanations of how they were generated.

## 5. Conclusion

The pursuit of unknown signals using high-speed photon counting certainly can be challenging, but well worth it to those who are appropriately inclined:

*“One must not pursue goals that are easily achieved. One must develop an instinct for what one can just barely achieve through ones greatest efforts.”*

--Albert Einstein

*“We can’t predict when a signal will be found, only that it won’t be found if we don’t look”*

--Jill Tarter

*“One must not do comet hunting for the find; one must be satisfied with the search”*

--David Levy

## 6. References

Drake, F.D., How can we detect radio transmissions from distant planetary systems? *Sky & Telescope* 19 (1960) 140.

Howard, B., Optical SETI using a 3 beam coincident photometer, *Proc. 34th Annual Symposium on Telescope Science, Ontario, CA, (2015) pp 79-82.*

Schwartz, R.N., C.H. Townes, Interstellar & interplanetary communication by optical masers, *Nature* 190 (1961) 205.

Stanton, R.H., Triple Photometer: design and initial results, *Proc. 34th Annual Symposium on Telescope Science, Ontario, CA, (2015) pp 69-77.*

Stanton, R.H., Exploring optical SETI’s middle ground, *Acta Astronautica* 156 (2019) 92-99.

Tarter, J, et al., Advancing the search for extraterrestrial intelligence, SETI Institute (2009) [https://henry.pha.jhu.edu/Tarter\\_SETI\\_PSF.pdf](https://henry.pha.jhu.edu/Tarter_SETI_PSF.pdf).

Tellis, N.K., G.W.Marcy, A search for laser emission with megawatt thresholds from 5600 FGKM Stars, *AJ* 153 (2017) 251.

Turnbull, M.C., J. Tarter, Target Selection for SETI: A catalogue of nearby habitable stellar systems, (2002), <https://arxiv.org/pdf/astro-ph/0210675.pdf>.



Wright, S.A. et al, Panoramic SETI: An all-sky fast time-domain observatory, Astro2020 APC, <https://assets.pubpub.org/g7h2fy6z/31598545737208.pdf>.

# Observing the O’Connell Effect in Eclipsing Binary Stars

Eric R. Craine

Western Research Company, Inc. and GNAT, Inc.  
4681 N Cerritos Drive, Tucson, AZ 85745  
ercraine@wrc-inc.com

---

## Abstract

This document is a brief summary of an oral/Powerpoint presentation by the author at the annual SAS Symposium of 2024 June 20-22. The goal of the presentation is to summarize aspects of the O’Connell effect, considered by many to be one of the most important remaining puzzles of the manifestation of certain close eclipsing binary stars, and to encourage collaborative observation of a sample of these stars under study by the Global Network of Astronomical Telescopes (GNAT).

---

## 1. Introduction

As early as 1906 note had been made in the astronomical literature to the effect that absolute dimensions of a close binary-type variable star might be determined as a result of detailed knowledge of the system orbit and the precise light travel times associated with that orbit (Roberts 1906). In his development of the mathematics of such a solution he noted that “the eclipse alone would not always account for all of the phenomena of variation”. Specifically, two stars that he studied, *U Pegasi* and *RR Centauri*, showed “distinct evidence....of two unequal maxima”. Roberts attributed these observations to tidal distortion of the stars near periastron resulting from elliptical orbits.

Unequal maxima following either or both the primary and secondary eclipses seen in some close binary stars are known to be relatively frequent though still rather confounding phenomena (Knote et al. 2022). This phenomenon is now known as the O’Connell effect in recognition of early pioneering work of O’Connell (1951), in which he attempted to quantify the effect and studied its amplitude as a function of color. His stellar samples for the 1951 study were quite constrained however and did not include stars for which the effect can be profoundly variable, nor did he include W UMa type stars for which the stellar components exhibit strong effects on one another.

Among the parameters used to characterize this effect is delta-m, the magnitude difference between successive maxima, also sometimes known as the O’Connell Effect Size (OES) (as distinguished from  $\Delta m$  the instantaneous differential magnitude of the star). It is interesting that many of the stars for which the O’Connell effect were studied in the earlier papers,

and even in many instances in modern papers, exhibit a very small, barely discernible OES. In fact, the effect can be astonishingly large (see Figure 1).

Not only can the O’Connell effect be quite large, but it can vary substantially and in several ways. O’Connell’s original studies focused on systems for which the effect was static with time, but, in fact the amplitude of the effect can change significantly over time frames of days or weeks, which in many phased curves calculated over many cycles results in phased light curve maxima that look at first to be extremely noisy, but simply reflects the temporal variation in the maxima. Further, the variation of the O’Connell effect can take place not just in the amplitude of the maxima, but also in the shapes of the maxima. For example, compare Figure 2 with Figure 1.

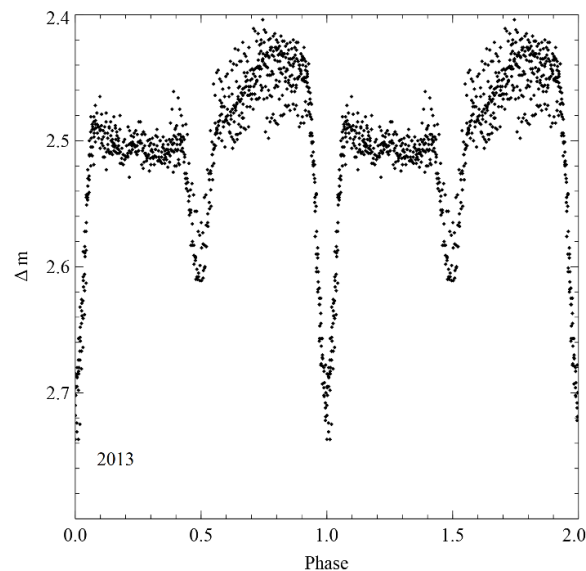


**Figure 1. A phased lightcurve of MG1-1995959 obtained during 2013 (Goodricke-Pigott Observatory).**

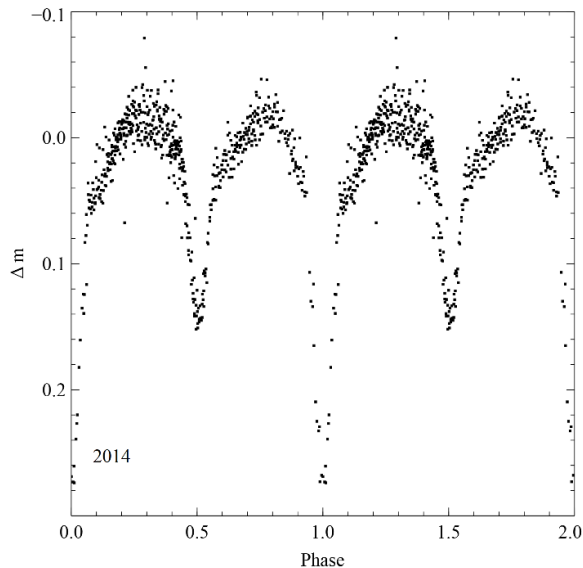


**Figure 2. A phased lightcurve of MG1-1995959 obtained during 2014 (Goodricke-Pigott Observatory).**

The 2014 observations of Figure 2 are not only of significantly different OES, or delta-m, they also have a completely different morphology.

An important challenge for these stars is to determine the mechanism(s) that give rise to these asymmetrical light curves during maxima. The ellipsoidal shape of the stars in elliptical orbits which might show such effects at periastron, as originally proposed in Robert's paper, fails to explain the phenomenon in circular orbits. This is especially problematical as one expects older contact binary systems to have long since circularized their orbits.

Among other explanations that have been fielded are star spots, mass exchange impacts, and circumstellar disks. The invocation of star spots as a source of asymmetrical maxima was especially popular during the late 20<sup>th</sup> century. More recent studies cast doubt on star spots as a unique or universal source of the O'Connell effect; c.f. Wilsey and Beaky (2009).

The current state of confusion and controversy with respect to the O'Connell effect renders it an interesting and important study. Because of a wide variety of close binary systems giving rise to the effect it is necessary to characterize as many of these stars as possible over extended periods of time. Of considerable assistance here is the use of various photometric sky surveys. The star in Figures 1 and 2 is just one example of many such stars found in the MOTESS-GNAT Variable Star Catalogs (c.f. Kraus et al. 2007 and Craine et al. 2021). The virtue of these

data is that they span a period of over 20 years and are very helpful in selecting candidates for follow-up observation.

More comprehensive space-based surveys have recently begun to provide valuable coverage of such candidate stars as well. Notable are *Kepler* observations of Knote et al. (2022) which yielded a Kepler Eclipsing Binary Catalog (KEBC) containing 2,907 eclipsing binaries, of which 212 (7.3%) were found to exhibit the O'Connell effect.

## 2. GNAT Collaborations

Because a variety of types of stars exhibit a range of behaviors collectively grouped as the O'Connell effect, it is necessary to collect a large amount of varied data to facilitate their interpretation. The data needed fall into two broad categories: 1) comprehensive sets of time series photometry, and 2) spectra suitable for spectral classification and radial velocity measurements. The former can be provided by collaborating small telescope operators; the latter requires telescopes of about two meters aperture or larger equipped with suitable spectrographs. Both categories present some challenging problems in implementation.

O'Connell effect candidate stars in the GNAT program range in brightness from about 13-17mag in V; most are rather red in color. The desired photometry is high cadence, time series measures, ideally in two or three spectral bands (typically V, R, and clear channel). The clear channel observations (which approximate the GAIA "G" band) are collected to help recruit a larger number of observers for whom the fainter stars are more challenging targets.

Orbital periods for these stars typically range from 0.5 to a few days (<10). It is desirable to sample the light curve as frequently and completely as possible. In some instances it is possible for an observer to catch a complete orbital cycle per night of observation. One goal of the project is to monitor the time scales of change in the O'Connell effect, so having multiple observers collaborating together is critical even for the very short period systems.

Longer period systems tend to rely even more on collaborative teams of observers. Also, the longer period systems would benefit greatly from longitudinally distributed observers.

Another factor is that many of these stars are separated only a little in longitude, so that in principle many could be observed simultaneously. However, at the desired time resolution (~ 5min) this means multiple observing teams to adequately cover multiple stars. This ultimately requires a large number of collaborators, though it could lead to more

advantageous parsing of targets among the observers such that smaller aperture operators work on the brighter stars, while larger aperture telescopes focus on fainter systems.

### 3. Collaborator Protocols

Small telescope observers wishing to collaborate with this GNAT program are encouraged to contact us to arrange observing schedules. Such collaborators will become affiliated with our research teams and will share in co-authorship of published results. We outline below the most useful observing protocols that collaborators will be expected to follow.

The optimal program (often not achieved) typically involves use of a 10-24in aperture telescope with a CCD or CMOS camera imaging a field on order 10-30 arcmin size. The system is equipped with a filter wheel and V, Rc, and clear channel filters. The telescope is equipped with an auto-guider and a means for maintaining focus over the course of several hours. The whole is driven by a telescope control system allowing at least semi-automated operation.

The optimal observing protocol is to acquire the target star early in the evening and to follow it until the hour angle prohibits useful observing. The desired imaging cadence is on order 5-10min, and filter switching between successive images is highly desirable. It is useful if the observer can calibrate the acquired images on a nightly basis and, using a GNAT suggested header format, upload the calibrated FITS images to a proprietary GNAT drive.

Ideally, these observations would be made on all clear nights for the duration of the observing season for the target star, at which point they would transition to the next star in the program list.

Project collaborators will have access to all of the data as it is collected and will have the opportunity to participate in research group discussions as the data are analyzed and prepared for publication.

Observers who cannot meet the parameters of this ideal observing program, either as a consequence of limited hours available for observing (due to personal schedules or equipment limitations), or can only observe with a single filter, or have other limitations, should still consider participating in this program as all of the data collected have potential value. Any given program star generally benefits from the efforts of multiple observers.

This program also benefits greatly from spectroscopic observations. Because of the typical brightness range of these stars the spectroscopic work requires spectrographic telescopes of about 2-m aperture or greater, thus effectively placing these observations in the realm of mostly professional observatories, so collaborating astronomers from several such facilities are also sought for this program.

If interested in collaborating, please contact Dr. Eric R. Craine at [ercraine@wrc-inc.com](mailto:ercraine@wrc-inc.com).

### 4. Acknowledgements

This project has prepared its first paper (on the close binary MG1-1995959) for submission for publication and has benefitted greatly from the collaborative work and joint discussions of the authors of that paper: E.R. Craine, B.L. Craine, C.J. Corbally, A.S. Kulesa, R.B. Culver, G. Boyce, T. Hunter, W. Marwood, and M. Miller. This project was also well informed by our colleague R.A. Tucker (deceased).

### 5. References

- Craine, B.L., Craine, E.R., Tucker, R.A., Culver, R.B., and Anderson, R., "MG Sky Surveys: Data Pipeline and Project Status" (2021). *SAS Symposium* **40**, 31-38.
- Knote, M.F., Caballero-Nieves, S.M., Gokhale, V., Johnston, K.B., and Perlman, E.S., "Characteristics of *Kepler* Eclipsing Binaries Displaying a Significant O'Connell Effect", (2022). *ApJ Suppl. Ser.* **262** (10), 32pp.
- Kraus, A.L., Craine, E.R., Giampapa, M.S., Scharlach, W.W.G., and Tucker, R.A., "The First MOTESS-GNAT Variable Star Survey", (2007), *AJ*, **134**, 1488-1502.
- O'Connell, D.J.K., "The So-Called Periastron Effect in Close Eclipsing Binaries" (1951). *Publ. Riverview Coll. Obs.*, **2**, 85-99.
- Roberts, A.W., "On a Method of Determining the Absolute Dimensions of an Algol Variable Star" (1906). *MNRAS* **66**, 123-141.
- Wilsey, N.J., and Beaky, M.M., "Revisiting the O'Connell Effect in Eclipsing Binary Systems" (2009). *SAS Symposium* **28**, 107-116.

# New Technologies and Dangerous Questions in Astronomy Education

*Rachel Freed*

---

## Abstract

We are convening a meeting for astronomy educators from around the country to discuss the future of undergraduate astronomy education. We hope to fundamentally change the approach to teaching introductory and successive astronomy courses by incorporating the latest technologies, such as remote robotic telescope networks, as well as data analysis tools specifically designed to work with large telescope survey data. We also want to re-define what astronomy exactly is, in relation to physics and geosciences and to help clarify the goals of astronomy education.

21st century technology enables astronomy educators to offer our students unprecedented hands-on learning experiences. Rather than simply lecturing about Kepler's Laws, with a few minutes' effort students can collect a sequence of images of a gas giant and model the orbits of its moons to determine the planet's mass. After winking back and forth to demonstrate the parallax shift in upheld thumbs, we can now actually image an asteroid simultaneously with robotic telescopes in two hemispheres and use the apparent shift to measure its distance. Instead of giving oversimplified descriptions of how star clusters teach us about stellar evolution, with reference to cartoon diagrams, introductory astronomy students can gather their own photometric data and perform their own complete cluster analysis in the time allotment of a single weekly lab. Those same students can now collect their own radio telescope data to measure the moon's temperature, observe a pulsar and sonify the signal, measure the rotation rate of the Milky Way, or that of a distant spiral galaxy and estimate its distance using the Tully-Fisher relation. The list of possibilities that already exists—that many are already implementing in their own classrooms—goes on and on.

The advent of robotic telescopes that enable remote—even unattended—collection of photometric, spectroscopic and even radio telescope observations, the proliferation of time domain and multiwavelength data from world-class facilities that can be accessed anywhere, by anyone, to make new discoveries, and the availability of advanced computing resources, provide opportunities for 21st century Astronomy students to learn and participate in modern Astronomy—even in introductory courses. Instead of direct transmission lecturing at our students about all the amazing discoveries astronomers have made, about all the things we've learned about our universe, we now have the option for them to BECOME the astronomers, by letting them collect their own observations - or utilize online repositories of high-quality data - to make those discoveries for themselves!

We have entered a new era in Astronomy Education, in which mastering Astronomy concepts through lectures, textbooks, and simulated experiments are being replaced by data-focused learning that provides a more authentic experience for introductory Astronomy students. This allows us to address many important open questions in the field. It is the intention of this meeting to make a concerted effort to work on answers to these questions as well as provide skills, techniques and experience for those yet unaware of the great changes that have occurred in the past decade.

---

**Richard F. Caris Observatory  
An Off-the-Shelf, Fully Instrumented Research Facility  
Shared By Rural Community Colleges and High  
Schools**

*Lou Jackson  
Eastern Arizona College  
Bushido Technical Solutions  
1113 S. Palomino Circle  
Payson, AZ 85541  
Lou.Jackson@Payson-AZ.com*

*Russell Genet  
Eastern Arizona College  
Fairborn Institute  
610 E. Tahoe Vista Circle  
Payson, AZ 85541  
RussellGenet@FairbornInstitute.org*

*Ann Knights  
Eastern Arizona College  
201 N. Mud Springs Road  
Payson, AZ 85541  
Ann.Knights@EAC.edu*

*Michael-James Ellis  
Payson High School  
Eastern Arizona College  
301 S. McLane Road  
Payson, AZ 85541  
Michael.Ellis@PUSD10.org*

*Eric Blackhurst  
PlaneWave Instruments  
1375 N. Main Street  
Adrian, MI 40221  
EBlackhurst@PlaneWave.com*

*Cameron Vittiglio  
PlaneWave Instruments  
1375 N. Main Street  
Adrian, MI 40221  
CVittiglio@PlaneWave.com*

*Paul McCudden  
Colorado Mountain College  
1275 Crawford Avenue  
Steamboat Springs, CO 80487  
PMcCuden@ColoradoMTN.edu*

---

## Abstract

This paper describes a half-meter telescope instrumented for wide- and narrow-field imaging and low-resolution spectroscopy that is mounted on a sturdy rolling pier and stored in a converted Conex shipping container when not in use. The complete turn-key system was purchased from PlaneWave Instruments with a single purchase order. The system will eventually be placed on an elevated pier and equatorial wedge under a 16-foot Ash dome. The initial roll-out configuration allows the system to be used during the somewhat lengthy process of building an observatory on a college campus. The observatory will be used by rural community college and high school students in the southwest to obtain original data for student published papers.

---

## 1. Introduction

Professional astronomers and their graduate students have access to nationally funded and operated ground and space telescopes. Many research universities have their own observatories. However, small rural community colleges and high schools often find it difficult to provide access to observational facilities for their students. For small amounts of observing time, individual schools can request that observations be made for them by Las Cumbres Observatory, or they can rent small amounts of time from iTelescope or other commercial firms that operate multiple remote robotic telescopes at what are often called telescope “farms.”

However, to obtain time-series photometry of eclipsing binaries, exoplanet transits, or cataclysmic variables (each observation which can take many hours of observing time) it may make sense for several schools in a region to form a consortium to purchase and share a robotic telescope. The shared telescope could be placed at a commercial telescope farm, such as Sierra Remote Observatory near Yosemite National Park, or El Sauce Observatory in the Atacama Desert of Chile. Alternatively, the telescope could be placed at one of the campuses of the participating schools.

There are four powerful advantages to the remote farm option: (a) the schools would not have to worry about providing a shelter, (b) they would not be involved in the telescope’s installation, (c) ongoing operation and maintenance would be handled by others, and (d) the remote sites would be good-weather sites with dark skies and good seeing.

A major disadvantage to placing a telescope at a remote farm is the recurring fees, which over 20 years could exceed the cost of installing the observatory on a campus (and observatories usually last much longer than 20 years). This expense could be offset, however, by the cost of maintaining an on-campus observatory. A more serious disadvantage, however, would be the difficulty of providing students (or the public) physical access to the telescope, given that telescope farms are distant, and their operation is online and autonomous, never in-person.

In the case of the Richard F. Caris Observatory discussed in this paper, we decided on an on-campus telescope located at a rural community college in Payson, Arizona. We felt that the motivational and experiential advantages of hands-on-the-telescope research for students, and the importance of having a prominent research facility available to the larger community, were compelling advantages.

However, since it was the objective of our observatory to provide observations for student researchers at other community colleges and high schools in the Four Corner States region (AZ, CO, NM, and UT), it was vital that we offer the same remote real-time and fully automatic options provided by the commercial telescope farms. Thus, there needed to be three operational modes for the observatory: (1) in-person, hands-on-the-telescope; (2) remote real-time operation where the telescope and its instruments are controlled over the Internet by a remote student or instructor; and (3) fully automatic operation where the system itself selects and observes targets on its own.



**Figure 1:** Initial roll-out configuration features the PlaneWave Instruments 0.5-meter telescope on a rolling pier. The telescope is stored in the Conex shipping container when not in use on the Payson campus.

Designing and building an on-campus observatory is a long and complex process. It typically

requires a site survey, architectural design, drawings, obtaining a building permit, soliciting bids from contractors, etc. We decided that while this long process of designing and building a permanent on-campus observatory was taking place we would, in parallel, operate the telescope in a roll-out mode. The telescope would be placed in a Conex shipping container when not in use and would be rolled out onto a small concrete pad for use on clear nights. Once rolled out, the telescope would be operated either in person at the telescope, or more typically over the Internet from a nearby warm room in the school.

This paper describes the telescope (Figure 1) and its instrumentation, initial roll-out configuration, the transfer to the permanent Ash dome, and the planned use of the Richard F. Caris Observatory by Four Corner States community college and high school students.

## 2. Telescope

A PlaneWave Instruments telescope was chosen based on PlaneWave's proven track record of producing and supporting fully robotic research telescopes that operate with high reliability in harsh mountaintop or desert environments. Direct drive motors and high resolution on-axis encoders eliminate the need for gears, thereby precluding backlash and periodic error. Direct drive mounts also counter wind gusts with their precise servo feedback. The fused silica mirrors and carbon fiber trusses minimize the effects of rapid temperature change. An aperture of 0.5-meters was chosen as the sweet spot on the aperture-versus-cost curve.



**Figure 2: The PlaneWave Instruments CDK-500 0.5-meter aperture optical tube assembly and the L-500 direct drive mount.**

A portable (rolling) pier allows the telescope to be moved in and out of the Conex. A wedge provides an inclined plane for movement of the telescope in and out of the Conex which sits ~ three inches above a concrete pad. An electric winch moves the ~600 lb. telescope up the ramp when placing it back in the Conex.

The system includes a motorized focuser for automatic focus, and a rotator that allows the entire instrument package to be rotated to any desired angle. This allows the image field to be de-rotated when the telescope is used in Alt-Az mode. This will also allow, later on, when the telescope is placed in a dome on an equatorial wedge, for wide-field images to be ideally framed, speckle interferometry images to be taken at multiple angles to reduce uncorrelated background noise, and the spectrograph's slit to be optimally situated.

## 3. Instrumentation

### 3.1 Instrument Selector

A fully robotic instrument selector is required to switch between the astrometric, photometric, and spectroscopic instruments. The Baader Instrument Multi Port IMP85 selector was chosen because the IMP85 provides a straight through (no mirror) path to the wide-field camera (Port 1), while two individually adjustable 40x40mm fused silica mirrors can be electronically inserted into the light path with high repeatability to redirect the light to a high-resolution camera on Port 2, or a spectrograph on Port 3. The instruments are connected to the three ports via individual custom adapters to make the imagers near-parfocal.





Figure 3: The Baader multi-port instrument selector.

### 3.2 Wide-Field Camera

A wide-field, high speed, low read noise, complementary metal oxide semiconductor (CMOS), QHY600M-PH camera is mounted on the straight-through Port 1. This camera was chosen not only for its high speed and low noise capabilities, but also for its large format sensor which, with the telescope's F/6.8 optics, provides a generous field of view.



Figure 4: The wide-field QHY CMOS camera and filter wheel.

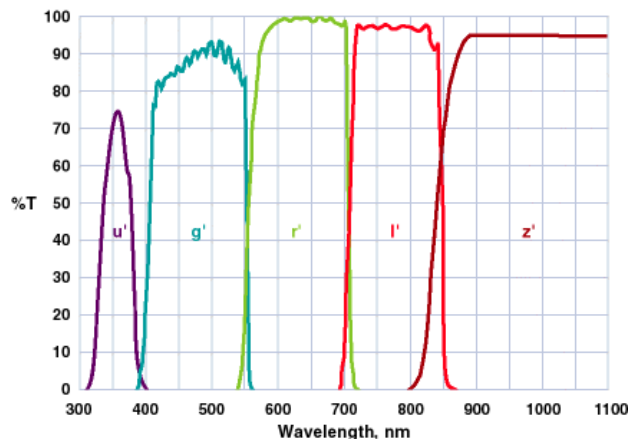


Figure 5: The response curves of the five Sloan filters.

The camera is preceded by a seven-position filter wheel with 50 mm filters. The filters are the five Sloan  $u'$ ,  $g'$ ,  $r'$ ,  $i'$ , and  $z'$  filters, and a clear filter (all from Chroma Technology), as well as a dark (opaque) “filter” from Astronomic.

### 3.3 High-Resolution Camera

The high-resolution camera and filters are identical to the wide-field camera, except they are located behind a two-inch, two-power Televue Barlow lens which magnifies the image to the resolution limit of the 0.5-meter telescope. Although the high-resolution camera's field-of-view is smaller than the wide-field camera (only 1/4<sup>th</sup> the area), some types of high-speed imaging, such as speckle interferometry of close double stars and lucky imaging of planets, benefit from obtaining images at the resolution limit of the telescope.

While these small field-of-view observations do not themselves require a large format camera such as the QHY-600, the large format of this camera allows plate solutions to be obtained which, in turn, allow precise identification and centering of targets within a region-of-interest before the high-speed exposures are made (typically a thousand exposures, each just tens of milliseconds long).

### 3.4 Spectrograph

Remote robotic spectroscopy presents several challenging issues:

- Placing the target on the slit of the spectrograph and holding it there through long exposures (tens of minutes to an hour or more). This requires that the pointing and tracking be extremely accurate.

- The spectrograph must be thermally and mechanically very stable to minimize shifts in internal focus and wavelength calibration as the telescope moves to different pointing directions and the night cools.
- The spectrograph needs to include an internal wavelength-calibration source and flat-lamp, both of which must be remotely operated.
- The spectrograph's internal optics must be reasonably well-matched to the telescope's optics.
- The spectrograph must provide an effective interface for auto-guiding and a view of the telescope focal plane to ensure that the correct target is on the slit (which is only a couple of arc-seconds wide).

The Shelyak Alpy instrument meets these requirements, providing a spectral resolution of  $R \approx 500$  and a free spectral range covering the entire optical region (roughly  $3750\text{\AA}$  to  $7250\text{\AA}$ ). Its internal optics are F/5, making it a good match to the PlaneWave Instruments F/6.8 CDK-500 telescope. Its internal calibration module (Ne-Ar lamp) and guiding module are designed for completely hands-off remote operation. Several observatories have demonstrated its effectiveness in reliable robotic operation and have obtained scientifically useful spectra.

### 3.5 Instrument Assembly

The instruments, as assembled on the back of the telescope, are shown in Figure 7. This is a complex setup, but that is required for a system that will serve many different projects. The system does not have an eyepiece, so in-person operation is via a control paddle, keyboard, mouse, and a large monitor.



**Figure 6: The Shelyak Alpy spectrograph. The calibration module is the white unit on the right, followed by the slit and guiding module with its blue camera, and the grism dispersing element and red spectral camera.**



**Figure 7: The fully instrumented PlaneWave Instruments CDK-500 telescope in its initial Conex shelter.**

The instrument rotator and focuser are almost flush with the backplate of the telescope. The Baader three-port instrument selector directs the light straight through to the filter wheel and wide-field camera, up through a custom Barlow lens, filter wheel, and narrow-field camera, or down to the Alpy spectrograph and its two cameras and calibration source and flat-field light.

### 3.6 Computer and Software

An environmentally rugged, Industrial Edge, OnLogic IGN 700 computer with an Intel 10<sup>th</sup> generation i7 processor is mounted on the telescope. This fanless, all solid-state computer meets high environmental ruggedness standards. The computer contains all the software required to control the telescope and obtain data from the two cameras and the spectrograph.

## 4. Permanent Installation and Operation

Once the 16-foot Ash dome installation is completed, the telescope will be placed on an elevated steel pier and equatorial wedge very similar to the installation at the in Jordan shown in Figure 8. Weather sensors, dome control, emergency power backup, etc., will be included in the final installation.

This will provide what is needed to conduct all three modes of operation: in-person, real-time remote, and fully automatic.

**Figure 8: A PlaneWave Instruments CDK 500 telescope on an equatorial wedge under a 16-foot Ash dome at the King's Academy in Jordan. This is very similar to the final Richard F. Caris Observatory's configuration.**

The primary users of the Richard F. Caris Observatory, once it is completed, will be the member schools of the Corner States Community College Consortium as well as regional rural high schools. The primary objective of the observatory is to provide data for student research that results in published student team papers. Hands-on operation and data gathering with an accessible telescope provides an added level of insight, expertise, and ownership of the results not possible with purely robotic telescopes at a remote telescope farm. Potential student research projects include:

- Speckle interferometry of close binary stars, including potential new binary star discoveries suggested by Gaia, the European Space Agency's astrometric space telescope.
- Time series photometry of eclipsing binaries, exoplanet transits, and cataclysmic variable outbursts
- Spectroscopy of Be stars and other variable stars.

The observatory described in this paper will be an excellent fit for various student-run projects. Regular scheduled in-person observation runs will bring student teams to Payson to learn the techniques and skills of astronomical research.

## 5. Conclusions

Smaller institutions, such as rural community colleges and high schools, can share a robotic telescope which can be placed at a remote telescope

farm, or at a college campus. We chose to place our telescope on campus in a two-step process. The first step, while the observatory dome was being installed, was to place the telescope on a rolling pier and store it



in a Conex shipping container when not in use. The second step (once the 16-foot Ash dome installation is complete) will be to place the telescope on a tall pier and equatorial wedge.

Once fully operational, the Richard F. Caris Observatory should serve many rural and tribal community colleges and high schools in the Four Corner States of Arizona, Colorado, New Mexico, and Utah for many years, advancing student careers with published research and an understanding of the scientific research process.

## 6. Acknowledgements

We are most grateful for two grants from the Richard F. Caris Foundation: one for the telescope, instruments, and rolling pier, and the other for the Ash dome, weather sensors, etc., and their installation to constitute a fully robotic, remotely accessible observatory in Payson Arizona. We are also grateful for the support of PlaneWave Instruments, the Fairborn Institute, Eastern Arizona College, Payson High School, Colorado Mountain College, the MHA Foundation, and Gravic Inc.

# Brightness Measurements of RZ-Aries

*Richard Schmude, Jr.*  
Gordon State College  
419 College Dr., Barnesville, GA 30204  
schmude@gordonstate.edu

*Qasim Ahmed*  
Gordon State College  
419 College Dr., Barnesville, GA 30204  
qa279714@gordonstate.edu

*Rebecca Smyly*  
Gordon State College  
419 College Dr., Barnesville, GA 30204  
rs262073@gordonstate.edu

*Denis Martinez*  
Gordon State College  
419 College Dr., Barnesville, GA 30204  
dm279952@gordonstate.edu

---

## Abstract

This paper describes V-filter brightness measurements made of the variable star RZ-Aries from November 8, 2023 through March 30, 2024. If just a single period of variability is considered, the data is best fit by a single 58-day cycle of change. Two mathematical models are considered, which are a seventh-degree polynomial and a Sine function. The Sine function gives a lower value for the standard error of estimate.

---

## 1. Introduction

The variable star RZ-Aries (Rho2 Aries) is classified as a semiregular variable star (Hirshfeld and Sinnott, 1985), (Scovil, 1990). In one study, Percy et al. (2008) combined several years of photometry data to carry out a power spectrum analysis. They report possible periods of 37.7, 56.5 and 370 days. Percy and Deibert (2016) carried out a more extensive study. They describe RZ-Aries as a pulsating red giant. They go on to state that it has a variability period of 56.5 days with a longer secondary period of 479.4 days. It is classified as an M6 III giant star (Tabur et al., 2009). Konstantinova-Antova et al. (2023) state that RZ-Aries is at the beginning of the Asymptotic Giant Branch (AGB) stage. This group also points out that its core is close to being (or is) depleted of helium. This star is believed to have a mass of 1.5 solar masses (Konstantinova-Antova et al. 2023), (Tsuji, 2008).

The purpose of this work is to report new brightness measurements of this star in filters transformed to the Johnson B and V system and to carry out mathematical models of this star's brightness

change. A second purpose of this work is to introduce undergraduate students to the exciting field of variable star astronomy.

## 2. Method and Materials

A SSP-5 photometer along with an eight-cm refractor was used in collecting all B- and V-filter measurements. This small telescope was used since a permanent observatory is not available. An SSP-3 photometer was used in collecting the R- and I-filter measurements since the SSP-5 photometer is not sensitive to these wavelengths. All measurements were made near Barnesville GA which is at 84.15° W, 33.05° N and is at an altitude of about 260 m. Measurements were made in filters transformed to the Johnson B, V, R and I system. The comparison star for all B- and V-filter measurements was Rho3 Aries which has brightness values of V = 5.616, B – V = 0.433 (Westfall). Since there are no reliable R and I magnitudes for this star, Delta-Aries was used as a comparison star for the R and I measurements. The R

and I magnitudes for Delta-Aries are  $R = 3.60$  and  $I = 3.09$  (SIMBAD star database, 2024).

Transformation coefficients were measured using the two-method described elsewhere (Hall and Genet, 1988). The transformation coefficients for the B, V, R and I filters are  $-0.234$ ,  $-0.0402$ ,  $-0.101$  and  $-0.177$ . Alpha and Beta Aries are the stars that were used in measuring transformation coefficients.

Since the comparison star was within a degree of RZ-Aries, extinction corrections were small. Extinction coefficients were measured when RZ-Aries was near the horizon. At times when RZ-Aries was overhead, the extinction coefficients (in magnitude/air mass) were assumed to be  $0.38$  and  $0.26$  for the B and V filters, respectively.

The B-V value of RZ-Aries is reported to be  $1.51$  (Lee, 1970). However, this quantity may change as the star's brightness changes.

### 3. Results

Table 1 summarizes measurements made by the authors. The lower-case v measurements are corrected for extinction but not for color transformation. These are believed to be accurate to  $0.02$  magnitudes except for the two measurements made on March 10 and 14. The V-filter results can be computed by adding  $-0.04$  magnitudes to the results in Table 1.

Date	v-mag.	Date	v-mag.
Nov. 8.07	6.17	Jan. 14.03	5.98
Nov. 19.06	5.98	Jan. 16.06	5.92
Nov. 28.03	5.73	Jan. 17.13	5.90
Dec. 5.16	5.79	Jan. 21.12	5.81
Dec. 6.03	5.78	Jan. 30.03	5.82
Dec. 7.06	5.81	Feb. 1.07	5.85
Dec. 12.03	5.95	Feb. 3.03	5.92
Dec. 15.03	6.03	Feb. 6.10	5.96
Dec. 16.00	6.06	Feb. 7.12	6.01
Dec. 19.00	6.15	Feb. 14.11	6.09
Dec. 20.02	6.16	Feb. 15.12	6.11
Dec. 29.01	6.18	Feb. 20.03	6.19
Dec. 31.04	6.20	Feb. 21.11	6.17
Jan. 2.03	6.19	Feb. 25.04	6.18
Jan. 3.02	6.13	Mar. 5.04	6.09 <sup>a</sup>
Jan. 5.01	6.16	Mar. 14.05	5.98 <sup>a</sup>
Jan. 7.14	6.13	Mar. 19.05	5.77
Jan. 10.07	6.07	Mar. 20.04	5.72
Jan. 11.06	6.06	Mar. 24.05	5.62
Jan. 12.02	6.02	Mar. 30.05	5.66

**Table 1: Measurements of RZ-Aries in late 2023 & early 2024. These results are not corrected for color transformation.**

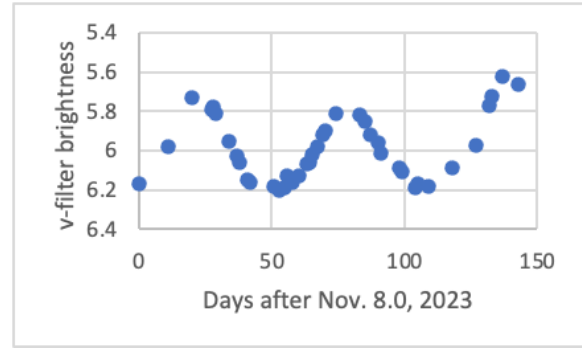


**Figure 1: A plot of v-filter brightness values in magnitudes versus time for RZ-Aries.**

### 3.1 Fitting the Data to an Equation

Figure 1 shows a graph of all the measurements in Table 1. The star RZ-Aries had brightness minima near Dec. 28.7, 2023 and Feb. 23.9, 2024. This star had maxima on Nov. 29.2, 2023 and Jan. 26.6, 2024. It undoubtedly reached a third brightness maxima around Mar. 25, 2024. If a single period is considered, the brightness went through a complete cycle in 58 days.

The maximum brightness values changed from magnitudes  $5.73$  to  $5.78$  to  $5.62$ . Part of this change may be the result of this star undergoing more than one change in brightness. This may be periodic or random. This star probably has a second longer period of perhaps  $479.4$  days (Percy and Deibert, 2016). Percy (2007) shows a graph of the brightness of RZ-Aries covering a period of over 12 years. There is some evidence that there may be a third period lasting around  $3000$  days.

The writers also decided to fit the data to a seventh-degree polynomial and to a Sine function. The objective is to generate a mathematical model with a minimum standard error of estimate (Larson and Farber, 2006). Such a model may yield insights into how RZ-pulsates. The standard error of estimate for the brightness of RZ-Aries (no variation) is  $0.17$  magnitudes. This should not be surprising since it is a variable star. The corresponding value for the seventh-degree polynomial is  $0.079$ . Bear in mind that the seventh-degree polynomial has seven adjustable parameter. Equation 1 gave the lowest standard error of estimate as  $0.054$  magnitudes.

$$M = 6.00 - 0.232 * \sin[320 + (D \times 6.20)/57.296] \quad (1).$$

In this equation  $M$  is the predicted brightness of RZ-Aries in magnitudes and  $D$  is the number of days after Nov. 8.000, 2023. The  $57.296$  term is needed to convert degrees to radians so that the Sine function, in Microsoft Excel, computes the proper value.

### 3.2 Color indexes of RZ-Aries

A total of 24 B-filter measurements were made during the study period. The B and V filters were fit using an iterative approach since transformation corrections needed to be made. The B – V value was the variable in this iteration. A mean B – V value of 1.35 was computed with a standard deviation of 0.047. This is based on 23 measurements. Part of the problem with this value is the combination of a large transformation coefficient and the large difference in color between the comparison star and RZ-Aries. Because of these two factors, the transformation correction for the B-filter brightness was on the order of 0.2 to 0.25 magnitudes. The V – R value for RZ-Aries was measured to be 2.62 on Feb. 3, 2024. The V – I value for RZ-Aries was measured to be 4.85 on Feb. 1, 2024. The respective color indexes reported by Lee (1970) are 2.42 and 4.59. It is not clear whether the color indexes change as RZ-Aries changes in brightness.

### 3.3 Basic Quantities

The mean brightness of RZ-Aries based on the first two complete cycles in Figure 1 is  $v = 6.02$  or  $V = 5.98$  magnitudes. The parallax of this star is 9.28 milliparsecs (Tabur et al., 2009). Therefore, based on the measurements made in this study, the absolute magnitude of RZ-Aries is 0.82. This along with the B – V value will place it within the range of Giants in the Hertzsprung-Russell diagram. (Fix, 2011).

### 4. Future Work

More V-filter brightness measurements are planned during the 2024-2025 observing session. These will hopefully be combined with measurements made by the AAVSO and the British Astronomical Association. It is hoped that a two- or three-period mathematical model can be developed.

### 5. Acknowledgements

We would like to thank Judy Andrews for making her dark site available for some of the measurements.

### 6. References

Burnham, R. Jr. "Burnham's Celestial Handbook An Observer's Guide to the Universe Beyond the Solar System." Vol. 1, (1978). Dover Publications Inc. Mineola, NY, 247.

Fix, J. D. "Astronomy Journey to the Cosmic Frontier." (2011). McGraw Hill, New York, Chapter 16.

Hall, D. S. and Genet, R. M. "Photoelectric Photometry of Variable Stars." Second edition (1988). Willmann-Bell, Inc., Richmond, VA. 199.

Hirshfeld, A and Sinnott, R. W. – editors, "Sky Catalog 2000.0 Volume 2: Double Stars, Variable Stars and Nonstellar Objects." (1985). Sky Publishing Corp. Cambridge MA and Cambridge University Press, London, pages XX and 226.

Konstantinova-Antova, R., Georgiev, S., Lèbre, A. et al. "A long-term study of the magnetic field and activity in the M giant RZ-Ari." (2023). Astronomy and Astrophysics in the press.

Larson, R. and Farber, B. "Elementary Statistics Picturing the World." Third edition (2006). Pearson, Upper Saddle River, NJ.

Lee, T. A. "Photometry of High-Luminosity M-Type Stars." (1970). The Astrophysical Journal 162, 217-238.

Percy, J. R. "Understanding Variable Stars." (2007). Cambridge University Press, Cambridge UK, Chapter 6.

Percy, J. R. and Deibert, E. "Studies of the Long Secondary Periods in Pulsating Red Giants." (2016). JAAVSO 44, 94-100.

Percy, J. R., Mashintsova, M., Nasui, C. O. et al. "Further Studies of the Photometric Variability of Bright Pulsating Red Giants." (2008). Publications of the Astronomical Society of the Pacific 120, 523-530.

Scovil, C. E. "The AAVSO Variable Star Atlas" (1990). American Association of Variable Star Observers, Cambridge, MA.

SIMBAD star database (2024) Online

Tabur, V., Bedding, T. R., Kiss, L. L. et al. "Long-term photometry and periods for 261 nearby pulsating M giants." (2009). Monthly Notices of the Royal Astronomical Society 400 (4) 1945-1961.

Tsuji, T. "Cool luminous stars: the hybrid nature of their infrared spectra." (2008). Astronomy and Astrophysics 489, 1271-1289.

Westfall, J. E. "Photometric Catalog of Zodiacal Stars" ALPO Monograph.

# Time Series Analysis of Variable Stars In Selected Globular Clusters

*Douglas Walker, Ph.D.*

*Department of Mathematics, Embry-Riddle University Worldwide  
Small/Scientific Telescope Engineering Learning and Astronomical Research  
walked35@erau.edu*

---

## Abstract

Globular clusters form a critical component of the Milky Way galaxy in which there are approximately 147 currently known with estimates of 10 to 20 more still undiscovered. Larger galaxies can contain many more clusters and it is estimated that the Andromeda Galaxy may contain as many as 500. Since all the constituent stars in a cluster are at the same distance, globular clusters are invaluable as testbeds for understanding stellar structure and evolution, and for serving as the basis for models of stellar populations.

An observing program has been established to image and analyze the variable stars in a selected set of globular clusters in the southern hemisphere including NGC 5139 (Omega Centauri or Caldwell 80), NGC 104 (47 Tucanae or Caldwell 106) and NGC 1261 (Caldwell 87) with the objectives of: 1. determining the observing depth possible within the crowded stellar field of the cluster with the CDK 24" telescope and 2. establishing a long-term time series analysis program of the variable stars in the cluster. This time series analysis will focus on topics such as variability of variable periods and changes in light curve patterns.

---

## 1. Introduction

Variable stars in clusters have been used as distance indicators and play an important role in our understanding of stellar evolution and cosmic distances. The determination of the distance moduli of globular clusters and of the absolute magnitude of the main sequence turnoff yielding the ages of the cluster, have relied heavily on observations of RR Lyrae (RRL) stars, Demarque (1973). Variable stars provide further tests of the theory of stellar evolution and from the calculated rates of evolution, it is possible to derive rates of period changes. The direction of evolution provides a test of the period changes, i.e., whether the period is increasing or decreasing. It also gives an explanation for more subtle effects such as the relative numbers of the shape and amplitude of the light-curve described as Bailey a, b and c type variables. Finally, the possibility that mass loss is of importance during the RR Lyrae phase in that it may affect the subsequent evolution of the star. Preliminary work on this on this subject was conducted by Laskarides (1974) at the University of Victoria.

An observing program has been established to image and analyze the variable stars in a selected set of globular clusters in the southern hemisphere. This list includes NGC 5139 (Omega Centauri or Caldwell 80), NGC 104 (47 Tucanae or Caldwell 106) and NGC 1261 (Caldwell 87). The objectives of this study are:

1. how well low magnitude variable stars within the crowded stellar fields of a globular clusters can be successfully imaged with a CDK 24" telescope and 2. determining whether establishing a long-term time-series analysis program of the variable stars in the clusters is possible. This analysis presented below will focus on topics such as the variability of the variable periods and changes in their corresponding light curve patterns.

### 1.1 RR Lyrae Variables as Standard Candlesticks

RR Lyrae and the associated class of pulsating variable stars that bears its name had a profound influence on astrophysics of the 20th Century. RRL stars are the cornerstone of the Population II distance scale and are members of an elite class of pulsating variables known as instability strip pulsators. These stars are all confined to a narrow region of the Hertzsprung-Russell diagram. The RR Lyrae have intermediate luminosities between those of the (brighter) Cepheids and (fainter) delta Scuti stars. The relationship between a pulsator's period and its luminosity is known as the Leavitt Law (SDSS, 2019). This relationship has been used to measure the distances to Cepheids, RR Lyrae, and delta Scuti stars within the Milky Way and the distances to galaxies

nearly 100 million light years away, Templeton, (2024, RR Lyrae, AAVSO).

In 1907 the Russian astronomer Sergei Blazhko first noticed the modulating amplitude of RW Draconis' pulsation light curve. Unlike other similar pulsators, its light curve wasn't regular from cycle to cycle, but changed in both amplitude and shape in a regular and predictable way. This effect came to be called the Blazhko effect and was soon discovered in many other high-amplitude RR Lyrae stars (those of type RRab).

## 1.2 The RR Lyrae Variable Period/Luminosity Relationship

RRL stars are not known for presenting a period-luminosity relation. Most researchers have utilized an average relation between absolute visual magnitude and metallicity  $[Fe/H]$  when deriving RRL-based distances. A theoretical calibration of the RRL Period-Luminosity (PL) relations in the Johnson-Cousins-Glass system was established by Catalan (Catalan et al, 2004). These PL relations can be summarized as follows:

$$M_I = 0.471 - 1.132 \log P + 0.205 \log Z \quad (1)$$

$$M_J = -0.141 - 1.773 \log P + 0.190 \log Z \quad (2)$$

$$M_H = -0.551 - 2.313 \log P + 0.178 \log Z \quad (3)$$

$$M_K = -0.597 - 2.353 \log P + 0.175 \log Z \quad (4)$$

$$M_V = 2.288 - 0.882 \log P + 0.108 (\log Z)^2 \quad (5)$$

Using the established periods to calculate the absolute magnitudes,  $M$ , and utilizing the apparent magnitude  $m$ , we can use the standard distance formula,  $D$ , to establish the distance:

$$D = 0.01 \text{ kpc} \times 1.585^{(m-M)} \quad (6)$$

As an example, using the published period of a RRL variable star in the cluster, NGC 1261 as 0.337568 days (Ferro, et al. 2019) and calibrating the  $Z$  value, we can establish the distance as 17.2 kpc to NGC 1261. This corresponds to the distance as published by Chehlaeh (2021). Taking the light curves of this variable from two observation periods taken on 12/02/2024, we get the light curves in Figures 1 and 2.

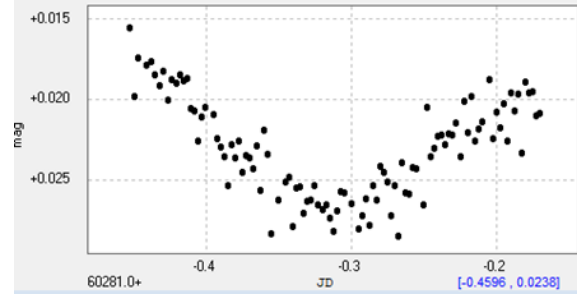


Figure 1. Light curve of first observation window of RRL variable in NGC 1261.

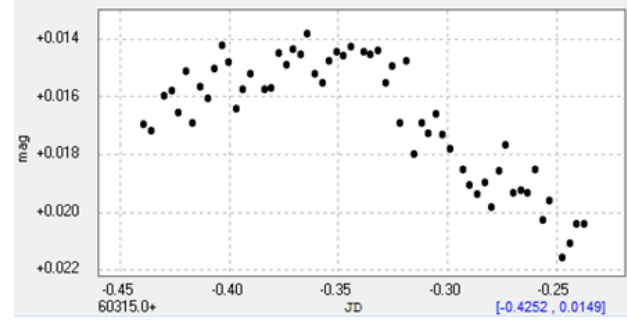


Figure 2. Light curve of 2nd observation window of RRL variable in NGC 1261.

Using standard period estimation algorithms, we get periods of 0.2519 and 0.2572 days respectively. Averaging these numbers, we end up with a period of 0.2546 days which has a difference of 0.0830 days or 32.5% from the published value in Ferro. Plugging this new estimate for the period into formulas (2) and (6), we get a calculated distance to NGC 1261 of 15.6 kpc. This is a difference of 1,639 parsecs. While there is more to estimating the distance in kpc, it is shown that the importance of accurate PL measurements cannot be over emphasized. It is hypothesized that long-term observations and analysis of PL measurements could help refine these distances.

## 1.3 Globular Clusters Under Study

Three globular clusters in the southern hemisphere were selected for observation and analysis. Images of the clusters taken with the CDK 24" telescope are shown in Figures 3 through 5 for NGC 5139, NGC 1261, and NGC 104 respectively. Observation runs for NGC 5139 were conducted in the March and April 2023 timeframe while those for NGC 1261 and 104 were conducted over the October through December 2023 timeframe.



### 1.3.1. NGC 5139

NGC 5139, also known as Omega Centauri ( $\omega$  Cen) is a globular cluster in the constellation of Centaurus visible from the southern hemisphere. Omega Centauri had been listed in Ptolemy's catalog as a star and it was Edmond Halley who was the first to document its non-stellar nature in 1677 by listing it as "luminous spot or patch in Centaurus" in his historical list of six such objects.

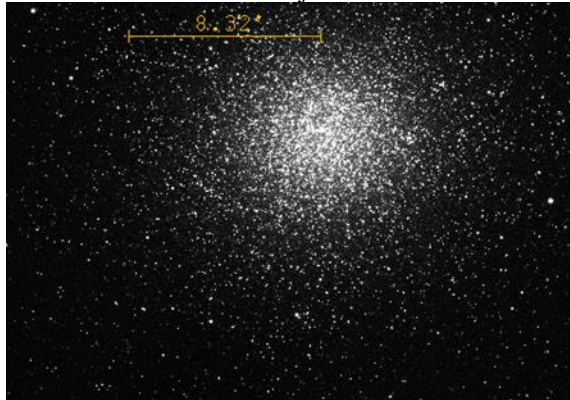


Figure 3. CK24 image of NGC 5139.

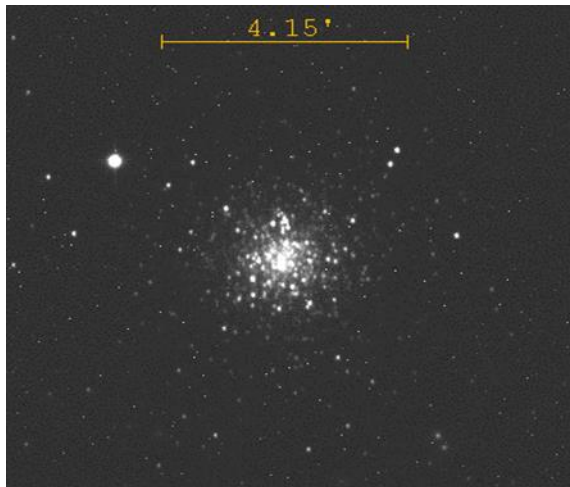


Figure 4. CK24 image of NGC 1261.

GC 5139 is located at RA 13h26m47.28s, Dec  $-47^{\circ}28'46.1''$ , has a heliocentric radial velocity of 231.1 km/s, distance of 5.24 kpc and a [Fe/H] value of -1.53 (Harris, 2010). It is the biggest of all globular clusters in the Milky Way galaxy, being about 10 times as massive as other globular clusters and containing about the same mass as the smallest whole galaxies. It is also the most luminous Milky Way globular, and the brightest globular cluster in the sky.

### 1.3.2. NGC 1261

NGC 1261 (also known as Caldwell 87) is a globular cluster of stars in the southern constellation of Horologium, first discovered by Scottish astronomer James Dunlop in 1826. Distances to this cluster have ranged from 15.5 kpc based on Gaia DR2 (Gaia Collaboration 2018; Baumgardt et al. 2019), to farther values out to 17.2 kpc.

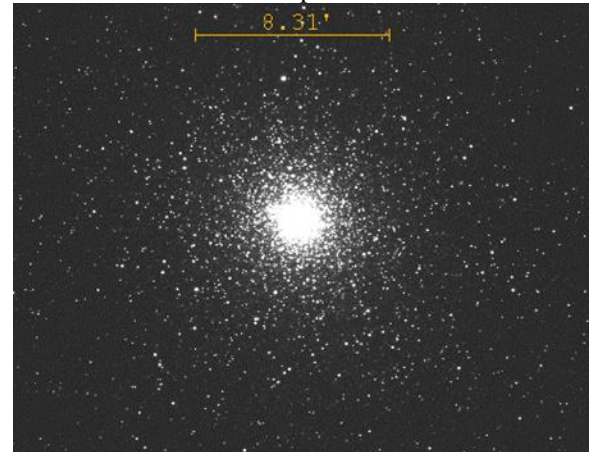


Figure 5. CK24 image of NGC 104.

A total of 22 RR Lyrae variables have been discovered in this cluster, along with two long-period variables, three SX Phoenicis variables, and an eclipsing binary. It was determined to be an Oosterhoff type I cluster, based on the periods of fourteen of the RR Lyrae variables. Eighteen probable blue straggler candidates have been identified.

### 1.3.3. NGC 104

47 Tucanae or 47 Tuc (also designated as NGC 104 and Caldwell 106) is a globular cluster located in the constellation Tucana. It is about  $4.45 \pm 0.01$  kpc away from Earth, (McLaughlin, D.E.; et al., 2006) and 120 light years in diameter (47 Tuc). 47 Tuc can be seen with the naked eye, with an apparent magnitude of 4.1. Due to its far southern location,  $18^{\circ}$  from the south celestial pole, it was not catalogued by European astronomers until the 1750s, when the cluster was first identified by Nicolas-Louis de Lacaille from South Africa.

47 Tucanae is the second brightest globular cluster after Omega Centauri, and telescopically reveals about ten thousand stars, many appearing within a small dense central core.

## 2. Photometry and Processing Chain

A data pipeline and photometry processing chain were developed to take the raw imagery data, perform photometry on the images and run it through a process to be able to produce lightcurves and periods of the variables of interest. This processing chain consists of selecting a target list for clusters, collecting the imagery over multiple observing runs utilizing a CDK 24" ground-based system, loading the imagery to cloud, downloading the data to the local disk storage, performing plate solving all the images, and aligning the images to the WCS reference system. Once all images have been aligned, the photometry tool, AstroImageJ was used to extract lightcurves resulting in data text files. These files were then processed through the Persano 3 period analysis tool to get period estimates and light curves and folded phase curves. This processing sequence is shown Appendix A.

### 2.1 Instrumentation

Observations of the clusters of interest were conducted utilizing the fully robotic observatory located in the Rfo Hurtado Valley, in the south of the Atacama Desert in Chile.

The telescope is a PlaneWave CDK24 with the following specifications:

- Aperture: 610 mm (24")
- Focal Length: 3974 mm
- Focal Ratio: F/6.5
- CO: 47%
- Tertiary Mirror: No

The mount is a PlaneWave L-600 on equatorial wedge. Pointing accuracy is <10-arcsecond RMS with PointXP Model, pointing precision is 2 arcseconds at sidereal velocity.

Camera equipment include:

- QHY600M-Pro
- Sensor: Sony IMX455-K Monochrome back-illuminated CMOS
- Pixel size: 3.76 microns
- Sensor size: 36mm \* 24mm (Full Frame)
- QE: Peak at 80%.

Filters include Sloan Digital Sky Survey (SDSS) of R, G and B filter bands.



**Figure 6. El Sauce Observatory (Observatorio El Sauce), Atacama Desert in Chile. Latitude: -30.4703073°, Longitude: -70.7646581°, Altitude: 1453m**

### 2.2 Photometry and Period Processing

The photometry processing tool utilized for this project is AstroImageJ which is a very robust and flexible photometry tool. Once photometry is produced, the period analysis tool, Persano 3, is used for period analysis.

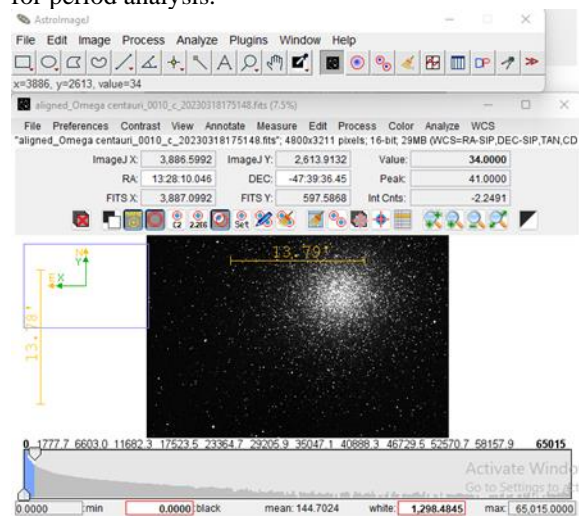


**Figure 7: AstroImageJ user interface.**

#### 2.2.1. AstroImageJ

AIJ is an interactive, easy-to-use research-grade image analysis software. AIJ is built on ImageJ, which is used extensively in the field of biology and bioinformatics. The 'astro' edition of ImageJ has added to it many astronomy-specific data reduction, analysis, modeling and plotting capabilities.

#### 2.2.2. Persano

Persano 3 is the leading light curve and period analysis software in astronomy. It offers a complete set of powerful analysis functions to work with large,

multi-night astronomical data sets, collected by a variety of observers. It is equally effective for the individual observer, who wants to analyze his observations of one or more nights.

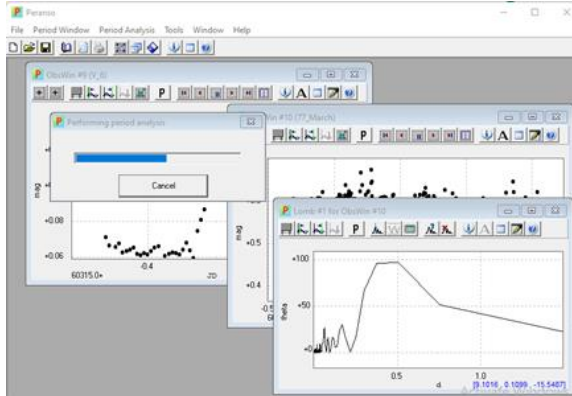


**Figure 8: Persano user interface and period analysis results.**

A variety of period analysis algorithms are included with Persano which are used for light curve period estimation and analysis. These include:

- Lomb-Scargle (LS) periodogram (Scargle, 1982)
- Phase Dispersion Minimization (PDM) (Stellingwerf, 1978)
- Analysis of Variance (ANOVA)
- Discrete Fourier transform (DFT) (Deeming)
- and others.

For the period estimation, average values using a multiple of algorithm solutions are used to obtain a final period number.

### 3. Variable Star Analysis

Utilizing the tool set and processing flow described above and in Appendix A, a series of variable stars in the selected globular clusters were analyzed for variability variance and changes.

#### 3.1 NGC 5139

The University of Toronto Department of Astronomy and Astrophysics globular cluster website (NGC 5139 / C1323-472 / Omega Centauri) indicates as of 2017, a total of 460 variables have been identified for  $\omega$  Centauri. A recent JAAVSO publication listed the discovery of 97 new variable stars in  $\omega$  Centauri (Walker, 2023). A potential new RR Lyrae variable was discovered in this study with small amplitude as shown in Figure 9. This variable was recovered and characterize to determine its period and compare changes to the initial approximation of the 2016 period

discovery of 0.2184 days. The phase curve for the 2016 discovery is shown in Figure 9 and demonstrates the characteristic curve of a RR Lyrae.

The light curve for the March 2023 observation run is shown in Figure 10.

Using the Persano period estimation algorithms and averaging the period estimates gives an estimate of period of 0.3778 days. This is different from the period of 0.2184 in Figure 9. The folded phase curve with an approximate trend line in Figure 11 shows the classic curve of the RR Lyrae variable.

The change in the estimated period is sufficient and warrants future study.

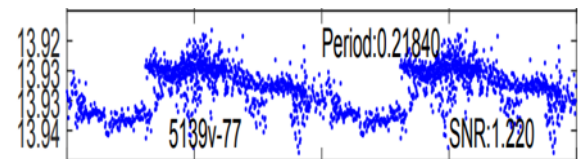


**Figure 9. Phase curve of potential new RR Lyrae.**

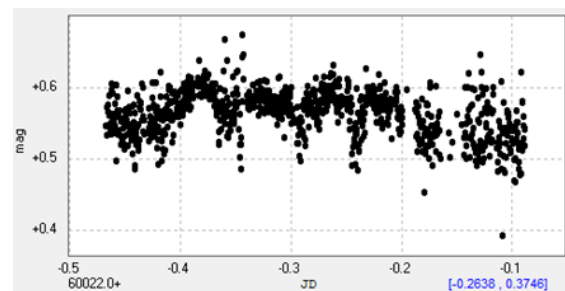


**Figure 10. Light curve for variable V-77.**

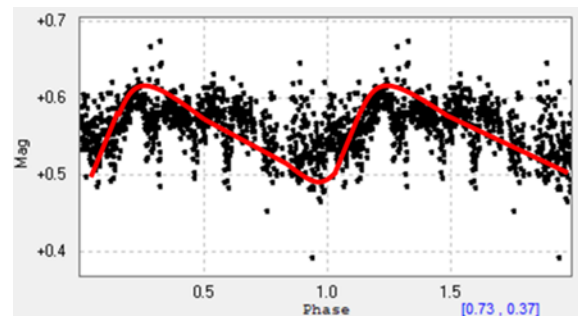


**Figure 11. Phase curve of variable V-77 with trend line.**

#### 3.2 NGC 1261

A time-series VI CCD photometry analysis of NGC 1261 was employed to study its variable star population by Ferro (Ferro, et al., 2019). The light curves of the member RR Lyrae stars were Fourier decomposed to calculate their individual values of distance, [Fe/H], radius and mass. This study was the focus used for variable star selection for this analysis.

### 3.2.1. Observations

The location of the variables on the cluster image are shown in Figure 12.

Observations occurred on the date 2023-12-02 with times between 01:00 to 07:00 hours UTC.

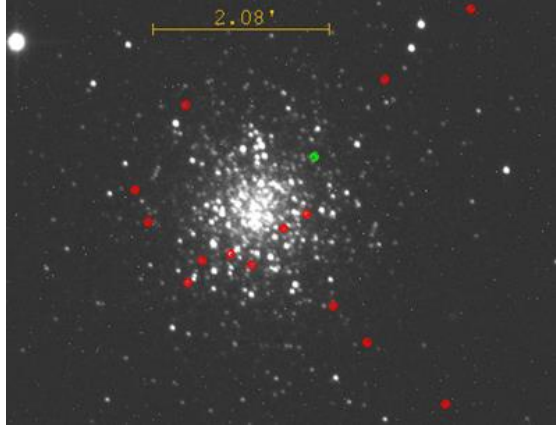


Figure 12: Location of selected variables on cluster NGC 1261 image.

### 3.2.2. Variables

The variable list from Ferro was taken and reduced based on the variables in the FOV and magnitude visibility. A total of 15 variables were selected for photometry and period analysis processing which are listed in Table 1. All magnitudes for these variables are in the 16.25 to 16.85 range in the V band.

### 3.2.3. Processing Results

Following the processing flow as described in Section 2, periods were obtained using the LS, PDM and ANOVA algorithms. These values were averaged when appropriate and are shown in Table 2.

A graphical representation of the period differences is shown in Figure 13.

ID	RA 03 hrs	Dec -55 deg	Period (days)	Mag (V)
V2	12 11.28	12 22.0	0.5857	16.78
V3	12 21.78	13 50.7	0.5370	16.25
V4	12 18.56	13 28.4	0.4928	16.33
V5	12 11.93	13 01.9	0.5133	16.69
V6	12 25.05	13 08.6	0.5641	16.76
V7	11 58.44	10 37.3	0.3335	16.84
V8	12 00.44	15 16.4	0.5382	16.28
V9	12:20.40	13:35.3	0.2972	16.85
V10	12 21.99	11 45.9	0.5834	16.80
V11	12 05.50	11 27.7	0.6622	16.84
V12	12 26.15	12 45.8	0.6103	16.82

V13	12 07.01	14 33.1	0.3376	16.70
V14	12 09.75	14 07.6	0.5740	16.78
V16	12 13.90	13 12.9	0.5262	16.56
V22	12 16.49	13 38.1	0.3026	16.52

Table 1. List of NGC 1261 RR Lyrae variables selected for photometry analysis.

ID	Pub Period	Calculate (days)	Difference (days)	Variance %
V2	0.5857	0.5526	0.0331	5.7
V3	0.5370	0.5042	0.0328	6.1
V4	0.4928	0.1975	0.2953	59.9
V5	0.5133	0.2775	0.2358	45.9
V6	0.5641	0.3890	0.1751	31.0
V7	0.3335	0.2541	0.0794	23.8
V8	0.5382	0.5137	0.0245	4.6
V9	0.2972	0.3121	0.0149	5.0
V10	0.5834	0.6024	0.0190	3.3
V11	0.6622	0.5185	0.1437	21.7
V12	0.6103	0.5533	0.0570	9.3
V13	0.3376	0.4810	0.1434	42.5
V14	0.5740	0.5104	0.0636	11.1
V16	0.5262	0.4767	0.0495	9.4
V22	0.3026	0.2456	0.0570	18.8

Table 2. Comparison of periods for RR Lyrae variables between published and results from this study.

Calculating the period change as a percentage of the original numbers gives the last column in Table 2 with the corresponding graph shown in Figure 14.

Results within 10% of the published periods can possibly be attributed to measurement errors however, a couple of examples which have very good Signal Noise Ratios (SNRs) are greater than a 10% variance. Two examples showing possible period changes over time are shown in Figure 15 with variable V14 at 11.1% and Figure 16 of variable V22 at 18.8%.

This limited analysis indicates that period changes are taking place within certain variables and these changes are able to be captured with the CDK 24” system.

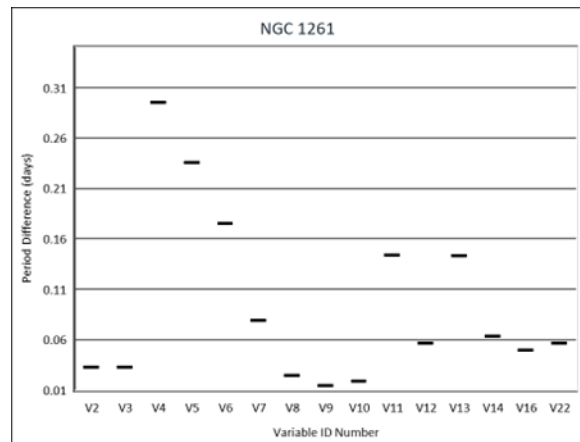


Figure 13. Period differences in days between studies by variable ID.

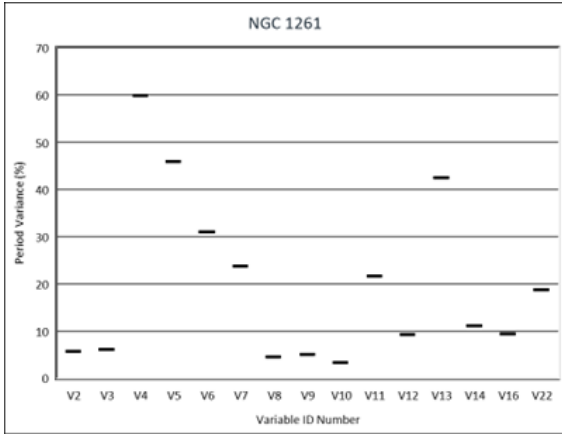


Figure 14. Period differences as a percentage of change.

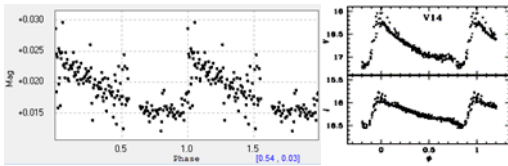


Figure 15. The recovered folded phase curve of V14 as compared to the exhibits provided by Ferro, et. al.

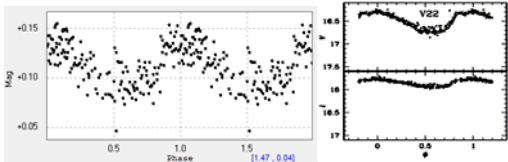


Figure 16. The phase curve of V22.

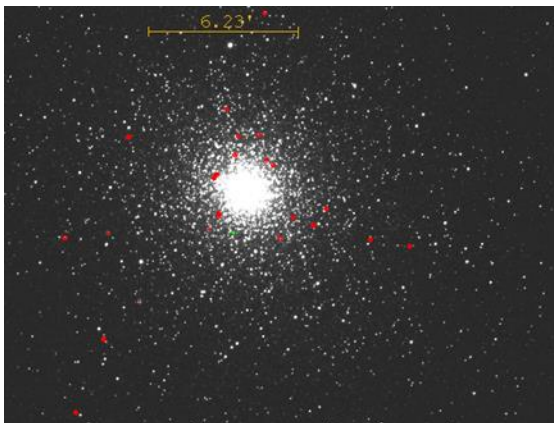


Figure 17: Location of a subset of variables on cluster NGC 104 image.

### 3.3 NGC 104

Reviewing the literature on variables in the 47 Tucanae cluster and using FOV and magnitude constraints, 25 variable stars were selected for photometry and period analysis. The locations in the cluster for a subset of these variables are shown in Figure 17.

#### 3.3.1. Observation Periods

Observations for NGC 104 occurred on the following dates (all dates UTC)

- 2023-10-05
- 2013-10-11
- 2023-10-19
- 2023-10-30
- 2023-10-31
- 2023-11-12
- 2023-11-14

Observing times were generally between 02:00 to 07:00 UTC.

#### 3.3.2. Variables

The 25 variables selected for analysis are shown in Table 3.

The target set is a mix of various variable types of details which are given below.

ID	RA 00 hrs	Dec -72 deg	Period (days)	Type
1	24 12.7	06 39.9	5.00	M
5	25 03.6	09 31.7	0.40	SR
6	24 25.7	06 30.0	1.00	SR
7	25 20.5	06 40.1	0.40	SR
9	23 40.5	06:00.0	1.07	RR0
13	22 58.4	06:56.1	0.70	L
15	25 43.9	06:50.9	0.30	L
16	25 23.2	11:05.3	0.20	L
17	23 55.7	57:28.6	0.10	L
18	25 09.2	02:39.7	0.50	L
22	24 10.0	02:38.2	0.25	L
25	23 58.9	02:34.6	0.20	L
52	25:11.1	12:14.6	0.22	E
WF2-V42	24:11.4	03:25.2	--	SR?
WF4-V22	24:20.0	05:51.8	--	SR?
WF4-V25	24:20.2	05:58.5	--	SR?
A19	24:21.8	04:13	0.70	L

LW1	23:22.3	05:40	0.20	L
LW2	23:29.2	06:20	0.30	L
LW3	23:47.4	06:53	0.35	L
LW4	23:51.3	03:49	0.20	L
LW6	23:54.7	03:39	0.10	L
LW17	24:16.3	01:31	0.10	L
LW19	24:23.2	04:23	0.15	L
KalW14	22:36.8	07:11.9	0.037	SX

**Table 3. Comparison of periods for RR Lyrae variables**

### 3.3.3. Variables Classifications

Classifications of the variables indicated in Table 3 are the following according to the GCVS Variability Types and Distribution Statistics of Designated Variable Stars.

(cdsarc.u-strasbg.fr/ftp/cats/B/gcvs/vartype.txt)

L - Slow irregular variables have light variations which show no evidence of periodicity. If periodicity is present, it is very poorly defined and appears only occasionally. Stars are often attributed to this type because of being insufficiently studied. Many type L variables are really semiregulars or belong to other types.

SXPHE - Phenomenologically, these variables resemble the Delta Sct (DSCT) type variables and are pulsating subdwarfs with spectral types in the range A2-F5. They may show several simultaneous periods of oscillation, generally in the range 0.04-0.08 days, with variable-amplitude light changes that may reach 0.7 mag in V. These stars are present in globular clusters.

SR - Semiregular variables are giants or supergiants of intermediate and late spectral types showing noticeable periodicity in their light changes. Many times these variations are accompanied by various irregularities. Periods lie in the range from 20 to >2000 days. The shapes of the light curves are different and variable with amplitudes which may range from several hundredths to several magnitudes (usually 1-2 mag in V)

M- Mira (Omicron) are Ceti-type variables with long periods. These long-period variables are giants with characteristic of late-type emission spectra (Me, Ce, Se) and light amplitudes from 2.5 to 11 mag in V. Their periodicity is well pronounced, and the periods lie in the range between 80 and 1000 days.

RR Lyrae stars are sometimes called short period Cepheids or cluster-type variables. The majority of

these stars belong to the spherical component of the Galaxy and are present in large numbers, in some globular clusters, where they are known as pulsating horizontal-branch stars. Like Cepheids, maximum the maximum light. giants with characteristic late-type emission spectra (Me, Ce, Se) and light amplitudes from 2.5 to 11 mag in V. Their periodicity is well pronounced, and the periods lie in the range between 80 and 1000 days. Infrared amplitudes are usually less than in the visible and may be <2.5 mag. For example, in the K band they usually do not exceed 0.9 mag. If the amplitudes exceed 1 - 1.5 mag, but it is not certain that the true light amplitude exceeds 2.5 mag, the symbol "M" is followed by a colon, or the star is attributed to the semiregular class with a colon following the symbol for that type (SR).

### 3.3.4. Processing Results

Light curves for the variables in Table 3 are shown in Appendix C. The majority of these variables are long term or Mira type variables. One variable was listed as RR Lyrae and a detailed analysis on this variable is performed below.

### 3.3.5. RR Lyrae – variable no. 9

Out of Table 3, only variable listed as no. 9 with a period of 1.07 days is identified as a RR Lyrae type of which is of interest in this study. The light curves cross all seven observations windows identified in section 3.3.1 are shown in Figure 18.

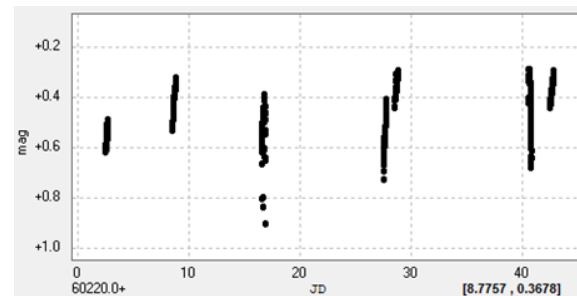


**Figure 18. AstrolmageJ window of all 7 observation periods.**

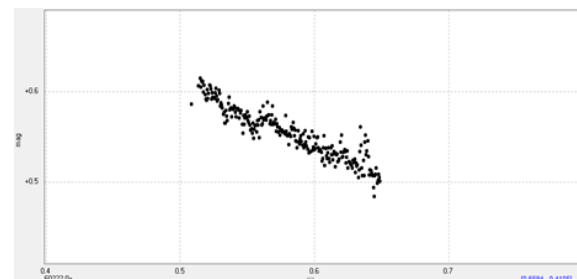


Figure 19. 2023-10-05 observation window for RR0.

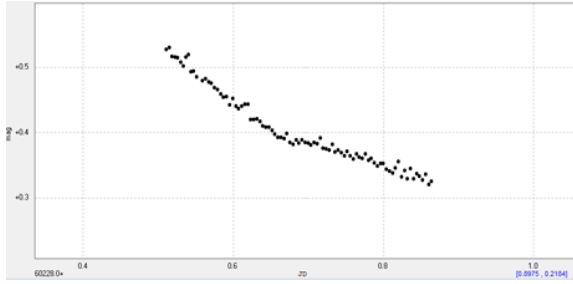


Figure 20. 2023-10-11 observation window for RR0.

Running our standard processing analysis algorithms, we get a period = 0.7367 days. Figures 19 through 25 show enlargements of the individual observation windows.

Generating the folded phase curve for the light curves across all seven observation windows gives us Figure 26 which clearly shows the RR Lyrae curve.

To view the data from a different perspective, the photometry data was taken and plotted for the data sequence in Excel resulting in Figure 27. The characteristic curve of a RR Lyrae can be clearly seen.

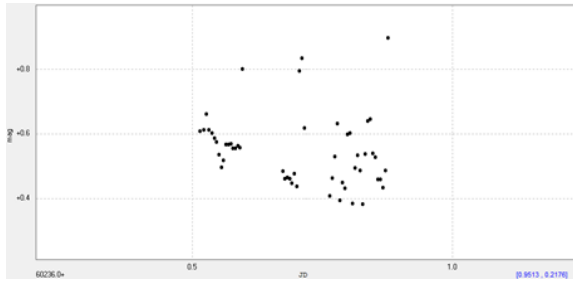


Figure 21. 2023-10-19 observation window for RR0.

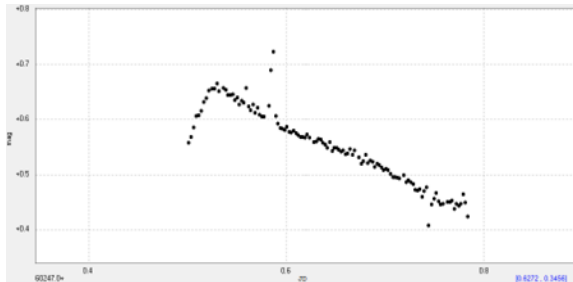


Figure 22. 2023-10-30 observation window for RR0.

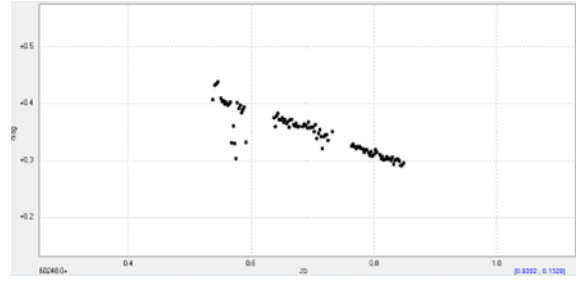


Figure 23. 2023-10-31 observation window for RR0.

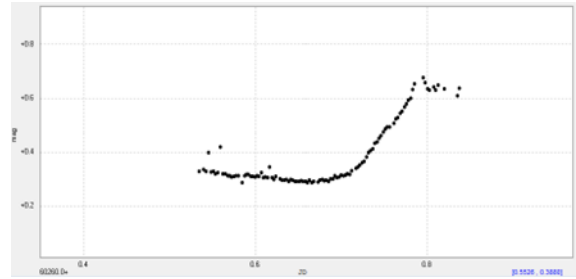


Figure 24. 2023-11-12 observation window for RR0.

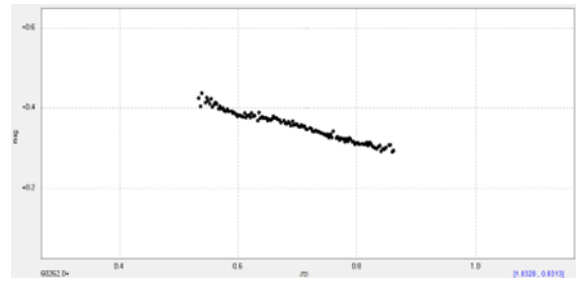


Figure 25. 2023-11-14 observation window for RR0.

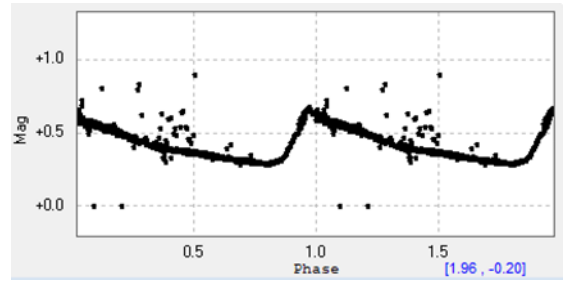


Figure 26. Phase light curve for RR Lyrae variable, no. 9

## 4. Conclusion

Utilizing the PlaneWave CDK24 ground based telescope for photometry image collection and the data processing chain developed for light curve extraction and period analysis, it has been shown that time-series analysis of variables in crowded stellar fields in globular clusters can be successfully undertaken. This study has demonstrated that variable stars in globular clusters as faint as approaching 17 magnitude can be

successfully recovered and processed to determine their periods. In many of these variables, the periods have been shown to have changed significantly from results published only a few years earlier.

A long-term time-series analysis of variables of various types can be undertaken for scientific investigation and discovery. The results from these studies should be of quality to be published in established astrophysical journals.

## 5. Acknowledgements

Thanks to the Boyce Astro Research Initiatives and Education Foundation (BRIEF), San Diego, California, USA for funding the operation of the CDK 24" observing system which provided all the observational photometry data utilized in this research project. A special thanks go to Leon Bewersdorff and Nick Hardy, members of the Small/Scientific Telescope Engineering Learning and Astronomical Research for observing operations and data collection and Dave Rowe, CTO of Planewave Instruments, Adrian, MI, USA, for his encouragement and always positive comments during review of preliminary results.

## 6. References

Demarque, P. (1973). Variable Stars and Evolution in Globular Clusters. In: Fernie, J.D. (eds) Variable Stars in Globular Clusters and in Related Systems. Astrophysics and Space Science Library, vol 36.

Springer, Dordrecht. [https://doi.org/10.1007/978-94-010-2590-4\\_27](https://doi.org/10.1007/978-94-010-2590-4_27)

Laskarides, P.G. A possible theoretical explanation of the erratic period changes of the RR Lyrae variables in globular clusters. *Astrophys Space Sci* 27, 485–488 (1974). <https://doi.org/10.1007/BF00643892>

"A century of cepheids: Two astronomers, a hundred years apart, use stars to measure the Universe" (Press release). Sloan Digital Sky Survey. 9 January 2018. Retrieved 23 September 2019

**Appendix A - Photometry and data processing chain.**

Templeton, M. (2024, January 1). RR Lyrae. AAVSO. Retrieved April 13, 2024, from [https://www.aavso.org/vsots\\_rrlyr](https://www.aavso.org/vsots_rrlyr)

Catelan, M. 2004a, *ApJ*, 600, 409 ———. 2004b, in *ASP Conf. Ser.* 310, Variable Stars in the Local Group, ed. D. W. Kurtz & K. Pollard (San Francisco: ASP), 11

Ferro, A. A., Fierro, I.H., Calderon, J.H, Ahumada, J.A., NGC 1261: A Time-series VI Study of its Variable Stars, 2019, *Revista Mexicana de Astronomia y Astrofisica*, 55. 337-350 (1029)

N Chehlaeh 2021 *J. Phys.: Conf. Ser.* 2145 012004

W.E. Harris. A Catalog of Parameters for Globular Clusters in the Milky Way. *Astronomical Journal*, 112:1487, 10 1996, 2010 revision.

Gaia Collaboration 2018; Baumgardt et al. 2019

"47 Tuc: A Great Globular Cluster of Stars". Astronomy Picture of the Day. August 26, 2008. Retrieved 25 May 2017.

McLaughlin, D.E.; et al. (2006). "Hubble Space Telescope Proper Motions and Stellar Dynamics in the Core of the Globular Cluster 47 Tucanae". *Astrophysical Journal Supplement Series*. 166 (1): 249–297.

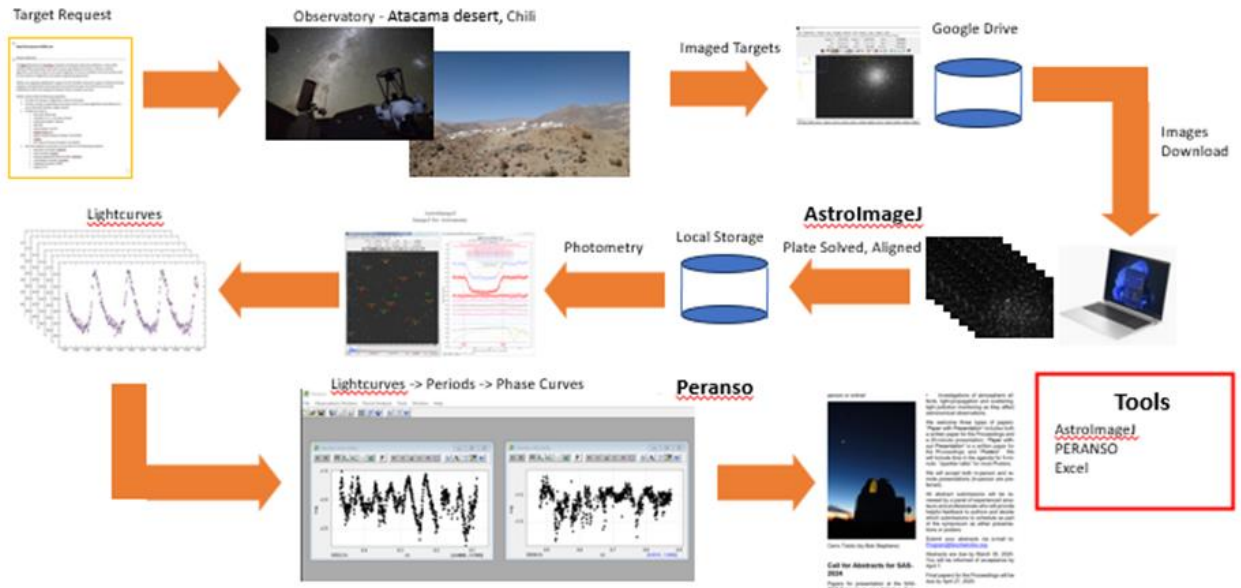
Walker, D., Albrow, M., "Ninety-Seven New Variable Stars in  $\omega$  Centauri". Volume 51 number 2 (2023)

*Revista Mexicana de Astronomía y Astrofísica*, 00, ??-?? (2007) NGC 1261: A TIME-SERIES VI STUDY OF ITS VARIABLE STARS A. Arellano Ferro,1 I.H. Bustos Fierro,2 J.H. Calderón,2,3 J.A. Ahumada,2

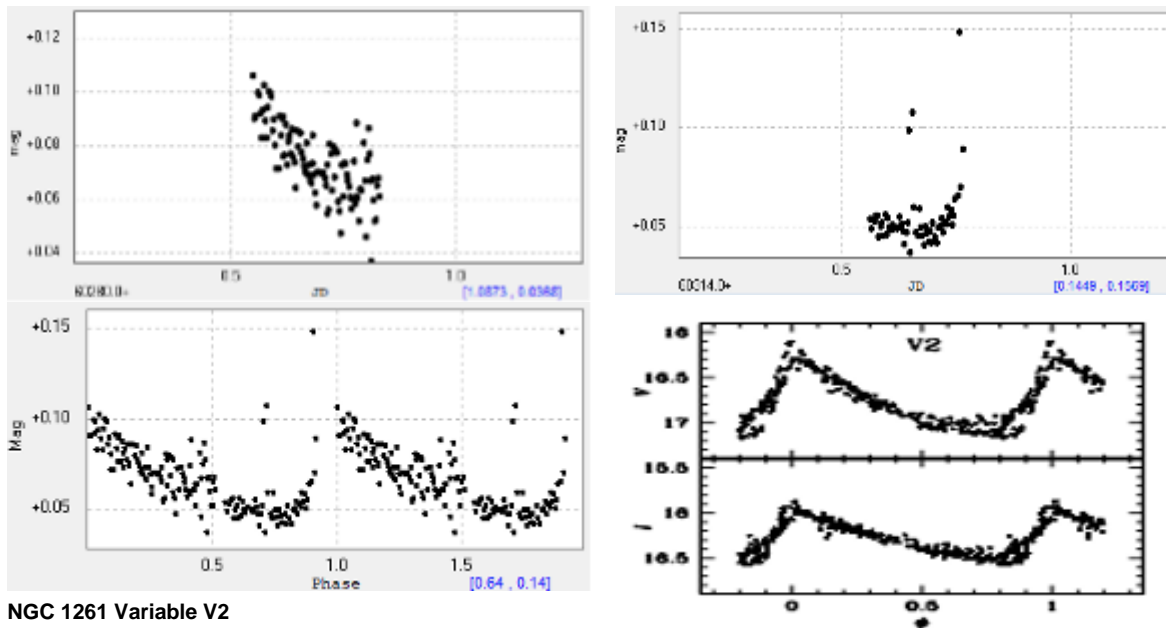
List of variables in NGC5139. <https://www.astro.utoronto.ca/~cclement/cat/C1323m>

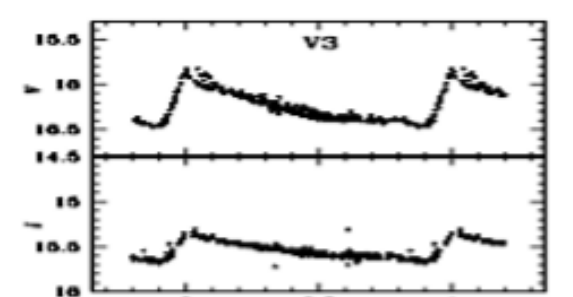
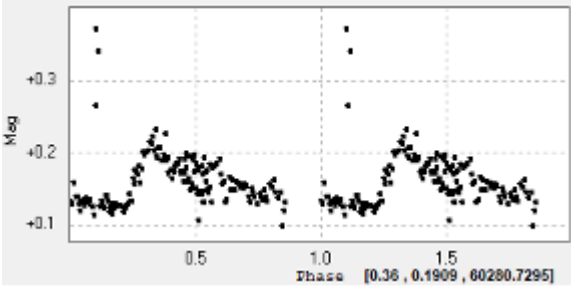
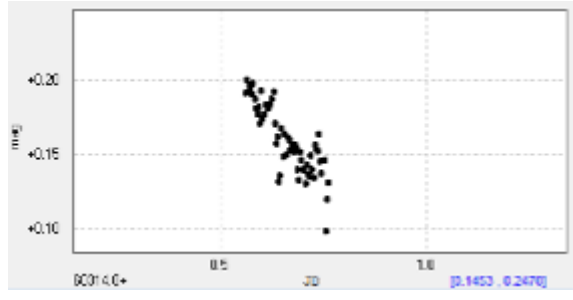
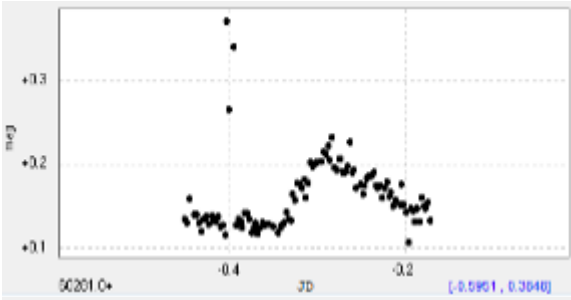


# Statistical Analysis of Globular Cluster Variable Stars

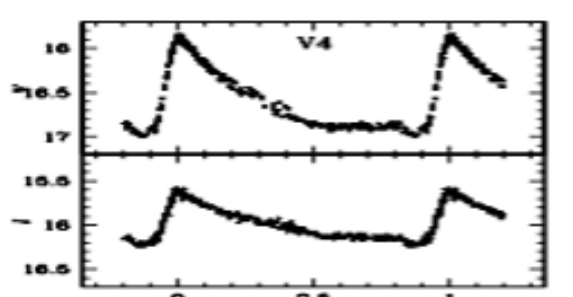
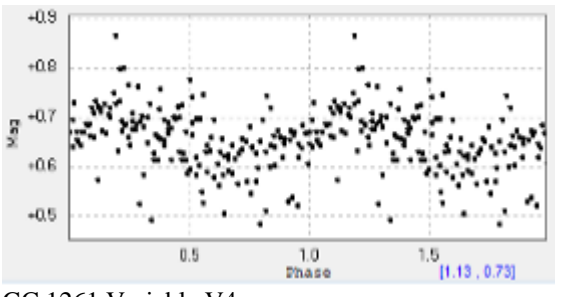
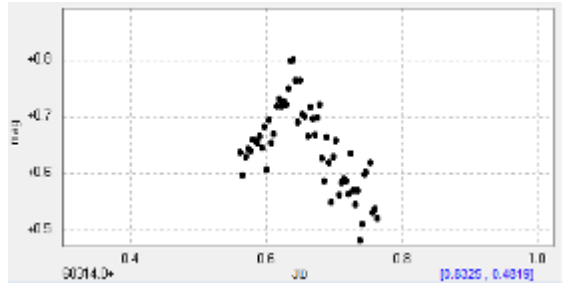
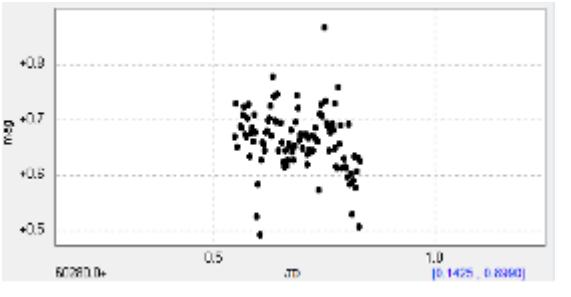


Appendix B - Light and folded phase curves for variables in NGC 1261. The first two panels are light curves for observation windows 1 and 2. Panel 3 is the folded phase curve and panel 4 are the phase curves from Ferro et al.

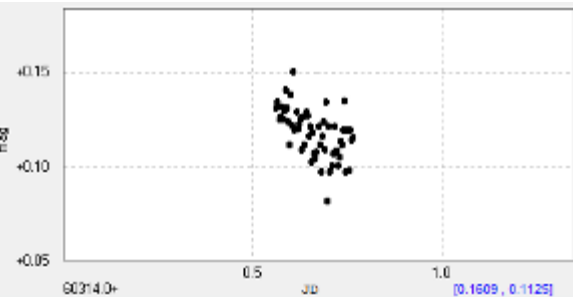
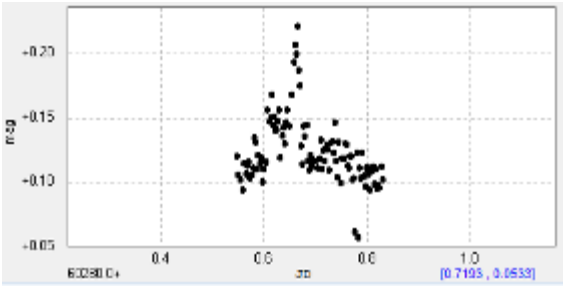


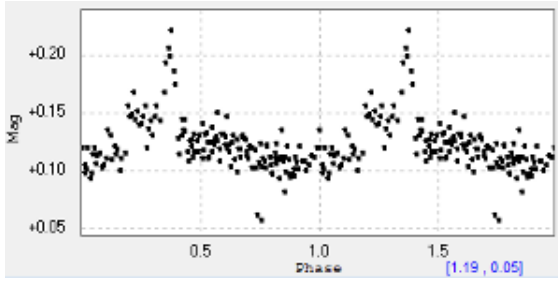


NGC 1261 Variable V3

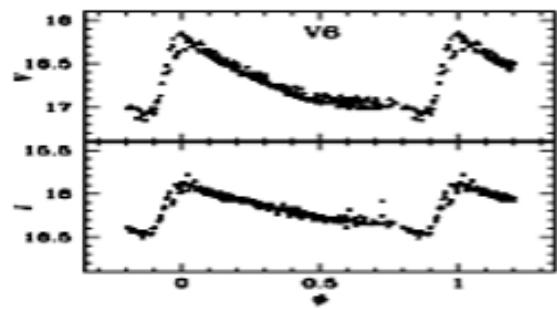
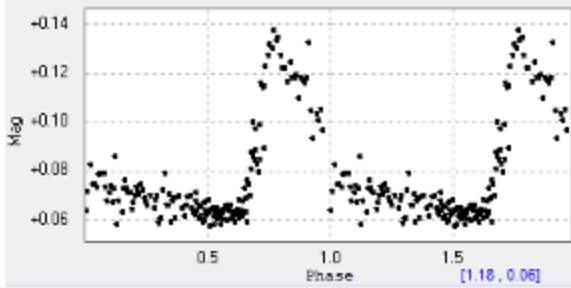
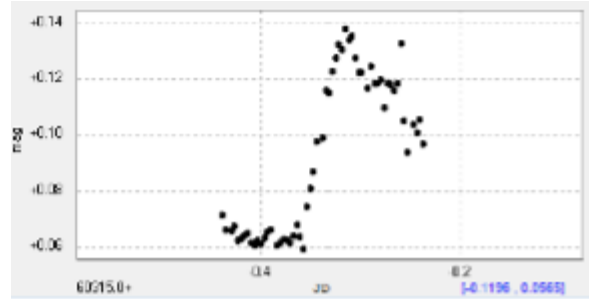
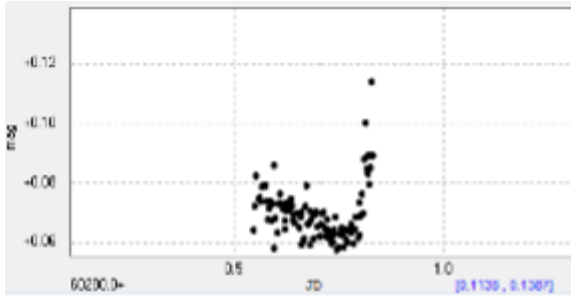
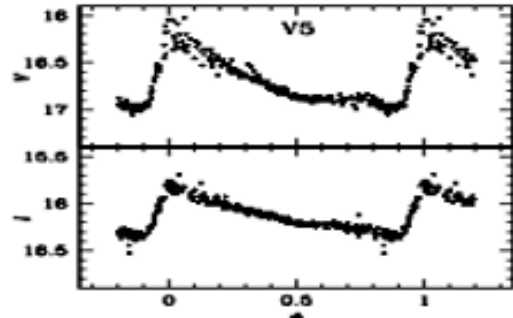


NGC 1261 Variable V4

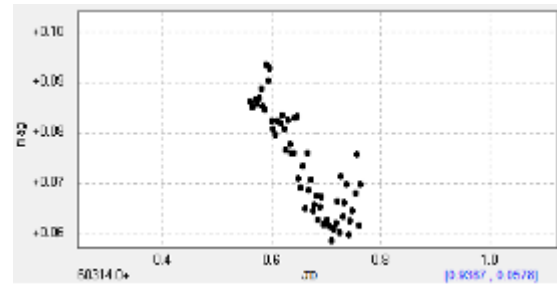
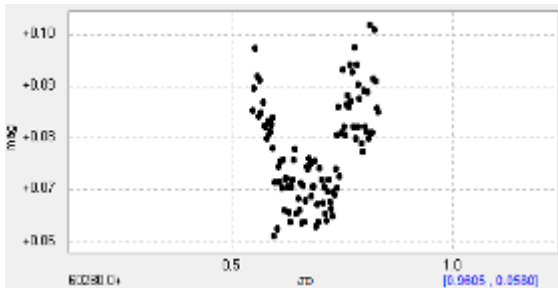


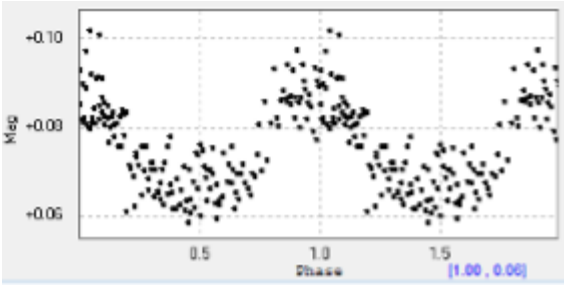


NGC 1261 Variable V5

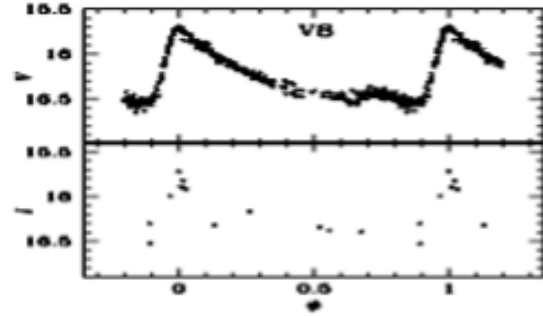
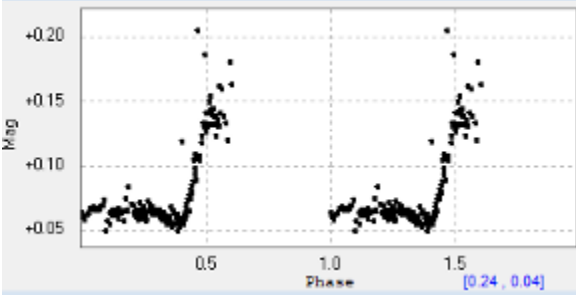
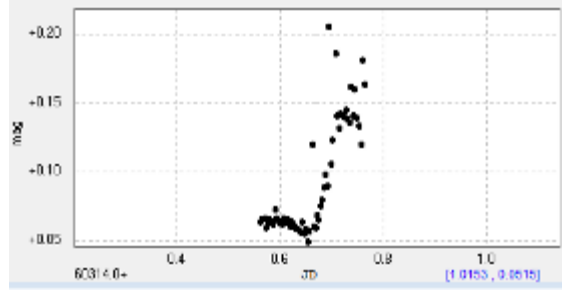
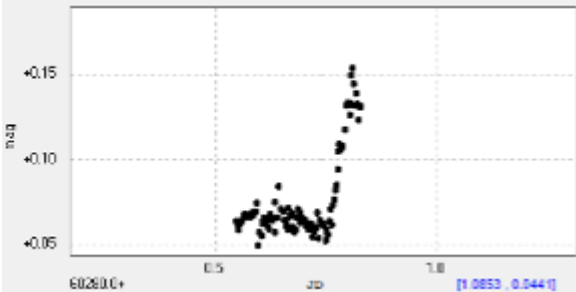
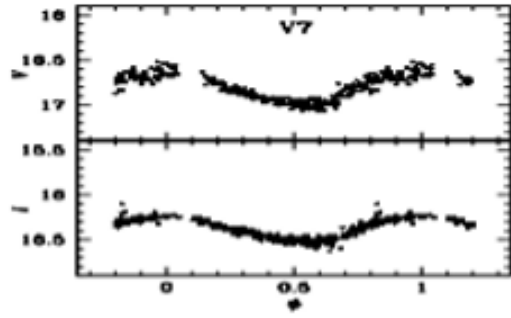


NGC 1261 Variable V6

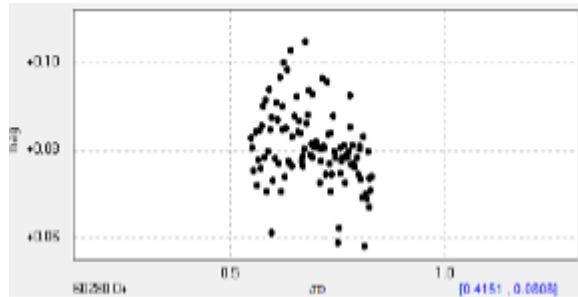
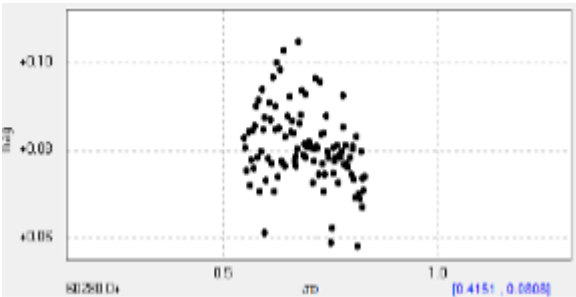


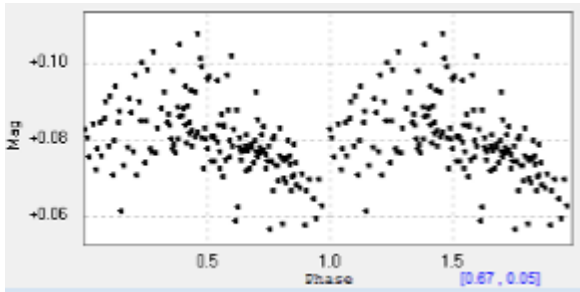


NGC 1261 Variable V7

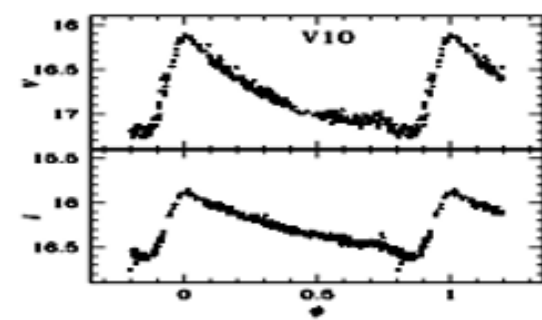
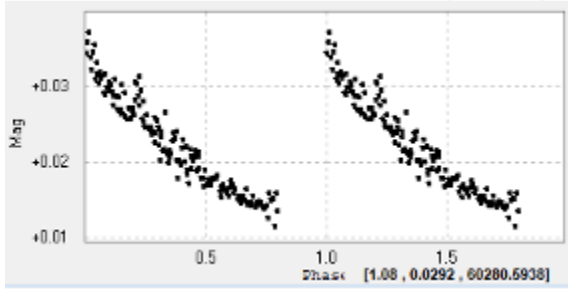
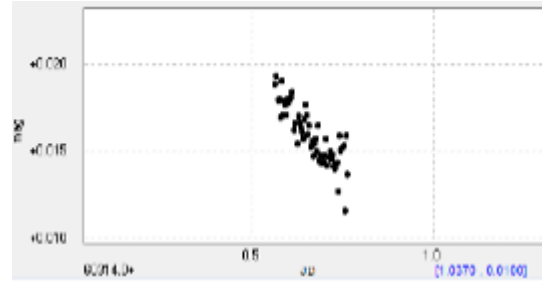
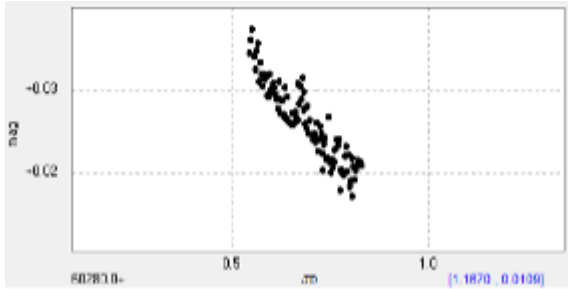
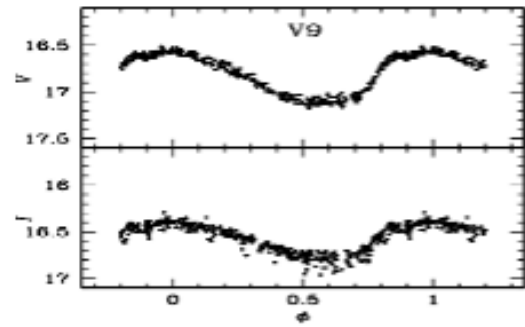


NGC 1261 Variable V8

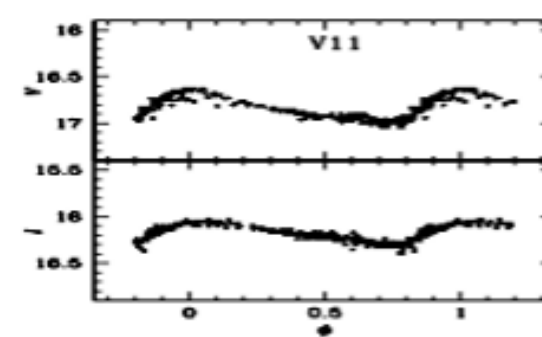
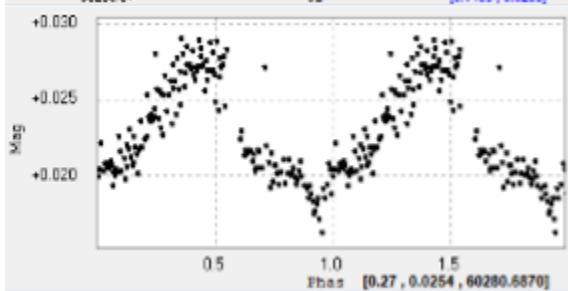
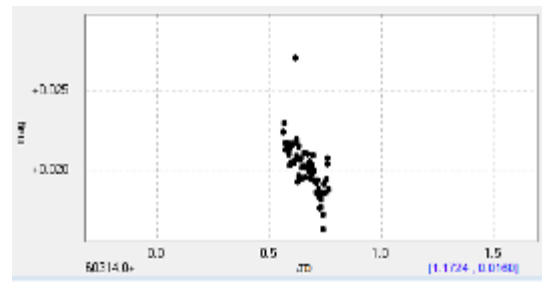
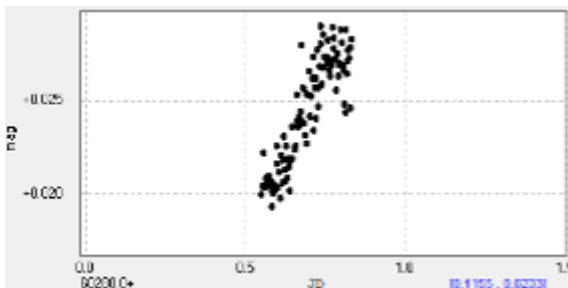




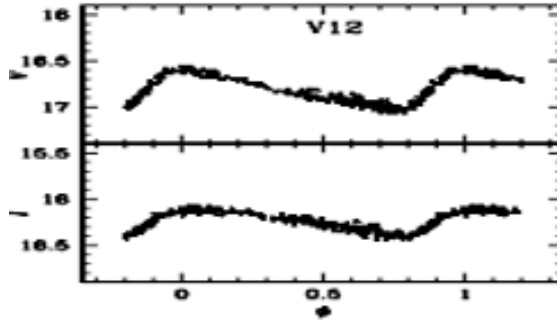
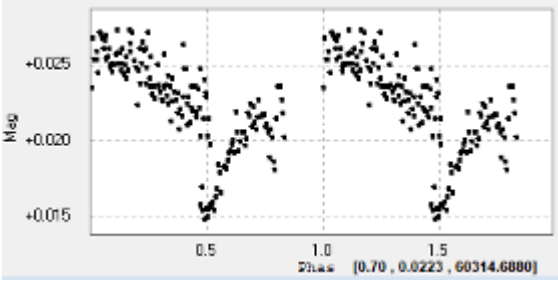
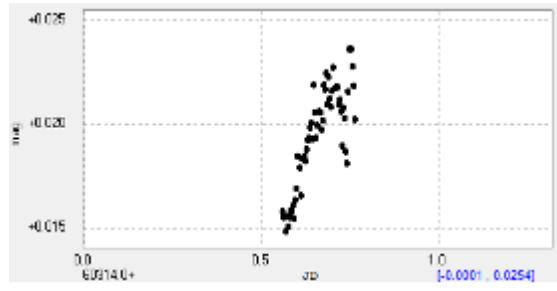
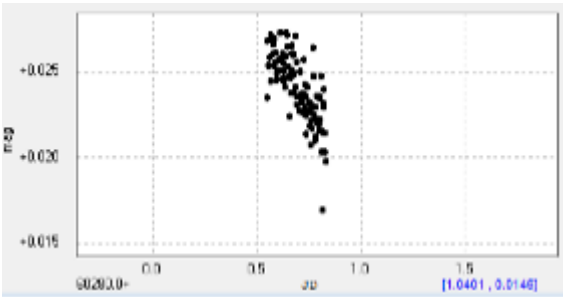
NGC 1261 Variable V9



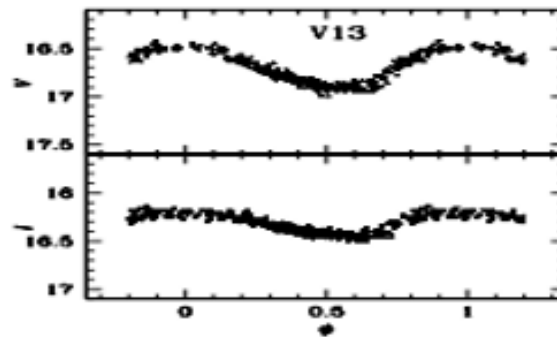
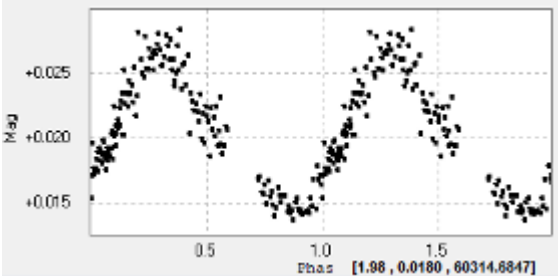
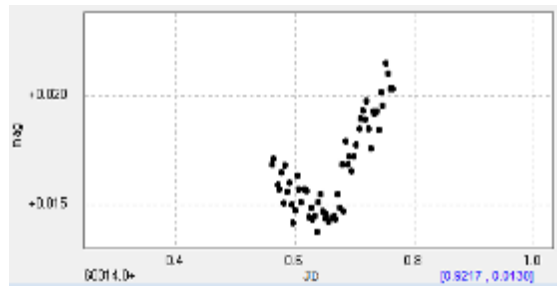
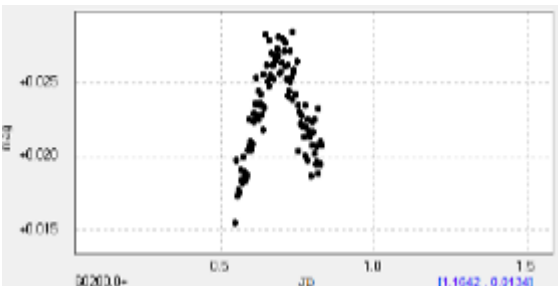
NGC 1261 Variable V10



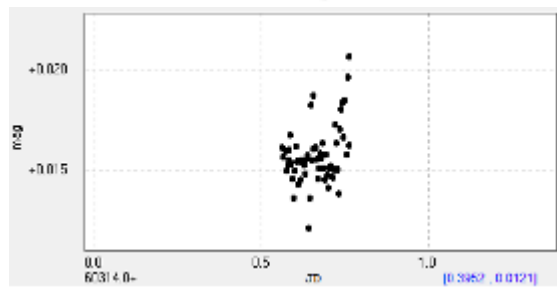
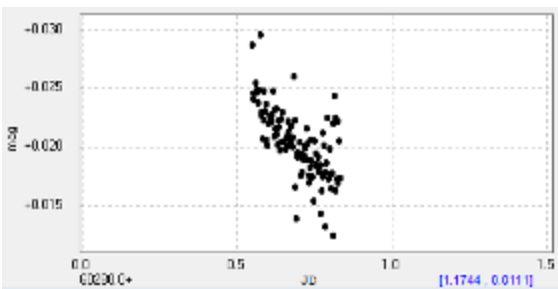
NGC 1261 Variable V11

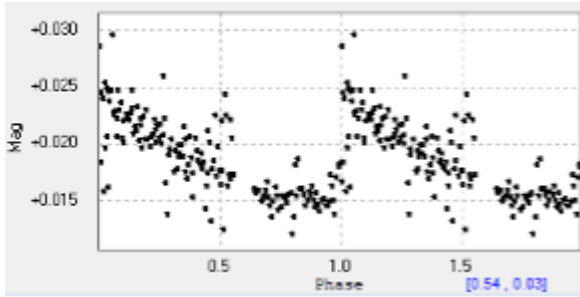


NGC 1261 Variable V12

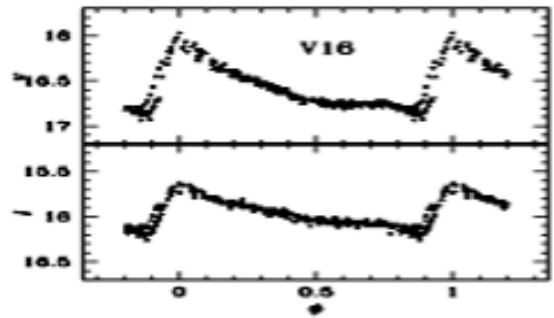
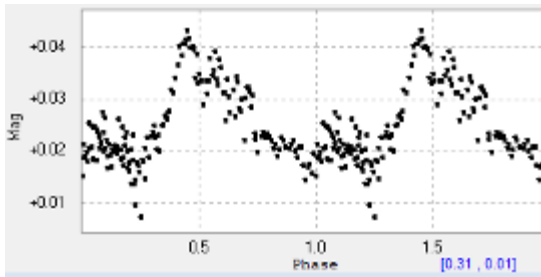
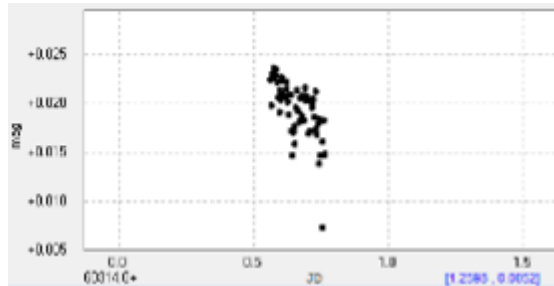
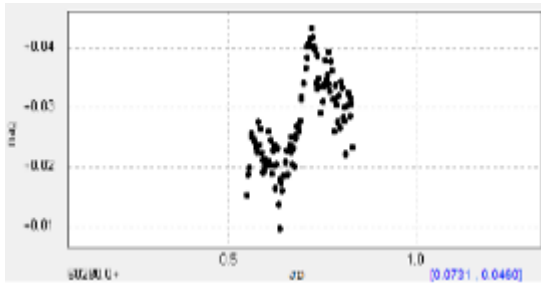
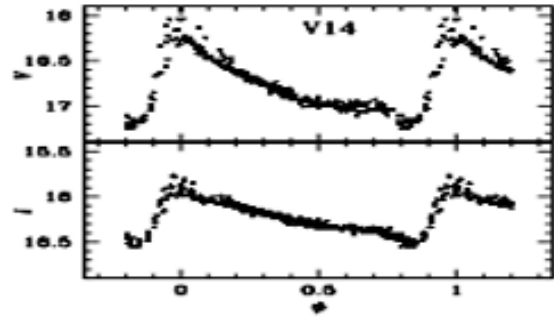


NGC 1261 Variable V13

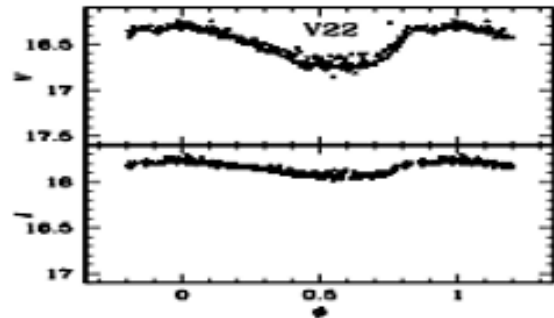
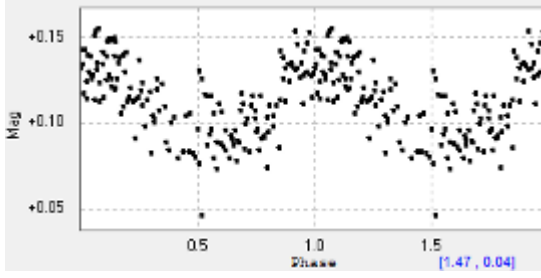
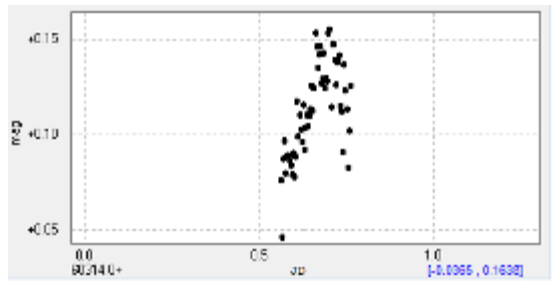
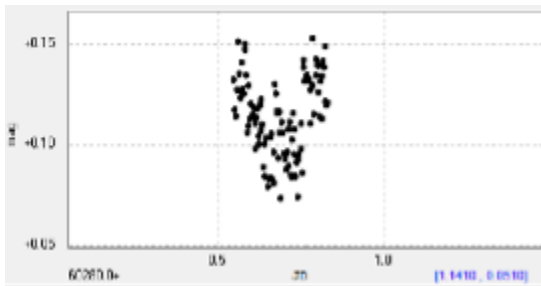




NGC 1261 Variable V14

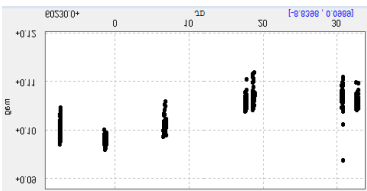


NGC 1261 Variable V16

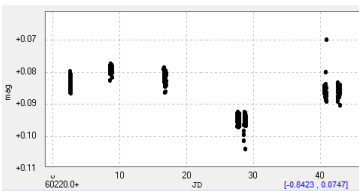
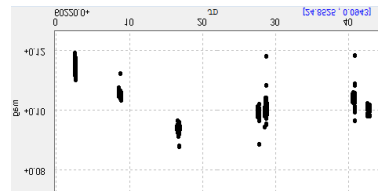
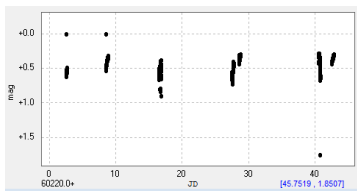


NGC 1261 Variable V22

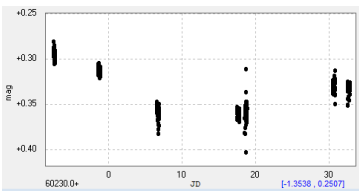
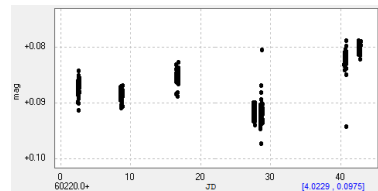
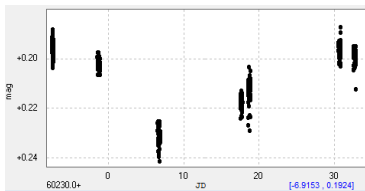
Appendix C - Light curves for variables in NGC 104. Each panel contains the data for all seven observation windows



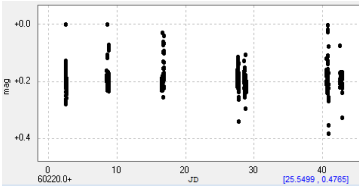
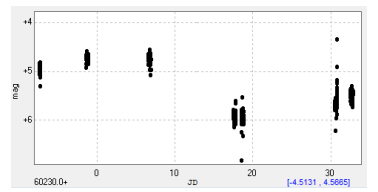
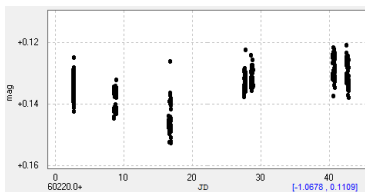
GC 104 Variables ID 7, 9, 13



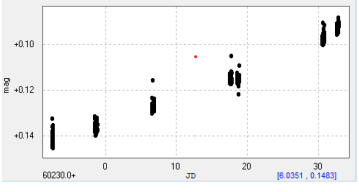
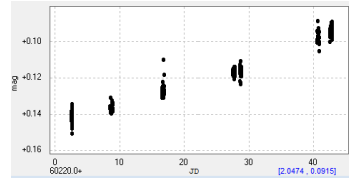
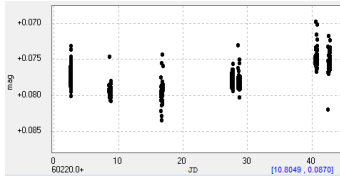
NGC 104 Variables ID 15, 16, 17



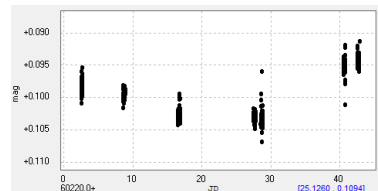
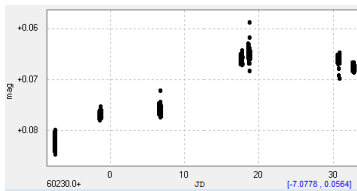
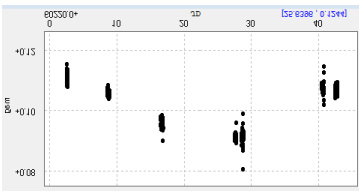
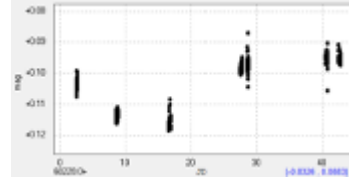
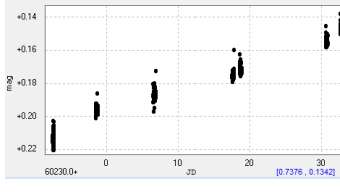
NGC 104 Variables ID 18, 22, 25



NGC 104 Variables ID 52, WF2-V42, WF4-V22

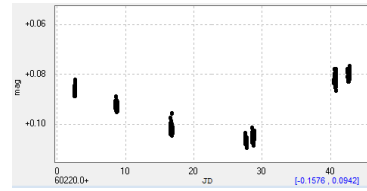
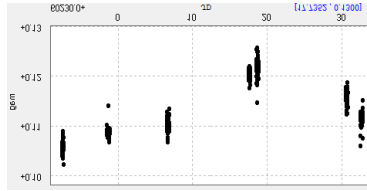
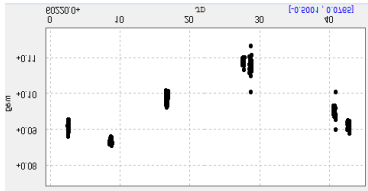


NGC 104 Variables ID WF-V25, A19, LW1

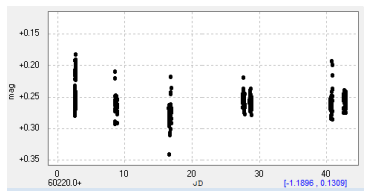
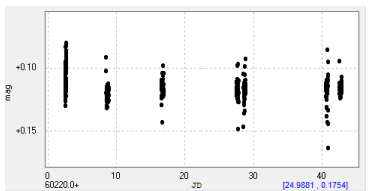




**NGC 104 Variables ID LW2, LW3, LW4**



**NGC 104 Variables ID LW6, LW17, LW19**



**NGC 104 Variables ID KalW14, KalE19**

# Analysis of SX Phoenicis Variable Stars in the Omega Centauri Globular Cluster

*Douglas Walker, Ph.D.*

*Department of Mathematics, Embry-Riddle University Worldwide  
Small/Scientific Telescope Engineering Learning and Astronomical Research  
walked35@erau.edu*

---

## Abstract

SX Phoenicis are variable stars found primarily in globular clusters and galactic halos. With a variability cycle demonstrating a period-luminosity relation, these stars exhibit a short period pulsation behavior that varies on time scales of 0.03–0.08 days, magnitude variations up to 0.7 and with spectral classifications in the range of A2-F5. They have a lower metallicity compared to main sequence stars which results in a reduced abundance of elements other than hydrogen and helium. All known SX Phoenicis variables in globular clusters are blue straggler stars and these properties distinguish the SX Phoenicis variables from their cousins, the Delta Scuti variables.

An analysis has been conducted on a set of SX Phoenicis variable stars in  $\omega$  Centauri utilizing a Dall-Kirkham (CDK) 24" robotic telescope located in the Río Hurtado Valley, in the south of the Atacama Desert. This system is operated by the Small/Scientific Telescope Engineering Learning and Astronomical Research and provides periodic imagery of this and other globular clusters. The focus of this research is to investigate whether SX Phoenicis variables in the  $\omega$  Centauri cluster have demonstrated period variation in comparison to previously published papers in referred journals.

---

## 1. Introduction

SX Phoenicis (SX Phe) are a type of variable stars of a class of high-amplitude Population II pulsators. They exhibit short period pulsation behaviors that varies on time scales of 0.03–0.08 days with spectral classifications ranges of A2-F5. Magnitudes can vary by up to 0.7. (GCVS Variability Types, General Catalogue of Variable Stars, 2010).

SX Phe variables oscillate in the fundamental radial mode (P0  $\sim$  0.05496 d) and the first overtone radial mode (P1  $\sim$  0.04277 d) with a marked beating effect in the light curve (Landes, et al. 2010). Many of the properties of SX Phe variables have been successfully modelled by Petersen & Christensen-Dalsgaard (1996) and it has been well documented that the periods of SX Phe change as a function of time with their rates of change being reported by several authors, Stock et al. (1972), Elst (1973), Coates et al. (1979), Coates, Halprin & Thompson (1982) and Thompson & Coates (1991). The derived long-term rates of change of these periods derived from quadratic fits to O–C data appear not to be constant, but this may be due to a constant long-term period increase or decrease being masked by much larger short-term changes. These uncertainties in period changes are an area of scientific research.

The objective of this study is to determine if a dedicated moderate size ground-based telescope (a

Dall-Kirkham (CDK) 24" robotic telescope) system can successfully image SX Phe variables in globular clusters in order to provide significant scientific data to the astronomical community. The advantage of a dedicated system is that long term time series studies can be performed on objectives of interest where larger systems are restricted in being time shared among a large group in the astronomical community.

Omega Centauri ( $\omega$  Cen, NGC 5139, or Caldwell 80) is a globular cluster in the constellation of Centaurus which is only observable from the southern hemisphere. At a distance of 17,090 light-years (5,240 parsecs), it is the largest-known globular cluster in the Milky Way Galaxy with a diameter of roughly 150 light-years. With an estimated 10 million stars, and a total mass equivalent to 4 million solar masses, Omega Centauri is the most massive-known globular cluster in the Milky Way. The  $\omega$  Cen cluster contains a large number of SX Phe variables.

An analysis has been conducted on a set of SX Phoenicis variable stars in  $\omega$  Centauri utilizing the CDK 24" robotic telescope located in the Río Hurtado Valley, in the south of the Atacama Desert. This system is operated by the Small/Scientific Telescope Engineering Learning and Astronomical Research group and provides periodic imagery of this and other globular clusters. In addition to determining whether SX Phe variables can be successfully imaged with the CDK 24" system, research is conducted to determine whether SX Phe variables in the  $\omega$  Centauri cluster

have demonstrated period variation in comparison to previously published papers in referred journals.

## 2. Instrumentation, tools, and processing data pipeline

A data pipeline and photometry processing chain were developed to take the raw imagery data from the CDK 24”, perform photometry on the images and execute a process to be able to produce lightcurves and periods of the variables of interest. This processing chain is described in detail in the 2024 SAS Symposium Conference talk, “Time Series Analysis of Variable Stars in Selected Globular Clusters” (Walker 2024).

This processing chain consists of selecting a target list for clusters, collecting the imagery over multiple observing windows, uploading the imagery to cloud, downloading the data to local disk storage, performing plate solving and aligning the images. Once all images have been aligned, the photometry analysis tool, AstroImageJ (AIJ), is used to extract lightcurves resulting in data text files which are then processed through the Persano period analysis tool to get period estimates and light and folded phase curves.

### 2.1 Instrumentation

Observations were conducted utilizing the fully robotic observatory located in the Río Hurtado Valley, in the south of the Atacama Desert in Chile.

The telescope is a PlaneWave CDK24 with the following specifications:

- Aperture: 610 mm (24”)
- Focal Length: 3974 mm
- Focal Ratio: F/6.5
- CO: 47%
- Tertiary Mirror: No

The mount is a PlaneWave L-600 on equatorial wedge with pointing accuracy <10-arcsecond RMS. Pointing precision is 2 arcseconds at sidereal velocity. Camera equipment include:

- QHY600M-Pro
- Sensor: Sony IMX455-K Monochrome back illuminated CMOS
- Pixel size: 3.76 microns
- Sensor size: 36mm \* 24mm (Full Frame)
- QE: Peak at 80%.

Filters include Sloan Digital Sky Survey (SDSS) of R, G and B filter bands.



**Figure 1. El Sauce Observatory (Observatorio El Sauce), Atacama Desert in Chile. Latitude: -30.4703073°, Longitude: -70.7646581°, Altitude: 1453m**

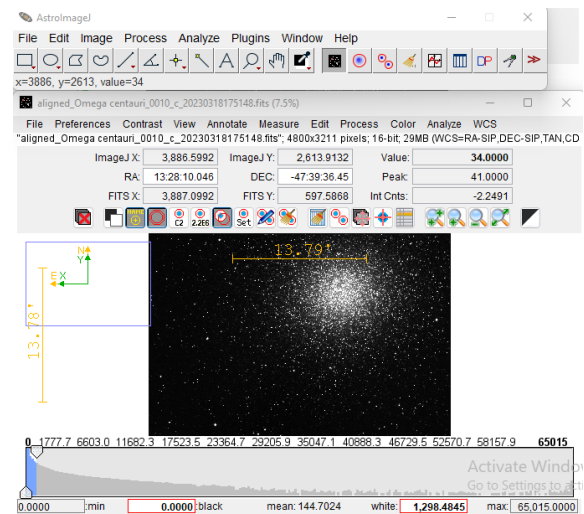


**Figure 2: AstroImageJ user interface.**

## 2.2 Processing Tools

### 2.2.1. Photometry

The photometry processing tool utilized for this project is AstroImageJ which is a very robust and flexible photometry tool. Once photometry is produced, the period analysis tool, Persano, is used for period analysis.

AIJ is an interactive, easy-to-use research-grade image analysis software. AIJ is built on ImageJ, which is used extensively in the field of biology and bioinformatics. The ‘astro’ edition of ImageJ has added to it many astronomy-specific data reduction, analysis, modeling and plotting capabilities.

### 2.2.2. Period Estimation and Analysis

Persano 3 is the leading light curve and period analysis software in astronomy. It offers a complete set of powerful analysis functions to work with large,

multi-night astronomical data sets, collected by a variety of observers. It is equally effective for the individual observer, who wants to analyze his observations of one or more nights.

A variety of period analysis algorithms are included with Persano which are used for light curve period estimation and analysis. These include:

- Lomb-Scargle (LS) periodogram (Scargle, 1982)
- Phase Dispersion Minimization (PDM) (Stellingwerf, 1978)
- Analysis of Variance (ANOVA)
- Discrete Fourier transform (DFT) (Deeming)
- and others.

For the period estimation, average values using a multiple of algorithm solutions are used as the final period number.

### 3. Selected SX Phoenicis Variables

Utilizing the University of Toronto Department of Astronomy and Astrophysics globular cluster website ([astro.utoronto.ca/~cclement/cat/C1323m472](http://astro.utoronto.ca/~cclement/cat/C1323m472)), a total of 40 SX Phe variables were selected for photometry analysis. Positions of these variables on the cluster are shown in Figure 4.

These 40 variables which meet the constraints of Field of View (FOV) on the image plates, magnitude and observability within the cluster center mass are shown in Table 1.

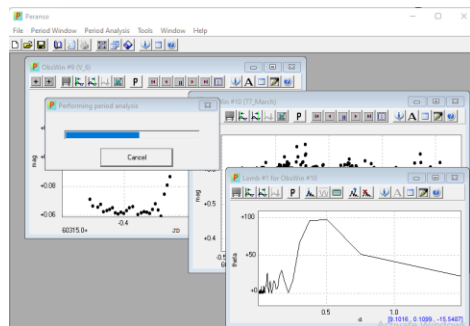


Figure 3. Persano results.

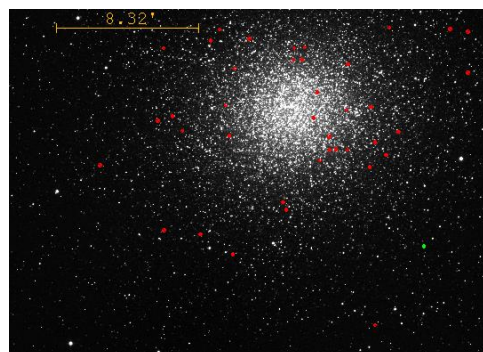


Figure 4. Approximate location of Sx Phe variables in the NGC 5139 cluster.

Seq#/Var ID	RA	Dec	Period (days)	Mag (V)
1-65	26:01.6	36:35.7	0.0627	14.922
2-194	27:53.9	31:53.9	0.0472	17.016
3-195	27:15.6	24:34.3	0.0655	16.780
4-197	26:20.5	31:59.2	0.0471	16.850
5-198	26:34.6	31:03.5	0.0482	17.533
6-199	26:28.7	28:37.9	0.0623	16.689
7-200	27:06.9	26:10.0	0.0495	16.568
8-204	27:08.0	37:05.1	0.0494	16.881
9-222	26:18.5	41:12.6	0.0389	17.310
10-225	27:02.3	24:36.5	0.0486	16.845
11-226	26:10.5	29:56.8	0.0379	17.299
12-227	26:14.4	23:53.7	0.0382	17.272
13-229	27:12.6	23:58.8	0.0375	17.407
14-231	27:19.1	35:53.8	0.0375	17.419
15-237	25:52.9	23:55.7	0.0656	16.861
16-238	27:34.0	29:22.8	0.0408	17.355
17-249	25:46.3	26:28.5	0.0349	17.435
18-250	27:31.7	35:41.6	0.0406	17.433
19-252	27:29.7	28:59.9	0.0466	17.445
20-294	27:32.1	25:03.5	0.0177	17.292
21-297	26:43.8	25:49.9	0.0339	16.628
22-298	26:50.3	34:03.3	0.033	17.410
23-300	25:46.5	24:00.4	0.0347	17.484
24-301	27:25.2	29:49.3	0.0354	16.974
25-302	26:47.0	25:44.4	0.0355	17.081
26-306	27:11.0	28:24.2	0.0384	17.528
27-309	26:20.2	28:39.1	0.0397	16.591
28-310	26:31.8	31:56.9	0.0402	16.791
29-312	26:40.4	29:11.2	0.0415	16.394
30-313	26:38.3	31:36.9	0.0418	17.678
31-314	27:08.9	30:08.3	0.0421	17.086
32-315	26:46.0	24:57.9	0.0423	16.392
33-316	26:14.9	31:10.3	0.0424	17.326
34-318	26:28.7	25:59.7	0.0437	16.799
35-319	26:28.6	31:02.4	0.0489	17.239
36-320	26:49.5	34:28.5	0.0472	17.294
37-322	26:38.9	27:38.6	0.0480	17.096
38-323	26:43.4	25:04.8	0.0494	16.638
39-324	26:18.2	30:34.6	0.0513	16.402
40-325	26:35.1	30:08.6	0.0535	16.410

Table 1. Selected SX Phoenicis for Analysis

The magnitudes for this set of variables range from a high of 14.9 to a low of almost 18 mag. (Figure 5). The corresponding periods for these variables range from 0.0177 to 0.063 days as shown in Figure 6 below. Notice the curious linearly increasing trend line

for periods for the higher variable number starting at 297.

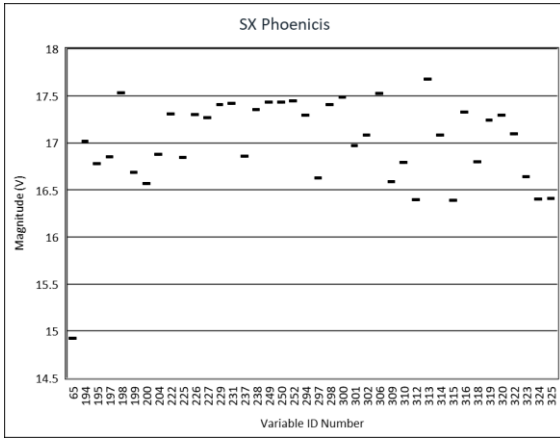


Figure 5. Magnitudes of variables under study.

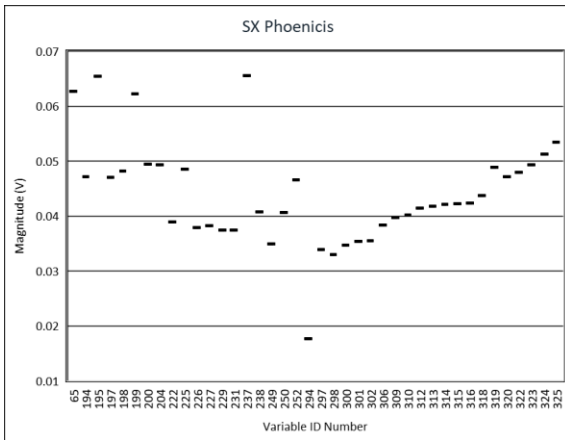


Figure 6. Periods in days of variables.

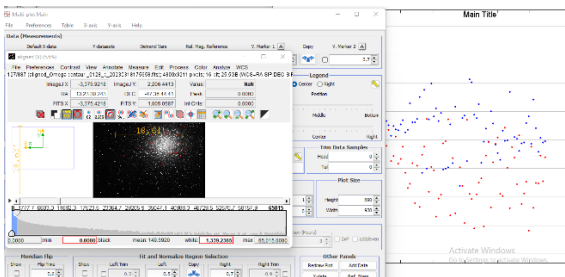


Figure 7. AstroImageJ processing photometry.

## 4. Photometry Results

Utilizing the AstroImageJ photometry analysis tool, the time series photometry of all 40 SX Phe variables were processed, and results saved off for period analysis. A typical processing run is shown in Figure 7.

Lightcurves are produced via the Persano observation window function. Examples of selected

light curves from the March and April 2023 runs are shown in Figures 8 through 15. It is clearly seen that the photometry from the April observations are not as crisp as those from March.

## 5. Period Analysis

Period calculations were performed using two separate approaches. The first utilized the processing as described in section 2.2.2 above with averaging results from multiple period estimation algorithms from the Persano period analysis tool. The second approach consisted of measuring the periods directly off the lightcurves where a clean enough curve was obtained to make this possible. Only a subset of the 40 variable set were able to produce periods via the measurement technique.

### 5.1 Period Analysis using Persano

It was found after running multiple experiments, that the period estimation results from the algorithms of LS, PDM, and ANOVA in Persano 3 produced the most consistent accurate estimates. An example of this process is shown in Figure 16. The resulting period estimates are reviewed in the Persano tool and adjusted to obtain the best folded phase curve, moved to an Excel spreadsheet, and then averaged to obtain the best estimate.

### 5.2 Periods Measured off the Lightcurves

Where lightcurves were distinct enough, measurements of the variable period were taken directed using the Julian Date timestamp. Twenty-one measurements were taken off the March observation run and only four were successfully taken off the April observations. An example of this measurement approach using the troughs of the periods is shown in Figure 17 for variable V194. Peaks of the periods can also be used as shown for V199 in Figure 18.

As with the Persano obtained estimates, multiple measurements are averaged to give the best period estimate.

### 5.3 Period Results

Using the measurement techniques described above, results are shown in Table 2.

A graphical comparison of the published periods for each variable against the calculated and measured periods for the March and April runs was taken from Table 2 and are shown in Figures 19-22.

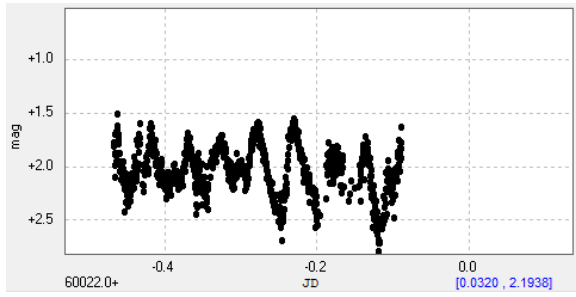


Figure 8A. Variable V65. March 2023.

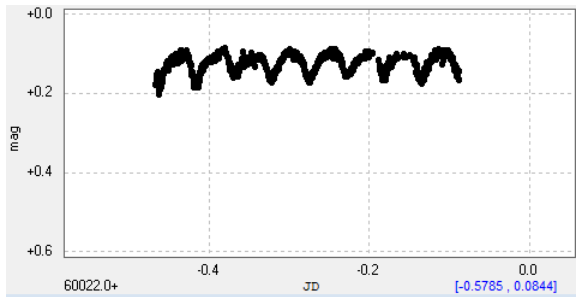


Figure 9A. Variable V194. March 2023.

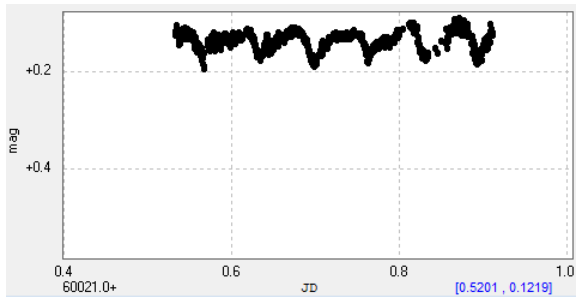


Figure 10A. Variable V195. March 2023.

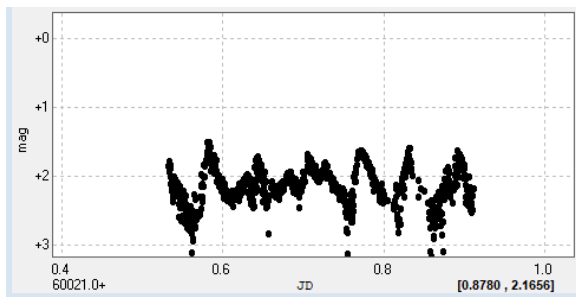


Figure 11A. Variable V198. March 2023.

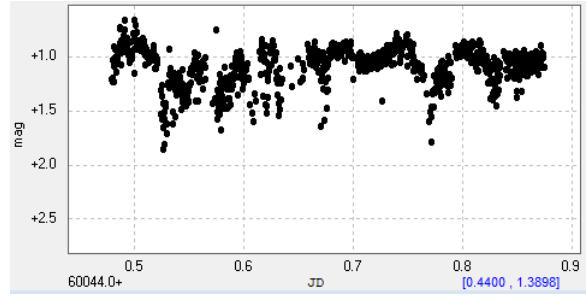


Figure 8B. Variable V65. April 2023.

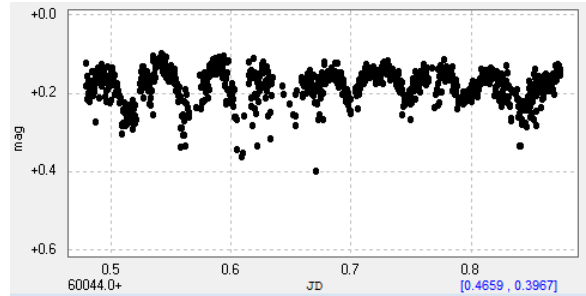


Figure 9B. Variable V194. April 2023.

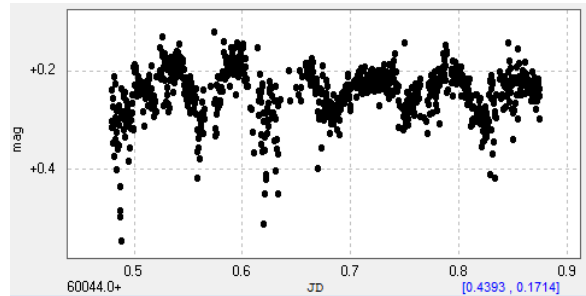


Figure 10B. Variable V195. April 2023.

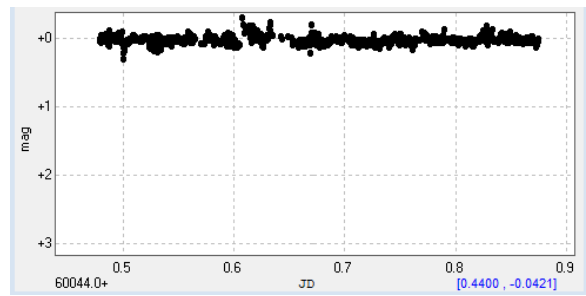


Figure 11B. Variable V198. April 2023.

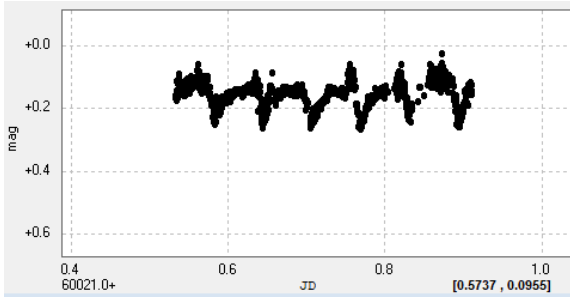


Figure 12A. Variable V199. March 2023.

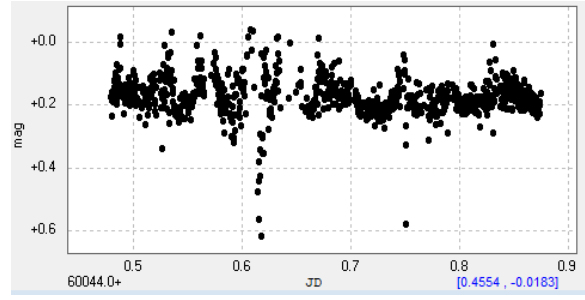


Figure 12B. Variable V199. March 2023.

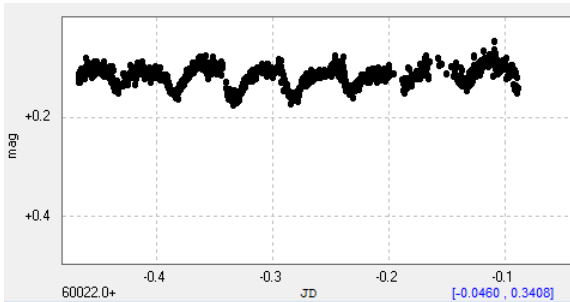


Figure 13A. Variable V200. March 2023.

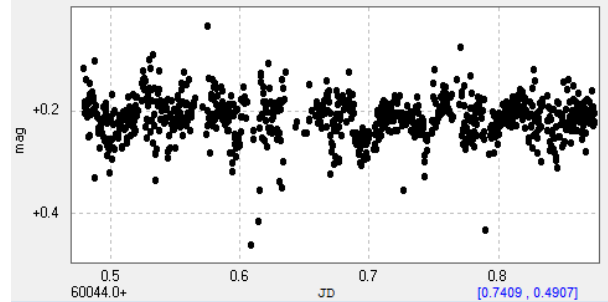


Figure 13B. Variable V200. April 2023.

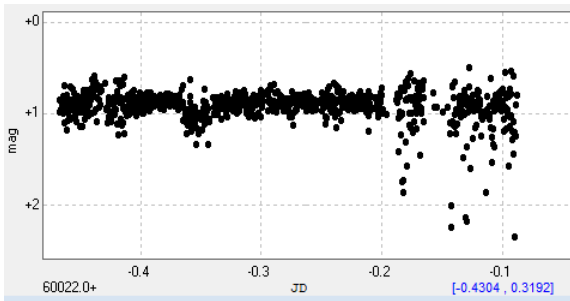


Figure 14A. Variable V301. March 2023.

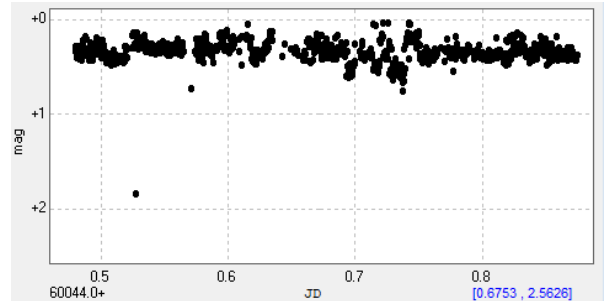


Figure 14B. Variable V301. April 2023.

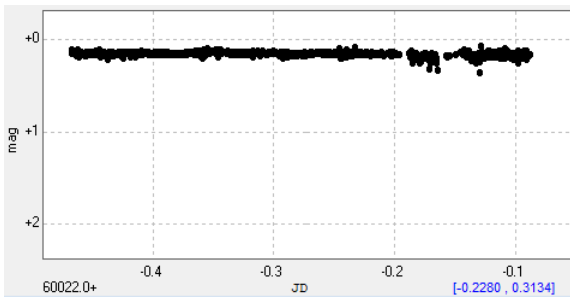


Figure 15A. Variable V310. March 2023.

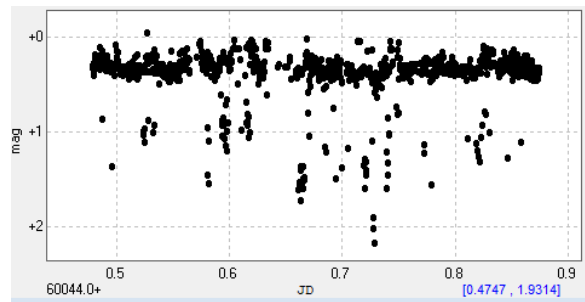


Figure 15B. Variable V310. April 2023.

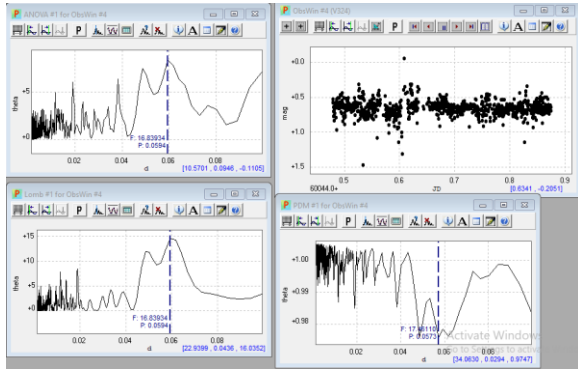


Figure 16. Period estimation results using Persano.

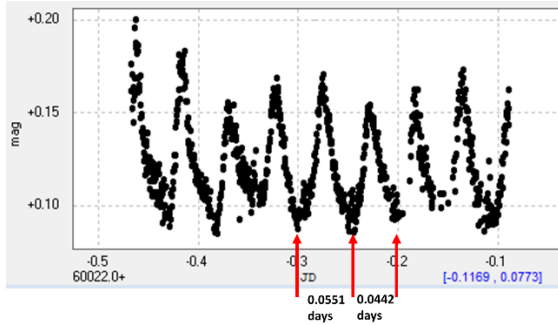


Figure 17. Period estimation directly off the lightcurve tough for variable V194.

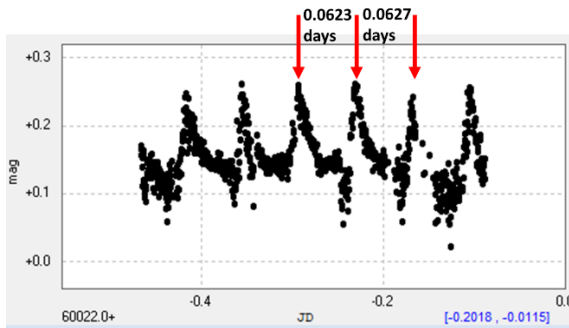


Figure 18. Period estimation directly off the lightcurve peak for variable V199.

## 6. Analysis of Variability Changes

Figures 23-25 show variables that have shown to exhibit significant changes in periods from the published 2017 periods. Variable 1 (var ID 65) in Figure 23 show changes from the published period to the March observation and back to the published value for April. Variable 5 (198) shows a steady increasing variable period.

In Figure 24, variables 12 (227) and 17 (249) show marked changes in periods with variable 249 showing a significant period change from published to March and especially to the April observation.

ID	March 2023			April 2023	
	Pub	Process	Measure	Process	Measure
65	0.0627	0.0469	0.0465	0.0613	-
194	0.0472	0.0478	0.0496	0.0472	0.0464
195	0.0655	0.0670	0.0665	0.0656	0.0687
197	0.0471	0.0468	0.0485	0.0483	-
198	0.0482	0.0576	0.0540	0.0707	-
199	0.0623	0.0596	0.0625	0.0236	-
200	0.0495	0.0885	0.0505	0.0488	-
204	0.0494	0.0502	0.0436	0.0501	0.0530
222	0.0389	0.0396	0.0541	-	-
225	0.0486	0.0360	0.0520	-	-
226	0.0379	0.0469	0.0511	0.0382	-
227	0.0382	0.0432	0.0626	0.1095	-
229	0.0375	0.0377	0.0543	0.0440	-
231	0.0375	0.0436	0.0588	0.0329	-
237	0.0656	0.0674	0.0642	0.0630	0.0668
238	0.0408	0.0472	-	0.0430	-
249	0.0349	0.0633	-	0.1876	-
250	0.0406	0.0404	-	0.0347	-
252	0.0466	0.0390	-	-	-
294	0.0177	0.0294	-	0.0685	-
297	0.0339	0.0564	0.0566	0.0749	-
298	0.0330	0.0460	0.0591	0.0740	-
300	0.0347	0.0374	-	0.0438	-
301	0.0354	0.0561	-	0.0367	-
302	0.0355	0.0377	-	0.0365	-
306	0.0384	0.0400	-	0.0347	-
309	0.0397	0.0611	-	0.0334	-
310	0.0402	0.0576	-	0.0734	-
312	0.0415	0.0685	-	0.0514	-
313	0.0418	0.0400	0.0409	0.0210	-
314	0.0421	0.0541	-	0.0410	-
315	0.0423	0.0404	-	0.0430	-
316	0.0424	0.0463	-	0.0650	-
318	0.0437	0.0512	-	0.0350	-
319	0.0489	0.0461	0.0501	0.0319	-
320	0.0472	0.0513	0.0545	0.0359	-
322	0.0480	0.0638	-	0.0436	-
323	0.0494	0.0611	-	0.0383	-
324	0.0513	0.0523	0.0531	0.0590	-
325	0.0535	0.0368	-	-	-

Table 2. Selected SX Phoenicis for Analysis

In Figure 25, variables 21 (297), 22 (298), and 28 (310) have exhibited significant changes in periods. The calculated and measured period for variable 21 (297) for March is essentially on top of each other. The April data shows a steady increasing period.

As shown in Figures 23 - 25, there are several variables which demonstrate potential period changes not only from the previous published values from 2017 but from measurements in the March and April observation runs. Additional study of these variables are needed to better determine behavior over time.



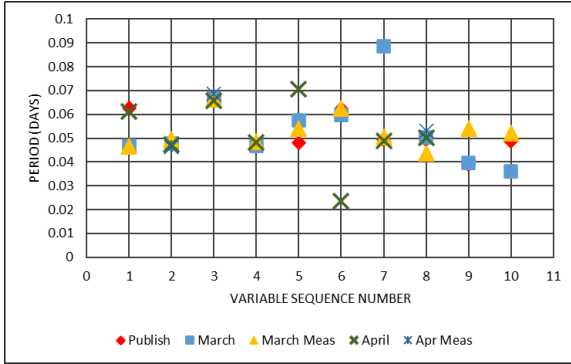


Figure 19. Comparison of periods for variables sequences numbers 1-10 (see Table 1 for variable ID)

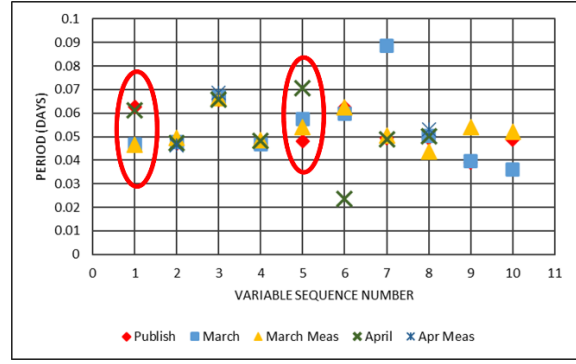


Figure 23. Significant changes in variables 65 and 198

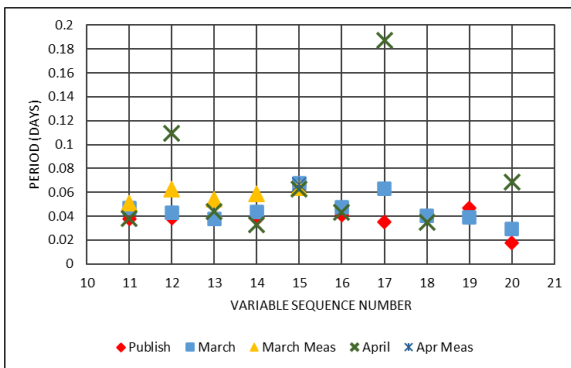


Figure 20. Comparison of periods for variables 11-20.

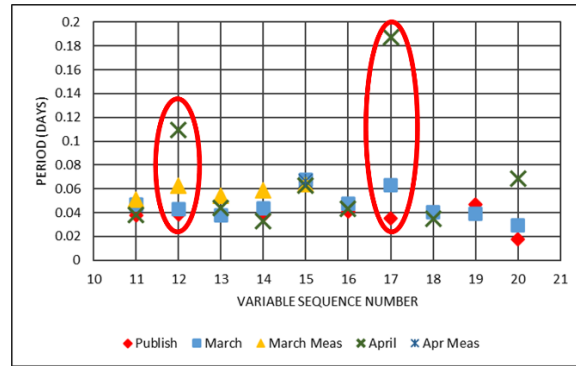


Figure 24. Changes in variables 227 and 249

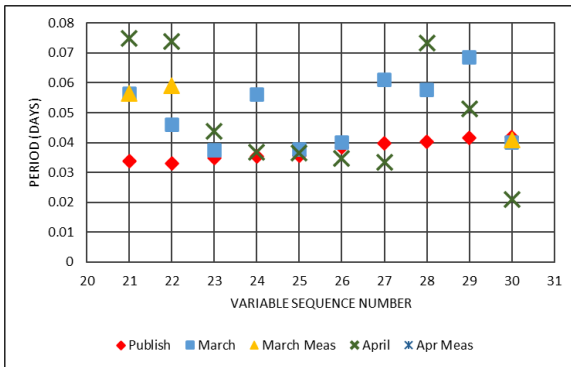


Figure 21. Comparison of periods for variables 21-30.

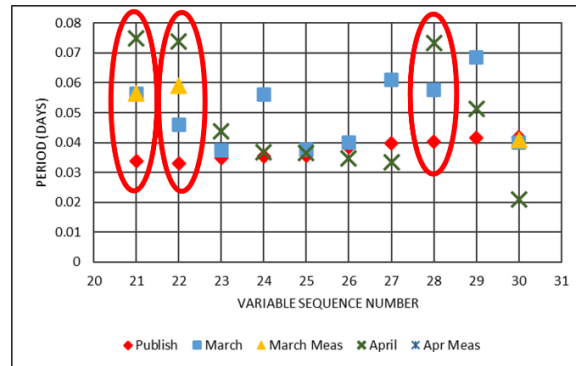


Figure 25. Changes in variables 297, 298 and 310.

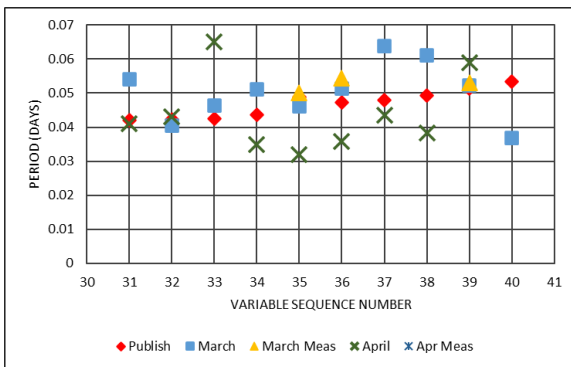


Figure 22. Comparison of periods for variables 31-40.

## 7. Conclusion

This research project has shown that persistent observation of variable stars in the crowded field of globular clusters is possible, and the corresponding time series analysis of the photometry data can yield potentially important scientific results.

This project has only demonstrated the potential for use of small ground-based telescope systems in long term observations of targets of interest. Much additional work is required to produce scientifically important results which can be reported in peer-reviewed publications.

## 8. Acknowledgements

Thanks to the Boyce Astro Research Initiatives and Education Foundation (BRIEF), San Diego, California, USA for funding the operation of the CDK 24" observing system which provided all the observational photometry data utilized in this research project. A special thanks go to Leon Bewersdorff and Nick Hardy, members of the Small/Scientific Telescope Engineering Learning and Astronomical Research for observing operations and data collection and Dave Rowe, CTO of Planewave Instruments, Adrian, MI, USA, for his encouragement and always positive comments during review of preliminary results.

## 9. References

GCVS Variability Types". General Catalogue of Variable Stars. Moscow, Russia: Russian Foundation for Basic Research, Sternberg Astronomical Institute. Retrieved 2010-03-17.

Landes, H., Bamberg, K.R., Coates, D.W., Thompson, K., 2007, Publications of the Astronomical Society of Australia, 24, 41-45

Petersen, J. O. & Christensen-Dalsgaard, J., 1996, A&A, 312, 463

Stock, J., Kunkel, W. E., Hesser, J. E. & Lasker, B. M., 1972, A&A, 21, 249

Elst, E. W., 1973, A&A, 23, 285

Coates, D. W., Dale, M., Halprin, L., Robinson, J. & Thompson, K., 1979, MNRAS, 187, 83

Coates, D.W., Halprin, L. & Thompson, K., 1982, MNRAS, 199, 135

Thompson, K. & Coates, D. W., 1991, PASA, 9, 281  
List of Milky Way Globular Clusters.  
<https://www.astro.utoronto.ca/~cclement/cat/listngc.html>

List of variables in NGC5139.  
<https://www.astro.utoronto.ca/~cclement/cat/C1323m>  
N. R. Lomb. Least-squares frequency analysis of unequally spaced data. Astrophysics and Space Science, 39:447–462, 2 1976.

J. D. Scargle. Studies in astronomical time series analysis. II - Statistical aspects of spectral analysis of unevenly spaced data. The Astrophysical Journal, 263(1):835–853, 1982

# Deneb and the $\alpha$ Cygni Variables

Joyce A. Guzik  
Los Alamos National Laboratory  
MS T-082, Los Alamos, NM 87545, USA  
joy@lanl.gov

Brian Kloppenborg  
American Association of Variable Star Observers  
185 Alewife Brook Parkway, Suite 410  
Cambridge, MA 02138, USA  
bkloppenborg@aavso.org

Jason Jackiewicz  
Department of Astronomy, New Mexico State University  
PO BOX 30001, Las Cruces, NM 88003, USA  
jasonj@nmsu.edu

---

## Abstract

Deneb, the prototype  $\alpha$  Cygni variable, is a yellow supergiant that shows irregular variability with quasi-period around 12 days in brightness and radial velocity. Abt et al. (2023) found that larger amplitude 12-day variations appear to resume abruptly and at an arbitrary phase and damp out after several cycles, with an interval of around 70 days between these resumptions. Here we make use of an 8.6-year photometric data set for Deneb from the Solar Mass Ejection Imager (SMEI) to better characterize this behavior. We find that the interval between pulsation resumptions is not exact, with the most common intervals between 100 and 120 days. Sometimes one or more intervals are skipped. We also examine AAVSO and Transiting Exoplanet Survey Satellite (TESS) light curves for  $\alpha$  Cyg variables Rigel, Saiph, and Alnilam in Orion, Aludra in Canis Major, and 6 Cas to compare with the behavior of  $\alpha$  Cyg. Except for 6 Cas, the time series are too short, or the observations too infrequent to draw any conclusions about similarities between the behavior of these stars and  $\alpha$  Cyg. We also summarize results of evolution and pulsation modeling for Deneb and  $\alpha$  Cyg variables from the literature. The  $\alpha$  Cyg variables may not be a homogenous group with a common mechanism for their variability. It has not been determined whether they are on the first crossing of the Hertzsprung-Russell diagram toward the red supergiant phase or are on their second crossing after having been red supergiants. Future plans include the examining BRITe Constellation data for Deneb, processing SMEI data for other bright  $\alpha$  Cyg variables, and comparing 6 Cas light curves from AAVSO and TESS data taken concurrently.

---

## 1. Introduction

Deneb, the prototype  $\alpha$  Cygni variable, is a bright spectral-type A2 Ia supergiant that shows a 12-day quasi-period with varying amplitude. Analysis of radial velocity and photometry from 1930 to the present shows evidence of abrupt resumptions of higher-amplitude pulsations occurring with an interval around 70 days (Abt et al. 2023, Guzik et al. 2023). Examples of this behavior are shown in the radial velocity data of Paddock (Fig 1) and the Transiting Exoplanet Survey Satellite (TESS, Ricker et al. 2015) photometry (Fig. 2).

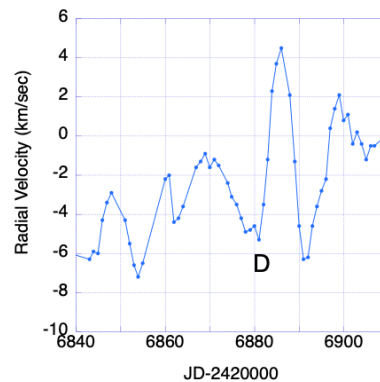
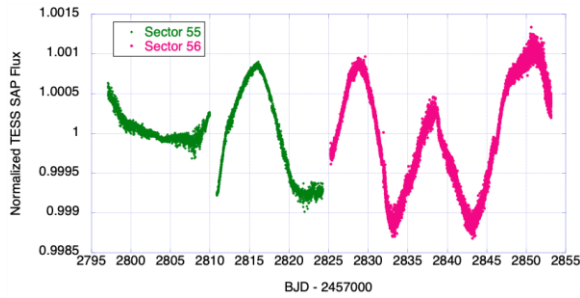


Figure 1: Deneb radial velocity data taken by Paddock May 12-July 21, 1932. The point labeled D shows an instance of an abrupt resumption of larger-amplitude pulsations.



**Figure 2: Deneb photometry from the TESS spacecraft August 5-September 1, 2022. Pulsations resume abruptly during Sector 55 (green).**

These analyses raise several questions:

- What is the cause of Deneb’s pulsations with quasi-period 12 days? Why 12 days?
- Why do the larger amplitude pulsations damp out and resume, perhaps every 70-80 days?
- Do other  $\alpha$  Cygni variables show similar behavior?

To begin to address these questions, we compare/contrast the behavior of Deneb with several other bright  $\alpha$  Cygni variables. More than one hundred  $\alpha$  Cygni variables are listed in the American Association of Variable Star Observers (AAVSO) Variable Star Index (VSX, Watson et al. 2006) database (<https://www.aavso.org/vsx/>). We make use of an 8.6-year photometric data set from the Solar Mass Ejection Imager (SMEI) to quantify evidence for any 70-day periodic pulsation resumptions in Deneb. We also examine light curves from TESS and AAVSO data for  $\alpha$  Cygni variables Rigel, Saiph, and Alnilam in Orion, Aludra in Canis Major, and 6 Cas. We review evolution and pulsation modeling results for Deneb and  $\alpha$  Cygni variables and identify simulations that could be carried out using, for example, the open-source MESA code.

## 2. Deneb SMEI Data

After results on Deneb were presented at the 112<sup>th</sup> AAVSO Annual meeting, Kloppenborg offered unpublished photometric data on Deneb from the Solar Mass Ejection Imager taken from 2003 through 2011 (Jackson et al. 2004, Clover et al. 2011). The SMEI spacecraft was in a Sun-synchronous polar orbit with a 102-minute period. While the spacecraft was designed to measure solar coronal mass ejections (CMEs), it also observed almost every bright ( $V < 6$ ) star. It had three cameras equipped with non-linear optics that provided each camera with a  $3 \times 120$  degree field-of-view of the sky. These data require processing

to remove camera-to-camera zero-point offsets, angle-dependent flux loss causing a  $\sim 100$  day curvature or change in slope, and other spacecraft-related noise and artifacts.

### 2.1 Deneb SMEI light curve

Figure 3 shows the 8.6-year Deneb SMEI light curve after some processing to partially remove curvature and offsets. One data point is taken each spacecraft orbit, i.e., every 102 minutes or 1.7 hours. Figures 4-6 zoom in on portions of the light curve where the  $\sim 12$ -day Deneb pulsation period can be discerned. These light curve segments also show some discontinuities of unknown origin that may be intrinsic to the star or may be remnants of incomplete removal of offsets. These discontinuities are outlined by many SMEI data points, and therefore not the consequence of a single bad data point. Since other Deneb time-series data sets also show discontinuities (see, e.g., the Richardson et al. (2011) data plotted in Abt et al. 2023), we are reluctant at this point to rule out intrinsic stellar behavior as the source.

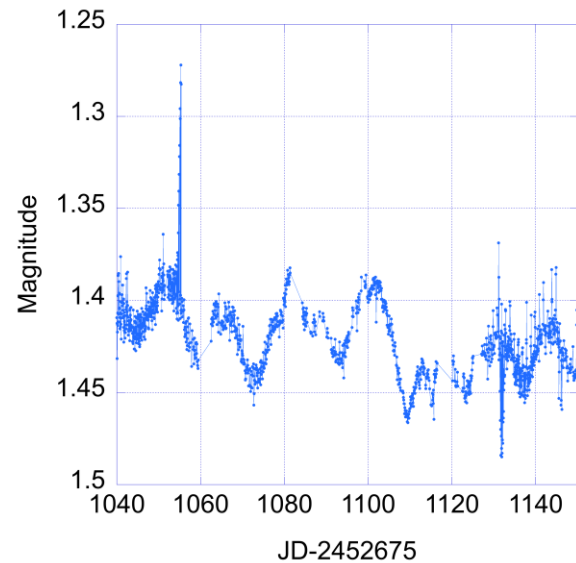


**Figure 4: Magnitude vs. Julian date for Deneb SMEI data, showing some oscillations with quasi-period 12 days, and two discontinuities**

### 2.2 Statistics of events

We attempted to quantify the intervals between resumption of a few cycles of larger-amplitude 12-day pulsations as seen in Figures 4-6, as well as the intervals between the discontinuities. Figure 7 shows a histogram of the days between the discontinuities. The most common interval is in the third bin after 50

days, i.e., between 75 and 87.5 days. This period is close to but a little longer than the intervals suggested by Abt et al. (2023) for abrupt resumptions in pulsations.

Figure 8 shows a histogram of the number of days between resumptions of larger amplitude pulsations with quasi-period 12 days. The interval is less pronounced but appears to peak between 100 and 125 days.

As hoped, the Deneb SMEI data has high-enough cadence and accuracy to identify resumptions of  $\sim 12$  day pulsations. In the SMEI data, the abrupt excursions, if intrinsic to the star, are not correlated with the resumption of larger-amplitude pulsations. The pulsation resumptions seem to occur at longer and more irregular interval than the 70 days hypothesized by Abt et al. (2023). The abrupt excursions do not appear to ‘reset’ the pulsation phase, except perhaps in the one example of Figure 5.

We also applied Fourier analysis to the entire SMEI data set. Not unexpectedly, the amplitude spectrum (Fig. 9) does not show any well-defined periodicity.

### 3. Other $\alpha$ Cyg Variables

To begin to answer the question of whether other  $\alpha$  Cyg variables have light-curve properties similar to Deneb’s, we chose a few of the brightest  $\alpha$  Cyg variables from the AAVSO VSX database: Rigel, Saiph, and Alnilam in Orion, and Aludra in Canis Major. We also decided to look at 6 Cas because this  $\alpha$  Cyg variable was mentioned in Abt et al. (2023) as having a similar spectral type and age as Deneb.

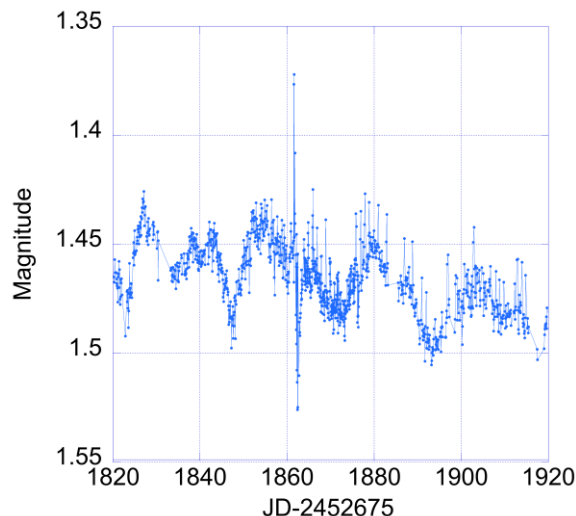


**Figure 5: Magnitude vs. Julian date for Deneb SMEI data, showing a few oscillations with quasi-period 12 days, and one abrupt discontinuity that seems to interrupt the phase of one of the oscillations**

We found data for all of these stars in the AAVSO International Database (Kloppenborg 2023). The data for Aludra were sparse, and the data for Rigel, Saiph, and Alnilam did not have the precision to follow pulsational variations in detail. The data for 6 Cas were more extensive and will be discussed below.

We also found TESS data for all of these stars at the Mikulski Archive for Space Telescopes (mast.stsci.edu). We discuss the High-Level Science Product (HLSP) light curves for each star below. These light curves have been processed by various investigators using special pipelines starting from the TESS full-frame images or target pixel files.

### 3.1 Rigel

Rigel ( $\beta$  Ori, HD 34085, TIC 231308237) has V magnitude 0.13 and spectral type B8 Iae. TESS observed Rigel during two 27-day sectors, Sector 5 and Sector 32. However, an HLSP light-curve product is only available for Sector 5. The 30-min cadence light curve (Fig. 10) shows some interesting variations, but a longer time series is needed to identify any quasi-periodicities or to draw any comparisons with Deneb or other  $\alpha$  Cyg variables. There are some artifacts remaining in the light curve after data processing (vertical lines at nearly regular intervals).

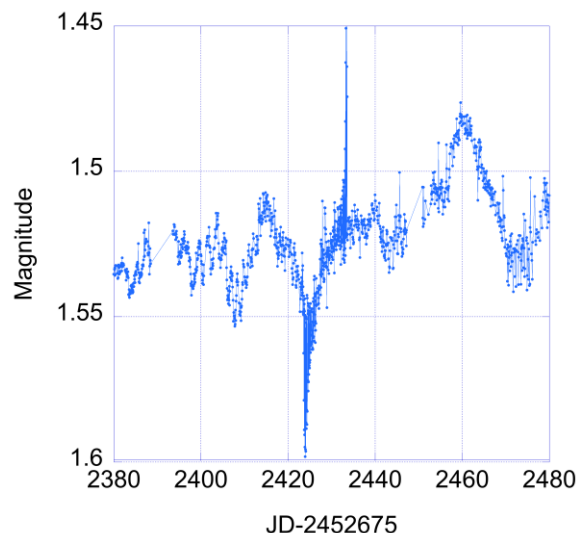


**Figure 6: Magnitude vs. Julian date for Deneb SMEI data, showing a few oscillations with quasi-period 12 days, and two closely spaced discontinuities**

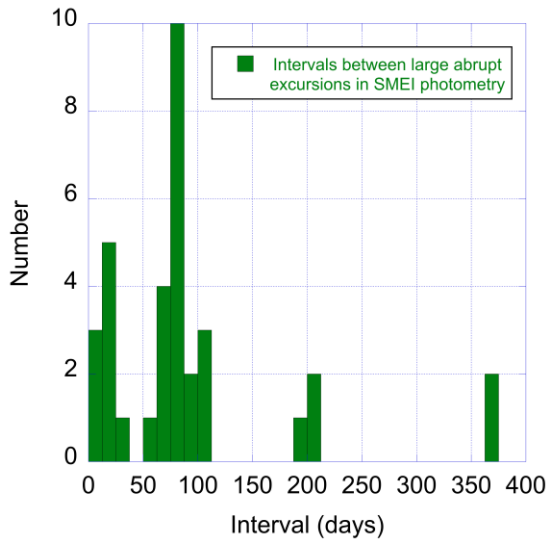


Figure 7: Intervals between discontinuities in Deneb SMEI photometry

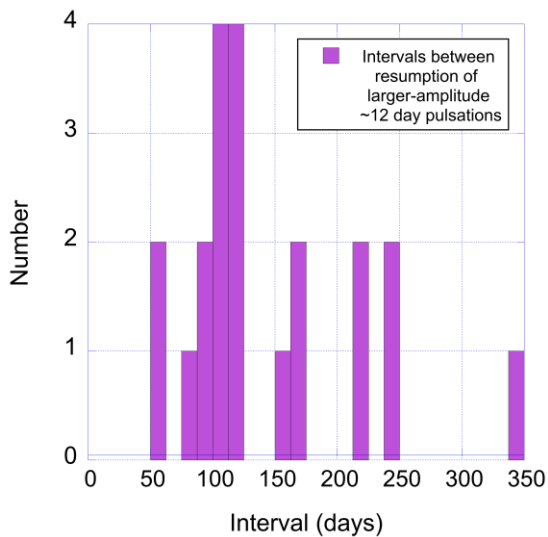


Figure 8: Intervals between resumption of a few cycles of ~12-day larger amplitude pulsations in Deneb SMEI photometry

### 3.2 Saiph

Saiph ( $\kappa$  Ori, HD 38771, TIC 427451176) has V magnitude 2.06 and spectral type B0.5 Ia. TESS observed Saiph during two 27-day sectors, Sectors 6 and 33. Figure 11 shows the TESS HLSP light curve for Sector 6 with 30-min cadence, and Figure 12 shows the TESS HLSP Sector 33 light curve with 10-min cadence. The Sector 6 light curve has been detrended more successfully than the Sector 33 light curve. Both light curves show aperiodic variability, with some interesting larger excursions to high and low

amplitudes. Again, longer time-series data are needed to make any comparisons between Saiph and Deneb.

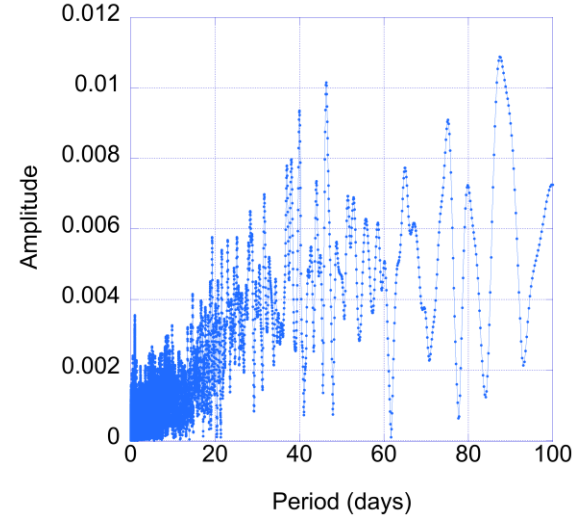


Figure 9: Amplitude spectrum of Deneb SMEI data, showing that there is no well-defined periodicity

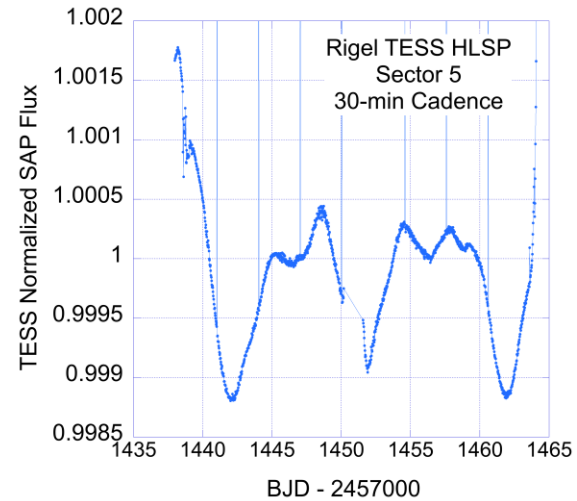


Figure 10: Rigel TESS HLSP Sector 5 light curve

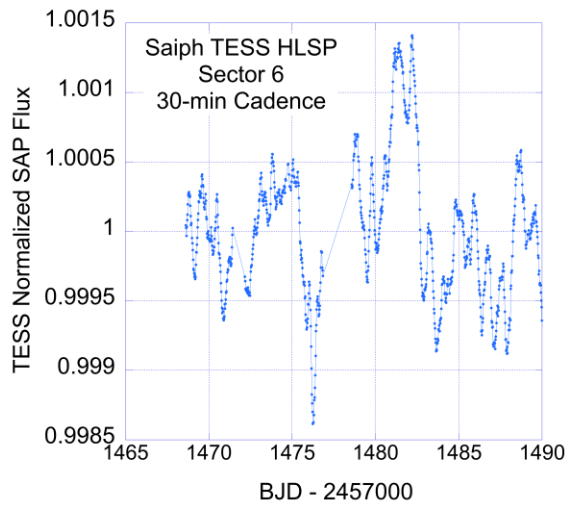


Figure 11: Saiph TESS HLSP Sector 6 light curve

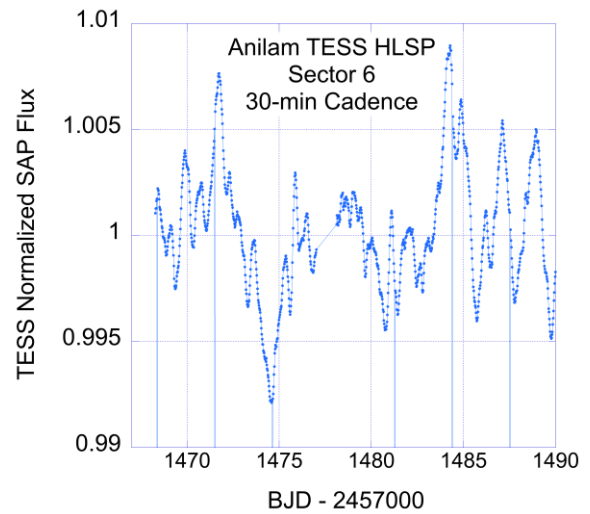


Figure 13: Anilam TESS HLSP Sector 6 light curve

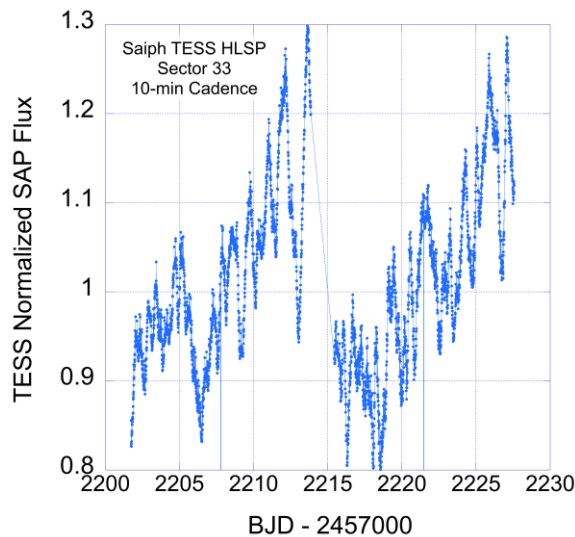


Figure 12: Saiph TESS HLSP Sector 33 light curve

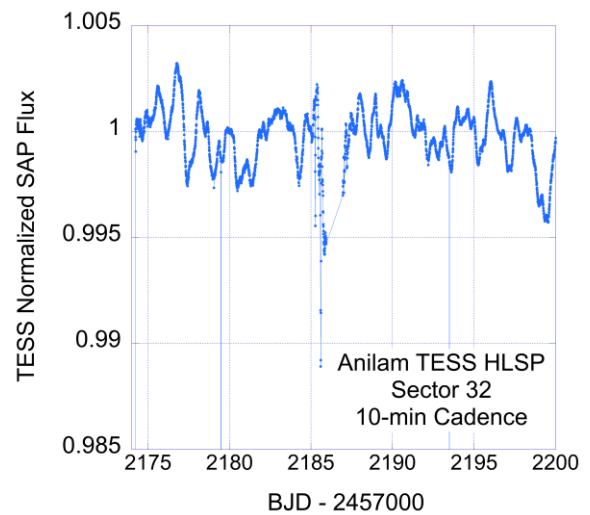


Figure 14: Anilam TESS HLSP Sector 32 light curve

### 3.3 Anilam

Anilam ( $\epsilon$  Ori, HD 37128, TIC 427451176) has V magnitude 1.69 and spectral type B0 Ia. Anilam was observed by TESS during Sector 6 and Sector 32. Figures 13 and 14 show the TESS HLSP light curves. A few data artifacts remain, but the HLSP light curves were detrended well. There appear to be some larger dips and peaks in the light curves. A longer time series may help to identify any regularities in the occurrence of these features.

### 3.4 Aludra

Aludra ( $\eta$  CMa, HD 58350, TIC 107415639) is the bright star in the tail of Canis Major. Aludra has V magnitude 2.45 and spectral type B5 Ia. Aludra was observed by TESS during Sectors 34 and 61. The HLSP TESS light curves (Figs. 15 and 16) appear to have been detrended well, but still contain a few artifacts. As was the case with Anilam, a couple of high and low brightness excursions are identifiable, but a longer time series is needed to identify any periodicities in the appearance of these excursions.

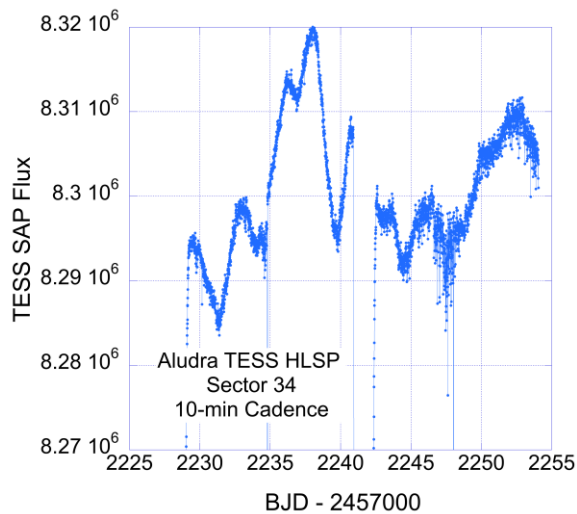


Figure 15: Aludra TESS HLSP Sector 34 light curve

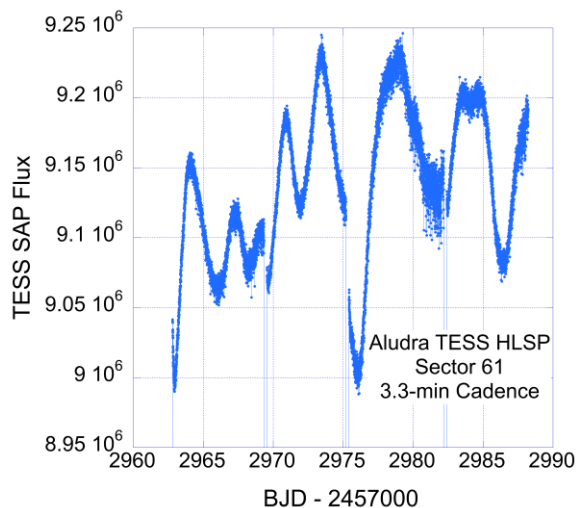


Figure 16: Aludra TESS HLSP Sector 61 light curve

### 3.5 6 Cas

6 Cas (V566 Cas, HD 233835, TIC 470694175) is listed as a double or multiple star in the SIMBAD database, with the two stars having spectral types A2.5 I+O9.8 II. Presumably the A2.5 I star, with nearly the same spectral type as Deneb, is the  $\alpha$  Cyg variable. The V magnitude of 6 Cas varies between 5.34 and 5.45 with a strongest periodicity of 37 days (Koen and Eyer 2002).

6 Cas has been observed extensively by several AAVSO observers at U, V, B, R, and I wavelengths during the past two years. Figure 17 shows the AAVSO light curves. The  $\sim$ 37-day period is prominent in the observations taken between JD 245850 and JD 245910.

6 Cas was observed by TESS during five sectors: 17, 18, 24, 57, and 58. The HLSP data from these sectors needs further detrending. Figure 18 shows the Sector 18 light curve. Since the time series of TESS sectors is only 27 days, prospects may be better using AAVSO data to look for instances of the 37-day periodicity.

## 4. Stellar Evolution and Pulsation Modeling

The evolutionary state and cause for variability of  $\alpha$  Cyg stars continues to be an area of active research. Some modeling results are found in Gautschy (2009), Georgy et al. (2021), Saio (2011), Saio et al. (2013), and Saio et al. (2016). Evolution modeling of massive stars incorporates treatments for physical processes that are not well constrained, among them, mass-loss rates, rotational mixing, and the treatment of convection. Enhancing mass loss, and to some extent,

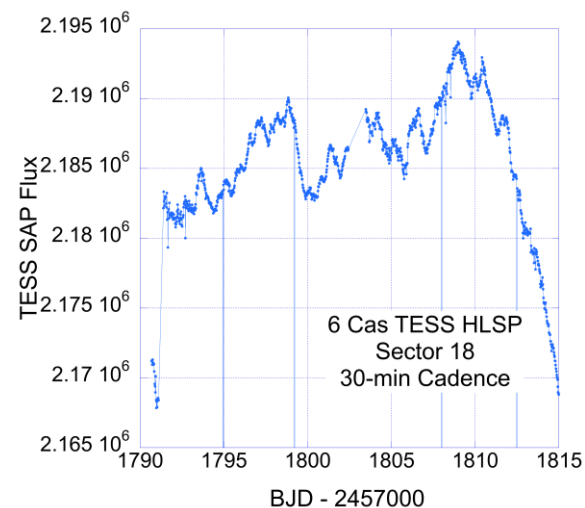


Figure 18: 6 Cas TESS HLSP Sector 18 light curve

rotational mixing, can cause evolution models for stars of initial mass greater than 14 solar masses to ‘blue loop’ back into the blue and yellow supergiant regions of the Hertzsprung-Russell (H-R) diagram after having first evolved across the H-R diagram to become red supergiants.

To explore whether the variability of  $\alpha$  Cyg stars is caused by pulsational instabilities, analyses have been carried out to search for mechanisms to excite pulsations with the observed periods of  $\alpha$  Cyg variables. Several mechanisms have been proposed and debated. Gautschy (2009) found, for models crossing the H-R diagram for the first time, that nonradial dipole and quadrupole gravity modes are overstable in the stellar envelope above a convection



zone overlying the hydrogen-burning shell. Georgy et al., Saio (2011), and Saio et al. (2013, 2016) find that the pulsation properties of  $\alpha$  Cyg variables can only be explained by models that have ‘blue-looped’ after the red supergiant phase. Their analyses find both radial and nonradial modes excited by the kappa (opacity valving) mechanism in ionization regions associated with the Fe opacity bump, 2<sup>nd</sup> helium ionization, or hydrogen ionization, depending on the effective temperature and evolution state. They also find modes excited by so-called strange-mode instabilities for stars with luminosity-to-mass ratio in excess of 10,000 times that of the Sun, and ‘low-degree oscillatory convection (nonadiabatic g-) modes’ associated with a convection zone produced around 200,000 K by Fe ionization. However, these 2<sup>nd</sup>-crossing models have an observational issue--in order to get the models to blue loop, enhanced mass loss, aided by rotational mixing, is needed. This mass loss and mixing, in conjunction with convective ‘dredge-up’, results in increased surface helium abundances and nitrogen-to-oxygen (N/O) and nitrogen-to-carbon (C/O) ratios at the stellar surface, since helium and nitrogen produced from deep nuclear burning are mixed to nearer the surface and exposed by mass loss. The helium abundance and N/O, and C/O ratios predicted are too high compared to those observed in  $\alpha$  Cyg variables. Using the Ledoux criterion for convective stability in the core, instead of the usual Schwarzschild criterion, reduces the amount of convective mixing. This model change almost works to restore agreement with observations for the bluest supergiants, but not for  $\alpha$  Cyg.

These authors note that the  $\alpha$  Cyg variables may not be homogeneous class in terms of evolutionary state, and their pulsations may not have a single explanation. The variations may not even be caused by pulsations, but rather by some other surface-layer instability.

The evolution and pulsation results discussed here were conducted with non-open-source codes, but models could be explored (and prior results verified) using the open-source Modules for Experiments in Stellar Astrophysics (MESA, Jermyn et al. 2023) code, (<https://docs.mesastar.org/en/release-r24.03.1/>), and the associated stellar pulsation codes GYRE (Townsend and Teitler 2013) and RSP (Paxton et al. 2019).

It is likely that modeling codes with capabilities beyond MESA are needed to make progress to understand massive star variability, for example, 2-D or 3-D codes that can model the hydrodynamics of stellar envelopes, or codes that can look at the response of the atmosphere in the presence of strong stellar winds, pulsations, and/or shocks.

## 5. Conclusions and Future Work

The long time-series high-cadence SMEI data was very helpful in answering some of our outstanding questions about Deneb. The larger amplitude  $\sim$ 12 day pulsations do not appear to resume at exact intervals, but sometimes skip intervals, with typical intervals closer to 100 days, longer than the 70-day interval hypothesized by Abt et al. (2023). There does not seem to be strong evidence for abrupt events that interrupt the pulsation phase. There are some discontinuities in the SMEI data which involve multiple data points per event—it is not clear whether these are instrument or data-reduction artifacts, or intrinsic to Deneb’s behavior. These events do not appear correlated with the resumptions, and the interval between them is on average shorter, around 75-90 days.

We have examined TESS and AAVSO data for several other  $\alpha$  Cyg variables. The TESS data is of high cadence and has excellent precision needed to follow  $\alpha$  Cyg variations. The data need further detrending in some cases; the time series lengths are too short to make additional comparisons with the behavior of Deneb.

The AAVSO data for 6 Cas appear promising for investigating properties of its long-term variations. There is even some overlap in time of the AAVSO data with the TESS Sector 57 and 58 data that will be valuable for intercomparison. The other  $\alpha$  Cyg variables Rigel, Saiph, Aludra, and Anilam discussed here have some AAVSO data, but the precision is not adequate to do much more than verify that their variations are consistent with  $\alpha$  Cyg variables.

We have recently found Deneb data taken using the BRITTE constellation satellites (Weiss et al. 2014) spanning June 11 to Nov. 24, 2014 and June 8 to Nov. 2, 2015. We hope to work with the BRITTE principal investigators to compare this data to the SMEI data set to confirm some of our conclusions.

Since the Solar Mass Ejection Imager observed many stars brighter than 6<sup>th</sup> magnitude, we hope to mine this data set for light curves of additional  $\alpha$  Cyg variables.

Finally, we may delve into using the MESA code to continue to gain insight on the evolution state and causes of variations for  $\alpha$  Cyg variables.

## 6. Acknowledgements

This research made use of data from the Mikulski Archive for Space Telescopes (MAST), the SIMBAD database (<https://simbad.u-strasbg.fr/simbad/>), and

TOPCAT (<https://www.star.bris.ac.uk/~mbt/topcat/>) software. We acknowledge with thanks the variable star observations from the AAVSO International Database contributed by observers worldwide and used in this research. J.G. acknowledges support from Los Alamos National Laboratory, managed by Triad National Security, LLC for the U.S. DOE's NNSA, Contract #89233218CNA000001. We made use of the Discrete Fourier Transform program FWPEAKS kindly supplied by A. Pigulski, written by Z. Kołaczowski, G. Kopacki, and W. Hebisch (Astronomical Institute, Wrocław University, Poland).

## 7. References

- Abt, H.A., Guzik, J.A., and Jackiewicz, J. 2023, The Abrupt Resumptions of Pulsations in  $\alpha$  Cygni (Deneb), *PASP* **135**, 1054, 124201
- Clover, J.M., et al. 2011, Epsilon Aurigae light curve from the Solar Mass Ejection Imager, *AAS Meeting Abstracts* **217**, 257.02
- Gautschy, A. 2009, Deneb's variability: a hint of a deep-lying convection zone?, *A&A* **498**, 273-279
- Georgy, C., Saio, H., and Meynet, G. 2021, Blue supergiants as tests for stellar physics, *A&A* **650**, A128
- Guzik, J.A., Abt, H., Jackiewicz, J., and Kloppenborg, B.K. 2023, Abrupt Periodic Pulsation Resumptions in Deneb, Proceedings of the 112th Annual Meeting of the AAVSO, <https://www.aavso.org/112>
- Jackson, B.V., et al. 2004, The Solar Mass-Ejection Imager (SMEI) Mission, *Sol. Phys.* **225**, 177
- Jermyn, A.S., et al. 2023, Modules for Experiments in Stellar Astrophysics (MESA): Time-dependent Convection, Energy Conservation, Automatic Differentiation, and Infrastructure, *ApJS* **265**, 15J
- Kloppenborg, B.K. 2023, Observations from the AAVSO International Database, <https://www.aavso.org>
- Koen, C. and Eyer, L. 2002, New periodic variables from the Hipparcos epoch photometry, *MNRAS* **331**, 45
- Paddock, G.F. 1935, Spectrographic Observations of Alpha Cygni, *Lick Obs. Bull.* **17**, No. 472, 99
- Paxton, B., et al. 2019, Modules for Experiments in Stellar Astrophysics (MESA): Pulsating Variable Stars, Rotation, Convective Boundaries, and Energy Conservation, *ApJS* **243**, 10P
- Richardson, N.D., Morrison, N.D., Kryukova, E.E., and Adelman, S.J. 2011, A five-year spectroscopic and photometric campaign on the prototypical  $\alpha$  Cygni variable and A-type supergiant star Deneb, *AJ* **141**, 17
- Ricker, G.R., et al. 2015, Transiting Exoplanet Survey Satellite, *Journal of Astronomical Telescopes, Instruments, and Systems*, Volume 1, id. 014003
- Saio, H. 2011, Linear analyses for the stability of radial and non-radial oscillations of massive stars, *MNRAS* **412**, 1814-1822
- Saio, H., Georgy, C., and Meynet, G. 2013, Evolution of blue supergiants and  $\alpha$  Cygni variables: puzzling CNO surface abundances, *MNRAS* **433**, 1246-1257
- Saio, H., Georgy, C., and Meynet, G. 2016, Progress and problems in massive star pulsation theory, *Astronomy in Focus*, Focus Meeting 17 XXXIXth IAU General Assembly, August 2015, ed. Piero Benvenuti, doi:10.1017/S1743921316006.41
- Townsend, R.H.D. and Teitler, J. 2013, GYRE: an open-source stellar oscillation code based on a new Magnus Multiple Shooting scheme, *MNRAS* **435**, 3406T
- Watson, C.L., Henden, A.A., and Price, A. 2006, The International Variable Star Index (VSX), *Society for Astronomical Sciences Annual Symposium*, Vol. 25, p. 47
- Weiss, W.W., et al. 2014, BRITe-Constellation: Nanosatellites for Precision Photometry of Bright Stars, *PASP* **126**, 573

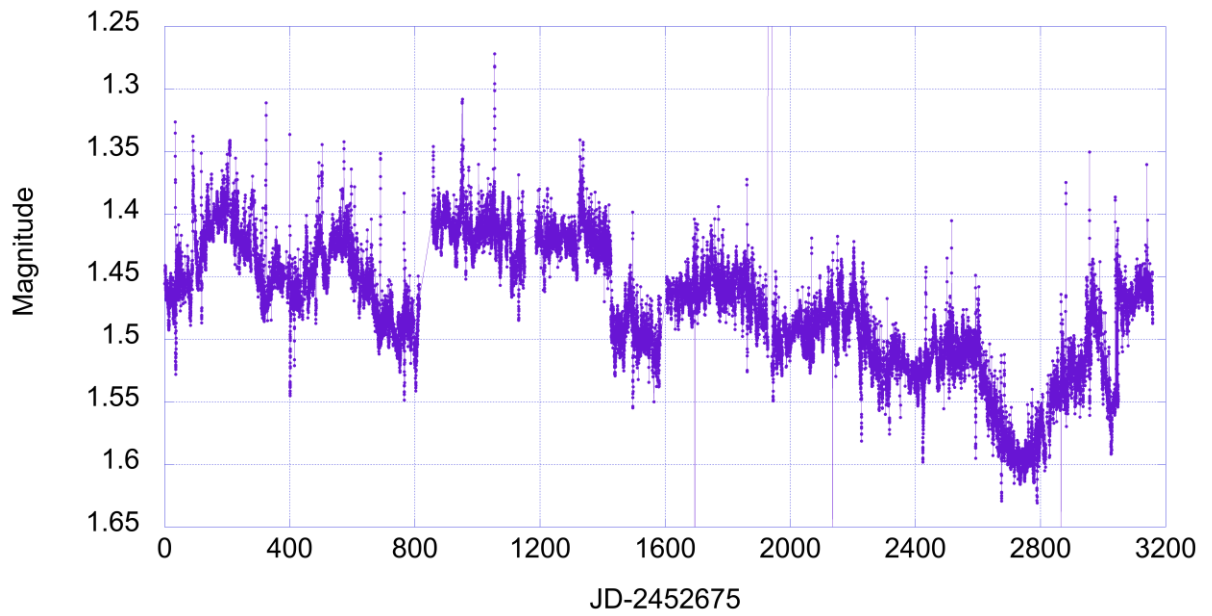


Figure 3: Deneb 8.6 year partially processed light curve from Solar Mass Ejection Imager (SMEI)

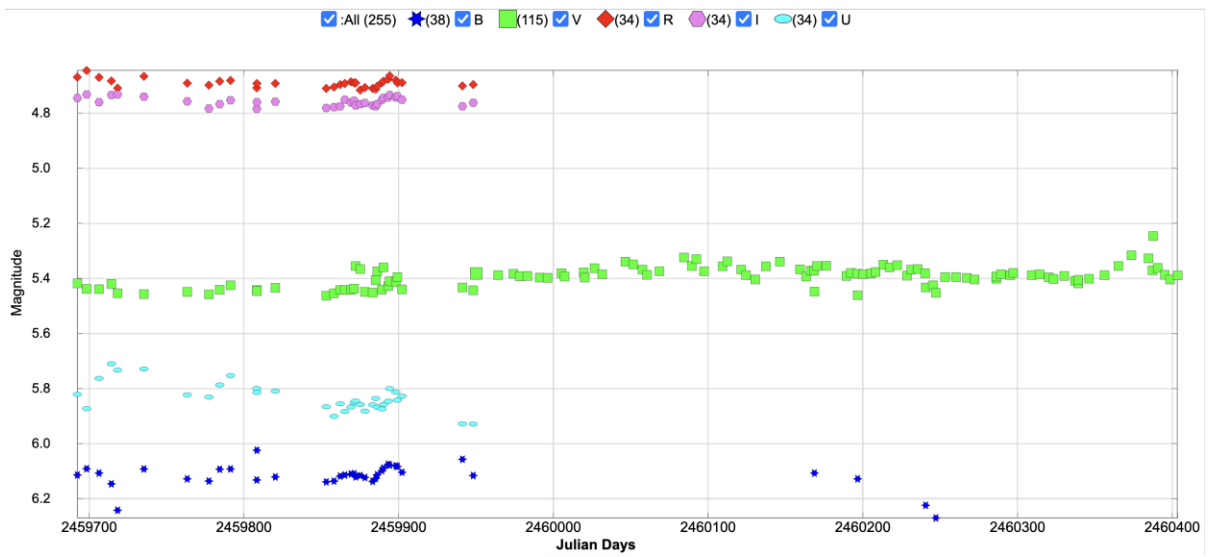


Figure 17: 6 Cas light curves from AAVSO database from April 2022 through April 2024

# A Lifetime of Total Solar Eclipses

John Menke  
130 E 3d St  
Frederick, MD 21701

---

## Abstract

We review our 60 years of travels to past eclipses, with special attention to the 2024 event, including the various attempted observations, casual and scientific.

---

## 1. Introduction

Virtually all amateur astronomers have attempted to attend at least one total solar eclipse. Some seem to collect eclipses like baseball caps, while others are satisfied with one, or a few. By happenstance, my experience has probably been in the middle: I have attempted to see six eclipses and have been at least partially successful in each. But each one has been different, in both positive and negative ways.

Here is the list:

July 20, 1963	Maine (Jackman)
March 7, 1970	Dismal Swamp (Va)
February 26 1998	Curacao, South America
March 29, 2006	Turkey (Mediterranean)
August 21, 2017	Missouri
April 8, 2024	Illinois

Serendipitously I found out about the 1963 Maine eclipse days before I drove to Maine for a vacation in the woods in Jackman, Maine. Indeed, I learned that the eclipse centerline would pass only 13 miles from the cabin in which I would stay, on the very weekend I had planned to be present. The afternoon of the event had mixed clouds, but we were in one of the holes and our view, if not perfect, was in fact perfectly awesome. There were also some fussy engineers seeking to do some eclipse measurements who used the primitive satellite data of the day to move some ten miles away to get better skies. With, of course, the result that they were completely clouded out. I did borrow a pair of opera glasses to get a better view of totality.

Seven years later, at the last minute, loaded up family in the 57 Chevy SW, and headed down into Virginia to the Dismal Swamp. Yes, it was pretty dismal. But there was relatively little traffic, and we simply pulled off the road with about ten minutes to go. The swamp produced just the best total eclipse sounds: Frogs, birds, snakes, alligators(?). My optical aid was part of a WWII x7 tank telescope taped onto a

super-8 movie camera. Handheld. Yes, I still have the movie, and yes, it does get very bright, very fast as the sun comes back into view.

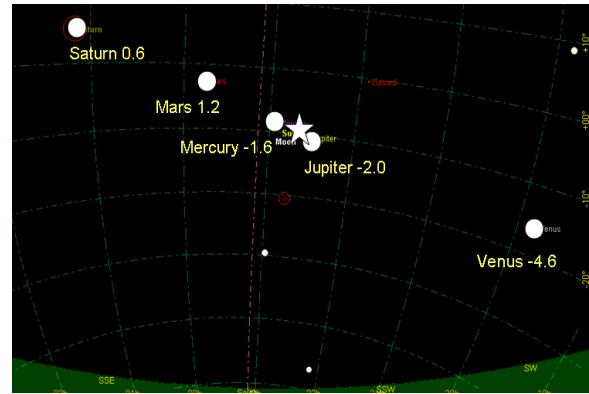


Figure 1. Sky for 1998 total solar eclipse

Then came a long lapse of 28 years until 1998. This eclipse curved down into South America, and we joined a small astronomy tour group from Washington DC. Just North of South America, Curacao is a small and very delightful Dutch island. The eclipse day began with overcast and rain, but it began to clear as we arrived at the observing area. At eclipse time, the sky was the darkest I've ever seen, with Saturn, Mars, Mercury, Jupiter, and Venus literally lined up across the sun—Copernicus would be pleased. This eclipse introduced us to that strange phenomenon experienced since—loud, unrestrained singing, cheering, and shouting from most people around. Well, at least they were not (I hope) carrying-on to make the sun reappear!

Only seven years later, we arranged a trip to Turkey (“always wanted to go there”) coincident with the 2006 eclipse. All kinds of great adventures (talk to me offline). But this time, I prepared an experiment with my little Meade 4inch and the venerable (and weird) DSS7 spectrometer to record the flash spectrum. So we are on the beach with the Mediterranean, and stunningly clear skies. I set up on

the card table. Everything working. Two minutes to go, do one more check that the imaging is fine, everything aligned. Click the button, and lo! Instead of the sun, I see that beautiful Blue Screen of Death on my Toshiba. It will take at least 3-5 minutes to get going again. Might as well look at the spectacle in the sky. Thank you, Bill Gates.

Number five comes in 2017, the first of the American eclipses. We are in Missouri, on a corner of a beautiful winery. This time I plan a spectro-polarization measurement using an 8-inch scope. But nature intervenes, as the temperature rises. And rises. And goes up. No shade (didn't think of that). No hat (oops). And it gets hotter. It got so hot I could not function, or even think straight. And it got hotter. The eclipse did happen, it was good, and the singers and yellers were somewhat muted across the pond. Got no data but learned some things. Like hats.



Figure 2. Path of totality for April 8, 2024

## 2. Total Solar Eclipse 2024

This eclipse path went from Texas up through Maine. Totality could be seen in a path about 100 miles wide; however, at the edge of the path totality would be very brief, while at the center it would be about 4 minutes. Meg (my wife) and I planned to go, and were to be joined by Meg's sister from Iowa.

My very first total eclipse in 1963 I enjoyed outside my cabin at Henderson Camps in far north Jackman, Maine. The centerline of this 2024 eclipse would pass only a few hundred yards across the same place: Wow! What a temptation. But this is 61 years later, and I had some science to do. Thus choosing where to go balanced primarily distance vs. predicted likelihood of clear skies rather than nostalgia.. The weather was predicted to be only about 50:50 along the path, but with somewhat better chance of being

clear toward the south end of the path. We chose as our base camp the extreme west end of Kentucky near the confluence of the Ohio, Cumberland, and Tennessee Rivers in the city of Paducah (well known for very little). The center line was across the Ohio in Southern Illinois, with lots of space and many small towns averaging 15 miles apart, having lots of potential observing places and dispersed traffic. We focused on the town of Anna, population about 4500, where Google showed many big lots, fields, parks, etc. in pretty countryside.

Making a reservation in December for a hotel in Paducah was easy...if you were willing to pay \$500-1000/night, three night minimum, with no cancellation. But, we found a place for a straight \$90/night directly across from one charging these amounts (and ours turned out to be the best place we stayed on the trip).

A week ahead, the Anna weather for Eclipse Day was predicted to be a sunny day, slight breeze, about 70F. While forecasts along the rest of the path seemed to change each day (usually for the worse), Anna's changed almost not at all. Indeed, as predicted, the three days before the eclipse were cloudy/rainy, the three days after were rainy/cloudy, but the Eclipse Day itself turned out to be exactly right: beautiful.

From Paducah, Anna looked to be about 1.5 hours away, which turned out to be the actual driving time. After about a half hour surveying downtown Anna, we found a beautiful spot next to the unfilled municipal swimming pool at the City Park. Grass, level, parking 20 feet away, and no one else there: what could be better?

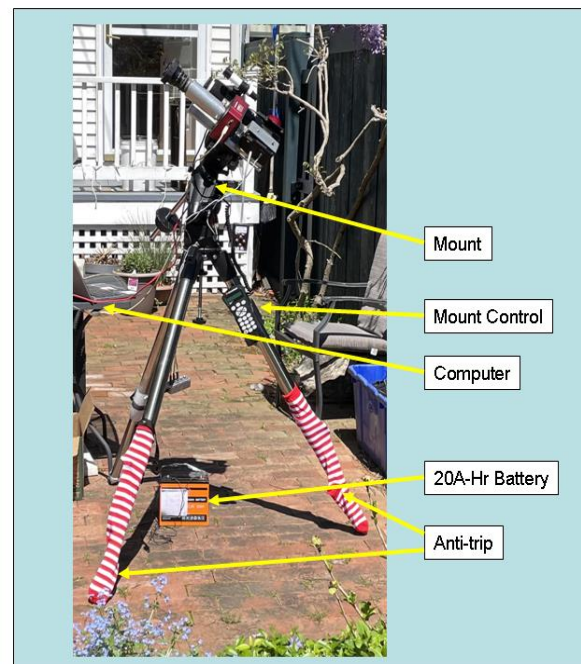


**Figure 3. Setup for 2024 total solar eclipse.**

Besides admiring the eclipse, I had planned four “experiments”. First (Ex1) was to get a series of exposures of the corona during the four minutes so that I could prepare a nice corona image showing streamers and structure in the corona extending well out from the sun. The second (Ex2) was to obtain spectra from the edge of the sun at the beginning (Contact 2) of totality, with the hope of recording the so-called “flash spectrum” when dark absorption lines change to emission lines for a few seconds. The third experiment (Ex3) was to obtain the spectrum of the corona during totality. Ex4 was to obtain the flash spectrum from Contact Four at the end of totality.

Each experiment had its own challenges. I assembled two small telescopes and cameras on a medium size equatorial mount (Celestron AVX) that would track the sun. The mount worked fine. The camera/telescope used for Ex1 itself was one of my own standbys, but the spectral camera (Ex2/3/4) was a new one that would deliver color, plus more than 5 images per second. This camera ended up requiring that I use a new, rather complex, imaging software (SharpCap) that I had to learn. After much internal debate, I chose to run both cameras from the same PC, each using a different imaging program running simultaneously. Although a bit scary, this worked well. To assure power, I obtained a 20Ahr battery (much better than the standard lead acid) which worked extremely well, and my tests showed it could power everything for at least 4-5 hours.

The spectrometer design for Ex2/3/4 went through several iterations during my testing and design. I ended up with a setup that used my 20-year-old SBIG DSS7 spectrometer, with a few of my own modifications to make it more suitable. Although the DSS7 is a bit weird in its design, with its modifications (mostly a much longer slit) it worked well for this. Because the DSS7 allows the user to move the slit in/out, the DSS7 can be switched between a typical slit spectrometer, and a slit-less (similar in use to placing a non-collimating grating in an imaging train). This allows formation of a spectrum anywhere in the FOV thus removing the need for accurate alignment of the slit on the object being analyzed. This would be essential for the Contact 4 flash spectrum when the position of the sun peeking out would be hard to track..

All four experiments required that the exposure and duration of each image had to be reasonably accurate, so I spent much preparation time on that issue. This was done mostly by testing the systems with a simulated eclipsed sun in my basement, then calibrating using the nearly full moon in our sky at night. Although Ex2/3/4 used the same setup (except

for the Contact 4 slit removal), each required radically different filtering. Ex2 worked with raw sun thus requiring a very dark filter (about x50,000 light attenuation) because raw sunlight would be entering it, while Ex3 required less than <500 attenuation. I had to change filters right after totality began, but this worked well.

We had about 1.5 hours before totality, seemingly sufficient time to assemble the rig. Besides the optics, there had to be a table, a small tent for shade (to be able to use the PC). Early experiments had shown a major problem to be tripping over the tripod legs, so I painted their bases white, and then had candy striped stockings pulled over them. Setup went a bit slow but was more or less done less than ten minutes before totality (due at 1:59 PM local time), leaving very little time to review the coming operations. Yes, this turned out to be the Achilles heel of the day.

As totality began, there were steps to take to assure proper pointing, focus, tracking. Everything had to be checked and rechecked (eg., 2-3 minutes before totality, I discovered that the scope tracking had somehow become turned off—never did figure that one out). But as totality began, I did the various steps to begin observations, with glances up at the wonderful hole in the sky (never got a good look because I had to keep reading glasses on to see the PC).

The screen showed that both setups were receiving good data, with very good exposures, focus, pointing, tracking, etc. However, it was clear within about a minute that both setups were having a problem saving the results. The new software was particularly difficult to understand what it was doing, or not doing. And I had the fear that if I was misunderstanding and things were in fact ok, by doing anything I could “break” the process. Very frustrating but reflected the lack of having done way too little test running of data taking. Under normal circumstances, it would be easy to identify and fix these problems—but this was not a normal circumstance.

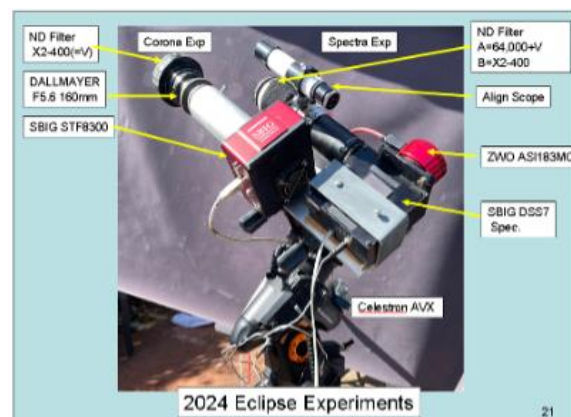


**Figure 4. 2024 total solar eclipse experiments.**

In any case, the four minutes rushed by. I did eyeball the great data coming into the PC, including actually seeing the “flash spectrum” with bright lines in place of the normal dark lines; however, only a small portion of data from each experiment was actually recorded. Reminded me of the recent SpaceX rocket test—everything worked great...until the rocket blew up. It took me two days before I got up the nerve to look at the limited results in the PC.

The corona photo sequence was heavily truncated, with only about 10% of the expected images made. The spectra should have taken gigabytes of storage, but only one extended file of 12MB was present. That had an “.ser” filetype which I had never used. After two weeks, I finally found that a few programs including Registax6 would handle it. However, decoding the file showed only a dark, plain field. Thus, no spectra were properly recorded.

Anyway, the eclipse was over as scheduled, we packed up, and headed for the hotel. Eclipse traffic was thick, so it took some five hours to return. With much time spent kicking myself for the failure to practice saving images when under time pressure (including recovering from errors).

### **3. Next Eclipse**

There is much buzz around the 2026 eclipse. Nominally in Iceland, it will also be visible from Greenland. But there are a few niggling problems. Actual viewing spots are very hard to get to. Plus the eclipse is very early in the morning, so the Sun is very low. And the weather looks problematic, at best.

But the next eclipse, on August 2, 2027, does look great. The centerline passes right through the Straits of Gibraltar, with Southern Spain to the North and Morocco to the South. Nearly five minutes, late in the morning. The weather is very likely hot, but clear. Now doesn't all that sound good?

### **4. Conclusion**

The total solar eclipse is surely one of the awesome sights we are privileged to have in our lives. Once would be awesome, but a half dozen draws gratitude. For a scientist, it is also an invitation to observe and record this fleeting event. However, Murphy's Law is as exacting as the laws governing the eclipse, only totally realistic and painful testing will allow success in eclipse science. But mere experimental failures do not detract from the wondrous event that is yours..for just looking up.

# AZ Cas Observations - a 12-year Summary

John Menke  
130 E 3d St  
Frederick, MD 21701  
john@menkescientific.com

## Abstract

AZCas is a 9 year, magnitude 9, eclipsing binary, having giant red and blue components. It was examined in 1977, but has had virtually no attention since. Using R=3000 spectrometers and photometry, we have been observing this system since 2012 with the goal of improving our understanding of this system.

## 1. Introduction

AZCas is a 9.3 mag, Eclipsing Binary of 9.3 year period and is composed of a red giant and a blue giant. It was analyzed in 1977 by Anne Cowley; however, virtually no work has been done on it since then to verify or advance our knowledge of the system.

Using a homebuilt 18in Newtonian and homebuilt spectrometers, I have been following the behavior of AZCas since 2012 when I serendipitously caught what appears to have been a major upset near the Ha line. After years of only occasional observations, in 2018 I began observations on every adequate night, with an average of 3-4 days cadence (the weather in MD is not conducive to continuous coverage!). To date, I have about 450 nights of data (over 1000 hours). A typical set of measurements includes a series of spectra of star SAO11931 (7 mag, B star), SAO11927 (7 mag K star) (both nearby in the sky), and AZCas (9mag red & 11mag blue components). The two SAO stars are used as wavelength checks.

The spectrometer used until early 2022 was a homebuilt Littrow R=3000 design having a bandwidth of about 700Å. After 2022, a new spectrometer was built of similar design, but having two (2) gratings with the light beam split into red and blue beams using a dichroic. This allows recording the red and blue spectra simultaneously on the same camera. The current camera is a ZWO 2600MM used in Bin-2 mode.

The blue star in AZCas is about mag 11, so the blue spectrum is near the lower sensitivity limit for this observing system. When the weather permits >1 hour total exposure, reasonably good results can obtain down to about 3800Å.

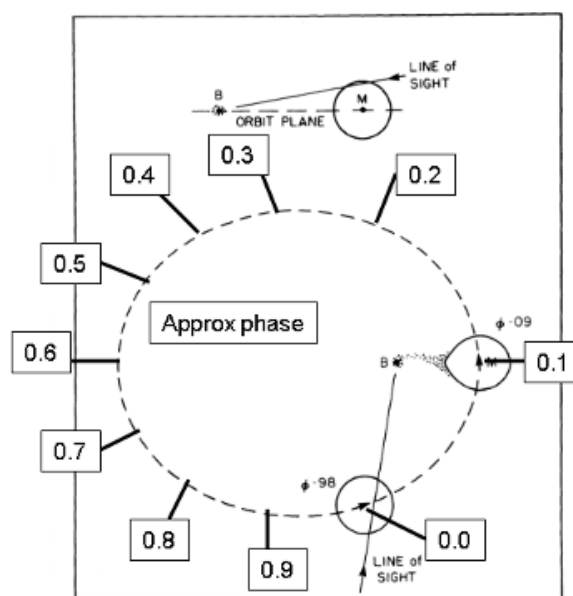


Figure 0. Orbital phase diagram for AZ Cas

Although the observing methods evolved over the period, in general the goal has been to obtain 3-4 hours of AZCas spectral data. The individual 300s spectral images are then calibrated, background subtracted, averaged (combined), then downloaded into spreadsheets. There the spectra are normalized (rectified) to a value of "1" in a region having little structure (6650 or 4600Å for the red or blue spectrum), displayed and inspected. Using reference spectra (usually SAO11927) the wavelength offset (calibration) was adjusted to fit the observed H lines.

In addition to the spectroscopy observation program, photometry is also conducted using an 11 inch RC scope, equipped with a four filter system (B,V,R,I). Observation is carried out at about 2-4 week intervals to record AZCas and a set of eight comparison stars.



## 2. AZCas

Most of what is known of AZCas comes from the only significant paper on the star written by Anne Cowley in 1977. Using historic and then-current photometric and spectroscopic data, she developed a model of the system. The system is shown in approximate schematic form. The eclipse shown is the primary eclipse (red star occulting blue star) at Phase=0.0. Periastron is approximately one year (0.11 phase) after the primary eclipse. The secondary eclipse (blue star in front of red star) at approx phase=0.2 is expected to be <0.002 mag in red, and even less so in blue, and is unlikely to be observable.

Cowley found evidence of mass transfer between the stars, especially near periastron. There has been almost no additional research on the system since Cowley's paper.

**Figure 1 is at the end of the paper.**

## 3. The 2012 Event

While testing a new homebuilt spectrometer (R=3000) in 2012, I observed many (Ha) emission stars. AZCas was present in several lists of Be stars, and being circum polar, was convenient to observe. On Aug 6, 2012, I began an approximate 6 hour observing run of AZCas under automatic control. The next morning, it was apparent that clouds had passed over during hours 3-4, and when clouds were present, the telescope had no particular guide star to follow. The Ha spectra from before (A=Red) and after (B=Black) the cloud event were strikingly different as shown in Figure 2.

The curves in this figure differ in some details from those published earlier by this writer as a result of a reanalysis of the Aug 6, 2012 data. The wavelength scale of both the A&B groups was carefully matched to details of structure in the spectra, then matched to later spectra that included comparison stars. Among other changes, a 2A difference between the A&B sets was noted and corrected.

The Green curve in Figure 1 shows data from 041323 (MMDDYY) near periastron, with all curves wavelength aligned to within 1 pixel (about 0.4A). In each curve, the absorption notch is at 6561A. In curve A and 041323, the deconvolved notch is approximately 0.5 in amplitude.

Note that during the 2012 event, the absorption and 6563 peaks remained at the same wavelength, the absorption peak increased to about 1.5 amplitude, and a brand-new emission occurred at 6559A. An analysis every 15 minutes showed no trends in either the A or

B sets of data of that date. The spectrum had returned to the red ("normal") curve two days after the event. There were no apparent differences anywhere else in the spectra with the possible exception that HeII (at about 6680A) appears not to be present.

There is no known instrumental or other artifact that could account for the 2012 event. The spectra show no other unusual effects.

## 4. Results of Observations

Having seen such a large, fast change in the spectrum of AZCas in 2012, I eventually decided to start a long-term observation of AZCas to learn more and to see whether this was a frequent occurrence. The AZCas observations to date have covered the phases from about 0.6 to 1.0 to 0.1 on virtually every night having even barely adequate conditions (approx. 1:4 nights in Maryland). No upsets near Ha similar to 080612 have been seen. Approximately 450 nights have been observed for over 1000 hours of observation.

Given the generally steady spectral shape (ie. the "normal" AZCas) I have observed (example in Figure 2), it also occurred to me that smaller upsets like August 2012 might occur too fast to show in a spectrum averaged over several hours. A search about 10 nights of particularly good data were made using 25 min (5 exposure) binning (vs the usual binning of all 2-4 hr of data) ; however, no sign of upsets was seen. Thus, the goal of observing more upsets has not been met, and what caused the 2012 upset is unknown.

As the AZCas Project has evolved, we have, of course, modified and improved the observing program. As evolved, the practice is to attempt up to 4 hours of five minute spectra of AZCas. The session also includes one or more spectra of comparison stars SAO11931 a 7 mag B blue star, and SAO11927 a K2 7 mag red star used for tracking wavelength and amplitude changes.

**Figure 2 is at the end of the paper.**

Far from periastron (phase up to 0.7 or so) one sees a broad emission feature near Ha centered on 6563 with a narrow absorption feature on the blue side at 6561. Fig 3 shows a representative sample: black curve is a comp B8 star, green is the Ha absorption in a K2 comp star used for wavelength calibration (at 6563A), while red is AZCas. The black broken line is the apparent broad Ha emission.

**Figure 3 is at the end of the paper.**

Approaching periastron, as shown in Fig 3 the Ha emission greatly increases in intensity and narrows to about 3A FWHM, with the blue absorption line showing only as a notch on the blue side of the Ha emission. Analysis of multiple curves shows that the almost buried absorption line remains essentially unchanged: amplitude about 0.5, the wavelength of 6561A, and width of about 2.0A (roughly the resolution of the spectrometer).

The result of the analysis showed that, within likely observational errors, the absorption feature remained essentially constant in all respects (wavelength and amplitude), even as the Ha emission increased nearly fivefold close to periastron! That is, the absorption feature 6651 is unaffected by the nearness of the two stars as periastron is approached, while the Ha emission feature is enormously affected. These characteristics will constrain any models that try to explain the spectroscopic features.

During this observing project, the only additional spectral changes of note have been the “wiggles” on the red side of the Ha emission, as partially seen in Fig 2. These wiggles come and go in hours to days with is no apparent periodicity. Their wavelengths are always the same, even as they appear and disappear. One can even see these in the Group A 080612 data during the upset.

## 5. Spectral Doppler Shift

To improve the understanding of the AZCas system, we have measured the Doppler shift of AZCas vs SAO11927 K2 used as a reference star nearby in the sky. Both stars are red, and have roughly similar spectra. In the first half of the campaign, I usually took reference star spectra four times during each observing session, later reducing this to one spectrum taken to simplify operations.

Figure 4 is at the end of the paper.

To measure the Doppler shift, we take advantage of the many common spectral lines in both AZCas and the reference star by calculating the correlation between the two spectra over a substantial wavelength interval (the wavelength region near Ha is excluded as it greatly distorts the correlation calculation). This calculation is done for twenty different 1 pixel offsets (shifts) of the two spectra. Plotting the resultant correlations will show the offset when the correlation will be at a maximum. The value of this offset is a measure of the offset, presumed to be the Doppler shift, between the spectra of the two stars.

We can then fit a curve to the correlation results to find the precise pixel offset where the correlation is

at a maximum. This allows a precision of about 0.1A (about 5km/s) in the wavelength shift, which is the approximate stability of the spectrometer during a run. This is substantially smaller than the 2A resolution of the spectrometer.

The result of these calculations is shown in Fig. 4 showing the apparent Doppler shift during this period. The larger scatter on the right half of the graph is partially due to a long series of poor spectra as the DGS was being debugged, as well as the reduced number of reference spectra (one vs four or so) being taken each night.

## 6. Emission Peak Evolution

Data from the Cowley paper and updated with the observed primary eclipse timing indicates that periastron for the AZCas system should occur on or about March 2023 (Mallama 2022). In fact, the Ha emission continues to build (Figure 3) until June 18, 2023 to an amplitude of about 6X, when the normalized background begins decreasing. It is worth noting in Fig 3 that the curve is steeper on the red (right) side, as compared to the left (blue) side: There is a distinct asymmetry in the curve.

Using the software tool “FindGraph”, we fitted the emission curves from each observing session to an “Aysmmetric Pearson” curve. This gave a somewhat better fit than asymmetric Gaussian, Sigmoidal, or Power peak curves, also available in FindGraph. Because FindGraph does not have a functioning external control system, we used a macro program (“MacroRecorder”) to semi-automate the fitting process. The results for each day of data in 2023 and selected days from 2022, and for each of the seven coefficients are shown in Figure 5. Fitting equation shown in the inset below.

$$y = \begin{cases} a + \frac{b}{\left[1 + \left|\frac{c-x}{d}\right|^2\right]^{\frac{1}{2}} \left[2^{\frac{1}{2}} - 1\right]} & x < c \\ a + \frac{b}{\left[1 + \left|\frac{c-x}{h}\right|^2\right]^{\frac{1}{2}} \left[2^{\frac{1}{2}} - 1\right]} & x > c \end{cases}$$

- Black diamonds show the zero offset in this region from the normalized spectrum. During this period the offset has a value of about 1.0 to 1.2.
- Red squares show the peak amplitude above the offset. This starts at a value of about 1, and rises through the year to an amplitude of about 6 on June 18, 2023.
- Yellow triangles show the wavelength “center” of the peak. The data were taken

from each night's spreadsheet. The wavelength in each case was represented in Angstroms, but the "center data" is the number of wavelength data points from the beginning of the data set. The average shown is about 15, with a +/- scatter of about 1. Most of this variation is due to a +/- one division ( $\approx 0.4\text{\AA}$ ) scatter in the wavelength calibration of each data set. There is no sign of a trend in this parameter that might show a trend in the center wavelength of this emission peak.

- Pale blue x is a parameter closely related to the left (blue) width of the emission peak. A larger value indicates that the width is increasing. In the final month of the amplitude rise, this shows a large rise in the apparent width in the blue side of the emission peak.
- Brown squares show an unused second fitting parameter (g) from the blue side.
- Brown diamonds show the relative width on the right (Red) side of the curve. In the final several weeks before June 18, again there is an increase, similar to (but smaller) than the increase on the left (blue) side.
- Dark green, similar to brown squares, shows the unused second fitting parameter (k) on the red side.

**Figure 5 is at the end of the paper.**

In summary, as periastron is approached, with the normalized spectrum  $\approx 1$ , the Ha peak rises from around 1-2 up to  $\approx 6$ . During this change, the left (blue) side of the Ha peak increases in width substantially greater than does the red side of the peak.

One of the bigger questions is why there is such a large discrepancy between the predicted periastron date March 2023 (Mallama 2023), and the date of greatest amplitude of this emission feature of June 18, 2023. Is this some form of geometric effect, or does it reflect an error in the periastron date? If the latter, is it within the expected error limits?

## 7. Photometric Observations

The photometric observations have been made more difficult by significant equipment issues as well as necessary changes in the equipment (eg., converting several of the filters from glass to evaporated film filters to improve operational life in the humid environment), and the failure of the initial camera requiring a different camera with a bigger chip and

modifications to the optical train. Further, Maryland skies are not very good, thus very often limiting the quality of photometric observation.

One of the most crucial photometric measurements was of the primary eclipse, which fortunately came at a time of minimal equipment problems and relatively good weather. The result is an excellent light curve in all four colors. During the eclipse another feature of the system was shown—namely, the Ha emission feature discussed above continued without change. That is, the Ha emission feature is clearly not part of the blue star and is likely located on or near the red star. No other changes in the two spectral bands were observed during the eclipse except, of course, for the disappearance of short (blue) spectral wavelength signals from the blue star during the eclipse.

Note that the secondary eclipse (blue star passing in front of the red star) will occur in several more years. However, because the blue star has a diameter of only a few percent of the red star, it will diminish the red star light by only by the ratio of a few percent squared. This small obscuration, combined with likely minor variations in the red star brightness, will likely render the secondary eclipse extremely faint and unlikely to be observable.

**Figure 6 is at the end of the paper.**

## 8. Conclusion

This extended AZCas project is yet another demonstration of what an amateur can do, even with relatively modest equipment. While it is disappointing that there has been so little interest in this star by either the professional or amateur community, it is also satisfying (so far as I know) to be the only human to have observed the eclipse last year. Our data on this system are available to any analyst with the proper skills to derive revised system parameters.

Long live AZCas!

## 9. References

Cowley 1977. A.P. Cowley, J.B. Hutchings, D.M. Popper. The Masses of Cool Supergiants: the Interacting System AZ Cassiopeiae p.(882-895) Dec 1977 ASP

Mallama, Tony. Private communication re AZCas timing predictions.

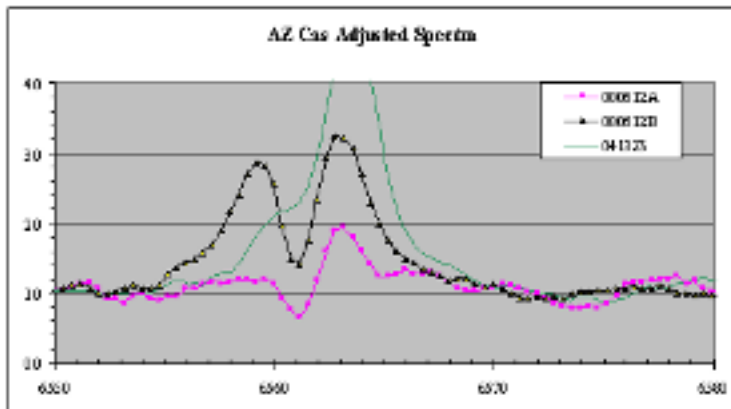


Figure 1. AZ Cas upset.

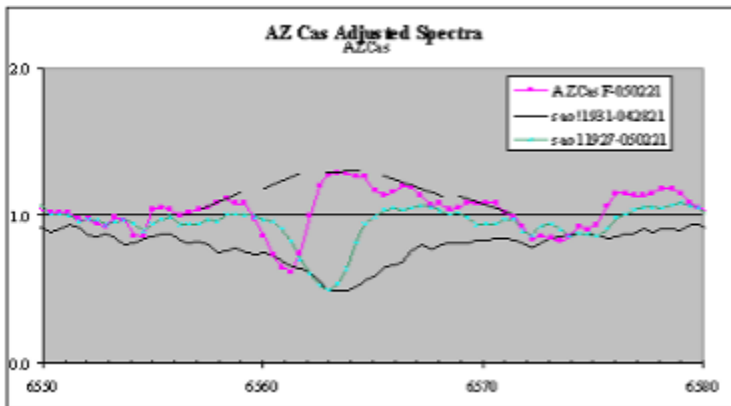


Figure 2. AZ Cas H-alpha features.

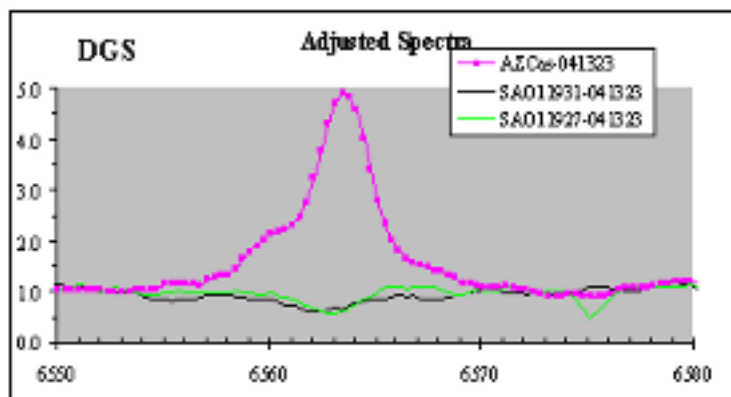


Figure 3. AZ Cas H-alpha near periastron.

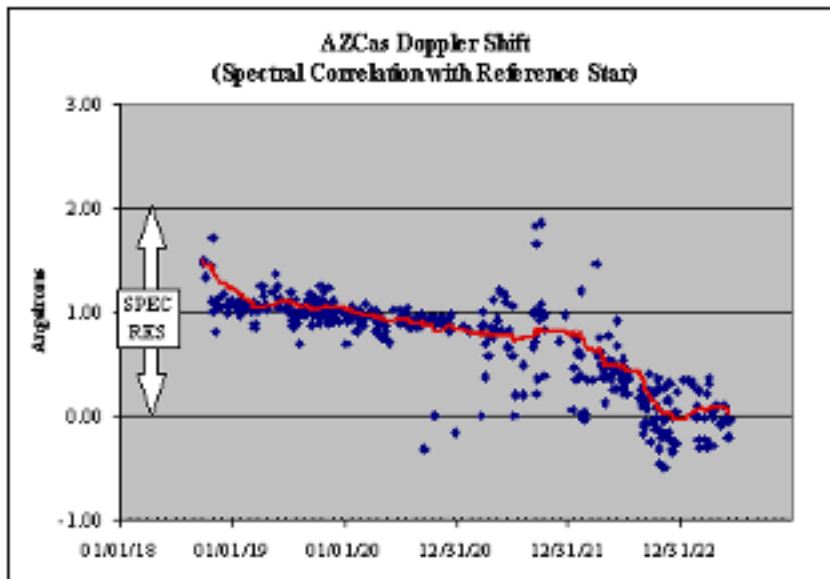


Figure 4. Spectral Doppler Shift.

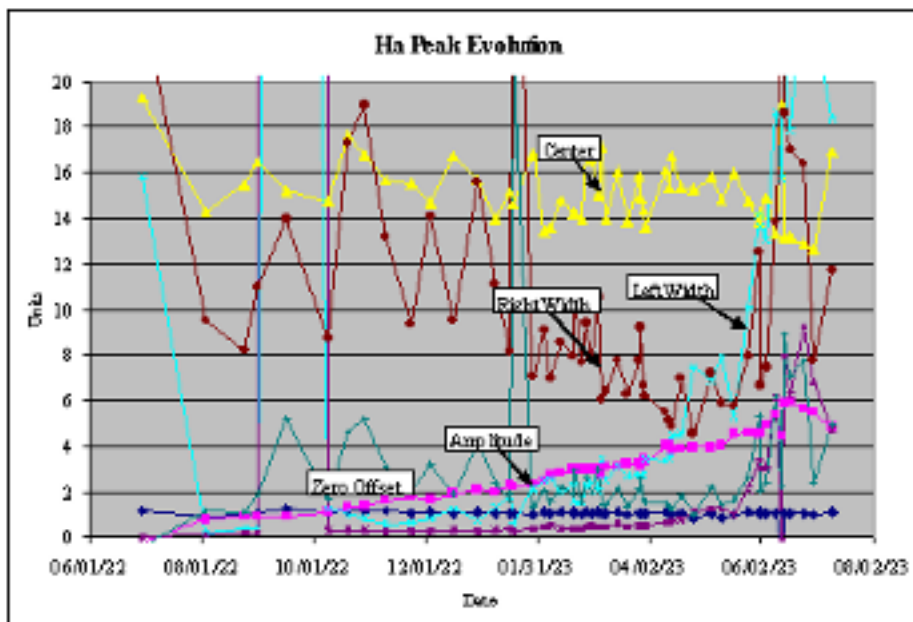


Figure 5. H-alpha peak emission evolution.

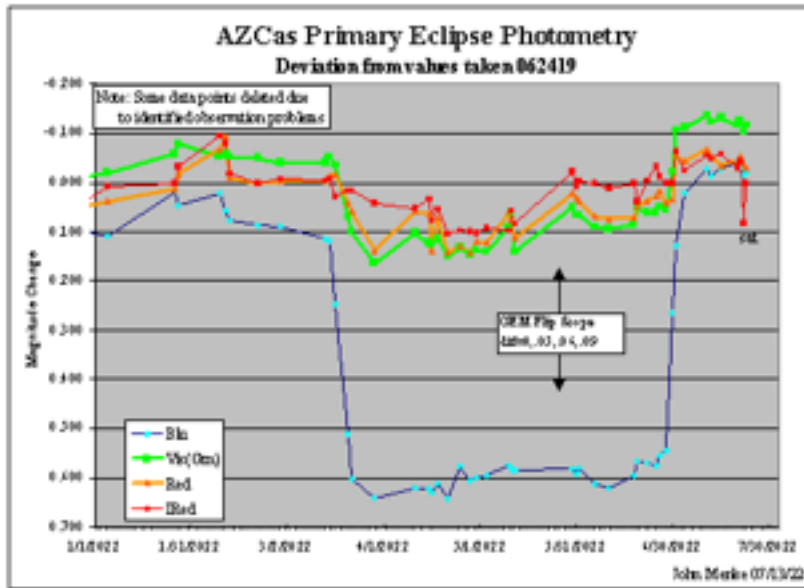


Figure 6. AZ Cas primary eclipse.

# Spectroscopic observations of the 2024 eclipse of V695 Cyg

Robert K. Buchheim  
Lost Gold Observatory,  
Gold Canyon, AZ (USA)  
Bob@RKBuchheim.org

---

## Abstract:

The eclipsing binary star V695 Cyg = HD192577 = 31 Cyg is one of the “Giants of Eclipse” (Ake & Gunn, 2015, Eds.). In February 2024, it began its once-per-decade eclipse, during which the hot component (B3V) passes behind the cool supergiant component (K4 Ib). I report here on spectroscopic observations of the event, from a few days before occultation of the hot star, to mid-eclipse. The disappearance of the hot component is clearly seen in the spectra. Follow-on observations will be made for about two months following reappearance of the hot star. These will (hopefully) map the chromospheric features in the red giant’s atmosphere/wind that are encoded onto the hot star’s spectrum.

---

## 1. The V695 Cyg system

V695 Cyg is an eclipsing binary system consisting of a red supergiant (K4Ib) star and a hot dwarf (B3V) star, in a  $\approx 10$ -year orbit. During the 2024 eclipse event, the blue star disappears behind the red supergiant, as illustrated in Figure 1. These eclipses provide some interesting opportunities. During the few days between 1<sup>st</sup> contact and 2<sup>nd</sup> contact, we can watch the spectrum change as the hot star is gradually occulted. During the total eclipse, we can watch for changes in the spectrum and brightness of the supergiant star, uncontaminated by the hot dwarf star’s light. Then, during the couple of months following 4<sup>th</sup> contact, the hot dwarf star’s light is passing through the giant’s outer atmosphere and wind, acting as a moving “probe” of the tenuous stellar atmosphere. A wonderful history of the study of this star is given by Griffin (2008).

This is a bright target:  $V_{\text{mag}} \approx 3.80$ , and  $B_{\text{mag}} \approx 5.08$  (when out of eclipse).

AAVSO Alert Notice 851 was released on Feb 14, 2024, requesting time-series photometry and spectroscopy throughout the eclipse. Of specific interest was U- and B-band photometry, and spectroscopy shortward of  $4500\text{\AA}$ . The goal is to use these observations, in conjunction with HST observations in the UV, to determine the circumstellar absorption from the supergiant’s wind.

The circumstances of the 2024 eclipse found the star very low in the east before morning twilight. I could only start observing it a week before first contact (hence missing most of the first “chromospheric eclipse” phase). Happily, I was able to record spectra as the hot star disappeared behind the red giant.

Several spectra taken during the total eclipse phase didn’t show any obvious variations in the supergiant star (despite photometric B-band variations of  $\pm 0.1$  mag).

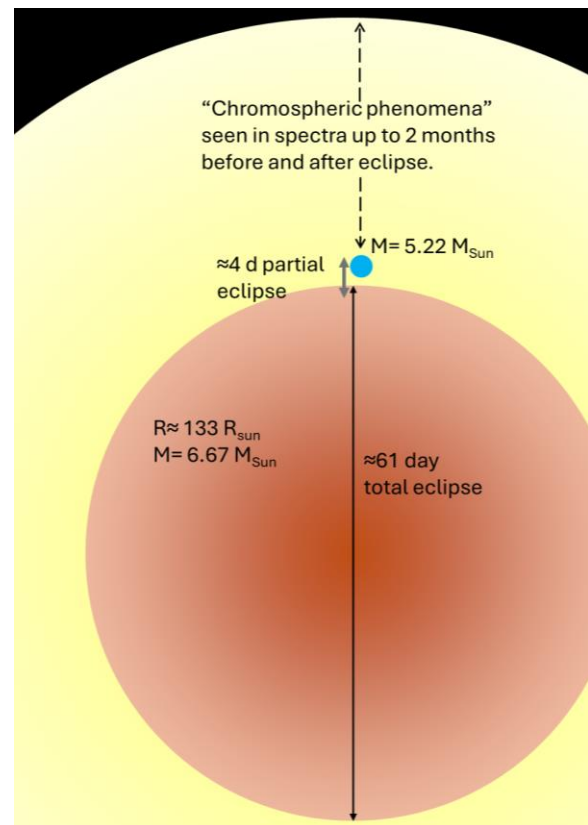


Figure 1: Schematic overview of the V695 Cyg system

The transition from 3<sup>rd</sup> contact to 4<sup>th</sup> contact was observed during UT2024-04-17 to -23. Observations will be continued with the goal of monitoring the chromospheric eclipse at a nightly cadence for at least a couple of months following 4<sup>th</sup> contact.

## 1.1 Prior Eclipse Observations

Observations of prior eclipses have shown pronounced changes in spectral absorption features during the “chromospheric eclipse” phase, as the hot star’s light is modified by passing through the supergiant’s atmosphere on its way to us. As the apparent separation between stellar limb and the hot star grows, the hot star’s light is probing the stellar atmosphere at increasing distances from the stellar surface (hence its more tenuous layers). Changes in the spectrum are indicative of changes in the temperature and density of the supergiant’s atmosphere vs. height above the stellar surface.

In the 1951 eclipse, Underhill (1954) saw Fe I lines ( $\lambda=3920\text{\AA}$ ,  $3922\text{\AA}$ ,  $3927\text{\AA}$ ,  $3930\text{\AA}$  appear just a few days before 2<sup>nd</sup> contact: “barely visible” 12 days before 2<sup>nd</sup> contact, but “quite distinct” at 10 days before 2<sup>nd</sup> contact. In contrast, the lines of Ca II (H) and (K) were apparent two to three months before 2<sup>nd</sup> contact. In the few days just before 2<sup>nd</sup> contact, a variety of other lines also appeared in the spectrum (Ti I, Cr I, Zr I, V I).

Bauer (1994) reported that during the 1982 eclipse, the strength of the Balmer lines changed as the chromospheric eclipse proceeded. While most of the Balmer absorption in the out-of-eclipse spectrum is due to the B3V star, some of it is attributed to the chromospheric absorption (from 2<sup>nd</sup> contact to about 16 days after 2<sup>nd</sup> contact). Bauer (1994) also measured radial velocity of the chromospheric lines: a few km/s offset (presumably due to the K4I star’s rotation), sometimes accompanied by satellite lines offset by up to 100 km/s.

During the 1994 eclipse, Eaton & Bell (1994) saw an array of shell lines, whose strengths changed as the B star probed different positions relative to the K star’s limb. These included Ca II K ( $3933.6\text{\AA}$ ) and H ( $3968.5\text{\AA}$ ), other Ca II lines ( $3736.9\text{\AA}$ ,  $3706.0\text{\AA}$ ), Hydrogen Balmer lines ( $3970.07\text{\AA}$ ,  $3889.0\text{\AA}$ ,  $3835.4\text{\AA}$ ), and a variety of Ti II lines and Fe I lines. Their paper also describes the physics and mathematical approach to translating the time-series spectra into a model of the chromosphere’s properties.

Griffin (2008) notes the history of observed radial velocity shifts in the chromospheric lines, that suggests “mass motions of large bodies of gas in the atmosphere if the K star”, rather than a simplistic radial wind. Reported velocities range up to 100 km/s.

## 2. Equipment and Processing at Lost Gold Observatory

The 2024 eclipse of V695 Cyg seemed like a great opportunity to apply my Shelyak UVEX spectrograph. The 600 l/mm grating was set to center wavelength  $\lambda_c \approx 4700\text{\AA}$ , giving a useful spectral range of  $\Delta\lambda \approx 3640 - 5800\text{\AA}$ . The spectral resolution is  $R=\lambda/\Delta\lambda \approx 1200$  in this range. The science camera on the UVEX is a ZWO ASI-183MM. The UVEX, with its Calibration Module and Guiding Module, is mounted on a TPO 16-inch RC telescope, as shown in Figure 2.

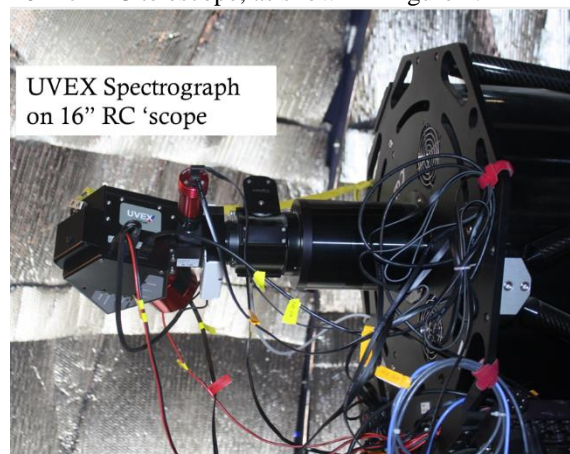


Figure 2: UVEX set up on TPO-16-inch RC at Lost Gold Observatory

Because of the brightness of the target, typical exposures were 15-30 sec (CMOS camera,  $G=200$ ), depending on seeing and sky transparency. In order to maximize the SNR in the short-wavelength portion of the spectra, each observation session accumulated at least 60 minutes of shutter-open time.

Wavelength calibration uses a quadratic fit to a set of 14 Ne-Ar lines, ranging from  $3868\text{\AA}$  to  $5739\text{\AA}$ . Cal Lamp images were taken before and after the target sequence, with the average CalLamp image used to determine the calibration equation. Typical formal calibration error is  $\sigma \approx 0.10\text{\AA}$ . The UVEX calibration is pretty stable. The typical intra-night shift (temperature change and pointing changes, including a meridian-flip) is less than  $0.7\text{\AA}$ . The change from night to night is less than  $\pm 2\text{\AA}$ .

Each night’s observation of the target is accompanied by observation of “Reference Star” HD180163 (typically 30sec X 25 exposures to achieve good SNR). This star is  $V_{mag}= 4.4$ , SpType B2.5 IV, located near the target (separation =  $13.3$  deg), so it provides a good representation of the atmospheric path through which the target is observed. The MILES spectrum of HD180163, along with its raw spectrum



profile, is used to determine the Instrument+Atmospheric response function, which is then used to correct the observed target spectrum to exo-atmospheric Relative Flux.

Image processing (dark subtraction, geometric correction for tilt and slant, average-combine of multiple images) and spectral processing (wavelength calibration, sky subtraction, determination of Instrument+Atmospheric response, and response-correction of target spectra) are all done with the software “ISIS” (Buil, 2021, v6.1.0) following standard procedures.

Relative-flux spectra are flux-calibrated based on the observed B-magnitude of the target at the time of observation, following the procedure of Boyd (2020). The CalSpec Vega spectrum is used as the B=0 magnitude reference.

### 3. Photometry

Figure 3 [in the Section “Page Width Figures” at the end of this paper] shows an annotated lightcurve of V695 Cyg drawn from the AAVSO database (Kloppenborg, 2023), spanning about one month and centered at the onset of totality (= 2<sup>nd</sup> contact, when the K4Ib star completely occults the B3V star). It shows the time period pre-eclipse, the transition to disappearance of the B3V star, and the fully-eclipsed state.

The brightness drop from pre-eclipse to totality is a strong function of the observation filter/band: tri-color Green  $\Delta TG \approx 0.11$  (quite small), tri-color Blue  $\Delta TB \approx 0.18$  (only marginally greater), and in Johnson B-band is much larger  $\Delta B \approx 0.467$ . The observation that blue light is preferably lost is consistent with the occultation of the hot (B3V star), but I was surprised that the drop in tri-color blue (TB band) is so much smaller than the drop in Johnson B-band. This will be discussed in Section 5.2.

### 4. Spectroscopy

Representative spectra of V695 Cyg are shown in Figure 4 [in the Section “Page Width Figures” at the end of this paper]. The out-of-eclipse spectrum shows both stars (taken about a week prior to 1<sup>st</sup> contact on UT 2024-02-16). The spectrum in total eclipse shows just the K4Ib star, since the B3V star is occulted by the red supergiant (taken on UT 2024-03-21). These spectra are shown as “relative flux” vs. wavelength, and have been cropped to show only the blue half of the complete observed spectrum, since that is where the features of interest appear.

These two spectra clearly show the effect of the disappearance of the B3V star.

Figure 5 provides an illustration of the circumstances of all of the spectra reported in this paper:

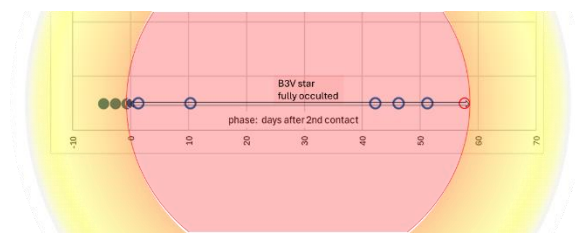


**Figure 5: Illustration of the hot star position relative to supergiant, for the spectra described in this paper.**

Figure 5 is illustrative – not definitive – showing the stars approximately to scale. However, there is no evidence that I am aware of that the eclipse is central (as simplistically shown in Figure 5). The spectra span the time from a week before 2<sup>nd</sup> contact, through the total phase of the eclipse, ending just before the anticipated 3<sup>rd</sup> contact.

Figure 6 [in the Section “Page Width Figures” at the end of this paper] shows a compilation of the spectra taken during the total phase of the eclipse, showing just the spectrum of the red supergiant (the B3V star being totally occulted). All seven “total eclipse” spectra overlay each other almost perfectly. The implication is that there were no observable changes (at  $R \approx 1200$ ) in the supergiant’s spectrum over this interval of time.

The reappearance of the blue star (from 3<sup>rd</sup> contact to 4<sup>th</sup> contact) is shown in Figure 7 [in the Section “Page Width Figures” at the end of this paper]. This nightly series of spectra shows the start of the “chromospheric eclipse”, that will be monitored for the next couple of months.

## 5. Analysis

### 5.1 Brightness of the component stars

The AAVSO B-band photometry facilitates determination of the individual brightness of each star.

Before the eclipse, we see flux from both stars:  $[F_K + F_B]$

When fully eclipsed, we see flux from only the cool (K4I) star:  $[F_K]$

Using the B-band photometry,

$$\Delta mag = -2.5 \log\left(\frac{[F_K]}{[F_K + F_B]}\right) = 0.467$$

$$\text{call } A = 10^{(-\Delta mag / 2.5)}$$

and solve to find that:  $F_B = \left(\frac{1-A}{A}\right) F_K = 0.537 F_K$

When the hot star is fully occulted, the observed Bmag of the K4Ib star (alone) = 5.350

Since the hot star provides 0.537X the flux of the cool star, their individual magnitudes (in B-band) are related by:

Bmag of B3V star alone = 5.350 - 2.5\*log(.537) = 6.024

This result will be used to compute a synthetic spectrum for V695 Cyg in Section 5.3 below.

## 5.2 $\Delta B$ versus $\Delta TB$

V695 Cyg's drop in brightness during eclipse is 0.467 mag in B-band, but only 0.180 mag in the tri-color TB band. Why? The answer seems to be related to the very red color of the star, the fact that the eclipse preferentially removes blue light, and the noticeably different spectral passbands of the "B" vs "TB" bands.

Unlike the Johnson B-band, there is no "standard" response curve for tri-color sensors. Cardiel, et al (2021) examined a large collection of DSLR models, and computed "average" response curves for TB, TG and TR. I also have a CMOS TB band response curve for a ZWO camera (used with a UV/IR blocking filter) from Hawkins (2023, personal communication).

Figure 8 [in the Section "Page Width Figures" at the end of this paper] shows the two tri-color response curves and the Johnson B-band response (all normalized to peak response = 1.0). The two "TB" band response functions are noticeably different from each other, and they both differ significantly from the B band in terms of central wavelength and short-wavelength response. The tri-color response curves are negligible at wavelengths less than 4000Å, whereas the B-band response extends to about 3800Å

Figure 9 [in the Section "Page Width Figures" at the end of this paper] shows these response curves overlaid on the spectrum of V695 Cyg, in-eclipse and out-of-eclipse (plotted as relative flux).

The TB curves over-emphasize the wavelengths longer than 4400Å, where the eclipse has a very small effect; and completely miss the loss of flux below 4000Å during eclipse. Thus, tri-color TB photometry is expected to see a much shallower eclipse than B-band does.

## 5.3 Creating a synthetic spectrum of the target

It is well accepted that V695Cyg consists of two stars, spectral types B3V and K4Ib. Knowing their individual magnitudes (from the calculations above), I created a synthetic spectrum that illustrates the

anticipated spectrum of V695 Cyg. In order to ensure that it matches the resolution of my UVEX spectrograph, I made spectra of two (single) stars: HD 020365 which is a B3V dwarf, and HD 017506 which is a K3I supergiant (not exactly identical to the supergiant component of V695 Cyg, but the closest analog that was available). These two spectra were flux-calibrated to B= 6.025 and B= 5.350 respectively, and summed, as shown in Figure 10 [in the Section "Page Width Figures" at the end of this paper].

The synthetic spectrum shows that the B3V component dominates the flux at wavelengths below about 4300Å (as expected). But even at these blue wavelengths, the red supergiant's contribution is not negligible. Its features are obviously present in the combined spectrum.

## 5.4 Flux-calibrated spectra from observations

A more realistic spectroscopic view of the eclipse is obtained by flux-calibrating each spectrum to the B-band photometry. Where necessary, gaps in the photometry were linearly interpolated to the time the spectra were taken. The observed time-series spectra from pre-eclipse to complete occultation of B3V star are shown in Figure 11 [in the Section "Page Width Figures" at the end of this paper].

## 5.5 Evidence of chromospheric features in pre-eclipse spectra

In Figure 12 [in the Section "Page Width Figures" at the end of this paper], I overlay the observed pre-eclipse spectrum of V695 Cyg (in black) and the synthetic spectrum (sum of two stars). In general, the synthetic spectrum is a pretty good match to the "observed" spectrum (UT2024-02-16) taken a few days before 1<sup>st</sup> contact.

However, close examination of the blue-wavelength portion of this graph shows some pronounced differences, highlighted in Figure 13 [in the Section "Page Width Figures" at the end of this paper].

In particular, the Ca II (K) line is observed to show a sharp, deep absorption feature that is not seen in a normal B3V spectrum, nor in a normal K4Ib spectrum. This sharp deep absorption feature is – presumably – the signature of the blue star's light being absorbed as it passes through the lower atmosphere of the supergiant star.

Similarly, there is an absorption feature at  $\lambda \approx 3671\text{Å}$ : presumably absorption by Ti II within the

supergiant’s atmosphere. A similar, but less intense, feature at  $\lambda \approx 3859\text{\AA}$  may be the signature of Fe I in the supergiant’s atmosphere.

Assuming these features are, indeed, as tentatively identified, they will be measured and mapped with daily spectra as the B3V star reappears and passes through different portions of the supergiant’s atmosphere.

Eaton and Bell (1994) described an approach to computing the absorption profile of the supergiant’s atmosphere from its effect on the hot star’s light. The concept is that the spectrum we observe is the sum of the supergiant’s spectrum, plus the hot star’s spectrum modified by the chromospheric absorption:

$$Obs(\lambda) = K4Ib(\lambda) + [B3V(\lambda) * Chromo(\lambda)]$$

Which can be solved for the chromospheric absorption:

$$Chromo(\lambda) = \frac{Obs(\lambda) - K4Ib(\lambda)}{B3V(\lambda)}$$

I use the B3V profile of HD020365, and the K3I profile of HD017506 as a surrogate for the K4Ib star, and following Eaton and Bell (1994) rectify the result to eliminate inevitable slopes in the computed chromospheric profile. The result is shown in Figure 14 [in the Section “Page Width Figures” at the end of this paper].

The enhanced absorption in the Ca II (K) line is obvious, and the blend of Ca II (H) with H $\epsilon$  is also enhanced. There are strong hints of Ti II absorption lines at  $\lambda = 3685\text{\AA}$ ,  $3759\text{\AA}$  and  $3761\text{\AA}$ .

This result is tentative but encouraging. Further work on wavelength alignment before manipulating the spectra, and identifying the features, remains in the future.

On the other hand, caution is in order: the modest resolution of UVEX may be hiding some features, and confusing others. Figure 15 [in the Section “Page Width Figures” at the end of this paper] shows a comparison of my UVEX spectrum ( $R \approx 1200$ ) with a higher-resolution spectrum from AAVSO observer Gerald Persha (PGD) with  $R \approx 7700$ . The spectrum of a red supergiant is a complicated pattern of closely-spaced absorption features, which are not properly sampled at UVEX’ resolution.

## 6. Next step: Reappearance of the B3V component

The end of the total eclipse phase (3<sup>rd</sup> contact) is predicted to occur on UT 2024-04-18. I plan to make

frequent (every 1-2 days) observations from just prior to 3<sup>rd</sup> contact through mid-May, to monitor the evolution of the chromospheric features in the spectrum.

All of the spectra from this first phase of the project have been submitted to AVSpec (see [aavso.org](http://aavso.org)), where they are freely available to all users. Future spectra will also be archived on AVSpec.

## 7. Conclusions:

The scientific value of these observations toward characterizing the supergiant’s atmosphere is still uncertain. If nothing else, this has been an opportunity to replicate some observations from a few decades ago, and it has been an educational journey.

I am pleased with the ability of the UVEX spectrograph to take good-quality spectra in the far-blue optical region.

## 8. References

AAVSO Alert Notice # 851 at <https://www.aavso.org/aavso-alert-notice-851>

Ake, Thomas B., & Griffin, Elizabeth (ed’s) “Giants of Eclipse: The  $\zeta$  Aurigae Stars and Other Binary Systems”, Astrophysics and Space Science Library 408, Springer, 2015

Bauer, Wendy Hagen, PASP 1994, “Spectroscopic Observations of the 1982 eclipse of 31 Cygni”, PASP 106,

Boyd, D., 2020 “A method of calibrating spectra in absolute flux using V magnitudes”, BAA, <https://britastro.org/wp-content/uploads/2021/05/absfluxcalibration.pdf>

Buil, Christian, 2021: Integrated Spectrographic Innovative Software (ISIS), <http://www.astrosurf.com/buil/isis-software.html>

Cardiel et al, “Synthetic RGB photometry of bright stars: definition of the standard photometric system and UCM library of spectrophotometric spectra” MNRAS, 2021 (arXiv:2103.17009v1)

Eaton, Joel A. and Bell, Coretta, “The 1992/93 Eclipse of 31 Cygni”, Astronomical Journal, v108, n6, December 1994

Griffin, R.F. 2008, “Spectroscopic binary orbits from photoelectric radial velocities, Paper202: 31 and 32 Cygni”, The Observatory, v128,

Kloppenborg, B. K., 2023, Observations from the AAVSO International Database, <https://www.aavso.org>

Underhill, Anne B., MNRAS 1954 “On the development of the Fe I chromospheric lines during the 1951 eclipse of 31 Cygni”, MNRAS, 114,

## 9. Acknowledgements:

I acknowledge with thanks the variable star observations from the AAVSO International Database contributed by observers worldwide and used in this research.

This research has made use of the SIMBAD database, operated at CDS, Strasbourg, France.

This research made use of the STILISM on-line tool for determination of interstellar reddening, provided by the Observatoire de Paris.

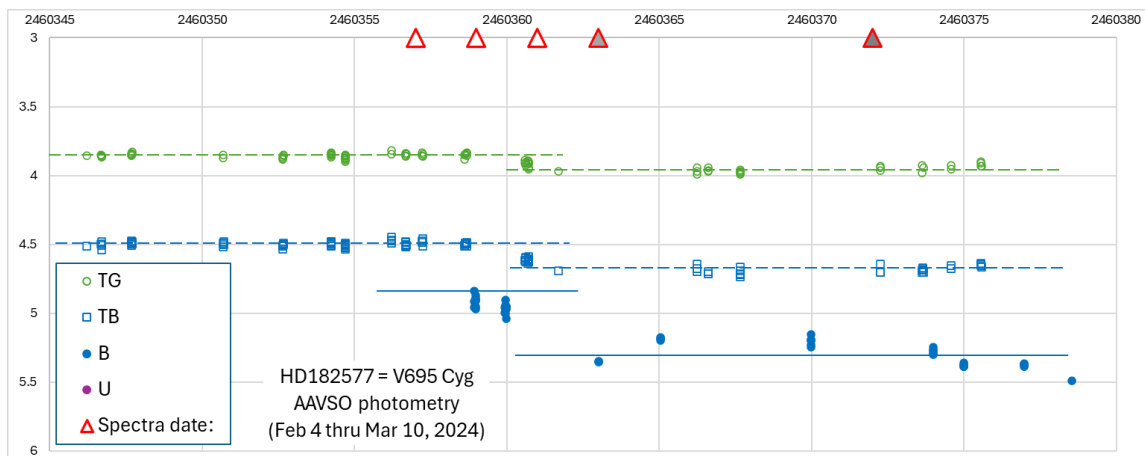


Figure 3: Lightcurve (from AAVSO) of the start of the 2024 eclipse.

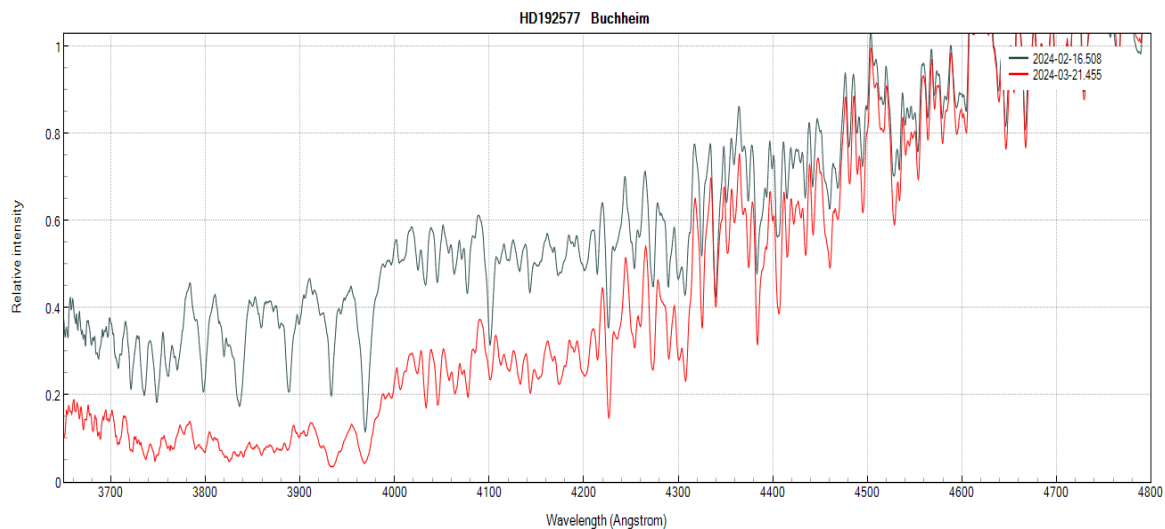


Figure 4: Representative spectra of V695 Cyg, out-of-eclipse and during total eclipse.

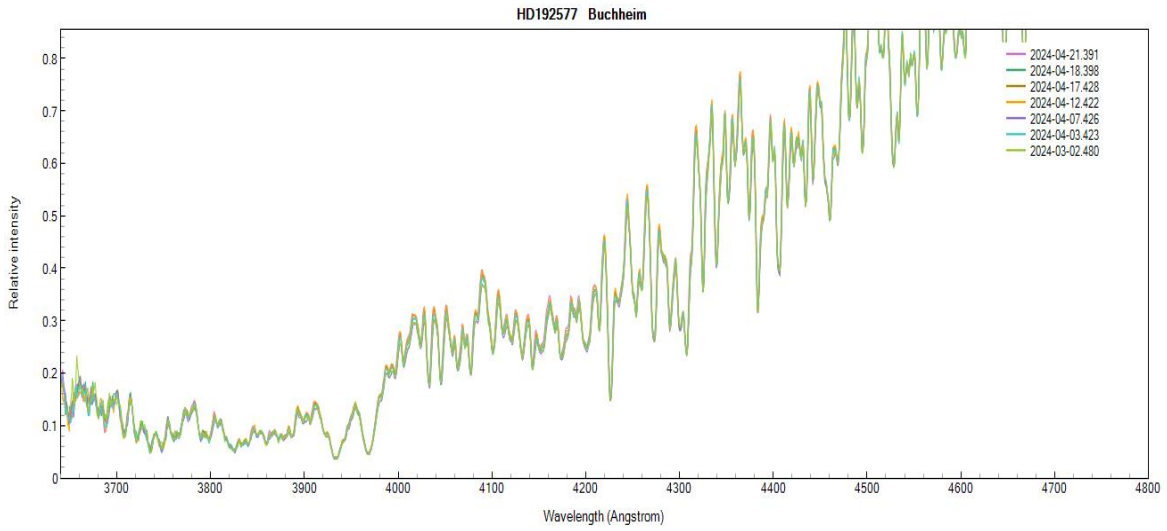


Figure 6: Compilation of spectra taken during totality, showing the K4 Ib star only.

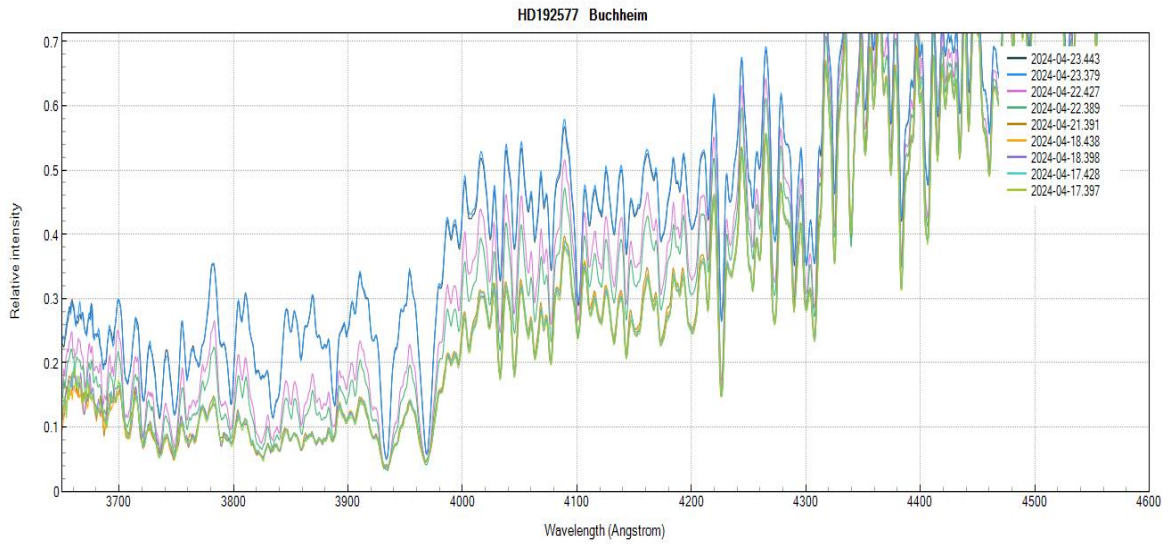


Figure 7: Time-series spectra showing the reappearance of the B3V star (approximately 3<sup>rd</sup> contact to 4<sup>th</sup> contact).

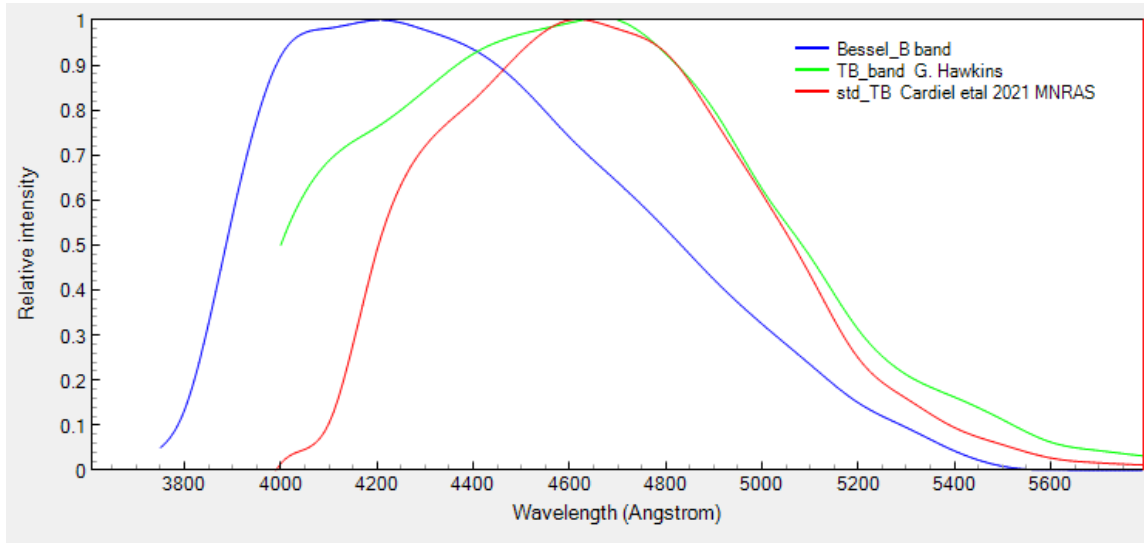


Figure 8: Tri-color “TB” response compared to Johnson B-band response.

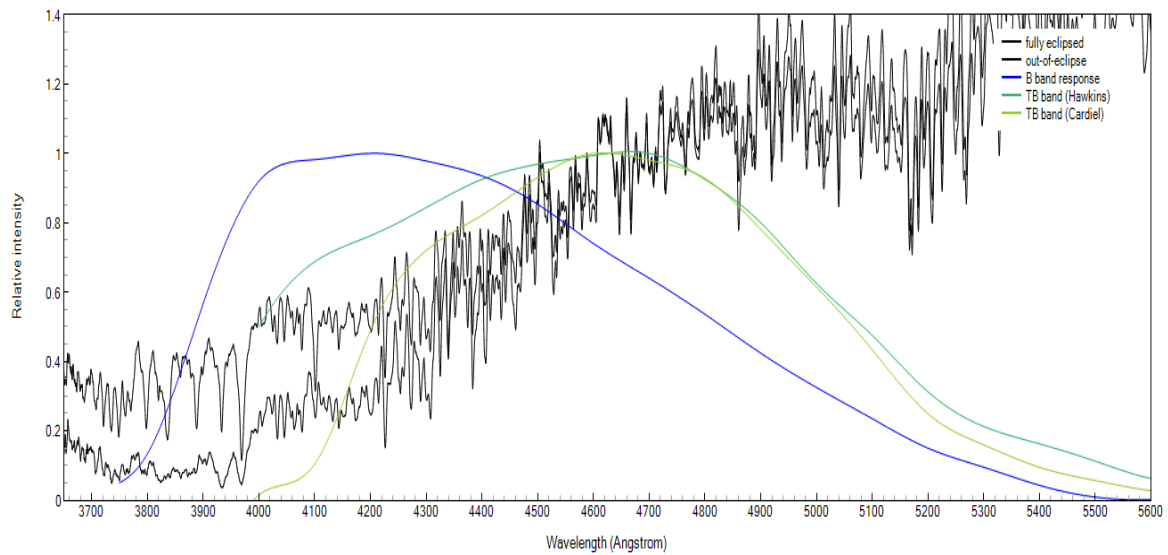


Figure 9: Photometric passbands compared to spectra profile of V695 Cyg.

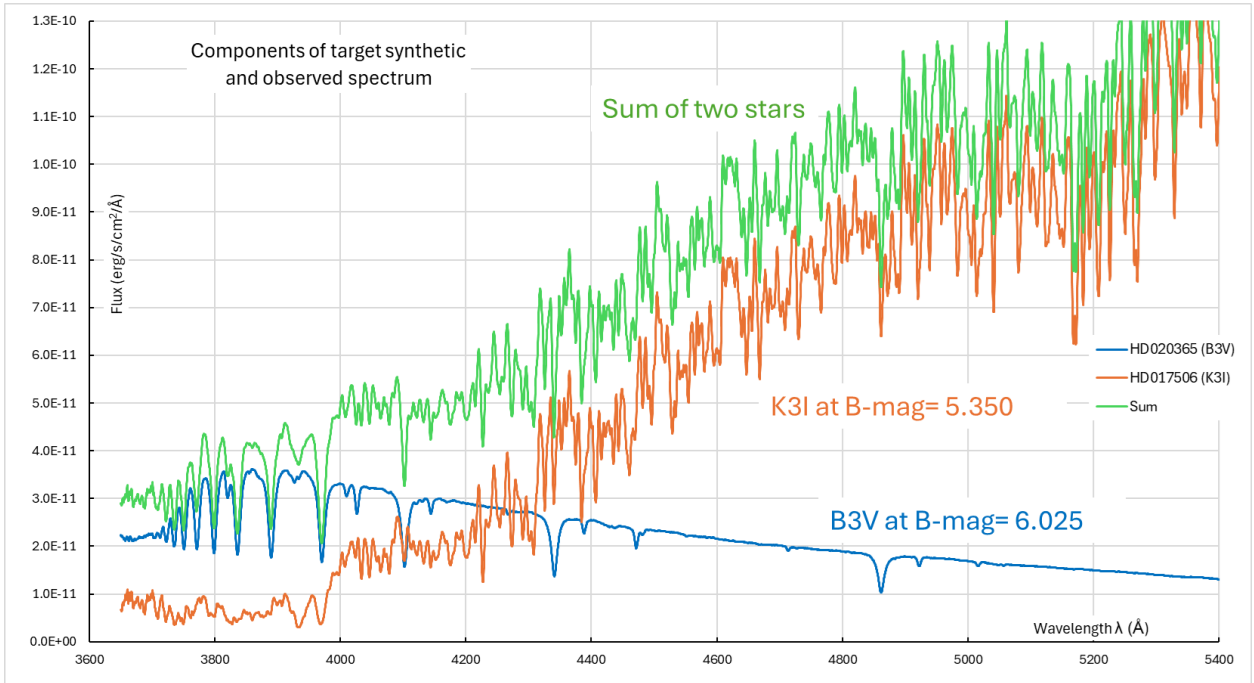


Figure 10: Creation of synthetic spectrum for B3V + K4Ib (scaled to the component magnitudes of V695 Cyg).

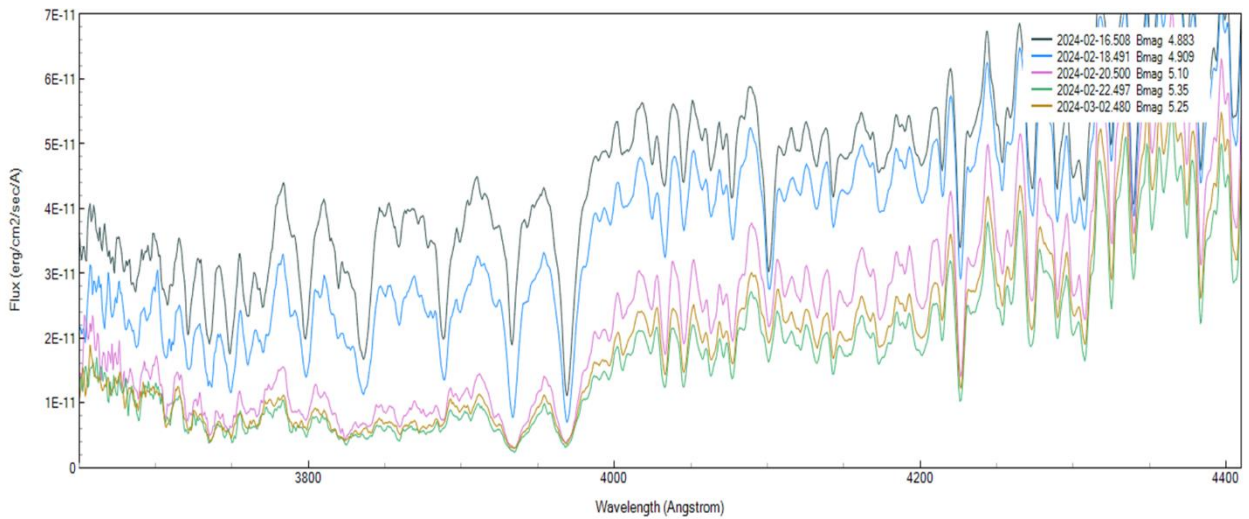


Figure 11: Flux-calibrated time series spectra across the start of the eclipse, showing the gradual disappearance of the hot (B3V) component.

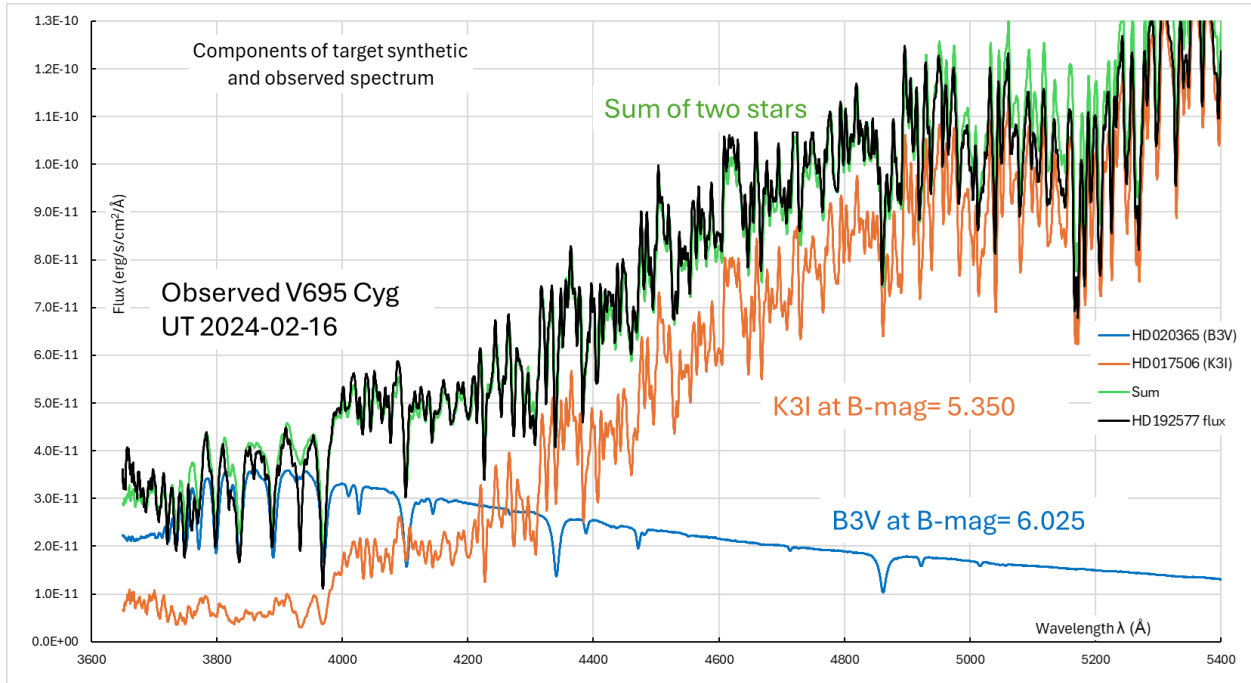


Figure 12: Observed spectrum of V695 (out-of-eclipse, in black) is well-matched by the synthetic “B3V + K4Ib” spectrum shown in Figure 9.

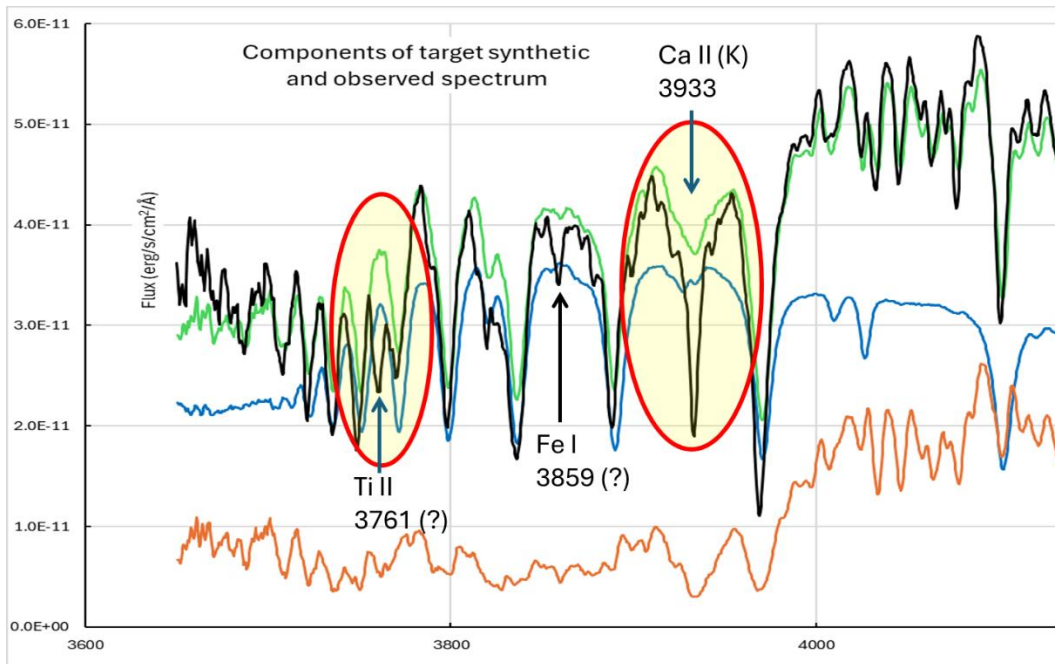
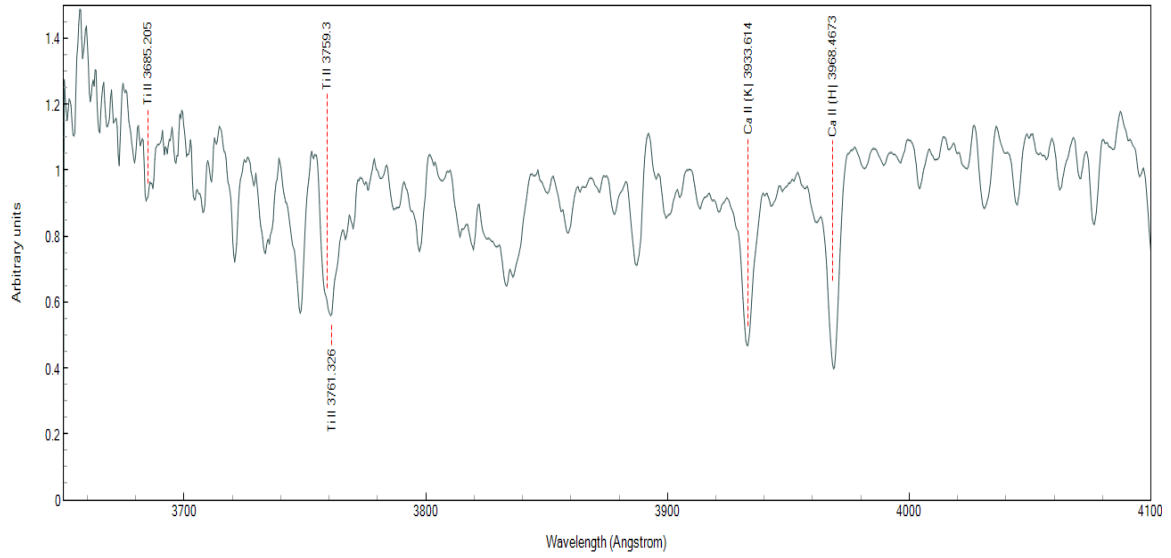
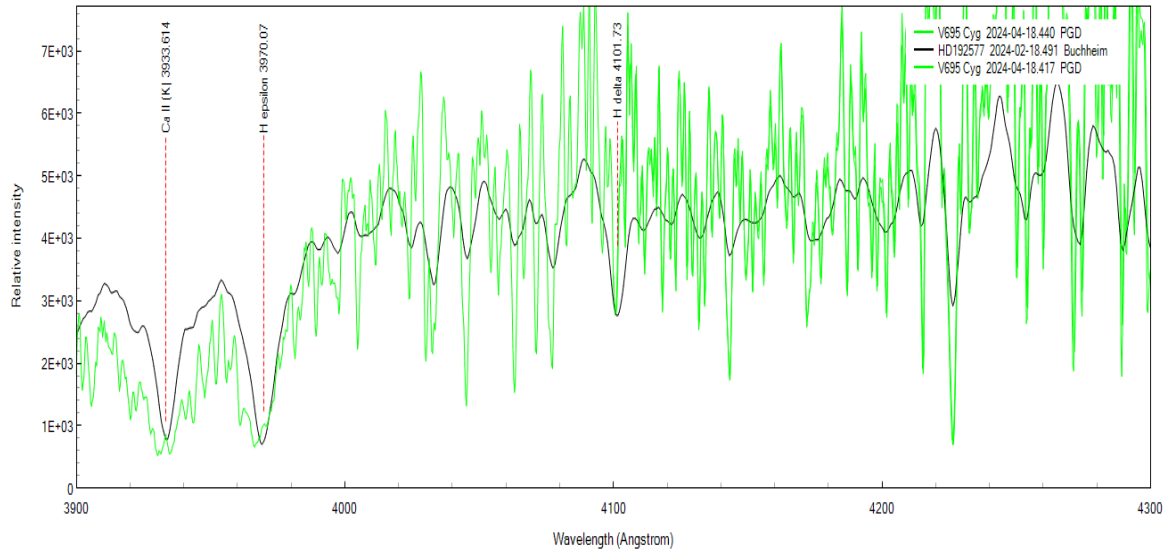


Figure 13: Evidence of chromospheric features in the observed spectrum Ca II K, Ti II(?) and Fe I (?).





**Figure 14: Chromospheric absorption, calculated from spectrum observed on UT 2024-02-16 (4.86 days before 1<sup>st</sup> contact).**



**Figure 15: Comparison of UVEX resolution ( $R \approx 1200$ ) with  $R \approx 7700$  spectrum of V695 Cyg, taken within a few hours of each other.**